Development of Ion Conducting Polymer Temperature Sensors

Thesis by

Nicole Juliet Higdon

In Partial Fulfillment of the Requirements for
the Degree of
Doctor of Philosophy in Chemistry

CALIFORNIA INSTITUTE OF TECHNOLOGY
Pasadena, California

2026
(Defended June 2nd, 2025)

ACKNOWLEDGEMENTS

First, I would like to thank my advisor Professor Chiara Daraio. You energetically welcomed a chemist into your engineering lab and provided me with the support, encouragement, and guidance to find my stride. You enabled me to work on a variety of hard problems and I learned much from you not only scientifically, but also how to manage a group and research projects. Without your mentorship and the fantastic group you have crafted, I do not know if I would be leaving Caltech with a PhD.

I would also like to thank my committee members starting with my committee chair, Professor Harry Gray. Your lectures and stories both inspired me as a scientist and left me with a greater understanding and appreciation for magic that is inorganic chemistry. Professor Mitchio Okumura, in many ways you were the first professor to welcome me to Caltech. I have learned much from working with you, teaching for you, and from our many conversations. It has always been a pleasure. Professor Hosea Nelson, I would like to thank you for the valuable insights you have provided to my work. I would also like to thank you for inviting us to utilize your laboratory to continue our work on shape memory polymers. While I have not worked directly with you much, I have had many interactions with your group and from them I have gained an appreciation of your leadership.

It takes many hands to work on interdisciplinary research and as such I would like to start this section by thanking the Daraio group as a whole. Rarely have I encounter such a welcoming and supportive environment. I would especially like to thank the following people: Vincenzo Costanza, you are an incredibly brilliant engineer and were a fantastic mentor both specifically for the HEA-AA project and grad studenting in general. Linghui Wang, your constant asking of questions pushed me to understand our systems and your knowledge of the polyelectrolyte literature is inspiring. I appreciate our many conversations. Joong Hwan Bahng, I am never going to forget the months spent working with you in the wet lab. Brian Ahn, working with you has been a pleasure and I look forward to how you will continue to push forward this project.

Thanks go to Frédéric Harny and Raphael Bingert. Our collaboration on the commercialization of HEA-AA has taught me so much. Raphael, you have left me with a strong taste for French wine and a desire to explore Europe which while my wallet does not, I greatly appreciate.

Outside of the pectin subgroup I would like to thank Max Kudisch and Gunho Kim for great conversations and for pulling me away from the ion conductive polymers to some truly fascinating work on shape memory polymers. Anthony Stephen, I have learned much from you about industry practices and have appreciated your mentorship. I would like to thank Chelsea Fox, Tommaso Magrini, Jagannadh Boddapati, and Alexander Ogren for explaining to me their own research in depth and patiently trying to teach the chemist how to think like a mechanical engineer. Israel Kellersztein, you have been a joy to work with over the many years, and I look forward to seeing what you do soon, Professor. The work in the lab would hit a standstill without the hard efforts of Carolina Oseguera.

Beyond the Daraio group, I would like to thank Alexandra Barth, Gautam Stroscio, and Ruben Mirzoyan. I learned a lot of chemistry from you all and will never forget the time we spent in the basement of Noyes.

Special thanks go to Alison Ross and Professor Brian Stoltz. Without their help and support the bureaucratic complexities of grad school would have been much more daunting.

I would like to thank my advisors in undergrad starting with Professor Alison Butler. Working in your group taught me how to do real research and it fundamentally shaped me into the scientist I am today. Professor Richard Kaner, working in your lab taught me how to work on applied projects and how to think about problems simultaneously from a fundamental science and an applications viewpoint. Professor Songi Han, my time in your group was short, but from it I learned more about EPR and ODNP than I appreciated at the time.

Richard Smith, thank you for putting up with me for all these years. Eight years is a long time to live with a randomly assigned roommate. Our conversations about sensor design have helped in developing this thesis.

Seven Dupont, I would like to thank you for your friendship and for consistently reminding me that there is sunlight and things to do outside of Caltech’s sub-basements.

Finally last but most important, I would like to thank my family. To my brother Tom, I can’t even define what an impact you had on my life or how much I value our conversations and your support. To the other professional chemist who did their dissertation in an engineering lab, my sister Cara, words cannot describe how grateful I am for your support, nor how much I have learned from you. To my mom and dad, I would not be the person I am today, and would not be standing at Caltech if not for you. From you I learned the curiosity and ingenuity that has enabled this career on the edge of science and engineering, and for that I am eternally grateful.

ABSTRACT

Improvements to flexible polymer temperature sensors have the potential to substantially improve human health through a variety of devices such as core body temperature sensors, temperature mapping, and IR imaging. In this thesis we examine a novel resistive ion conducting polymer-based temperature sensitive material. This material outperforms vanadium oxide and other leading temperature sensing materials for the temperature range 15-65 °C allowing for high performance use in medical devices. Unlike conventional materials, this polymer can be readily integrated into flexible devices.

In this thesis we explore both the fundamental science and applications of this material. In Chapter 2 of this thesis, we explore the electrical and chemical properties of this polymer through impedance spectroscopy, Fourier transform infrared spectroscopy, and thermogravimetric analysis. We explore the formation of interpolymer complexes exhibited by this copolymer. We demonstrate its application to temperature mapping and infrared light detection. Chapter 3 explores the effects of water on ion transport within the polymer. Demonstrating that the metal cation is the charge carrier, and that water uptakes primary effect is the lowering of the polymers' glass transition temperature. Through visible spectroscopy we additionally demonstrate tetrahalocobaltate formation in this and a related polymer. In Chapter 4, we demonstrate an ultra-thin dual heat flux core body temperature sensor leveraging this polymer. We evaluate its response time then verify its functionality by leveraging an agar tissue phantom. We explore the formation of thin film sensors in Chapter 5. We demonstrate a simple sensor with a thin film architecture and discuss in depth the engineering challenges presented by commercialization of this architecture in the context of roll-to-roll fabrication. We demonstrate the sensor is strongly affected by external humidity and develop and demonstrate humidity buffer materials inspired by humidity fixed point salt solutions to address this problem.

In conclusion this thesis provides a window into the mechanism of a novel temperature sensing polymer and explores its commercialization and future applications.

PUBLISHED CONTENT AND CONTRIBUTIONS

[1] Tae Hyun Kim , Zhou Zhun, Yeong Suk Choi, Vincenzo Costanza, Linghui Wang, Joong Hwan Bahng, Nicholas J. Higdon, Youngjun Yun, Hyunbum Kang, Sunghan Kim and Chiara Daraio. Flexible biomimetic block copolymer composite for temperature and long-wave infrared sensing. Science Advances, 9. 2023. DOI:10.1126/sciadv.ade0423

N.J.H. provided technical support for FTIR analysis. N.J.H. provided comments and revisions to the manuscript.

[2] Linghui Wang*, Vincenzo Costanza*, Nicole J Higdon, Tae Hyun Kim, and Chiara Daraio. Ion Transport Phenomena in Thermally Responsive Polyelectrolytes (in preparation).

N.J.H. participated in the design of the research. N.J.H. designed, conducted, and analyzed all FTIR and UV/Vis studies and all cobalt experements discussed in this paper. N.J.H. participated in the writing of this paper.

[3] Vincenzo Costanza, Dmitriy V. Zhukov, Johnathan Knecht, Nicole J. Higdon, Naresh Menon, and Chiara Daraio. Organic Temperature Sensitive Polyelectrolyte for Core Body Temperature Measurement. IEEE Sensors Journal (under revision).

N.J.H. provided technical support. N.J.H. participated in preparing the manuscript. N.J.H revised the manuscript.

TABLE OF CONTENTS

LIST OF ILLUSTRATIONS

LIST OF TABLES

Chapter 1

INTRODUCTION

1.1 Research Objectives

In this thesis, we examine poly(acrylic acid-co-2-hydroxyethyl acetate)'s (HEA-AA) functionality as an ion conduction based temperature sensor and develop its application space. The main objectives of this research are:

- Develop a fundamental understanding of the high temperature response exhibited by HEA-AA, the mechanism of charge transport, and the factors affecting both.
- Explore applications for the uniquely high response of HEA-AA
- Examine and resolve the roadblocks preventing HEA-AA from moving from the laboratory to the household or clinic.

This research provides insights into the mechanisms of ion transport in polyelectrolytes, in addition to developing temperature sensing materials and devices that have the potential to significantly improve human health both in the clinic, on the job, and at home.

1.2 The Nature of Temperature Sensing

Measuring temperature directly is a fundamentally difficult approach. As such, many approaches to measure temperature have been developed and all rely of how temperature leads to changes in other measurable properties of a well characterized material. There are many exceptional reviews on temperature measurement, here we are not attempting to provide a thorough review, but instead to touch on some of the methods that are utilized.[1,2]

The traditionally thought of thermometer relies on measuring the thermal volumetric expansion of a liquid. Bimetallic strips and gas thermometers function leveraging this same approach of thermal expansion.[1] Beyond these thermocouples are an extremely common device that relies on the thermoelectric effect. However, one of the largest fields of temperature measurement are resistive devices. The “gold-standard” resistive device are the platinum resistance thermometers. However, due to the high cost of platinum resistance thermometers, devices relying instead on changes in the resistance of semiconductor materials are some of the most common temperature measurement devices today.[1] Many other methods of temperature measurement have been developed, but amongst these the majority of traditional temperature measuring devices rely upon rigid materials.

As we have seen a growth in wearables there has been a corresponding growth in the development of flexible temperature sensing devices typically functioning in a resistive or thermoelectric manner.[3–6] Recently there has been increased interest in ionic temperature sensors operating through a variety of methods including resistive, capacitive, and thermoelectric.[7] In this thesis we will explore a flexible resistance / impedance based ion conducting polymer temperature sensor.

1.3. Research Impacts

The development of high-performance temperature sensing materials that can be leveraged in low-cost manufacturing approaches has the potential to substantially improve human life.

1.3.1 Core Body Temperature Measurement

Core body temperature measurement is a powerful tool in wearables for monitoring a person’s overall health.[8] The core temperature is modulated by a wide variety of feedback mechanisms and can provide useful insights into various bodily cycles.[9–12] Beyond monitoring typical changes in body temperature, it can provide a powerful tool for detecting the onset of illnesses prior to the occurrence of overt symptoms.[13–16] This can enable early treatment and isolation to prevent the spread of sicknesses. For first responders, military, and outdoor workers another key application arises, environmental illness detection.[17–19] Environmental illness occurs when the CBT is driven too high or two low by enviormetnal factors and represents a significant risk to these personnel. By leveraging wearable core body temperature sensors, environmental illnesses can be detected and addressed prior to severe bodily harm.

However, current CBT approaches suffer from significant issues that limit their utility in day-to-day wearables. The "gold-standard" approach for CBT monitoring requires surgical placement of a sensor in the patient's aorta, this is obviously not an option for wearable sensors. [20,21]

Other approaches of measuring a person's temperature have been utilized. Skin temperature is trivial to measure, however it does not provide meaningful insights into CBT. Patients with elevated CBT can show normal skin temperatures as it is heavily modulated by perfusion.[21] Oral temperatures see widespread use, however the action of mouth breathing can significantly skew the measured temperature value. For this reason, oral temperatures only stabilize after 7-11 minutes of nasal breathing. Thus oral temperature is not a reliable approach for wearables especially for athletes.[20–22] Tympanic temperature see widespread clinical use, however, it has been found to lose accuracy in exercising patients.[18,21,22] Rectal temperature has often been treated as a gold standard, however it shows a significant time lag and is disfavored due to discomfort.[20,21,23] Esophageal temperature is similarly too uncomfortable for wearable applications.[23]

Gastrointestinal pills are the first of the temperature measurement approaches discussed here that has been used extensively in exercising patients.[23] However, a multi-pill trial has shown significant variations in the reported temperature up to 1.1 °C presumably due to differences in pills location.[20] Furthermore, gastrointestinal pills are expensive and not suitable for day-to-day use. As there has been a movement away from gastrointestinal pills, we have seen a growth in algorithmic methods.[23,24] These methods extrapolate from pulse rate, respiration, and motion to estimate CBT. However, these approaches require making many assumptions about the patient and have yet to be proven reliably accurate in diverse patients.

An alternative approach known as the zero heat flux sensor has been found to be highly accurate. In this method, a temperature flux sensor is applied to the patient's skin at select regions. A heater is attached to the top of the flux sensor and the sensor is heated until no temperature flux is measured across the sensor. This zero-flux state occurs when the heater reaches CBT.[25] While these sensors can be highly accurate, they suffer from high power demands and as such are not viable for wearable devices.[26] Alternatively, a single heat flux sensor leverages a heat flux sensor applied to a specific location of the body.[27,28] These sensors can be accurate however, they rely on assumptions about the underlying tissue that are not always accurate.

In contrast, the dual heat flux sensor is extremely promising for this application. By leveraging two heat flux sensors with differing thermal resistances the resistance of the underlying tissue can be eliminated and thus measurements can be made with minimum assumptions.[26] However, current dual heat flux sensor's performance is directly limited by the accuracy of the individual sensing elements.[29] This leads to thick sensors often with rigid components. Further work is needed to refine the dual heat flux sensor and improve these individual sensing elements. In Chapter 4, of this thesis we explore a DHF CBT device developed utilizing the HEA-AA polymer that is 20x thinner than the next thinnest device in the literature and is highly flexible.

1.3.2 Contact Temperature Mapping in Medical Applications

Beyond CBT we foresee other healthcare applications for high performance, flexible temperature sensors that can be fabricated at a low cost. Contact temperature mapping approaches can provide powerful insights into skin inflammation.[30] This can be utilized to monitor wound healing and for early detection and monitoring for infections.[31] A specific application of interest is the detection and monitoring of skin ulceration. By enabling early detection, ulceration treatment can be initiated prior to skin breakage which improves patient care outcomes.[32–34] As such, the development of large sheet sensors to monitor for ulceration in bedridden patients represents a promising application for this technology.[35–37] Additionally, diabetic foot ulceration represents an immense cost in healthcare reaching $9 -

$13 billion in the US alone and causes > 50% of all lower limb amputations.[38] Early detection can greatly improve outcomes and can be approached through the development of smart insoles.[39–41] However, conventional temperature sensors are typically rigid materials that may cause discomfort during wear. By leveraging flexible soft polymer-based approaches, we believe we can create temperature mapping insoles that will enable comfortable long-term wear. Additionally, properties of HEA-AA allow for potentially far lower fabrications cost compared to conventional mapping sensors. While Chapter 5 does not focus on the temperature mapping aspects, it represents significant progress toward the commercialization of flexible thin-film temperature sensors intended for integration into temperature mapping and other applications in healthcare and industry.

1.3.3 IR Imaging

IR imaging has seen utilization for screening of passengers for infections during the Covid-19 pandemic.[42,43] Furthermore, it can represent a powerful tool for monitoring patient's for signs of localized inflammation or circulation issues.[44,45] Beyond healthcare, IR imaging has broad applications towards industry, security, and defense. Current uncooled IR imaging devices utilize arrays of microbolometer sensors (Fig. 1.1). These sensors are fabricated by suspending a film of thermistor type temperature sensing material above the wafer. IR photons are focused onto the sensing material and the temperature of the material increases.[46] By increasing the response of this sensing material, the sensitivity of the microbolometer can be increased.[47] Additionally, by moving to a sensing material that can be deposited through spin-coating instead of other deposition processes, we believe that the cost of device fabrication can be significantly decreased. Chapter 2 briefly touches on IR detection with HEA-AA.

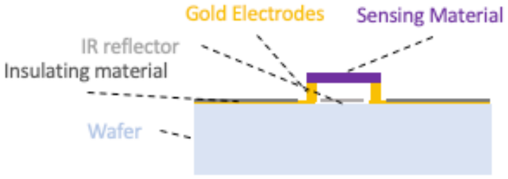

Figure 1.1: Diagram of microbolometer sensor.[48]

1.4 Conclusions

This thesis explores the development of ion conduction based temperature sensors. These temperature sensors exhibit high responses and have the potential to significantly improve human health both in the clinic and at home. Beyond healthcare, improved low-cost flexible temperature sensors have the potential to significantly impact both industry and consumer devices. In this thesis we will both explore the fundamental science of this material in addition to applications and the commercialization of it.

1.5 Chapters Outline

In this thesis, we explore an ion conductive polymer approach to temperature sensing. The research carried out on this project can be broken into: 1) exploring the fundamental science surrounding the structure and mechanisms of the polymer, 2) applications and commercialization of this material.

Chapter 2 introduces this material through the biomimetic temperature sensing polymer variant. In this chapter, we leverage various techniques to demonstrate the basic behaviors of the polymer and explore some of the mechanistic details of the polymer.

Chapter 3 provides an in-depth mechanistic study into the role of water within the polymer. We explore how charge conduction occurs. Furthermore, we investigate how water affects the dynamics of the polymer and its effect on the temperature response. We additionally explore the formation of tetrahalocobaltate within the polymer.

Chapter 4 represents a shift into applications with the development of DHF CBT sensors. In this chapter we explore the fabrication and theoretical performance of ultra-thin CBT sensors. We demonstrate the electrical properties of HEA-AA films prepared with a variety of metal chlorides. We then demonstrate the time response of our sensor and its accuracy leveraging an agar tissue phantom.

Chapter 5 explores the necessity of humidity buffer materials for thin-film sensors. Here, we explore the challenges of commercialization of HEA-AA through the roll-to-roll fabrication of thin-film sensors. We discuss the limitations of thin film moisture barriers and demonstrate the necessity to develop humidity buffer materials. We discuss the development of these materials and the results to date in integrating these materials into sensors.

In Chapter 6, we discuss observations and predictions made about HEA-AA that are not found in other chapters. We additionally discuss future directions with the HEA-AA material.

In Chapter 7, we provide a summary of the main conclusions of the thesis.

References

(1) Childs, P. R. N.; Greenwood, J. R.; Long, C. A. Review of Temperature Measurement. *Rev. Sci. Instrum.* **2000**, *71* (8), 2959–2978. https://doi.org/10.1063/1.1305516.

(2) Ross-Pinnock, D.; Maropoulos, P. G. Review of Industrial Temperature Measurement Technologies and Research Priorities for the Thermal Characterisation of the Factories of the Future. *Proc. Inst. Mech. Eng. Part B* **2016**, *230* (5), 793–806. https://doi.org/10.1177/0954405414567929.

(3) Arman Kuzubasoglu, B.; Kursun Bahadir, S. Flexible Temperature Sensors: A Review. *Sens. Actuators Phys.* **2020**, *315*, 112282. https://doi.org/10.1016/j.sna.2020.112282.

(4) Li, Q.; Zhang, L.-N.; Tao, X.-M.; Ding, X. Review of Flexible Temperature Sensing Networks for Wearable Physiological Monitoring. *Adv. Healthc. Mater.* **2017**, *6* (12), 1601371. https://doi.org/10.1002/adhm.201601371.

(5) Liu, R.; He, L.; Cao, M.; Sun, Z.; Zhu, R.; Li, Y. Flexible Temperature Sensors. *Front. Chem.* **2021**, *9*. https://doi.org/10.3389/fchem.2021.539678.

(6) Butt, M. A.; Kazanskiy, N. L.; Khonina, S. N. Revolution in Flexible Wearable Electronics for Temperature and Pressure Monitoring—A Review. *Electronics* **2022**, *11* (5), 716. https://doi.org/10.3390/electronics11050716.

(7) Zhao, Z.; Shen, Y.; Hu, R.; Xu, D. Advances in Flexible Ionic Thermal Sensors: Present and Perspectives. *Nanoscale* **2025**, *17* (1), 187–213.

https://doi.org/10.1039/D4NR03423F.

(8) Cramer, M. N.; Gagnon, D.; Laitano, O.; Crandall, C. G. Human Temperature Regulation under Heat Stress in Health, Disease, and Injury. Physiol. Rev. **2022**. https://doi.org/10.1152/physrev.00047.2021.

(9) Coyne, M. D.; Kesick, C. M.; Doherty, T. J.; Kolka, M. A.; Stephenson, L. A. Circadian Rhythm Changes in Core Temperature over the Menstrual Cycle: Method for Noninvasive Monitoring. *Am. J. Physiol.-Regul. Integr. Comp. Physiol.* **2000**, *279* (4), R1316–R1320.

(10) Van Veen, M.; Sandra Kooij, J.; Marije Boonstra, A.; Gordijn, M.; Van Someren, E. Delayed Circadian Rhythm in Adults with Attention-Deficit/Hyperactivity Disorder and Chronic Sleep-Onset Insomnia. *Biol. Psychiatry* **2010**, *67* (11), 1091–1096.

(11) Baker, F. C.; Siboza, F.; Fuller, A. Temperature Regulation in Women: Effects of the Menstrual Cycle. *Temperature* **2020**, *7* (3), 226–262. https://doi.org/10.1080/23328940.2020.1735927.

(12) Refinetti, R. Circadian Rhythmicity of Body Temperature and Metabolism. *Temperature* **2020**, *7* (4), 321–362. https://doi.org/10.1080/23328940.2020.1743605.

(13) Aulick, L. H.; McManus, A. T.; Mason Jr, A. D.; Pruitt Jr, B. A. Effects of Infection on Oxygen Consumption and Core Temperature in Experimental Thermal Injury. *Ann. Surg.* **1986**, *204* (1), 48.

(14) Kluger, M. J. Body Temperature Changes during Inflammation: Their Mediation and Nutritional Significance. *Proc. Nutr. Soc.* **1989**, *48* (3), 337–345.

(15) Martelli, D.; Yao, S. T.; McKinley, M. J.; McAllen, R. M. Reflex Control of Inflammation by Sympathetic Nerves, Not the Vagus. *J. Physiol.* **2014**, *592* (7), 1677–1686.

(16) Tesch, T.; Bannert, E.; Kluess, J.; Frahm, J.; Hüther, L.; Kersten, S.; Breves, G.; Renner, L.; Kahlert, S.; Rothkötter, H.-J.; others. Relationships between Body Temperatures and Inflammation Indicators under Physiological and Pathophysiological Conditions in Pigs Exposed to Systemic Lipopolysaccharide and Dietary Deoxynivalenol. *J. Anim. Physiol. Anim. Nutr.* **2018**, *102* (1), 241–251.

(17) Buller, M. J.; Davey, T.; Fallowfield, J. L.; Montain, S. J.; Hoyt, R. W.; Delves, S. K. Estimated and Measured Core Temperature Responses to High-Intensity Warm Weather Military Training: Implications for Exertional Heat Illness Risk Assessment. *Physiol. Meas.* **2020**, *41* (6), 065011. https://doi.org/10.1088/1361-6579/ab934b.

(18) Roossien, C. C.; Heus, R.; Reneman, M. F.; Verkerke, G. J. Monitoring Core Temperature of Firefighters to Validate a Wearable Non-Invasive Core Thermometer in Different Types of Protective Clothing: Concurrent in-Vivo Validation. *Appl. Ergon.* **2020**, *83*, 103001. https://doi.org/10.1016/j.apergo.2019.103001.

(19) Tamura, T.; Huang, M.; Yoshimura, T.; Umezu, S.; Ogata, T. An Advanced Internet of Things System for Heatstroke Prevention with a Noninvasive Dual-Heat-Flux Thermometer. *Sensors* **2022**, *22* (24), 9985. https://doi.org/10.3390/s22249985.

(20) Taylor, N. A. S.; Tipton, M. J.; Kenny, G. P. Considerations for the Measurement of Core, Skin and Mean Body Temperatures. *J. Therm. Biol.* **2014**, *46*, 72–101. https://doi.org/10.1016/j.jtherbio.2014.10.006.

(21) Hymczak, H.; Gołąb, A.; Mendrala, K.; Plicner, D.; Darocha, T.; Podsiadło, P.; Hudziak, D.; Gocoł, R.; Kosiński, S. Core Temperature Measurement—Principles of

Correct Measurement, Problems, and Complications. *Int. J. Environ. Res. Public. Health* **2021**, *18* (20), 10606. https://doi.org/10.3390/ijerph182010606.

(22) Moran, D. S.; Mendal, L. Core Temperature Measurement. *Sports Med.* **2002**, *32* (14), 879–885. https://doi.org/10.2165/00007256-200232140-00001.

(23) Dolson, C. M.; Harlow, E. R.; Phelan, D. M.; Gabbett, T. J.; Gaal, B.; McMellen, C.; Geletka, B. J.; Calcei, J. G.; Voos, J. E.; Seshadri, D. R. Wearable Sensor Technology to Predict Core Body Temperature: A Systematic Review. *Sensors* **2022**, *22* (19), 7639. https://doi.org/10.3390/s22197639.

(24) Falcone, T.; Cordella, F.; Molinaro, V.; Zollo, L.; Del Ferraro, S. Real-Time Human Core Temperature Estimation Methods and Their Application in the Occupational Field: A Systematic Review. *Measurement* **2021**, *183*, 109776. https://doi.org/10.1016/j.measurement.2021.109776.

(25) Lu, H.; Aratake, S.; Naito, H.; Nogawa, M.; Nemoto, T.; Togawa, T.; Tanaka, S. Development of a Core Body Thermometer Applicable for High-Temperature Environment Based on the Zero-Heat-Flux Method. *Sensors* **2023**, *23* (4), 1970. https://doi.org/10.3390/s23041970.

(26) Kitamura, K.-I.; Zhu, X.; Chen, W.; Nemoto, T. Development of a New Method for the Noninvasive Measurement of Deep Body Temperature without a Heater. *Med. Eng. Phys.* **2010**, *32* (1), 1–6.

(27) Tanaka, Y.; Matsunaga, D.; Tajima, T.; Seyama, M. Robust Skin Attachable Sensor for Core Body Temperature Monitoring. *IEEE Sens. J.* **2021**, *21* (14), 16118–16123. https://doi.org/10.1109/JSEN.2021.3075864.

(28) Ren, X.; Zhou, C.; Ye, X. A Novel Miniaturized Sandwich-Like Sensor for Continuous Measurement of Core Body Temperature. *IEEE Sens. J.* **2022**, *22* (17), 16742–16749. https://doi.org/10.1109/JSEN.2021.3071825.

(29) Żmigrodzki, J.; Cygan, S.; Łusakowski, J.; Lamprecht, P. Analytical Analysis of Factors Affecting the Accuracy of a Dual-Heat Flux Core Body Temperature Sensor. *Sensors* **2024**, *24* (6), 1887. https://doi.org/10.3390/s24061887.

(30) Speeckaert, R.; Hoorens, I.; Lambert, J.; Speeckaert, M.; van Geel, N. Beyond Visual Inspection: The Value of Infrared Thermography in Skin Diseases, a Scoping Review. *J. Eur. Acad. Dermatol. Venereol.* **2024**, *38* (9), 1723–1737. https://doi.org/10.1111/jdv.19796.

(31) Hattori, Y.; Falgout, L.; Lee, W.; Jung, S.-Y.; Poon, E.; Lee, J. W.; Na, I.; Geisler, A.; Sadhwani, D.; Zhang, Y.; Su, Y.; Wang, X.; Liu, Z.; Xia, J.; Cheng, H.; Webb, R. C.; Bonifas, A. P.; Won, P.; Jeong, J.-W.; Jang, K.-I.; Song, Y. M.; Nardone, B.; Nodzenski, M.; Fan, J. A.; Huang, Y.; West, D. P.; Paller, A. S.; Alam, M.; Yeo, W.-H.; Rogers, J. A. Multifunctional Skin-Like Electronics for Quantitative, Clinical Monitoring of Cutaneous Wound Healing. *Adv. Healthc. Mater.* **2014**, *3* (10), 1597–1607. https://doi.org/10.1002/adhm.201400073.

(32) Armstrong, D. G.; Holtz-Neiderer, K.; Wendel, C.; Mohler, M. J.; Kimbriel, H. R.; Lavery, L. A. Skin Temperature Monitoring Reduces the Risk for Diabetic Foot Ulceration in High-Risk Patients. *Am. J. Med.* **2007**, *120* (12), 1042–1046. https://doi.org/10.1016/j.amjmed.2007.06.028.

(33) Godavarty, A.; Leiva, K.; Amadi, N.; Klonoff, D. C.; Armstrong, D. G. Diabetic Foot Ulcer Imaging: An Overview and Future Directions. *J. Diabetes Sci. Technol.* **2023**, *17* (6), 1662–1675. https://doi.org/10.1177/19322968231187660.

(34) Chiwo, F. S.; Leizaola, D.; Amaro, S.; Hernández, M.; Sousa, R.; Ponce, J. P.; Mathis, S.; Armstrong, D. G.; Godavarty, A. Noninvasive Monitoring of Diabetic Foot Ulcers Healing Process by Using Optical-Thermal Imaging Techniques. In *Optical Diagnostics and Sensing XXV: Toward Point-of-Care Diagnostics*; SPIE, 2025; Vol. 13316, pp 62–68. https://doi.org/10.1117/12.3043405.

(35) Bilska, A.; Stangret, A.; Pyzlak, M.; Wojdasiewicz, P.; Szukiewicz, D. Skin Surface Infrared Thermography in Pressure Ulcer Outcome Prognosis. *J. Wound Care* **2020**, *29* (12), 707–718. https://doi.org/10.12968/jowc.2020.29.12.707.

(36) Bennett, S. L.; Goubran, R.; Knoefel, F. Long Term Monitoring of a Pressure Ulcer Risk Patient Using Thermal Images. In *2017 39th Annual International Conference of the IEEE Engineering in Medicine and Biology Society (EMBC)*; 2017; pp 1461–1464. https://doi.org/10.1109/EMBC.2017.8037110.

(37) Fard, F. D.; Moghimi, S.; Lotfi, R. Pressure Ulcer Risk Assessment by Monitoring Interface Pressure and Temperature. In *2013 21st Iranian Conference on Electrical Engineering (ICEE)*; 2013; pp 1–5. https://doi.org/10.1109/IranianCEE.2013.6599875.

(38) Makrantonaki, E.; Jiang, D.; Hossini, A. M.; Nikolakis, G.; Wlaschek, M.; Scharffetter-Kochanek, K.; Zouboulis, C. C. Diabetes Mellitus and the Skin. *Rev. Endocr. Metab. Disord.* **2016**, *17* (3), 269–282. https://doi.org/10.1007/s11154-016-9373-0.

(39) Najafi, B.; Reeves, N. D.; Armstrong, D. G. Leveraging Smart Technologies to Improve the Management of Diabetic Foot Ulcers and Extend Ulcer-Free Days in Remission. *Diabetes Metab. Res. Rev.* **2020**, *36* (S1), e3239. https://doi.org/10.1002/dmrr.3239.

(40) Abbott, C. A.; Chatwin, K. E.; Foden, P.; Hasan, A. N.; Sange, C.; Rajbhandari, S. M.; Reddy, P. N.; Vileikyte, L.; Bowling, F. L.; Boulton, A. J. M.; Reeves, N. D. Innovative Intelligent Insole System Reduces Diabetic Foot Ulcer Recurrence at Plantar Sites: A Prospective, Randomised, Proof-of-Concept Study. *Lancet Digit. Health* **2019**, *1* (6), e308–e318. https://doi.org/10.1016/S2589-7500(19)30128-1.

(41) Lazarou, I.; Fiska, V.; Mpaltadoros, L.; Tsaopoulos, D.; Stavropoulos, T. G.; Nikolopoulos, S.; Dafoulas, G. E.; Dailiana, Z.; Bargiota, A.; Kompatsiaris, I. Stepping Forward: A Scoping Systematic Literature Review on the Health Outcomes of Smart Sensor Technologies for Diabetic Foot Ulcers. *Sensors* **2024**, *24* (6), 2009. https://doi.org/10.3390/s24062009.

(42) Martinez-Jimenez, M. A.; Loza-Gonzalez, V. M.; Kolosovas-Machuca, E. S.; Yanes-Lane, M. E.; Ramirez-GarciaLuna, A. S.; Ramirez-GarciaLuna, J. L. Diagnostic Accuracy of Infrared Thermal Imaging for Detecting COVID-19 Infection in Minimally Symptomatic Patients. *Eur. J. Clin. Invest.* **2021**, *51* (3), e13474. https://doi.org/10.1111/eci.13474.

(43) Perpetuini, D.; Filippini, C.; Cardone, D.; Merla, A. An Overview of Thermal Infrared Imaging-Based Screenings during Pandemic Emergencies. *Int. J. Environ. Res. Public. Health* **2021**, *18* (6), 3286. https://doi.org/10.3390/ijerph18063286.

(44) Ring, E. F. J.; Ammer, K. Infrared Thermal Imaging in Medicine. *Physiol. Meas.* **2012**, *33* (3), R33. https://doi.org/10.1088/0967-3334/33/3/R33.

(45) Wang, H.; Jr, D. R. W.; Kam, J. IR Imaging of Blood Circulation of Patients with Vascular Disease. In *Thermosense XXVI*; SPIE, 2004; Vol. 5405, pp 115–123. https://doi.org/10.1117/12.545899.

(46) Yu, L.; Guo, Y.; Zhu, H.; Luo, M.; Han, P.; Ji, X. Low-Cost Microbolometer Type Infrared Detectors. *Micromachines* **2020**, *11* (9), 800. https://doi.org/10.3390/mi11090800.

(47) Yadav, P. V. K.; Yadav, I.; Ajitha, B.; Rajasekar, A.; Gupta, S.; Ashok Kumar Reddy, Y. Advancements of Uncooled Infrared Microbolometer Materials: A Review. *Sens. Actuators Phys.* **2022**, *342*, 113611. https://doi.org/10.1016/j.sna.2022.113611.

(48) Nicole J Higdon. *Bioinspired Temperature-Sensitive Polymer Electrolyte for Infrared Imaging Applications*; Candidacy Report; California Institute of Technology, 2021.

Chapter 2

BIOMEMETIC BLOCK COPOLYMER FOR TEMPERATURE SENSING

The work in this chapter has been adapted from:

Tae Hyun Kim , Zhou Zhun, Yeong Suk Choi, Vincenzo Costanza, Linghui Wang, Joong Hwan Bahng, Nicholas J. Higdon, Youngjun Yun, Hyunbum Kang, Sunghan Kim and Chiara Daraio. Flexible biomimetic block copolymer composite for temperature and long-wave infrared sensing. *Science Advances*, 9.6, 2023.

N.J.H. provided technical support for FTIR analysis. N.J.H. provided comments and revisions to the manuscript.

The section "Further Work on Mechanisms of this System" represents further laboratory work carried out by N.J.H. used to clarify the temperature response mechanism amongst the authors during the revisions of the manuscript and does not appear in the before mentioned Science Advances paper.

Supplementary information can be found in Appendix A.

2.0 Abstract

Biological compounds often provide clues to advance material designs. Replicating their molecular structure and functional motifs in artificial materials offers a blueprint for unprecedented functionalities. Here, we report a flexible biomimetic thermal sensing (BTS) polymer that is designed to emulate the ion transport dynamics of a plant cell wall component, pectin. Using a simple yet versatile synthetic procedure, we engineer the physicochemical properties of the polymer by inserting elastic fragments in a block copolymer architecture, making it flexible and stretchable. The thermal response of our flexible polymer outperforms current state-of-the-art temperature sensing materials, including vanadium oxide, by up to two orders of magnitude. Thermal sensors fabricated from these composites exhibit a sensitivity that exceeds 10 mK and operate stably between

15 ° and 55 °C, even under repeated mechanical deformations. We demonstrate the use of our flexible BTS polymer in two-dimensional arrays for spatiotemporal temperature mapping and broadband infrared photodetection.

2.1 Introduction

Organic electronic materials are emerging as competitive alternatives to conventional silicon-based microelectronics because of their low-cost manufacturing[1,2] and multifunctionality.[3,4] The ability to tailor their properties at the molecular level makes them appealing for a range of sensing applications, such as wearable and implantable devices, which require specific characteristics that are difficult to achieve with inorganic compounds, like flexibility and stretchability. The increasing demand for all-organic electronic devices has led to the developments of a growing number of soft and active materials for a variety of physical[5,6] and biochemical sensors,[7,8] paralleled by the advancements in elastic substrates and conductors,[9,10] as well as in their fabrication and integration strategies.[11,12]

Organic thermal sensors have also been proposed for remote health care, robotics, and environmental and industrial monitoring applications.[10,13] However, thermal sensing devices relying on organic materials are often limited by their response performance, which is not yet comparable to their inorganic counterparts. Several approaches have been suggested to improve materials' response to temperature, for example, by using inorganic fillers, nanocomposites, volume expansion, or the use of transistor-type devices for signal amplification.[14–17] However, these strategies generally involve complex fabrication steps and device architectures, function only in narrow temperature ranges, or provide limited response.

To overcome these limitations, it is necessary to develop organic materials that intrinsically present high thermal response and flexibility in a relatively simple scaffold that can be fabricated to scale with reproducible performance. However, the ability to design new materials depends on understanding the fundamental transport mechanism and structural dynamics in organic molecules[18,19] and on linking these properties to their functional characteristics. Although promising advances have been made, for example, with first principle simulations and data-driven approaches,[20,21] the field is still lacking predictive models for the design and synthesis of such materials. One approach to design new materials is to gain insights from building blocks found in biological matters and to emulate their structures in synthetic materials.

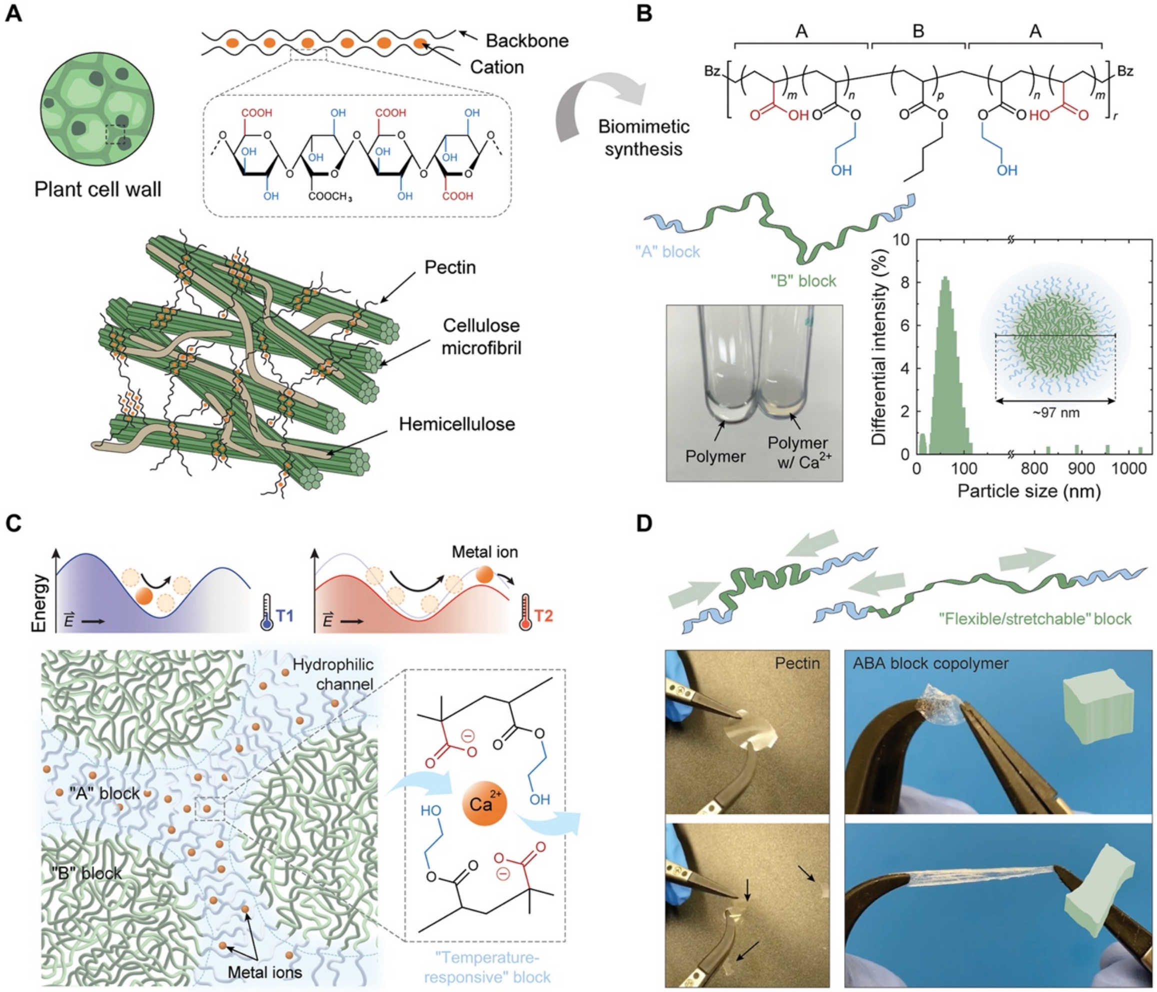

Figure 2.1: Biomimetic design of the flexible BTS polymer. (a) Schematic illustration of the plant cell wall structure and of pectin. (b) Design of the ABA-type block copolymer, with m = 5, n = 5, p = 100, and r = 85.7. The hydrophilic A block, rich in carboxyl (red) and hydroxyl (blue) groups, is designed to electrostatically interact with metallic cations. The hydrophobic B block, composed of poly(n-butyl acrylate), is designed to provide mechanical flexibility and stretchability to the network. As shown in the particle size measurement (bottom right), the synthesized polymer exists in a

colloidal state in ethanol due to phase separation. (c) Hypothesized mechanism governing the temperature response of the synthetic block copolymer. Rearrangement of the potential wells at low and high temperature in which the cations are confined (top). When an external electric field is applied, temperature rises cause an increase in ion migration through the hydrophilic channels formed between the colloidal particles in the polymer matrix (bottom). (d) Mechanical flexibility and stretchability of the synthetic block copolymer. The dried pectin film is prone to tear after a slight bending deformation (left), whereas the composite polymer is robust to repeated stretching motions because of the soft B block (right). The polymer is stretched 300% from its original shape.

Recent investigations of plant cell wall components reported that pectin, a structurally and functionally complex acid-rich polysaccharide,[22] has a remarkable response to temperature.[23–25] Pectin consists mostly of repeating units of d-galacturonic acid (Fig. 2.1(a)). At neutral pH, the d-galacturonic acid units of low-ester pectin form ionic bridges with Ca^{2+}, creating an "egg-box" complex in which cations are encapsulated.[26,27] Increasing the temperature of a Ca^{2+}–cross-linked pectin results in an exponential increase in ionic conduction.[23,24] However, pectin is most abundantly found in agricultural products, e.g., fruit peels, and its chemical composition is directly influenced by climate, plant origins, and extraction methods.[28] Hence, devices fabricated with pectin, as a sensing element, present inconsistent electronic properties and demonstrate poor structural stability.

Here, we introduce a new flexible biomimetic thermal sensing (BTS) polymer that emulates the structure and functional motifs of pectin. The synthetic BTS polymer composite exhibits superior thermal sensitivity while also being mechanically robust and flexible (Fig. 2.1(b)). The basic architecture consists of an ABA-type triblock copolymer, synthesized through reversible addition-fragmentation chain transfer (RAFT) polymerization (Fig. A.1.(a)), which is a versatile living radical polymerization method used to engineer structures with intrinsic mechanical flexibility (thermoplastic elastomers), suitable for organic electronic materials.[29–31]

2.2 Results

2.2.1 Design of the Flexible BTS Polymer

To mimic pectin's temperature response, we conceptualize the polymer architecture by reducing the complex pectin structure to a simpler backbone, bearing only the minimally required cues for the desired functions. We hypothesize that the carboxyl groups, hydroxyl groups, and the conformation of sugar pockets are all essential components within the d-galacturonic acid that chelate divalent cations forming the egg-box complex.[26,32] In the ABA architecture, the "A" blocks represent two flanking hydrophilic regions, displaying motifs that can bind with divalent cations, composed of random placement of 2-hydroxyethyl acrylate (HEA) and acrylic acid (AA). Upon chelating with divalent cations, the A blocks present a temperature response mechanism similar to that of pectin (Fig. 2.1(c)). However, the cationic interactions result in a "pseudo-cross-link," forming a hard segment with high glass transition temperature (T_g).[33] To add mechanical flexibility, the polymer is further modified by introducing low-T_g polymer molecules as soft segments. Poly(n-butyl acrylate), with low glass transition temperature ($T_g < -50$ °C),[34] is inserted in the middle block "B," to serve as an elastic strand in the network and to make the polymer membrane stretchable (Fig. 2.1(d)). In ethanol, the synthesized polymer exists in colloidal states with an average particle diameter of 96.9 nm (Fig. 2.1(b) and Fig. A.1(b)). The hydrophilic-lipophilic balance value of the hydrophilic A block, calculated on the basis of Davies' method, is 13.03, corresponding to the oil-in-water emulsifier range (table A.1).

To verify the functional roles of the polymer moiety relating to the temperature-dependent ion transport, we first characterize the structural components of the as-synthesized block copolymer, using gel permeation chromatography (GPC) and nuclear magnetic resonance (NMR) measurements (Fig. A.2). The synthesized polymer shows a weight-average molecular weight (Mw) of 113,600 g/mol with a dispersity of 1.08. This is similar to the Mw of natural pectin but with a much narrower weight distribution.[35] The monomer feed ratio of the hydrophilic (hard) and hydrophobic (soft) segments is 1:5 (tables A.2 and A.3).

Adding divalent calcium ions into the flexible BTS polymer solution results in a cloudy appearance, revealing a network formation through ionic cross-links. The cross-linked solution is cast on a plastic sheet and dried to remove the remaining solvent (Fig. 2.2(a)). During this process, the mixture is monitored in situ using attenuated total reflectance–Fourier transform infrared (ATR-FTIR) spectroscopy to examine the film formation behavior. The characteristic peaks clearly elucidate structures of the designed polymer (Fig. 2.2(b) and table A.4) and the presence of water contained inside (Fig. A.3). While the solvent evaporates, the neighboring chains of the block copolymer form interpolymer complexes (IPCs) between the AA-HEA functional groups. This interaction between the carbonyl oxygen and hydrogen of the hydroxyl group (hydrogen bonding) is suggested by the thermogravimetric analysis (TGA) profile (Fig. 2.2(c)).[36] Here, the IPCs may play a role in aggregating the colloidal particles to form ion transport channels between the interacting A blocks (Fig. 2.1(c)). At elevated temperatures, the number of ions overcoming the energy barrier increases, which leads to a higher diffusion constant and hopping rate between the coordination sites through the absorption of thermal energy and the polymer's segmental motion. Under an applied electric field, the probability of ions moving forward becomes favorable, generating a net current flow through the polymer network. The maximum amount of AA that can be involved in IPC formation is calculated as 86.13% (table A.6).

To interrogate the importance of chemical composition within the A block, series of copolymers with varying ratio of AA to HEA are synthesized (Fig. 2.2(d) and table A.7). The polymer film with even proportion of carboxyl-to-hydroxyl groups demonstrates the highest activation energy and temperature response. Modifying this ratio to approximately 1:2 results in a >7-fold decrease in response, while films consisting of only the carboxyl groups lead to a response depletion. The result reveals that both hydroxyl and carboxyl groups collectively play important roles in chelation of Ca^{2+} and the subsequent formation of the egg-box–type interactions analogous to the coordination environment in pectin. Moreover, the high temperature response can be explained by the high-energy barrier created by strong binding forces between these side chains and calcium ions.

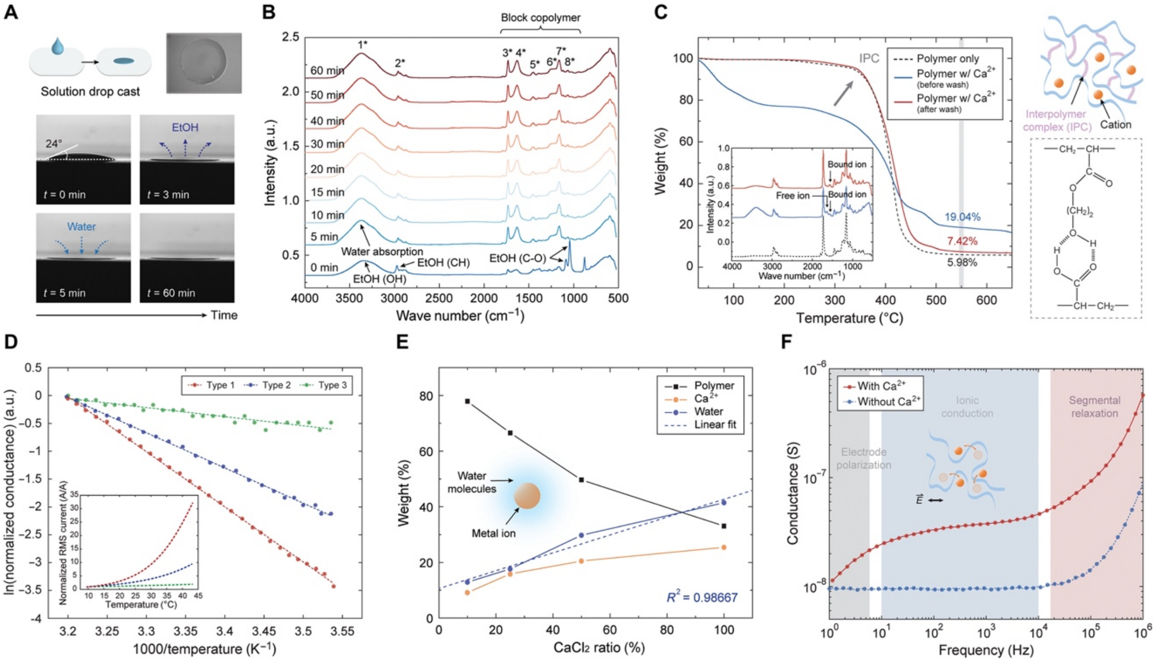

Figure 2.2: Film formation behavior and component analysis of the block copolymer. (a) Digital images of the cross-linked block copolymer solution drop-casted on a flexible plastic substrate. The amount of cross-linking metal ions used for all tests is fixed to 100% unless otherwise stated. a.u., arbitrary units; EtOH, ethanol. (b) Time series of ATR-FTIR spectra after polymer deposition. During 1 hour of air dry, ethanol starts to evaporate, and subsequently, water is absorbed and saturated by the hygroscopic regions in the polymer matrix. *Peak assignments of the ATR-FTIR spectra (table A.4). (c) TGA profile of the polymer film before and after washing in DI water. Titration analysis is performed to determine the percent of IPC formed in the composite film based on the amount of bounded metal ions after wash. Inset: Corresponding FTIR spectra of the films. (d) Arrhenius plot of different block copolymers. Activation energy compared between different polymer films with varying ratio of carboxyl to hydroxyl functional groups (type 1: m = 5, n = 5, p = 100; type 2: m = 4, n = 7, p = 100; type 3: m = 10, n = 0, p = 100). Inset: Corresponding thermal response of each type of polymer compared. Measurements are performed using the electrode design fabricated in Fig. A.6(b) with an AC voltage bias of 300 mV at 200 Hz. (e) Relation between the concentration of metal ions in the composite film and the amount of water adsorbed. Weight percentage of the polymer, Ca^{2+}, and water is calculated on the basis of the TGA profile and the coupled gas-phase FTIR spectra of the dried polymer films (Fig. A.5) with varying amount of CaCl$_2$ (table A.5). A linear relationship

is observed between the $CaCl_2$ concentration and water absorbed by the composite film. (f) Impedance spectra of the polymer film with and without Ca^{2+}.

By varying the concentration of ions, the films are further profiled using TGA-FTIR to verify components from gas-phase diffusion (Figs. S4 and S5). The linear relationship (R2 = 0.987) between Ca^{2+} concentration and water in the film indicates that water absorption is mainly caused by metal ions (Fig. 2.2(e)). Last, to investigate the conducting species within the polymer matrix, electrochemical impedance spectroscopy analysis is performed. Polymer films with and without Ca^{2+} are prepared, and the system's conductivity as a function of AC frequency is measured (Fig. 2.2(f)). The conductance profile of the film with no metal ions is flat until 10 kHz, whereas the one with Ca^{2+} shows an increase below 100 Hz due to electrode polarization followed by a plateau. This reveals that calcium cations are the major transporting charge carrier of the system.

2.2.2 Characterization of the Flexible BTS Polymer

To characterize the temperature response, we fabricate an array of circularly shaped interdigitated electrodes on a flexible plastic substrate and then drop cast and dry 5 μl of the cross-linked BTS polymer solution on the electrodes' surface (Fig. A.6(a-b)). After mounting the samples on a custom-built thermal cycler, the output current is measured while applying an AC voltage of 300 mV at 200 Hz. The alternating signals enable stable measurements over time, reducing the possibility of ionic charge depletion caused by DC bias. Here, 300 mV is chosen on the basis of the minimum level of current (to avoid self-joule heating) that could be stably read from the sensor considering the signal noise floor at room temperature (RT).

The hydration state of organic materials closely correlates to the ionic transport and the material's mechanical properties.[37] To monitor the effect of water in the polymer's performance, we dried the films under various conditions and repeat the measurements (Fig. 2.3(a)). When the polymer film is fully hydrated, a relatively low temperature response is observed. Under these conditions, conduction through water channels dominates the transport, suppressing the effect of ions, which is mainly responsible for the large temperature-dependent impedance changes. As the film is dried, removing unbound water from the chain, the response increases markedly, indicating the growing portion of Ca^{2+}-mediated transport.[25] However, further dehydration results in a decreased response due to loss of conduction paths. A maximum root mean square (RMS) current response ($I_{45°C}$ /$I_{15°C}$) of 80.04 A/A is exhibited over the defined temperature range. This normalization approach has been adopted to compare between state-of-the-art thermal sensing materials, characterized under different measurement conditions. By measuring the output current at constant temperature in air, a sensing resolution of less than 8.68 mK is obtained with negligible hysteresis (Fig. A.6(c-d)). Compared to the state-of-the-art thermal sensing materials, including vanadium oxide,[38,39] inorganic devices,[40–42] and natural pectin products,[23,24] the overall temperature response of the resulting flexible BTS polymer composite is orders of magnitude higher (Fig. 2.3(b)).

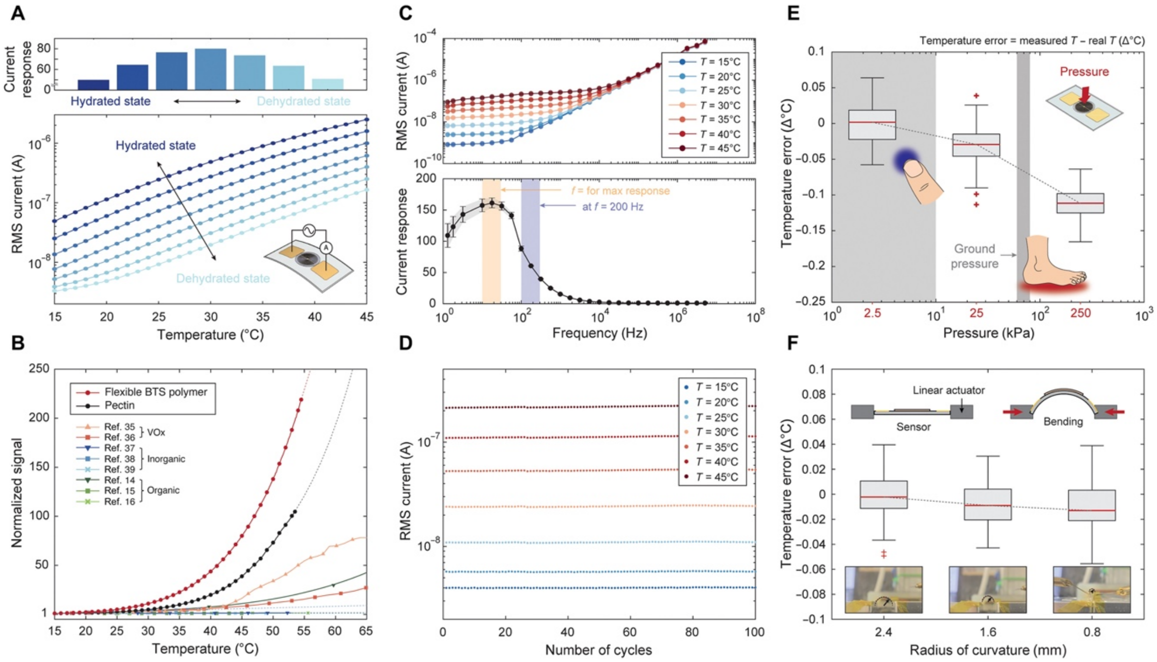

Figure 2.3: Characterization of the flexible BTS polymer sensor. (a) Current variation as a function of temperature, measured between 15 ° and 45 °C with an applied voltage of 300 mV at 200 Hz (bottom) and the corresponding current response calculated at different hydration levels (top). Darker blue lines represent higher hydration, and lighter blue lines represent lower hydration. Inset:

Device schematic and configuration for electrical measurement. (b) Response comparison between state-of-the-art temperature sensing materials and devices, normalized with signals at 15 °C. (c) Frequency-dependent current measured between 1 Hz and 5 MHz at varying temperatures (top) and the corresponding current response calculated when 300 mV was applied (bottom). Maximum response of 161.3 is obtained at 17.8 Hz. (d) Cyclic stability test over 100 cycles of continuous temperature oscillation between 15 ° and 45 °C. (e) Temperature error extracted from the thermal sensor as a function of normal pressure and (f) bending strain (curvature). All plots represent data from polymer solution cross-linked with 100% concentration of $CaCl_2$.

To evaluate the materials' response as a function of excitation frequency, we measure the samples' impedance spectrum between 1 Hz and 5 MHz using 300 mV (Fig. 2.3(c)). At lower frequencies, in which the transport is mainly induced by ion migration, change of temperature results in a large variation of current. A maximum current response of over 160 A/A is evident around 20 Hz. At frequencies above the charge relaxation, transporting ions within the polymer are not able to follow the alternating electric field (polarization dominated) and no longer contribute to the temperature-dependent conduction behavior.

After conditioning the polymer film to its optimal hydration status, cyclic stability is evaluated by heating the sensor from 15 ° to 45 °C for 6 hours while monitoring the current. Before measurements, a thin layer of parylene-C is conformally coated around the device to serve as a moisture barrier and electrical insulation. The device shows high stability (Fig. 2.3(d) and Fig. A.7) with minimum variation in current response, lying within the ±2.39% fluctuation boundary over 100 cycles of continuous use.

To characterize the effect of mechanical solicitations, the sensors are compressed or bent at different pressures and curvatures. Although a slight decrease in conduction is observed during compression (Fig. A.8), the average temperature error converted from the difference in current read-out, with and without loading, is less than 0.11 °C up to a pressure of 250 kPa (Fig. 2.3(e)). This demonstrates that the sensor response is relatively insensitive to strain. Under bending deformations, an even lower temperature error is detected (Fig. 2.3(f)). To test whether the strain insensitivity persists after repetitive mechanical loading, we subject the samples to 100 cycles of bending (bending radius = 1.6 mm) or compression (to a maximum pressure of 25 kPa). The current remains similar to that of the as-fabricated samples, indicating high mechanical stability and elastic recovery. In contrast, dehydrated pectin films are brittle and prone to tear (Fig. 2.1(d)).

2.2.3 Spatiotemporal Temperature Mapping

We exemplify the applicability of our flexible BTS polymer composite for spatiotemporal temperature mapping and long-wave infrared (IR) photodetection. First, we create a flexible temperature sensing sheet, consisting of a 10 by 10 array of uniformly spaced sensors, placed 1 cm apart (Fig. 2.4(a)). We attach the sensor matrix on a circular glass plate with a point heat source located on its center and monitor the thermal gradient evolving across the glass surface in real time. The continuous heat flow along the plate's radius is visualized in a time-dependent temperature map (Fig. 2.4(b)), obtained by measuring and interpolating the current variation on five polymer sensors. High temperature response, paired with its flexibility and compliance, offers opportunities in various engineering applications, such as batteries, packaging of perishable items, and wearable thermometers that require continuous spatial monitoring of temperature over three-dimensional surfaces.

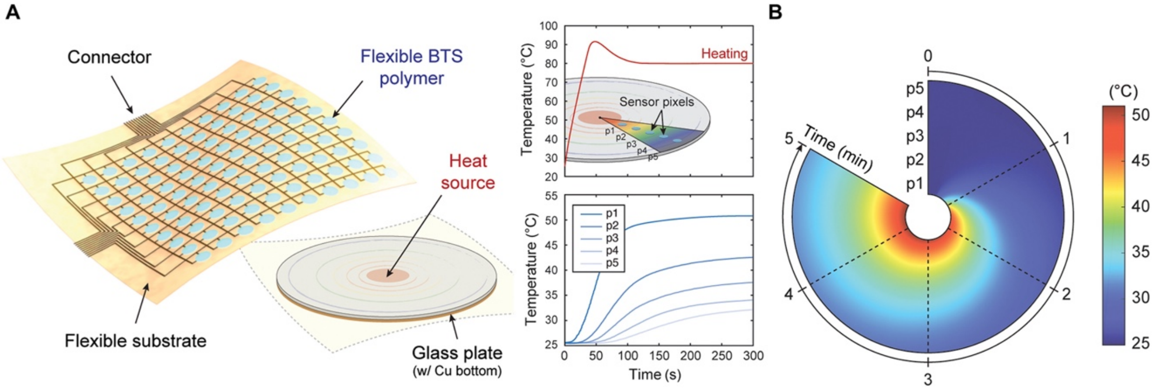

Figure 2.4: Temperature sensing array based on flexible BTS polymer. (a) Schematic diagram of a flexible thermal sensor for large-area, multipixel temperature mapping. The sensor is placed on top of a glass plate where a heat source in the middle is used to generate a thermal gradient across the surface. Inset: Time versus temperature profile of the heat source (top) and the measured temperature

value from each sensor (bottom). (b) Spatiotemporal reconstruction of the temperature evolution across the glass plate. Data are extracted from five sensor pixels along the radius of the glass slide.

Broadband long-wave IR sensing

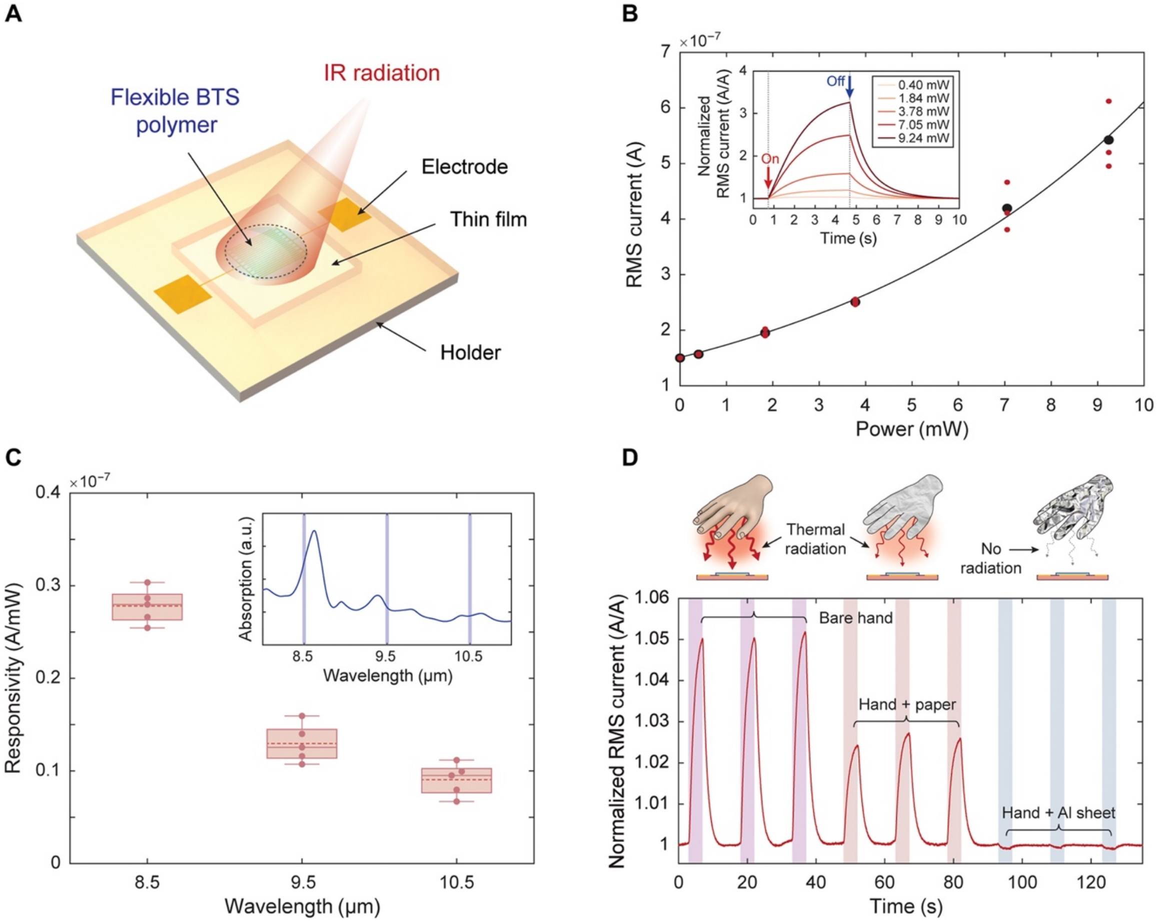

Figure 2.5: IR sensor based on flexible BTS polymer. (a) Schematic of the fabricated long-wave, thermal IR detector. (b) Current as a function of IR power irradiated at a wavelength of 8.5 µm. Inset: Representative current profile during a 4-s period of IR exposure in air with different power. Current is measured using an applied voltage of 1 V at 200 Hz. (c) Responsivity of the IR detector at different wavelengths. Inset: Wavelength-dependent absorption intensity of the block copolymer. (d) Real-time detection of thermal radiation generated by a hand wave motion. Covering the hand with a sheet of paper, the rise in current is reduced due to limited transmission of irradiation power. Covering the hand with an aluminum sheet, no change or decrease in current is observed due to IR reflection.

Next, we experimentally demonstrate an uncooled, long-wave IR sensor that can detect thermal radiation across a wide spectral range (Fig. 2.5(a)). To reduce thermal loss via heat conduction, we fabricate electrodes on a thin polyimide (PI) membrane (2 μm) (Fig. A.9(a-b)). To measure the responsivity (ΔI/P), the entire device was placed in a hermetically sealed chamber with a zinc selenide (ZnSe) transmission window (Fig. A.9(c)). The sensor was biased at 1 V AC at 200 Hz to increase the sensor's signal-to-noise ratio, ensuring no excessive self-heating caused by joule dissipation (Fig. A.10). Monitoring the current change as a function of applied power at 8.5-μm wavelength, we observe an exponential increase in current, following an Arrhenius behavior (Fig. 2.5(b)). To investigate the spectral responsivity of the sensor, we vary the wavelength of the incident IR with an applied power of 4 mW. The sensor responsivity is closely correlated to the spectral features of the polymer absorption spectrum, in which the characteristic peaks are located (8 to 14 μm) (Fig. 2.5(c)). Last, we use our sensor to detect IR-emitting objects near RT. With a hand waving motion above the sensor, a correlating current variation is detected (Fig. 2.5(d)). Current decrease is observed when the hand is covered with a sheet of paper. We repeat the measurement with an IR reflective aluminum sheet to verify whether this behavior is induced by thermal radiation. The aluminum layer blocks the irradiation emitted not only from the hand but also from the surrounding environment, resulting in a further decrease in sensor current.

2.3 Discussion

The results presented here demonstrate a biomimetic approach to design a thermally responsive polymer for organic electronics. Inspired by the functional motifs in the pectin-Ca^{2+} complex, we create a block copolymer that demonstrates an extremely high thermal response with a sensing resolution of below 10 mK. By using a versatile synthetic procedure, we also show the ability to tailor physicochemical properties that enables optimization of the material's temperature sensitivity and endows mechanical flexibility and stretchability. Additional functionalities can be introduced by tailoring the polymer architecture and its side chains, for example, increasing its electrical conductivity, response time, or IR absorption spectrum for diverse thermal sensing platforms. The resulting material is stable under cyclic loading and insensitive to mechanical solicitations, extending its capability and potential use for wearable sensors and consumer electronics. In particular, these aspects have promise to affect technological advances in the medical or health care field that can allow continuous and noninvasive personalized monitoring of minute pathophysiological thermal stresses caused by disruption in homeostasis, infection, inflammatory responses, and mental stresses or sleep deprivation.

Although our BTS polymer has shown promising results, several challenges and room for improvements remain. Because of its nonlinear, exponential response to temperature and hydration-dependent sensitivity, a precalibration curve needs to be acquired before initial measurements, and care must be taken during sensor packaging. In addition, an alternative synthesis procedure such as the continuous polymerization method will allow us to reduce batch-to-batch variation and enable mass production. Last, it will be of interest to further investigate the transport mechanism supplemented by molecular dynamic simulations to further delineate the thermal sensing behavior of the system to potentially improve the material sensitivity, dynamic range, or even the mechanical features by modifying the polymer composition and coordinating metal ions.

Interests on realizing all-organic electronic devices with functionalities that their inorganic counterparts cannot provide are on the rise. While many organic electronic components such as substrates, electrodes, and transistors have been developed, advancement and mechanistic understanding of the organic sensory elements have not progressed in parallel. To bridge this gap and to fully optimize the specific features of our flexible BTS polymer, further mechanistic studies accompanied by molecular dynamic simulations to delineate the exact origin of the high thermal response should be followed. We anticipate that our material and design concept can be used for fundamental studies of ion transport mechanisms in the form of such simplified polyelectrolytes, which can be generalized to different ionic conducting polymeric systems.

2.4 Further Work on Mechanisms

In this section, we will expand upon experiments that I carried out, which clarified the writing and revisions of the paper, however, did not find their way into the main text of the paper. While these experiments are included here, they were aimed as exploratory experiments with regards to various hypothesis and are less rigorous than those experiments intended for scientific publication. They principally center on the potential influence of IPC formation and calcium binding in the polymer system. While this paper focuses on BTS, a block copolymer with an ABA structure (the A blocks comprised of a random copolymer of acrylic acid and 2-hydroxyethyl acetate, the B blocks comprised of n-butyl acetate), these experiments where largely carried out with HEA-AA, a random copolymer of acrylic acid and 2-hydroxyethyl acetate that lacks the B blocks of the BTS polymer. We believe that this polymer should exhibit similar behaviors to the BTS polymer with identical charge transport mechanisms.

2.4.1 Solid Evidence of IPC Formation Within Our Polymer Under Select Conditions

Mixed solutions of poly(acrylic acid) (PAA) and poly(2-hydroxyethyl acetate) (PHEA) are well known to exhibit water insoluble IPC formation when mixed in water solutions. These formations are known to be pH dependent with IPC formation being arrested by deprotonation of the acrylic acid in higher pH solutions.[36] Our polymers (both BTS and HEA-AA) are especially interesting as they both contain the acrylic acid-co-2-hydroxyethyl acetate random copolymer motif. We would expect these polymers to exhibit self IPC formation. This unusual behavior can lead to a wide variety of proposed effects of self IPC formation on film formation, film structuring, and charge transport mechanism. In this section we will explore the evidence for IPC formation in these materials.

As discussed previously, IPC formation is implied by the TGA spectrum of BTS. PAA and PHEA exhibit staged decomposition spectra.[36] In PAA, this spectrum shape is attributed to a formation of cyclic anhydride rings during the decomposition. Meanwhile, in PAA-PHEA composites and other IPC forming materials, a single decomposition is observed.[36,43] This is attributed to the strong IPC hydrogen bonding networks disrupting the cyclization reaction.

This shift in TGA spectrum is used in the above discussion to conclude that IPC formation is likely within our films. This is only somewhat compelling evidence, as the PAA decomposition mechanism should be reduced in the BTS and HEA-AA polymers due to the nature of a random copolymer reducing the number of adjacent acrylic acid sites. These reductions lead to expected reductions in the number of acrylic acid decompositions that could be observed in the TGA spectrum.

A quintessential behavior of IPC forming solutions is the observation of pH dependent solubility in water. This behavior has been observed for HEA-AA solutions in water solutions. Fig. 2.6, compellingly demonstrating that HEA-AA can undergo IPC formation when in water solution. Interestingly, we find the critical pH (pH_{crit}) for the increase in turbidity to be pH 5-6, this is far higher than observed for equal mixtures of PAA and PHEA (2.4-2.8).[36] The implications of this change in critical pH value are unclear, further studies are warranted leveraging turbidity and viscosity titrations to explore this phenomenon.

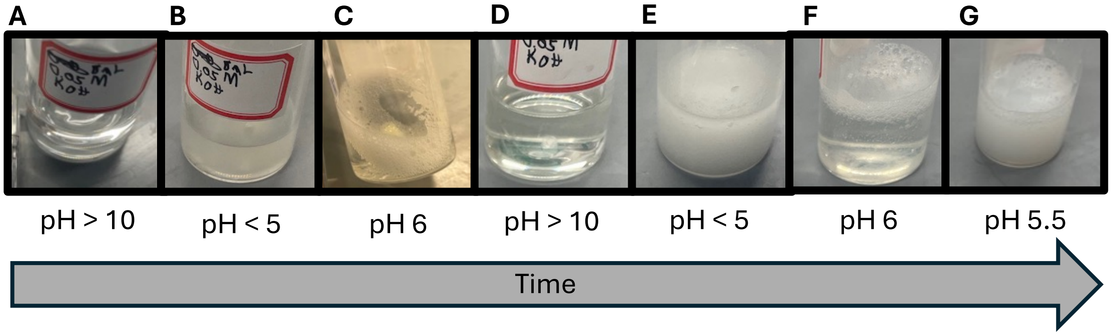

Figure 2.6: HEA-AA IPC formation in water solution. (a) 5 mL 0.05M KOH in water. (pH > 10 by pH strip) (b) Addition of 0.5mL of (0.15g/mL) HEA-AA in ethanol, white gum produced. (pH < 5) (c) Addition of 0.3M KOH in water, partially dissolved (pH 6). (d) Addition of further 0.3 M KOH in water, HEA-AA fully dissolved (pH > 10). (e) Addition of 1% HCl in water, cloudy solution resulted (pH < 5). (f) Addition of 0.3 M KOH in water, Clear solution observed with foamy surface (pH 6). (g) Addition of 1% HCl in water, cloudy solution resulted (pH ~ 5.5). From this we can

estimate pH_{crit} for HEA-AA as between pH 5 and pH 6. This is of note as it is far higher than for HEA/AA mixtures.

An interesting controversy within the lab is the question of the water solubility of HEA-AA. This unusual behavior was observed far before discussions of IPC formation were brought forth. It is observed when water is added to HEA-AA films that a small quantity of HEA-AA is dissolved, this can then be recast onto another surface leading again to an HEA-AA film. This effect is also observed in ion-HEA-AA films and is especially noticeable with $CoCl_2$-HEA-AA films. We now attribute this slight solubility to pH shifts in the water upon initial addition allowing for a small quantity to be dissolved. In essence the initial solubility of the polymer originates from the quantity of polymer needed to drop the pH of the solution beyond pH_{crit} for IPC formation.

In HEA-AA lacking metal ions, dried HEA-AA can be observed to form a white interface layer when water is added (Fig. 2.7). The HEA-AA is found to exhibit an unusual gummy texture. When dried, this water treated HEA-AA is found to remain gummy and is insoluble in ethanol, which typically is a good solvent for HEA-AA. We believe that this is indicative of the formation of strong IPC networks between polymer chains that is not observed in non-water exposed HEA-AA. This calls into serious question the degree of IPC formation in our active films.

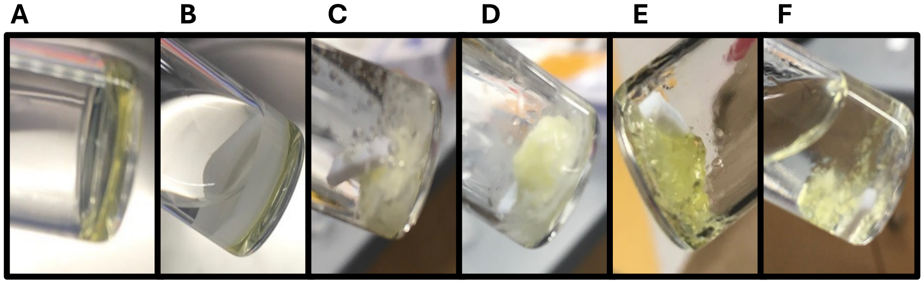

Figure 2.7: IPC behavior in water environment. (a) 0.15 g of HEA-AA dried for 25 hr at 90 °C (5 hr under vacuum prior to pump failure) (b) 1 mL water was added showing white layer at HEA-AA / water interface. The supernatant was poured off then both were dried, the polymer returned to its yellow coloration. 2.1 mg of HEA-AA, producing a visible film, was collected from the supernatant.

(c) The polymer was repeatedly mixed with water then the water poured off (~ 4 mL per aliquot, 75mL total) however no significant dissolving was observed. The polymer was then subjected to mechanical stirring and was observed to have a gummy texture. (d) Gummy texture of water exposed HEA-AA after pouring off the water. (e) Gummy texture of water exposed HEA-AA after drying under alternating heating at 90 °C and dry air spray. (f) 1 mL of ethanol was added to the dried water exposed polymer and the solution was stirred. The polymer was found to not redissolved in ethanol despite ethanol typically being a good solvent for HEA-AA.

2.4.2 Evidence That IPC Formation May Not Play a Major Role in Our Films

It was suggested, based on a paper looking at metal ion binding to arachidic acid, that metal ions bound to carboxylic acids cannot be extracted by water in absence of a strong acid.[44] This idea was used by a senior author on the paper upon which this chapter is based to conclude that the bound metal ions cannot function as the conducting species in this system. This was further used as the basis for table A.6 in the SI of this paper. Based on the evidence laid out below and in later chapters of this thesis, it can be concluded that these assumptions made in the paper are incorrect.

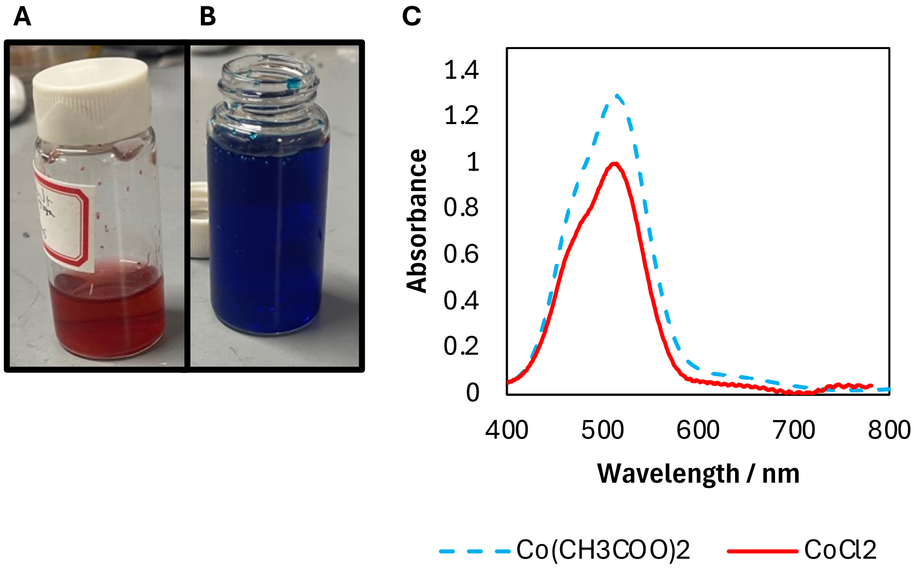

Figure 2.8: Cobalt acetate in water. (a) Cobalt acetate dissolved in water. (b) Cobalt acetate dissolved in water with lithium chloride. (c) UV/Vis spectra of cobalt acetate and cobalt chloride in

water. Note the spectra show identical peak shapes indicating both form cobalt hexaaqua upon being dissolved in water.

Upon dissolving cobalt (II) acetate in water, a pink solution resembling that of cobalt hexaaqua is formed. The addition of a saturated solution of lithium chloride in water causes the solution to exhibit a rapid color change to dark blue in line with the formation of tetrachlorocobaltate (Fig. 2.8(a-b)). The formation of this metal anion is explored further in Chapter 3. The UV/Vis spectrum of cobalt (II) acetate dissolved in water was obtained and then compared to the spectra of cobalt (II) chloride. The samples exhibit a high spectral similarity indicating that both form cobalt hexaaqua ions readily when mixed into a water solution (Fig. 2.8(c)). These observations imply that the cobalt-acetate bond is readily broken in aqueous solution in absence of a strong acid counter to the claims made above.

PAA is a useful analog for ion binding in the HEA-AA and BTS polymer systems. PAA cannot exhibit IPC formation alone, however, it exhibits ion binding and we suspect ion mediated chain crosslinking. It has been utilized within the Daraio group as an analog for spectroscopic studies and studies of ligand binding mediated formation of tetrahalometallates. PAA when drop-cast into a thin film under typical laboratory humidities and temperatures (20-70% relative humidity, 18-26 °C) forms a gooey sticky film. If the film is dried on a hot plate (70-90 °C) for an extended period (>3 days) an extremely brittle dry film result. Similarly when HEA-AA is cast under typical laboratory humidities and temperatures, a gooey, sticky film results that can be dried at elevated temperatures. However, the dried HEA-AA films exhibit lower brittleness than the PAA films.

When both PAA and HEA-AA films are drop-cast with divalent metal ions and briefly dried on a hot plate (60-90 °C, ≤ 1hr) the resulting films are solid and are found to not be tacky. This is especially interesting as we expect films containing ions to be more hydrophilic and as a result contain more water at a given temperature and humidity. This is notable as water is known to function as a plasticizer in this class of polymers, this is discussed in depth in Chapter 3.[45,46] As such one might expect ion containing films to exhibit softer properties, this is not what is observed. We attribute this change in properties to two factors. First, cation bridged chain crosslinking leading to an increase in the rigidity of the polymer. Second, the occupation of carboxyl sites by cations reduces/eliminates the tackiness of the polymer films. These mechanisms imply direct bonding of the divalent cations to the polymer's carboxyl sites. When dried PAA films containing calcium chloride or cobalt chloride are rinsed or immersed in water they immediately dissolve. This directly implies that the metal ion – carboxyl bond can be cleaved by water in solution counter to the claims used to draw conclusions in table A.6.

In order to further probe table A.6, films were cast and dried (70 °C) comprised of $CaCl_2$-PAA, $CaCl_2$-HEA-AA, and HEA-AA without added metal ions. These films were then immersed in water (Fig. 2.9(a)). In line with previous experiments it was observed that the $CaCl_2$-PAA film fully dissolved, the $CaCl_2$-HEA-AA film turned cloudy white, and the HEA-AA film turned an opaque white. The films were then subjected to a slight mechanical agitation consisting of running the gloved pad of a thumb over the films (Fig. 2.9(b)). The $CaCl_2$-HEA-AA film was observed to readily be removed from the surface. The HEA-AA film was found to far more robust, and was not completely removed. This implies that the crosslinking in submerged HEA-AA and $CaCl_2$-HEA-AA films are fundamentally different. The most likely mechanism of chain crosslinking in the HEA-AA film is the formation of IPC. The presumably extensive IPC networks lead to a robust film. In the $CaCl_2$-HEA-AA films, there are two mechanisms of crosslinking: 1) IPC formation, 2) metal-bridges. We have found from the PAA films that acrylic acid based metal-bridges are not robust to water immersion. We speculate here that the majority of $CaCl_2$ is stripped from the films during water immersion. In BTS polymer, it was observed that 88.38% of the $CaCl_2$ is stripped during extended water immersion. We expect acrylic acid sites involved in calcium binding are in a deprotonated state. When water is reintroduced and the $CaCl_2$ is stripped away, some of these sites may remain in a deprotonated state preventing them from engaging in IPC formation. We would expect this to reduce the mechanical strength of the films inline with what is observed. If we assume the $CaCl_2$ is readily stripped from acrylic acid sites by water, this begs the question of the origin of the remaining bound 11.62% Ca^{2+} in the BTS polymer TGA experiments. Here we hypothesize that as IPC formation occurs in the polymer, it limits the diffusion of water and $CaCl_2$, resulting in some trapped salt. We believe this is inline with the observations here for HEA-AA and PAA, in addition to being inline with experimental results for the BTS polymer. Follow up studies leveraging mechanical testing are warranted.

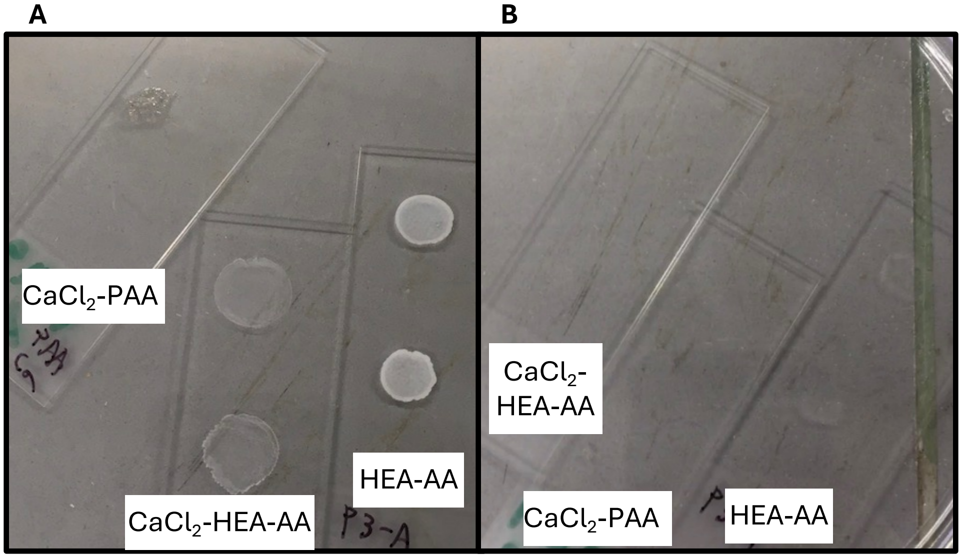

Figure 2.9: Submerged polymer films. (a) $CaCl_2$-PAA, $CaCl_2$-HEA-AA, and HEA-AA films submerged in water. The PAA film fully dissolves. The $CaCl_2$-HEA-AA film turns cloudy. The HEA-AA film turns opaque. (b) Films after being gently rubbed with pad of the thumb. Note, the $CaCl_2$-HEA-AA film is fully removed, while a portion of the HEA-AA film remains.

For the purposes of understanding ion binding to the polymer, one of the most useful tools is FTIR spectroscopy. It allows us to track how the water content in the polymer varies between polymer films. Furthermore, as discussed in Chapter 3, metal-carboxyl bonding leads to a distinct shift in the carboxyl stretching mode. This shift is on the order of 160 cm^{-1} from typically ~1700 cm^{-1} to 1550-1600 cm^{-1}. As such it is possible to qualitatively measure the degree of metal carboxyl bonding in the polymer system. In addition, PAA/PHEA IPC formation has been observed to cause a slight carboxyl peak shift corresponding to the hydrogen bond formation.[36] This peak shift is far smaller than that observed for metal-carboxyl binding.

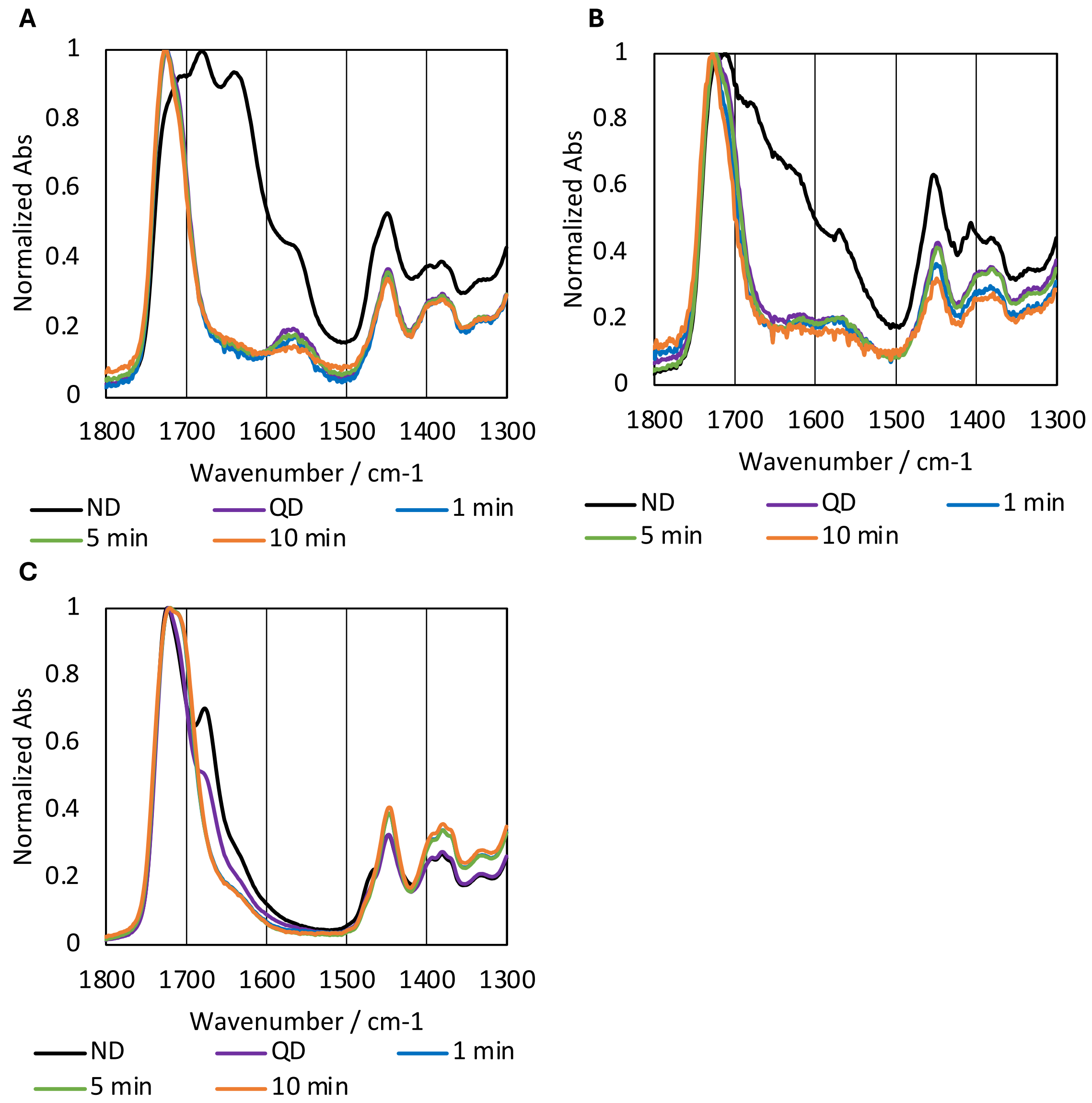

Figure 2.10: FTIR spectra of ion-HEA-AA films subjected to water immersion. (a) $CaCl_2$-HEA-AA, notice the significant reduction in the Ca^{2+}-carboxyl and the water peaks. (b) $CoCl_2$-HEA-AA notice the significant reduction in the $Co^{2\pm}$carboxyl and the water peaks. (c) HEA-AA without added ions. Notice the reduction in the water peaks and slight red shift to the carboxyl peak.

In order to better understand the stripping of metal ions from polymer films by water immersion, FTIR studies were carried out. Films were prepared by drop-casting 2.5uL of polymer solution onto glass slides, then drying the samples on a hotplate (70 °C, 1hr).

Samples were then placed in a water bath for a set amount of time, then dried again on a hot plate (70 °C, 1 hr). After this procedure, ATR-FTIR was obtained on a Nicolet 6700 FTIR spectrometer. For this analysis, the FTIR spectra were trimmed to 1300-2000 cm^{-1} and normalized. Films were prepared from $CaCl_2$-HEA-AA, $CoCl_2$-HEA-AA, and HEA-AA. For each material, control film was collected that was not dipped in the water bath (ND), one film was subjected to a quick dip less than 10 seconds (QD), and the remainder were subjected to fixed time intervals of 1, 5, and 10 minutes.

The $CoCl_2$-HEA-AA films were found to exhibit a slight blue coloration. This coloration disappeared once the films were soaked in water and redried. As discussed in Chapter 3, we now understand this coloration originates from the tetrachlorocobaltate anion. As we do not expect this anion to be bound to the polymer, this result is not unexpected.

In the control $CaCl_2$-HEA-AA and $CoCl_2$-HEA-AA films, we observe a clear peak feature around 1550-1600 cm^{-1} which we have identified in the metal-carboxyl peak, it is notable absent in the HEA-AA film, (Fig. 2.10(b-c)). Upon a quick dip in the water bath, the intensity of this peak dramatically decreases (decrease by ~60% in $CaCl_2$-HEA-AA and ~57% in $CoCl_2$-HEA-AA). By comparing the 10 min dip to the quick dip, we can observe that over time the metal ions continue to be stripped out of the polymer binding sites (a further decrease by ~26% for $CaCl_2$-HEA-AA and 22% for $CoCl_2$-HEA-AA, relative to the quick dip samples).

We can further examine the water peak located at ~1630-1650 cm^{-1}. This can be seen as a clear peak in the metal-HEA-AA films and as a shoulder in the HEA-AA film. Upon water immersion, the intensity of this peak dramatically decreases. Given water immersion seems to strip ions from the films, this result is not unexpected as water content in this class of films is known to correlate with salt content, this originates from the hydrophilicity of these salt complexes. Explaining this behavior in the ion-free HEA-AA film presents a larger challenge. We expect in this polymer, the inherent hydrophilicity originates from the polar carboxyl, ester, and hydroxyl functional groups and especially the ability of the carboxyl and hydroxyl groups to engage in hydrogen bonding with water. We hypothesize that water immersion drives the formation of robust hydrogen bonding networks between polymer chains, this is in line with the observation that HEA-AA immersed in water then dried is no longer soluble in ethanol as discussed above. We hypothesize here that once the HEA-AA forms these extensive IPC crosslinking bridges two things occur: 1) the hydrophilicity of the polymer is reduced as the number of free carboxyls and hydroxyl hydrogen binding sites are reduces, 2) the formation of these crosslinking bridges causes diffusion channels in the polymer to collapse, limiting the diffusion of both ions and water within the material, thus limiting the ability of water in reach potential binding sites within the polymer.

The peak at ~1675 cm^{-1} represents one of the fascinating mysteries in this system. A variety of internal density functional theory studies have failed to show any absorption peaks within this range. This peak does not correlate with bulk water content, see Chapter 3, and is found in films both containing and lacking metal ions. As noted in Chapter 3, this peak appears in films exposed to both water vapor and deuterium oxide vapor, therefore we suspect that it does not originate from a structure involving water. Here we see it greatly reduces in intensity with water immersion. We hypothesize that this originates from some form of unusual hydrogen bonding structure involving either the carboxyl or ester sites. We hypothesize that the formation of extensive IPC networks upon water immersion in some manner reduces these unusual structures.

A

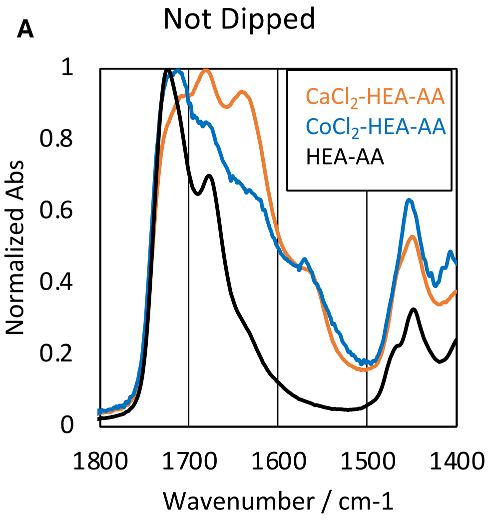
Not Dipped
1
0.8
0.6
0.4
0.2
0
Normalized Abs
1800
1700
1600
1500
1400
Wavenumber / cm-1
CaCl2-HEA-AA
CoCl2-HEA-AA
HEA-AA

B

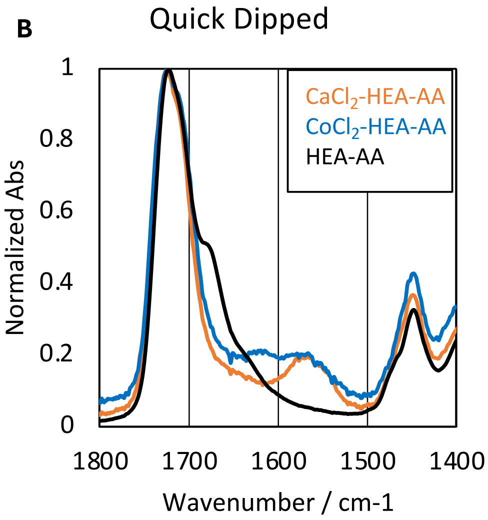
Quick Dipped
1
0.8
0.6
0.4
0.2
0
Normalized Abs
1800
1700
1600
1500
1400
Wavenumber / cm-1
CaCl2-HEA-AA
CoCl2-HEA-AA
HEA-AA

C

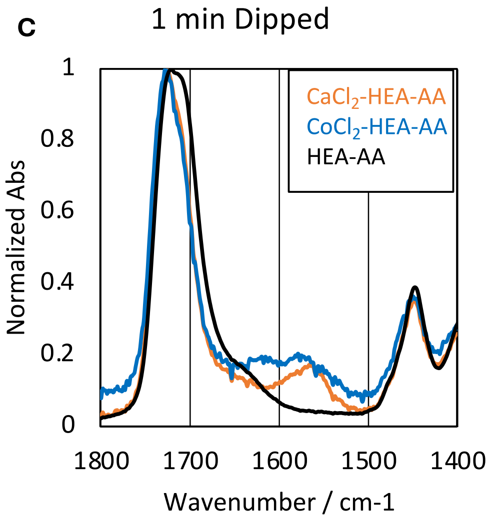
1 min Dipped
1
0.8
0.6
0.4
0.2
0
Normalized Abs
1800
1700
1600
1500
1400
Wavenumber / cm-1
CaCl2-HEA-AA
CoCl2-HEA-AA
HEA-AA

D

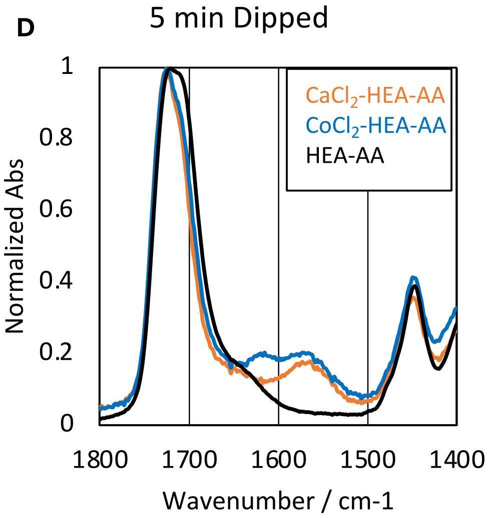
5 min Dipped
1
0.8
0.6
0.4
0.2
0
Normalized Abs
1800
1700
1600
1500
1400
Wavenumber / cm-1
CaCl2-HEA-AA
CoCl2-HEA-AA
HEA-AA

E

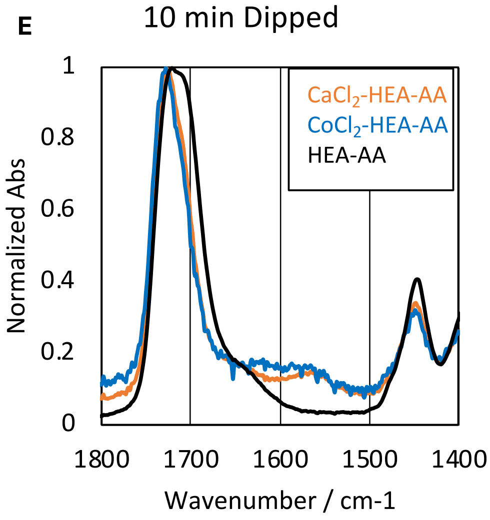
10 min Dipped
1
0.8
0.6
0.4
0.2
0
Normalized Abs
1800
1700
1600
1500
1400
Wavenumber / cm-1
CaCl2-HEA-AA
CoCl2-HEA-AA
HEA-AA

Figure 2.11. Film specific comparison at various water immersion times. (a) Films that were not dipped into water. Notice the large differences between each material. (b) Films that were dipped into a water bath for < 10 seconds) (c) Films immersed for 1 minutes. (d) Films immersed for 5 minutes. (e) Films immersed for 10 minutes. Notice the high similarity between the films, Some of the metal-carboxyl peak remains. The water peaks have largely disappeared. The HEA-AA carboxyl peak shows a notable red shift relative to the other samples.

The peak at 1750-1700 cm^{-1} originates from both the carbonyl and ester functional groups. In metal ion-HEA-AA films, a slight blue shift can be seen in this peak location with water exposure. The origin of this blueshift remains unknown. In films lacking metal ions, this peak shows a distinct red shift with water immersion. We speculate that this redshift originates from the formation of IPC binding sites. Density functional theory calculations have been carried out examining these potential IPC binding interactions. They were carried out utilizing ORCA quantum chemistry version 4.2.0, and leveraged the B3LYP functional and def2-TZVP basis set.[47–57] While these calculations are do not match our experimental data, they show a 48 cm^{-1} shift in the carboxyl peak from 1807 cm^{-1} to 1759 cm^{-1}. This may loosely correlate with the observed shift in the carboxyl peak in the HEA-AA films upon water exposure.

2.4.3 Conclusions of This Further Study

Our polymer films can engage in IPC formation, however, the degree of IPC formation in our cast films remains unknown. FTIR of the polymer demonstrates that the metal ions bind directly to the acrylic acid monomers, these bound metal ions can be stripped by bulk water. Any acrylic acids engaging in metal ion binding is unable to engage in IPC formation. Differences in the mechanical properties of films and the spectroscopic data implies the cast salt-HEA-AA films do not engage in extensive IPC formation. As shown in Chapter 3, the presence of the metal cation and polymer alone is necessary for the high temperature response behavior. From these we conclude that while further studies into IPC formation in this system may provide interesting insights, the mechanism of the polymer's high temperature response originates from the binding site of metal ions to the polymer and is tied to the overall structure of the polymer. We speculate here that IPC structures may play a role in the structuring of the polymer to enable charge transport, however, these remain speculations. Further work is needed.

2.5 Materials and Methods

2.5.1 Materials

HEA, tert-butyl acrylate (t-BA), n-butyl acrylate (n-BA) monomers, and a dual-functional chain transfer agent (CTA) S,S-dibenzyl trithiocarbonate (DBTTC) were purchased from Sigma-Aldrich. DBTTC was used to expedite the synthesis of the ABA polymer for multistep processing.[58] Azobis (isobutyronitrile) (AIBN), a radical initiator, was purchased from Sigma-Aldrich and recrystallized from methanol before use.

2.5.2 Synthetic Procedure of The ABA Block Copolymer

ABA-type block copolymers were prepared via RAFT polymerization (Fig. A.1(a)). During the entire polymer synthesis process, the resulting material was characterized using GPC and NMR (1H NMR) (Fig. A.2).[59] First, N_2-purged HEA 1 (1.16 g, 10 mmol) and t-BA 2 (1.28 g, 10 mmol) were dissolved in 2 ml of dimethylformamide (DMF), followed by DBTTC 3 (29 mg, 0.1 mmol). The mixture was further purged with N_2 for 3 min. Next, AIBN (0.81 mg, 5 μmol) was added into the reactor and lastly stirred at 75 °C under inert N_2 atmosphere. The reactor was cooled down and vented to air. The residual monomers (t-BA and HEA) were removed by vacuum, following precipitation in 100 ml of cold diethyl ether that resulted in a yellow oil of bis[p(t-BA_{10}-r-HEA_{10})] trithiocarbonate (macro-CTA). The yield of polymerization monitored using 1H NMR was 80% (2.02 g). Next, the macro-CTA was mixed with N_2-purged n-BA 4 (12.8 g, 100 mmol) and AIBN (0.81 mg, 5 μmol), along with 15 ml of DMF. The mixture was purged again under N_2 for 3 min, followed by stirring at 75 °C under N_2 atmosphere. The reactor was cooled down and vented to air. Residual n-BA was removed by vacuum to yield a protected form of ABA block copolymer, p[(t-BA_5-r-HEA_5)-b-$(n\text{-}BA)_{100}$-b-(t-BA_5-r-HEA_5)]r. Here, a conversion rate of 81% was achieved (11.24 g).

Last, 1 g of the protected polymer was dissolved in 3 ml of dichloromethane (DCM) and combined with 3 ml of trifluoroacetic acid (TFA). The deprotection reaction was carried out at RT and stirred overnight. DCM and TFA were removed by vacuum after precipitating the polymer in cold diethyl ether. As a result, a highly sticky yellow oil as the final form of the deprotected ABA block copolymer, p[(AA5-r-HEA_5)-b-$(n\text{-}BA)_{100}$-b-(AA_5-r-HEA_5)]r, was produced. The conversion of tert-butyl groups into AA was confirmed using 1H NMR from the deprotected block copolymer (100% conversion to AA form).

2.5.3 Polymer Characterization

The size of the colloidal particle formed in ethanol was measured using a zeta potential and particle size analyzer (Otsuka Electronics, ELSZ-2000) at RT (Fig. 2.1(b) and Fig. A.1(b)). After dissolving the samples in deuterated DCM (CD_2Cl_2), NMR spectra were obtained using Bruker Ascend 500 (500 MHz). Spectral analysis was performed using Topspin 3.2 software. GPC was carried out in tetrahydrofuran on two MZ-gel (10 μm) columns composed of styrene-divinylbenzene copolymer (Analysentechnik) connected in series with a miniDAWN TREOS multiangle laser light scattering detector. The film formation of the block copolymer was monitored in situ from the composite mixtures using ATR-FTIR spectroscopy using a Nicolet iS50 FTIR spectrometer. The synthesized block copolymer was dissolved in ethanol (1 mg/1 ml) with metal ions (0.3 M), mixed, placed on top of the ATR module, and continuously dried in air at 22 °C under 23% relative humidity. The ATR-FTIR spectra were obtained as a function of time. Table A.5 summarizes the composition of the tested mixtures.

TGA was carried out on dried composite films (20 mg) using a Discovery TGA (Thermo Fisher Scientific) with the following settings: ramp rate, 10 °C/min; temperature range, 30 ° to 650 °C; and N_2 flow rate, 10 ml/min. For material identification, TGA-FTIR measurements were performed in parallel to TGA to analyze the gas-phase FTIR spectra using a Nicolet iS50 FTIR spectrometer. The spectrometer was equipped with an auxiliary experiment module, composed of an optional mercury cadmium telluride detector, a 10-cm path-length nickel-plated aluminum flow cell, and an integrated digital temperature controller. After the integrated digital controller reached a constant 130 ° C temperature, FTIR spectra were collected every 5 min between 0 and 65 min. For each measurement, a total of 32 scans were averaged with 4 cm^{-1} resolution. Impedance spectroscopy analysis was performed using an impedance analyzer (Zurich Instruments MFIA). AC frequency was swept between 1 and 100 MHz (100 points) with a voltage biased at 1 V.

Percentage of IPC formed in the polymer film was calculated using the AA-Ca^{2+} titration method with the assumption that two AA functional groups are involved to form a coordination bond with a single Ca^{2+}. To begin with, the total amount of AA and metal ions (100% $CaCl_2$) in the polymer solution mixture was calculated (table A.6). Next, the TGA and FTIR spectrum of the composite film was measured before and after washing with deionized (DI) water (Fig. 2.2(c)). To completely rinse out the unbound metal ions from the polymer matrix, the film was soaked in 200 cm^3 of DI water excessively with continuous stirring (120 rpm) at RT for 72 hours and dried. The proportion of Ca^{2+} bound to the polymer was calculated by subtracting the weight percentage between the two TGA profiles at 550 ° C, which corresponds to the residual content of metal ions (chelated Ca^{2+} with AA = 11.62%, free Ca^{2+} = 88.38%). The free and bound Ca^{2+} ions were recognized from the FTIR spectra (inset of Fig. 2.2(c)) at 1640 and 1560 cm^{-1}, respectively. On the basis of the number of Ca^{2+} ions bound to the polymer film, the percentage of AA used to from IPCs was estimated as 86.13% (table A.6).

2.5.4 Device Fabrication

The block copolymer was dissolved in anhydrous ethanol at a concentration of 0.15 g/ml. Simultaneously, metal ion salt ($CaCl_2$) was dissolved in anhydrous ethanol at a concentration of 0.3 M. The ionically cross-linked polymer solution was obtained by mixing the two solutions at a volume ratio of 1:2. To fabricate the flexible temperature sensors, a thin sheet of polyester terephthalate (PET; 20 μm) was washed and attached to a 4-inch (100 mm) silicon wafer. On top, a layer of photoresist was spin-coated and patterned using the standard lithography process. The surface was then treated with O_2 plasma (Plasma-Therm SLR 720) followed by Ti/Au evaporation (CHA Mark 40 electron beam evaporator) with a thickness of 200/1000 Å. The entire sheet was immersed in acetone for metal lift-off, exposing the circularly shaped interdigitated electrodes (D = 4 mm, 30 μm wide with 20-μm spacing). Last, the PET sheet with the patterned electrodes was released, rinsed, and dried for use. Next, a total of 5 μl of cross-linked polymer solution was drop cast on top of each sensing pixel and dried at RT for 1 hour. To test different hydration status for optimal temperature response, the composite polymer was further dehydrated using dry air and sealed using a permeable PI tape. For cyclic studies, a thin layer of parylene-C (2 μm; ParaTech LabTop 3000 Parylene coater) was conformally coated around the devices to prevent water absorption or evaporation. External electrical connection was made using an anisotropic conductive film or an electrical probe set. The cross-sectional view of the fabrication process is shown in Fig. A.6(a).

The IR bolometers were fabricated following similar steps but with slight modifications. An 8-inch (200 mm) glass wafer was cleaned in piranha solution for 30 min, rinsed using DI water, and dried under a nitrogen stream. The dried wafer was then plasma-treated. PI solution [10 weight % in dimethylacetamide (DMAc)] was spin-coated to a thickness of 2 μm and baked on a hot plate at 250 °C for 60 min to cure the resin and fully remove the trapped DMAc in the film. Using a hard mask, a 100-nm-thick Au was thermally evaporated on the PI film to form the same interdigitated electrode design used above and rinsed using DI water, followed by a complete dry step. For handling purpose, a guiding layer of PI tape was placed on the wafer surface and cut into pieces with a knife. Last, each PI film containing a single electrode design was released and attached on a custom-made plastic holder with an opening at its center for air suspension (membrane structure). A total of 5 μl of cross-linked polymer solution was drop cast on top of the sensing pixel and dried at RT for 1 hour. Fig. A.9(a) illustrates the entire device fabrication process.

2.5.5 Experimental Setup

A measurement stage was built to evaluate the temperature sensor (Figs. A.7(a) and A.8(a)). The system was composed of a Peltier-Element (model Qc-31-1.4-8.5m) connected to a custom circuit board for controlled sample heating and cooling. The sensors were connected through electrical probes, and signals were measured using an impedance analyzer (Zurich Instruments MFIA). During measurements, the temperature of the Peltier block was continuously monitored with a Pt100 platinum resistance thermometer, which was calibrated by a FLIR thermal camera (model A655sc). For multiple cyclic tests, we generated a temperature sine wave between 15 ° and 45 °C through the dedicated control board.

For IR measurement, the bolometer was placed in a hermetically sealed chamber (MPS-PT, Micro Probe System, Nextron Corp.) with a zinc selenide (ZnSe) transmission window (68-503, Edmund Optics). Fig. A.9(c) illustrates the optical setup. A quantum cascade laser (QCL; MIRcat-QT Mid-IR Laser) was used to apply IR radiation to the device at various wavelengths. The beam size of the QCL was 4.8 mm in diameter. The power of the emitted IR was calibrated using a power meter (PM16-401, Thorlabs) or an IR detector (PVMI-4TE, VIGO System). For both temperature and IR measurements, RMS current and phase from the impedance analyzer were continuously logged and visualized using a custom software (Python, LabVIEW).

References

(1) Forrest, S. R. The Path to Ubiquitous and Low-Cost Organic Electronic Appliances on Plastic. *Nature* **2004**, *428* (6986), 911–918. https://doi.org/10.1038/nature02498.

(2) Sokolov, A. N.; Roberts, M. E.; Bao, Z. Fabrication of Low-Cost Electronic Biosensors. *Mater. Today* **2009**, *12* (9), 12–20. https://doi.org/10.1016/S1369-7021(09)70247-0.

(3) Ling, H.; Liu, S.; Zheng, Z.; Yan, F. Organic Flexible Electronics. *Small Methods* **2018**, *2* (10), 1800070. https://doi.org/10.1002/smtd.201800070.

(4) Kang, J.; Tok, J. B.-H.; Bao, Z. Self-Healing Soft Electronics. *Nat. Electron.* **2019**, *2* (4), 144–150. https://doi.org/10.1038/s41928-019-0235-0.

(5) Tee, B. C.-K.; Chortos, A.; Berndt, A.; Nguyen, A. K.; Tom, A.; McGuire, A.; Lin, Z. C.; Tien, K.; Bae, W.-G.; Wang, H.; Mei, P.; Chou, H.-H.; Cui, B.; Deisseroth, K.; Ng, T. N.; Bao, Z. A Skin-Inspired Organic Digital Mechanoreceptor. *Science* **2015**, *350* (6258), 313–316. https://doi.org/10.1126/science.aaa9306.

(6) You, I.; Mackanic, D. G.; Matsuhisa, N.; Kang, J.; Kwon, J.; Beker, L.; Mun, J.; Suh, W.; Kim, T. Y.; Tok, J. B.-H.; Bao, Z.; Jeong, U. Artificial Multimodal Receptors Based on Ion Relaxation Dynamics. *Science* **2020**, *370* (6519), 961–965. https://doi.org/10.1126/science.aba5132.

(7) Wang, N.; Yang, A.; Fu, Y.; Li, Y.; Yan, F. Functionalized Organic Thin Film Transistors for Biosensing. *Acc. Chem. Res.* **2019**, *52* (2), 277–287. https://doi.org/10.1021/acs.accounts.8b00448.

(8) Lee, M. Y.; Lee, H. R.; Park, C. H.; Han, S. G.; Oh, J. H. Organic Transistor-Based Chemical Sensors for Wearable Bioelectronics. *Acc. Chem. Res.* **2018**, *51* (11), 2829–2838. https://doi.org/10.1021/acs.accounts.8b00465.

(9) Sekitani, T.; Someya, T. Stretchable, Large-Area Organic Electronics. *Adv. Mater.* **2010**, *22* (20), 2228–2246. https://doi.org/10.1002/adma.200904054.

(10) Wang, J.; Lin, M.-F.; Park, S.; Lee, P. S. Deformable Conductors for Human–Machine Interface. *Mater. Today* **2018**, *21* (5), 508–526. https://doi.org/10.1016/j.mattod.2017.12.006.

(11) Wang, S.; Xu, J.; Wang, W.; Wang, G.-J. N.; Rastak, R.; Molina-Lopez, F.; Chung, J. W.; Niu, S.; Feig, V. R.; Lopez, J.; Lei, T.; Kwon, S.-K.; Kim, Y.; Foudeh, A. M.; Ehrlich, A.; Gasperini, A.; Yun, Y.; Murmann, B.; Tok, J. B.-H.; Bao, Z. Skin Electronics from Scalable Fabrication of an Intrinsically Stretchable Transistor Array. *Nature* **2018**, *555* (7694), 83–88. https://doi.org/10.1038/nature25494.

(12) Lim, H.-R.; Kim, H. S.; Qazi, R.; Kwon, Y.-T.; Jeong, J.-W.; Yeo, W.-H. Advanced Soft Materials, Sensor Integrations, and Applications of Wearable Flexible Hybrid Electronics in Healthcare, Energy, and Environment. *Adv. Mater.* **2020**, *32* (15), 1901924. https://doi.org/10.1002/adma.201901924.

(13) Lee, Y. H.; Kweon, O. Y.; Kim, H.; Yoo, J. H.; Han, S. G.; Oh, J. H. Recent Advances in Organic Sensors for Health Self-Monitoring Systems. *J. Mater. Chem. C* **2018**, *6* (32), 8569–8612. https://doi.org/10.1039/C8TC02230E.

(14) Ren, X.; Pei, K.; Peng, B.; Zhang, Z.; Wang, Z.; Wang, X.; Chan, P. K. L. A Low-Operating-Power and Flexible Active-Matrix Organic-Transistor Temperature-Sensor Array. *Adv. Mater.* **2016**, *28* (24), 4832–4838. https://doi.org/10.1002/adma.201600040.

(15) Trung, T. Q.; Ramasundaram, S.; Hwang, B.-U.; Lee, N.-E. An All-Elastomeric Transparent and Stretchable Temperature Sensor for Body-Attachable Wearable Electronics. *Adv. Mater.* **2016**, *28* (3), 502–509. https://doi.org/10.1002/adma.201504441.

(16) Yamamoto, Y.; Harada, S.; Yamamoto, D.; Honda, W.; Arie, T.; Akita, S.; Takei, K. Printed Multifunctional Flexible Device with an Integrated Motion Sensor for Health Care Monitoring. *Sci. Adv.* **2016**, *2* (11), e1601473. https://doi.org/10.1126/sciadv.1601473.

(17) Yokota, T.; Inoue, Y.; Terakawa, Y.; Reeder, J.; Kaltenbrunner, M.; Ware, T.; Yang, K.; Mabuchi, K.; Murakawa, T.; Sekino, M.; Voit, W.; Sekitani, T.; Someya, T. Ultraflexible, Large-Area, Physiological Temperature Sensors for Multipoint Measurements. *Proc. Natl. Acad. Sci.* **2015**, *112* (47), 14533–14538. https://doi.org/10.1073/pnas.1515650112.

(18) Bronstein, H.; Nielsen, C. B.; Schroeder, B. C.; McCulloch, I. The Role of Chemical Design in the Performance of Organic Semiconductors. *Nat. Rev. Chem.* **2020**, *4* (2), 66–77. https://doi.org/10.1038/s41570-019-0152-9.

(19) Fahlman, M.; Fabiano, S.; Gueskine, V.; Simon, D.; Berggren, M.; Crispin, X. Interfaces in Organic Electronics. *Nat. Rev. Mater.* **2019**, *4* (10), 627–650. https://doi.org/10.1038/s41578-019-0127-y.

(20) Mogurampelly, S.; Borodin, O.; Ganesan, V. Computer Simulations of Ion Transport in Polymer Electrolyte Membranes. *Annu. Rev. Chem. Biomol. Eng.* **2016**, *7* (Volume 7, 2016), 349–371. https://doi.org/10.1146/annurev-chembioeng-080615-034655.

(21) Friederich, P.; Fediai, A.; Kaiser, S.; Konrad, M.; Jung, N.; Wenzel, W. Toward Design of Novel Materials for Organic Electronics. *Adv. Mater.* **2019**, *31* (26), 1808256. https://doi.org/10.1002/adma.201808256.

(22) Höfte, H.; Peaucelle, A.; Braybrook, S. Cell Wall Mechanics and Growth Control in Plants: The Role of Pectins Revisited. *Front. Plant Sci.* **2012**, *3*. https://doi.org/10.3389/fpls.2012.00121.

(23) Di Giacomo, R.; Daraio, C.; Maresca, B. Plant Nanobionic Materials with a Giant Temperature Response Mediated by Pectin-Ca $^{2+}$. *Proc. Natl. Acad. Sci.* **2015**, *112* (15), 4541–4545. https://doi.org/10.1073/pnas.1421020112.

(24) Di Giacomo, R.; Bonanomi, L.; Costanza, V.; Maresca, B.; Daraio, C. Biomimetic Temperature-Sensing Layer for Artificial Skins. *Sci. Robot.* **2017**, *2* (3), eaai9251. https://doi.org/10.1126/scirobotics.aai9251.

(25) Costanza, V.; Bonanomi, L.; Moscato, G.; Wang, L.; Choi, Y. S.; Daraio, C. Effect of Glycerol on the Mechanical and Temperature-Sensing Properties of Pectin Films. *Appl. Phys. Lett.* **2019**, *115* (19), 193702. https://doi.org/10.1063/1.5121710.

(26) Grant, G. T.; Morris, E. R.; Rees, D. A.; Smith, P. J. C.; Thom, D. Biological Interactions between Polysaccharides and Divalent Cations: The Egg-Box Model. *FEBS Lett.* **1973**, *32* (1), 195–198. https://doi.org/10.1016/0014-5793(73)80770-7.

(27) Powell, D. A.; Morris, E. R.; Gidley, M. J.; Rees, D. A. Conformations and Interactions of Pectins: II. Influence of Residue Sequence on Chain Association in Calcium Pectate Gels. *J. Mol. Biol.* **1982**, *155* (4), 517–531. https://doi.org/10.1016/0022-2836(82)90485-5.

(28) Thakur, B. R.; Singh ,Rakesh K.; Handa ,Avtar K.; and Rao, M. A. Chemistry and Uses of Pectin — A Review. *Crit. Rev. Food Sci. Nutr.* **1997**, *37* (1), 47–73. https://doi.org/10.1080/10408399709527767.

(29) Matyjaszewski, K.; Xia, J. Atom Transfer Radical Polymerization. *Chem. Rev.* **2001**, *101* (9), 2921–2990. https://doi.org/10.1021/cr940534g.

(30) Yamago, S. Precision Polymer Synthesis by Degenerative Transfer Controlled/Living Radical Polymerization Using Organotellurium, Organostibine, and Organobismuthine Chain-Transfer Agents. *Chem. Rev.* **2009**, *109* (11), 5051–5068. https://doi.org/10.1021/cr9001269.

(31) Moad, G.; Rizzardo, E.; Thang, S. H. Toward Living Radical Polymerization. *Acc. Chem. Res.* **2008**, *41* (9), 1133–1142. https://doi.org/10.1021/ar800075n.

(32) Cao, L.; Lu, W.; Mata, A.; Nishinari, K.; Fang, Y. Egg-Box Model-Based Gelation of Alginate and Pectin: A Review. *Carbohydr. Polym.* **2020**, *242*, 116389. https://doi.org/10.1016/j.carbpol.2020.116389.

(33) Furukawa, J. A Theory of Pseudo Cross-Link. *Polym. Bull.* **1982**, *7* (1), 23–30. https://doi.org/10.1007/BF00264153.

(34) Dimarzio, E. A.; Gibbs, J. H. Glass Temperature of Copolymers. *J. Polym. Sci.* **1959**, *40* (136), 121–131. https://doi.org/10.1002/pol.1959.1204013609.

(35) Sayah, M. Y.; Chabir, R.; Benyahia, H.; Kandri, Y. R.; Chahdi, F. O.; Touzani, H.; Errachidi, F. Yield, Esterification Degree and Molecular Weight Evaluation of Pectins

Isolated from Orange and Grapefruit Peels under Different Conditions. *PLOS ONE* **2016**, *11* (9), e0161751. https://doi.org/10.1371/journal.pone.0161751.

(36) Mun, G. A.; Khutoryanskiy, V. V.; Akhmetkalieva, G. T.; Shmakov, S. N.; Dubolazov, A. V.; Nurkeeva, Z. S.; Park, K. Interpolymer Complexes of Poly(Acrylic Acid) with Poly(2-Hydroxyethyl Acrylate) in Aqueous Solutions. *Colloid Polym. Sci.* **2004**, *283* (2), 174–181. https://doi.org/10.1007/s00396-004-1115-2.

(37) Schymkowitz, J. W. H.; Rousseau, F.; Martins, I. C.; Ferkinghoff-Borg, J.; Stricher, F.; Serrano, L. Prediction of Water and Metal Binding Sites and Their Affinities by Using the Fold-X Force Field. *Proc. Natl. Acad. Sci.* **2005**, *102* (29), 10147–10152. https://doi.org/10.1073/pnas.0501980102.

(38) Wang, B.; Lai, J.; Li, H.; Hu, H.; Chen, S. Nanostructured Vanadium Oxide Thin Film with High TCR at Room Temperature for Microbolometer. *Infrared Phys. Technol.* **2013**, *57*, 8–13. https://doi.org/10.1016/j.infrared.2012.10.006.

(39) Dai, J.; Wang, X.; He, S.; Huang, Y.; Yi, X. Low Temperature Fabrication of VOx Thin Films for Uncooled IR Detectors by Direct Current Reactive Magnetron Sputtering Method. *Infrared Phys. Technol.* **2008**, *51* (4), 287–291. https://doi.org/10.1016/j.infrared.2007.12.002.

(40) Kim, J.; Lee, M.; Shim, H. J.; Ghaffari, R.; Cho, H. R.; Son, D.; Jung, Y. H.; Soh, M.; Choi, C.; Jung, S.; Chu, K.; Jeon, D.; Lee, S.-T.; Kim, J. H.; Choi, S. H.; Hyeon, T.; Kim, D.-H. Stretchable Silicon Nanoribbon Electronics for Skin Prosthesis. *Nat. Commun.* **2014**, *5* (1), 5747. https://doi.org/10.1038/ncomms6747.

(41) Park, J.; Kim, M.; Lee, Y.; Lee, H. S.; Ko, H. Fingertip Skin–Inspired Microstructured Ferroelectric Skins Discriminate Static/Dynamic Pressure and Temperature Stimuli. *Sci. Adv.* **2015**, *1* (9), e1500661. https://doi.org/10.1126/sciadv.1500661.

(42) Webb, R. C.; Bonifas, A. P.; Behnaz, A.; Zhang, Y.; Yu, K. J.; Cheng, H.; Shi, M.; Bian, Z.; Liu, Z.; Kim, Y.-S.; Yeo, W.-H.; Park, J. S.; Song, J.; Li, Y.; Huang, Y.; Gorbach, A. M.; Rogers, J. A. Ultrathin Conformal Devices for Precise and Continuous Thermal Characterization of Human Skin. *Nat. Mater.* **2013**, *12* (10), 938–944. https://doi.org/10.1038/nmat3755.

(43) Bayramgil, N. P. Thermal Degradation of [Poly(*N*-Vinylimidazole)–Polyacrylic Acid] Interpolymer Complexes. *Polym. Degrad. Stab.* **2008**, *93* (8), 1504–1509. https://doi.org/10.1016/j.polymdegradstab.2008.05.006.

(44) Bala, T.; Prasad, B. L. V.; Sastry, M.; Kahaly, M. U.; Waghmare, U. V. Interaction of Different Metal Ions with Carboxylic Acid Group: A Quantitative Study. *J. Phys. Chem. A* **2007**, *111* (28), 6183–6190. https://doi.org/10.1021/jp067906x.

(45) Blasi, P.; D'Souza, S. S.; Selmin, F.; DeLuca, P. P. Plasticizing Effect of Water on Poly(Lactide-Co-Glycolide). *J. Controlled Release* **2005**, *108* (1), 1–9. https://doi.org/10.1016/j.jconrel.2005.07.009.

(46) Vieira, M. G. A.; da Silva, M. A.; dos Santos, L. O.; Beppu, M. M. Natural-Based Plasticizers and Biopolymer Films: A Review. *Eur. Polym. J.* **2011**, *47* (3), 254–263. https://doi.org/10.1016/j.eurpolymj.2010.12.011.

(47) Neese, F. The ORCA Program System. *Wiley Interdiscip. Rev.-Comput. Mol. Sci.* **2012**, *2* (1), 73–78. https://doi.org/10.1002/wcms.81.

(48) Neese, F. Software Update: The ORCA Program System, Version 4.0. *WIREs Comput. Mol. Sci.* **2018**, *8* (1), e1327. https://doi.org/10.1002/wcms.1327.

(49) Weigend, F.; Furche, F.; Ahlrichs, R. Gaussian Basis Sets of Quadruple Zeta Valence Quality for Atoms H–Kr. *J. Chem. Phys.* **2003**, *119* (24), 12753–12762. https://doi.org/10.1063/1.1627293.

(50) Neese, F. An Improvement of the Resolution of the Identity Approximation for the Formation of the Coulomb Matrix. *J. Comp. Chem.*, 2003, *24*, 1740–1747. https://doi.org/10.1002/jcc.10318.

(51) Neese, F.; Wennmohs, F.; Hansen, A.; Becker, U. Efficient, Approximate and Parallel Hartree-Fock and Hybrid DFT Calculations. A "chain-of-Spheres" Algorithm for the Hartree-Fock Exchange. *Chem. Phys.*, 2009, *356*, 98–109. https://doi.org/10.1016/j.chemphys.2008.10.036.

(52) Grimme, S.; Antony, J.; Ehrlich, S.; Krieg, H. A Consistent and Accurate Ab Initio Parametrization of Density Functional Dispersion Correction (DFT-D) for the 94 Elements H-Pu. *J. Chem. Phys.*, 2010, *132*, 154104–XXXX. https://doi.org/10.1063/1.3382344.

(53) Grimme, S.; Ehrlich, S.; Goerigk, L. Effect of the Damping Function in Dispersion Corrected Density Functional Theory. *J. Comput. Chem.* **2011**, *32* (7), 1456–1465. https://doi.org/10.1002/jcc.21759.

(54) Izsak, R.; Neese, F. An Overlap Fitted Chain of Spheres Exchange Method. *J. Chem. Phys.*, 2011, *135*, 144105. https://doi.org/10.1063/1.3646921.

(55) Izsak, R.; Hansen, A.; Neese, F. The Resolution of Identity and Chain of Spheres Approximations for the LPNO-CCSD Singles Fock Term. *Molec. Phys.*, 2012, *110*, 2413–2417. https://doi.org/10.1080/00268976.2012.687466.

(56) Izsak, R.; Neese, F.; Klopper, W. Robust Fitting Techniques in the Chain of Spheres Approximation to the Fock Exchange: The Role of the Complementary Space. *J. Chem. Phys.*, 2013, *139*. https://doi.org/10.1063/1.4819264.

(57) Neese, F. Approximate Second-Order SCF Convergence for Spin Unrestricted Wavefunctions. *Chem. Phys. Lett.*, 2000, *325*, 93–98. https://doi.org/10.1016/s0009-2614(00)00662-x.

(58) Kang, H. U.; Yu, Y. C.; Shin, S. J.; Youk, J. H. One-Step Synthesis of Block Copolymers Using a Hydroxyl-Functionalized Trithiocarbonate RAFT Agent as a Dual Initiator for RAFT Polymerization and ROP. *J. Polym. Sci. Part Polym. Chem.* **2013**, *51* (4), 774–779. https://doi.org/10.1002/pola.26464.

(59) Hawthorne, D. G.; Moad, G.; Rizzardo, E.; Thang, S. H. Living Radical Polymerization with Reversible Addition−Fragmentation Chain Transfer (RAFT): Direct ESR Observation of Intermediate Radicals. *Macromolecules* **1999**, *32* (16), 5457–5459. https://doi.org/10.1021/ma990316v.

C h a p t e r 3

ION TRANSPORT IN THERMALLY RESPONSIVE POLYELECTROLYTES

The work in this chapter has been adapted from:

Linghui Wang*, Vincenzo Costanza*, Nicole J Higdon, Tae Hyun Kim, and Chiara Daraio. Ion Transport Phenomena in Thermally Responsive Polyelectrolytes *(in preparation).*

Supplementary information can be found in Appendix B.

3.0 Abstract

The understanding of transport phenomena in ion-conducting polyelectrolytes is crucial to enable progress in fields such as organic electronics, sensors, and energy storage and conversion. Recently, a new class of bio- and synthetic polyelectrolytes have gained significant attention due to their exceptional response to temperature changes. Earlier work suggested that the mechanisms responsible for these polyelectrolytes' exquisite temperature response arise from the interaction between the coordination complexes and the cross-linking ions, as well as from the presence of water. Here, we analyze the role of water in the conductivity and temperature response of 2-hydroxyethyl acrylate – acrylic acid (HEA-AA) cross-linked by $CaCl_2$. By combining thermogravimetric analysis (TGA), differential scanning calorimetry (DSC), and Fourier-transform infrared spectroscopy (FTIR), we show how the increase in water content changes the ion mobility without affecting the ions' number density. By examining visible spectroscopy, we see evidence of tetrahalometallate anion formation which we speculate directly affects the ions' number density. We analyze different transport phenomena, at a wide range of frequencies and water concentrations, using impedance spectroscopy. Our investigation reveals a strong correlation between the segmental motion of polymer chains and ion transport in HEA-AA, as evidenced by the

relationship between DC conductivities and segmental relaxation. Furthermore, we observe a decrease in DC temperature response with increasing water concentration. By analyzing the Arrhenius plot at various water concentrations and applying the Vogel-Tamman-Fulcher (VTF) model, we demonstrate that this reduction in the temperature response mainly originates from the decrease in the glass transition temperature, providing further evidence for the link between ion transport and segmental motion. We note that the effect of water content on the dielectric response of HEA-AA is similar to the effect of temperature over a broad range of frequencies, despite the fact that the concepts of time-humidity superposition and time-temperature superposition do not apply in our system.

3.1 Introduction

Ion transport in polyelectrolyte has been known to be sensitive to temperature and relative humidity level.[1,2] Recently, researchers have found ways to leverage this sensitivity to create sensors that are highly responsive.[3–6] These polyelectrolyte-based sensors have several advantages over traditional silicon-based sensors, including good flexibility, solution processability, lightweight, low cost, and biocompatibility.[7] These properties make them particularly well suited for use in wearable technology, robotics, and prosthetic devices, where flexible and conformal sensing materials that can be produced with a large area are required.[8,9] Previous research on ion conducting polyelectrolytes focuses mostly on their potential applications in energy storage and actuation, such as lithium-ion batteries and fuel cells.[10–12] A comprehensive examination of the underlying factors affecting the sensing properties of polyelectrolytes is necessary for the advancement of sensor technology.

Polyelectrolytes are polymers in which the monomeric unit bears an electrolyte group. The presence of these charged moieties allows polyelectrolytes to solvate ions and support ion transport without the need for a liquid solvent. Even though some polyelectrolytes could conduct solvent-free, for highly charged and therefore highly hydrophilic polyelectrolytes, water vapor adsorption is difficult to avoid. The hydration level of the polymer matrix is sensitive to the environment's relative humidity (RH) and could strongly affect and modify the transport properties of the material.[13,14] The role of hydration has been extensively studied in polyelectrolyte complex and polyelectrolyte multilayer, where oppositely charged polyelectrolytes crosslink with each other and form a complex.[13–15] However, for metal-ion cross-linked polyelectrolytes, the underlying features of the conduction mechanism are still not well understood. In this paper, we performed a comprehensive study on the transport mechanism and its relationship with the relative humidity level in $CaCl_2$ cross-linked 2-hydroxyethyl acrylate – acrylic acid (HEA-AA), a recent class of polyelectrolytes mimicking the functionality of pectin that has been shown to present outstanding temperature sensing properties.[3]

HEA-AA is composed of polar 2-hydroxyethyl acrylate (HEA) groups and acrylic acid (AA) groups, randomly distributed. Together, these functional groups have the ability to bind with metal cations, similar to pectin[3,16] (Fig. 3.1(a)). According to the general model of transport in an ion-conducting medium, the DC conductivity, σ, is given as the sum of the individual contributions from every conducting species, i:

$$\sigma = \sum_i \sigma_i = \sum_i N_i \mu_i q_i \quad . \tag{1}$$

Here, N_i is the number density of the carriers, μ_i the mobility, and q_i the charge of the i-th conducting species. In our case, besides calcium ions, protons could also disassociate from an acrylic acid monomer and contribute to the overall conductivity.

Water content can affect the conductivity of the polyelectrolyte in multiple ways:

(1) The plasticizing effect is another well-known impact that water may have on polyelectrolyte.[17] Water as a plasticizer could solvate the hydrophilic regions of the polymer backbone and screen the electrostatic interaction between the polymer chains. This screening effect results in an increase in the free volume and an enhancement in the segmental motion of polymer backbones and side chains. An increase in the chain's segmental motion further facilitates ion transport through co-diffusion.[18] As a result, the ion mobility increases leading to a rise in the ion conductivity (Fig. 3.1(b)).

(2) Water might also modify the way calcium ions interact with their coordinating environment. The hydration shell that surrounds the calcium ion, could reduce the

electrostatic interaction between the calcium ion and the negatively charged groups on the polymer backbone. This effect could lower the activation energy for ion hopping, enhance segmental motion and also generate free calcium ions that are solvated in water molecules(Fig. 3.1(c)).

(3) Similarly, increasing water content could potentially increase the proton mobility[19] and also boost its number density by assisting proton dissociation from carboxyl groups.

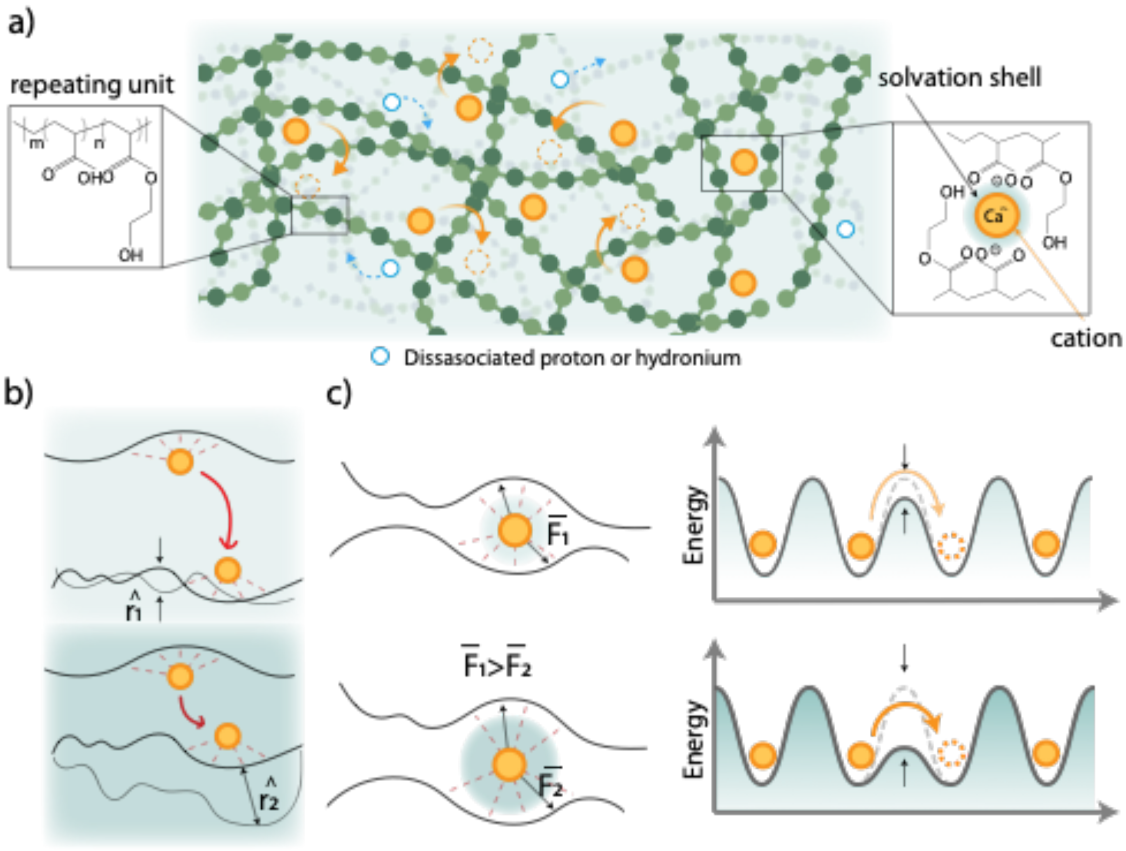

Figure 3.1: Schematic diagrams representing the conduction mechanisms in HEA-AA. (a) Crosslinking mechanism and ion transport in HEA-AA. (b)-(c) Effect of water concentration on the ion environment and the coordination complex.

Deconvoluting individual contributions is often not trivial, since multiple mechanisms can superimpose resulting in a single measured quantity, the conductance. In this work, conductances measured are proportional to corresponding conductivities with the same constant of proportionality because the electrode configurations remain always unchanged. Therefore, conductivity σ and conductance G are used interchangeably in the following discussions. In this paper, we first identify the dominant carrier responsible for the thermal response at low humidity levels, by performing controlled experiments. Then, combining the results obtained by gravimetric and calorimetric analysis, Fourier-transform infrared spectroscopy (FTIR), impedance spectroscopy, and temperature response as a function of water content, we evaluate the ion transport mechanism and determine the role of water within the polymer matrix.

3.2 Dominating Conducting Species at Low RH

Before diving into the effect of water on the overall conductivity, we need to first identify the dominant conducting species at low RH. In the $CaCl_2$-HEA-AA system, there are three possible conducting species: (i) chloride ions, (ii) calcium ions, and (iii) protons from the carboxyl groups. It is difficult to separate their contributions to the overall conductivity. However, the dominant conducting species is expected to play the most influential role in the temperature response, at low RH. Therefore, to identify the main charge carrier, we identify the ion species responsible for the temperature sensitivity (as defined in eq. 2). To do so, we compared the temperature response in three different polymer-salt compositions: (a) HEA-AA only, (b) HEA-AA and sodium chloride, and (c) HEA-AA and calcium chloride. In these three systems, the only possible carriers are (a) protons, (b) protons, sodium cations, and chloride anions, and, (c) protons, chloride anions, and calcium cations, respectively. In these three cases, the temperature response (R) will be proportional to the conductivity of the different conducting species:

$$\begin{aligned} \sum \sigma_a = \sigma_{H^+} \rightarrow R_a = \frac{\sigma_{H^+}(T_2)}{\sigma_{H^+}(T_1)} \\ \sum \sigma_b = \sigma_{H^+} + \sigma_{Cl^-} \rightarrow R_b = \frac{\sigma_{H^+}(T_2) + \sigma_{Na^+}(T_2) + \sigma_{Cl^-}(T_2)}{\sigma_{H^+}(T_1) + +\sigma_{Na^+}(T_1) + \sigma_{Cl^-}(T_1)} \\ \sum \sigma_c = \sigma_{H^+} + \sigma_{Cl^-} + \sigma_{Ca^{2+}} \rightarrow R_c = \frac{\sigma_{H^+}(T_2) + \sigma_{Cl^-}(T_2) + \sigma_{Ca^{2+}(T_2)}}{\sigma_{H^+}(T_1) + \sigma_{Cl^-}(T_1) + \sigma_{Ca^{2+}}(T_1)} \end{aligned} \tag{2}$$

with $T_2 > T_1$ being the two temperatures between which the response (R) is calculated. If $R_a \approx R_b \approx R_c$ then $\sigma_{H}+ >> \sigma_{Cl}-, \sigma_{Ca}2+$. On the other hand, if any R is larger than the others, it follows that the corresponding unique potential carrier is the main contributor to the conductivity. We characterized the temperature responses at RH 5% of (a) HEA-AA, (b) HEA-AA with sodium chloride (NaCl), and (c) HEA-AA with calcium chloride ($CaCl_2$). As shown in Fig. 3.2(a) , by adding NaCl, the temperature response doubled. Interestingly, adding $CaCl_2$ leads to an almost 9-fold increase in the temperature response. Following our previous reasoning, this result indicates that the calcium ion is the main contributor to the temperature response and the main current carrier. Although the increased response could partly be attributed to the change in glass transition temperature, we assume that the difference in glass transition temperature alone is not large enough to cause this 9-fold increase. To further confirm this result, we performed Density Functional Theory (DFT) calculations, to estimate the binding energy of calcium ions, sodium ions, and protons to the carboxylate group in HEA-AA (Fig. 3.2(b)).[20–30] A previous study suggested a positive correlation between the binding energy and the thermal response.[16] As expected, a calcium ion shows a larger binding energy to acrylate when compared to a sodium ion or a proton. These results demonstrate that the calcium ions are the dominating contributors to the high-temperature response, and therefore also the main conducting species in the $CaCl_2$-HEA-AA system at low RH.

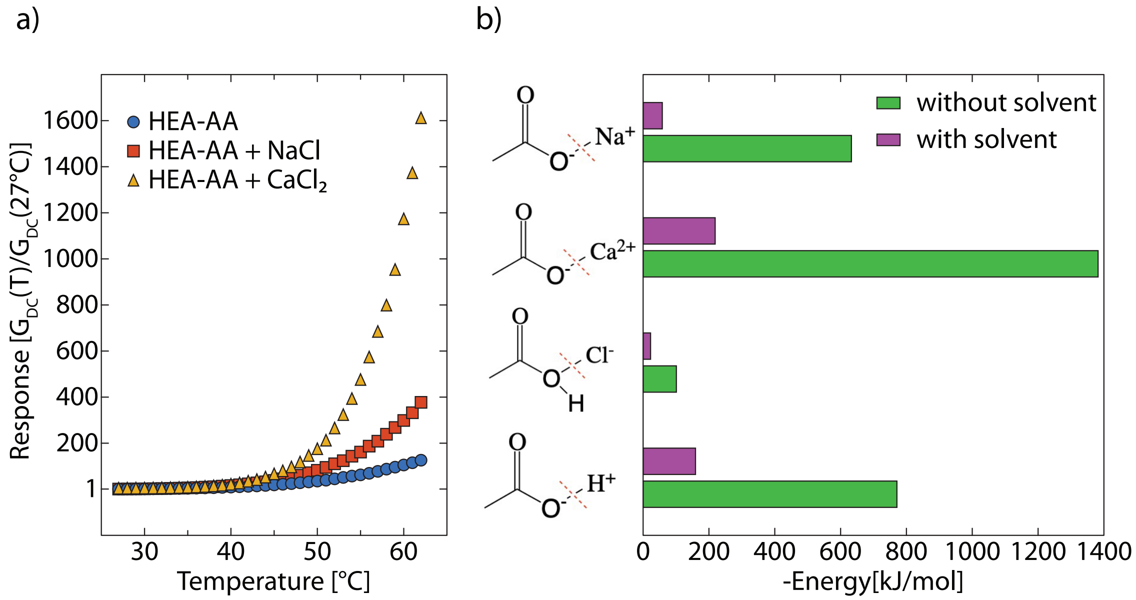

Figure 3.2: Dominating conducting species at low RH. (a) Normalized DC conductances of HEA-AA, HEA-AA cross-linked with NaCl, and HEA-AA cross-linked with $CaCl_2$ at a temperature between 27 °C and 62 °C. Conductivity curves were normalized by the conductivity value at 27 °C for temperature response comparison. (b) Binding energies calculated using DFT for proton, calcium ion, and sodium ion. The corresponding chemical equations are as follows from the top of the y-axis: Acetate + $Na^+ \rightarrow Na^+$(Acetate), Acetate + $Ca^{2+} \rightarrow Ca^{2+}$(Acetate), Acetic + $Cl^- \rightarrow Cl^-$(Acetic), Acetate + $H_3O^+ \rightarrow$ Acetic +H_2O. Green bars correspond to the binding energy in a vacuum. The purple bars correspond to the binding energy in an implicit water solvent.

While this paper focuses on $CaCl_2$-HEA-AA due to design parameters for medical devices, other divalent metal ions can provide a high temperature response. Preliminary work with cobalt-based systems provide further evidence that the metal cation is the conducting species. By reacting the insoluble cobalt carbonate salt with the HEA-AA polymer in ethanol solution, we can produce anion-free Co-HEA-AA films. Response testing of these films shows consistently similar behavior between the cobalt chloride and cobalt anion-free films (Fig. 3.3(a)) . This demonstrates that the chloride ions are not critical for the conduction behavior. By comparing the normalized maximum currents reached during response testing for cobalt anion-free films, cobalt chloride, cobalt bromide, and calcium chloride films, it becomes clear that the identity of the anion does significantly affect the hydration behavior of the film (Fig. 3.3(b)).

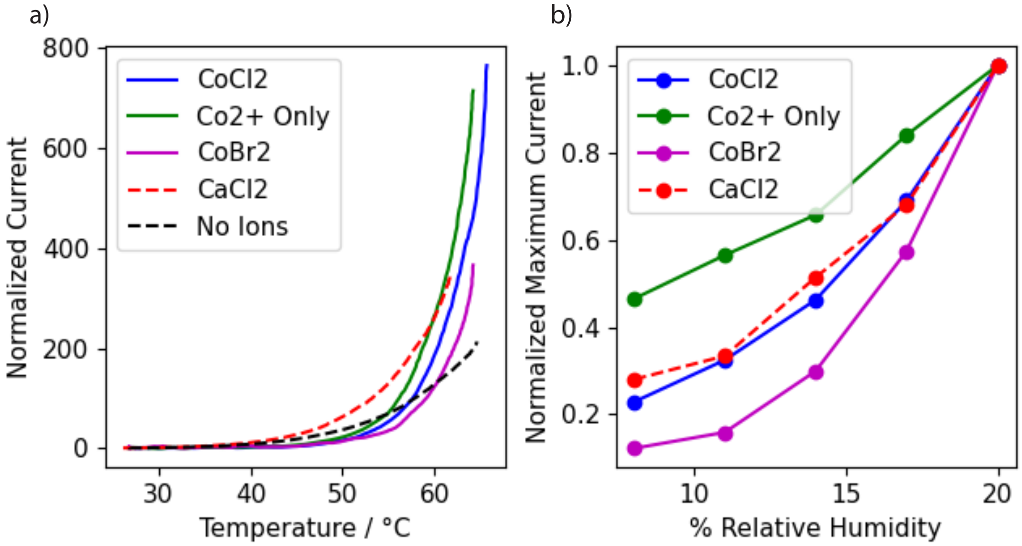

Figure 3.3: Effect of anion on temperature response. (a) Temperature response of various ion-HEA-AA systems showing the minimal effect of the anion. (b) Humidity response of various ion-HEA-AA systems showing the notable effect of the anion

3.3 Effect of Water on the Macroscopic Properties of HEA-AA

Varying the amount of water within the polymer matrix is usually obtained by exposing the sample to a saturated atmosphere at various RH values. In this study, we employed a custom-made humidity chamber in order to vary the RH from 5% to 50% in steps of 3%. The water absorption dynamics were evaluated gravimetrically through a precision quartz crystal microbalance. As shown in Fig. 3.4(a), an increase in the external RH results in a decrease in the resonance frequency of the quartz, indicating an increase in the resonating mass. Due to the hydrophilic character of the matrix and the presence of hygroscopic calcium cations, the water molecules present in the environment are absorbed both by the polymer backbone and the solvated ions. The dissipation factor of the resonating system similarly increases as a function of RH, suggesting an increase in the viscosity of this viscoelastic polymer. This behavior is further confirmed by the analysis of the glass transition temperature of HEA-AA. Fig. 3.4(b) shows the heat flow as a function of temperature as characterized by differential scanning calorimetry (DSC). A hydrated sample was placed in the DSC and cycled between -50 and 100 °C under nitrogen purge. Because of the temperature cycling and the dry nitrogen gas, after every cycle, the remaining free water evaporates (the cycling temperature is not high enough to induce polymer degradation) and the overall water content decreases. As expected, with decreasing water content the glass transition temperature increases (Fig. 3.4(b) (inset)). Water acts as a plasticizer in hydrophilic polymers, reducing the electrostatic interchain interactions. Fewer water molecules will favor stronger interchain interactions, less free volume, and weaker polymer segmental motion, leading to a higher glass transition temperature. In addition, lower water concentration will favor stronger coordination interactions between the metal ions and the polymer, which strengthens the cross-linking between polymer chains.

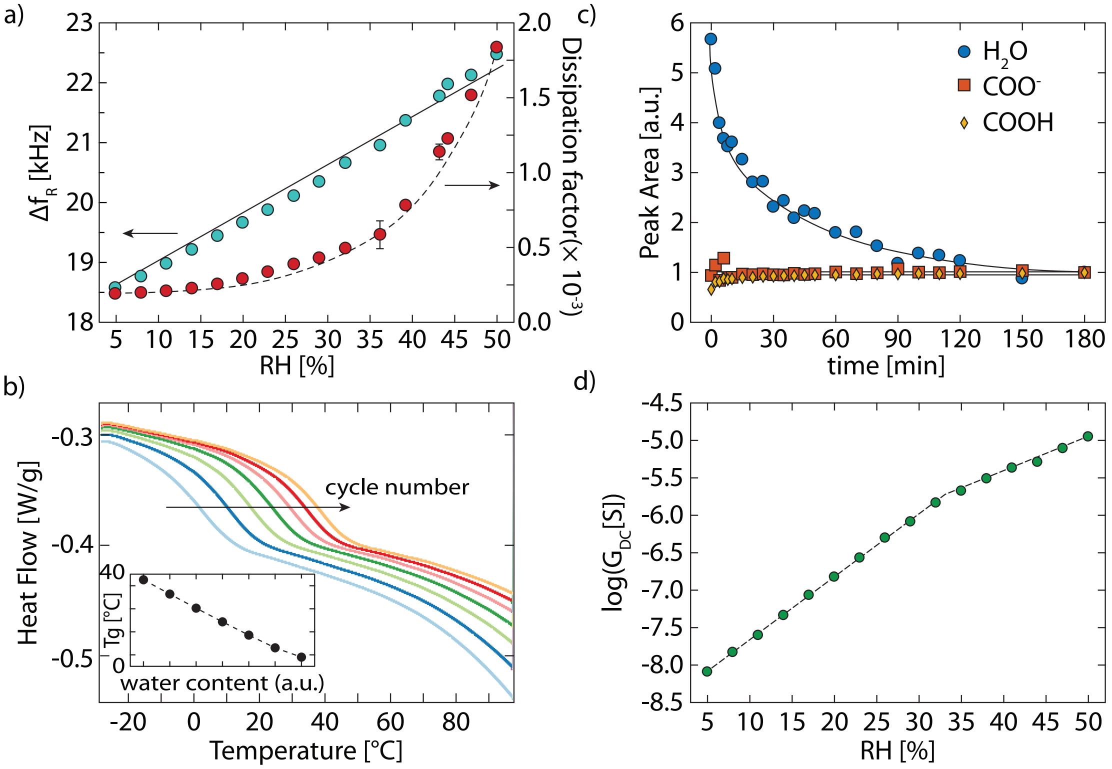

Figure 3.4: Water dependence of the macroscopic properties of HEA-AA. (a) Gravimetric Data as a function of RH. Blue dots shift from the fundamental resonance frequency of the empty cell, red dots dissipation factor of the resonator (for the points at RH 10%, 15%, 20%, 30%, 35%, 40%, 50%, 55% and 60% the error bars are smaller than the data marker). (b) Differential Scanning Calorimetry Data. Light blue, dark blue, light green, dark green, orange, red and yellow correspond respectively to the 1st, 2nd, 3rd, 4th, 5th, 6th and 7th cycle of the DSC run. Inset represents the calculated glass transition temperature as a function of water content (cycle number). (c) Normalized peak areas from fitting of FTIR spectroscopy of drying film (d) DC Conductance as a function of RH as calculated with the CTRW model.

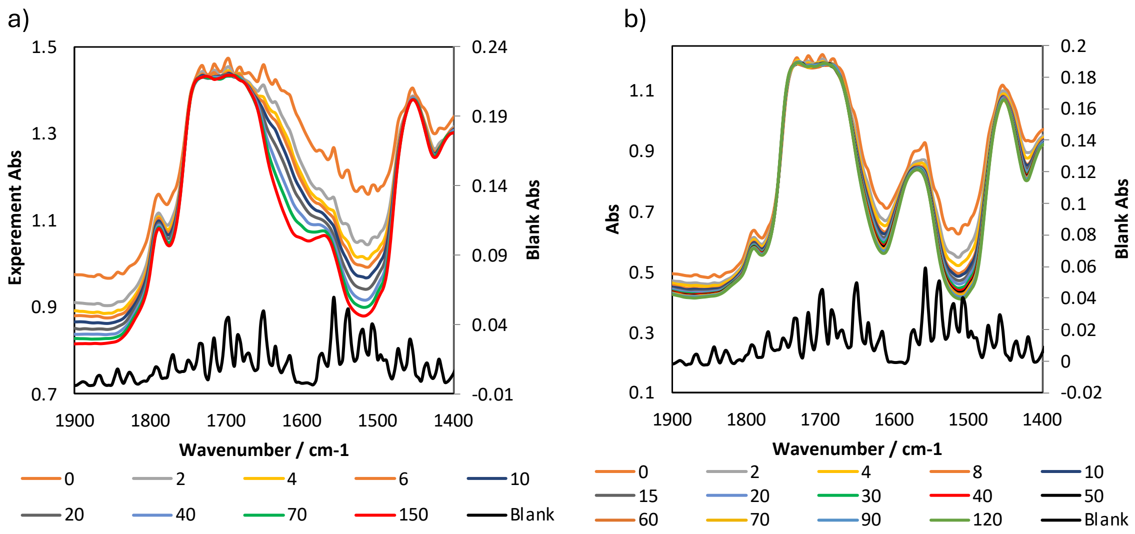

Figure 3.5: Transmission FTIR spectra of $CaCl_2$-HEA-AA films after high humidity exposure collected at set time points in minutes after closing the chamber (color lines) vs gas features detected in the blank sample immediately after closing the chamber (black line) (a) Film exposed to a water high humidity environment. (b) Film exposed to a deuterium oxide high humidity environment. In the case of the water exposed film, the intensity of the metal bound carboxyl peak's stationary nature requires extensive fitting to eliminate the affect of the high intensity water peak centered at ~1650 cm^{-1}. The fitting results can be seen in Fig. 3.4(c). In the deuterium oxide spectrum this aspect is far more apparent thanks to the broad low intensity absorption of D_2O in this region. Note the deuterium oxide in this study does contain a noticeable amount of water contamination.

As previously stated, increasing water content could weaken the binding between the calcium ion and the polymer and generate free water-solvated calcium ions. It could also lead to the dissociation of protons from acrylic acid monomers. In order to evaluate these effects on the ions' number density, we performed FTIR at different water contents. Because the protonated carboxyl group and the metal-ion bound (deprotonated) carboxyl group have two distinct absorption peaks at the range between 1500 cm^{-1} and 1850 cm^{-1}, we gauge how the bound calcium ion concentration and proton concentration change with water content, by calculating the corresponding peak areas. Similar to the procedure followed for the DSC experiment, we exposed a dried sample to a saturated humidity environment, then performed FTIR at regular intervals under nitrogen purging, to observe how the spectrum was modified. As time evolves, the area of the peak corresponding to water decreases, confirming the sample is dehydrating. At the same time, the area of the peaks associated with bound Ca^{2+} ions (i.e., the concentration of deprotonated carboxylic acids) and protons (carboxyl group) do not show any significant variation (Fig. 3.4(c)). Observation of this behavior is reliant upon peak fitting due to two key factors. First, when the chamber is sealed, an observable amount of water vapor, carbon dioxide, and other IR absorbing gases are within the chamber. These lead to a shifting background signal comprised of sharp peaks. Second, the broad high intensity absorption of the water peak between the carboxyl and metal-bound carboxyl peaks leads to a masking effect. In-order to reduce our reliance upon fitting, the experiment was repeated utilizing a deuterium oxide high humidity chamber (Fig. 3.5). Due to its nature, we do not expect the deuterium oxide to behave in this experiment chemically in any significant way different than the water. Note, because of the age of the deuterium oxide sample, there remains a spectroscopically visible water spectrum. Due to the rather broad absorption features of deuterium oxide in the region, the nature of the the ratio between the carboxyl and metal bound carboxyl peak becomes more apparent. Of note except for changes attributable to the water vapor / gas signals from the chamber, the peaks at ~1700 cm^{-1} and ~1560cm^{-1} are observed not to change in intensity. This implies that the number density of bound calcium ions and protons is not affected by changes in water concentration. The changes induced by water are solely in the ion mobilities. Such effects could be due to the combined role of improved segmental motion and lower binding energy between the ion and the coordination sites. As a result, the bulk conductivity strongly depends on RH (Fig. 3.4(d)): the conductivity increases logarithmically with water content and shows slight saturation for RH above 35%.

3.4 Effect of Anion on Number Density of Charge Carriers

Ion aggregation directly affects the number density of charge carriers in the system. The $CoCl_2$-HEA-AA films exhibit a characteristic blue coloration when stored under bench top conditions (23 °C, 20-50% relative humidity). $CoBr_2$-HEA-AA films show a similar blue coloration when dried under elevated temperatures. Whereas the anion-free Co-HEA-AA films only show blue coloration after undergoing extensive drying in a desiccator (Fig. 3.6(a)). It was observed that extensively dried films comprised of $CoCl_2$ in Poly(acrylic acid) (PAA) show a similar blue coloration. This is notable due to the similarity of possible binding sites between the HEA-AA and PAA polymers. UV/Vis spectroscopy shows that these polymers show nearly identical cobalt absorption peaks, indicating a nearly identical cobalt site between the two polymer systems (Fig. 3.7(a)). In order to better understand this absorption peak, $CoCl_2$ was dissolved in various solvents exhibiting potential oxygen coordination sites creating a variety of pseudo model complexes (Fig. 3.7(b)). What is especially notable is none of these pseudo model complexes are sufficiently redshifted to be related to the polymer complex. By adding hydrochloric acid to $CoCl_2$ in water, we can form a deep blue solution with its coloration originating from the formation of the tetrachlorocobaltate anion. The spectrum of this complex is significantly red shifted compared to the other $CoCl_2$ based complexes (Fig. 3.7(b). Samples where prepared in a variety of solvents by the addition of concentrated hydrochloric acid to solutions of $CoCl_2$. It is noteworthy that the peak locations and approximate intensities are conserved between these different samples (Fig. 3.7(c)). One caveat to this statement is that the addition of HCl requires the addition of water, further experimentation leveraging LiCl as the chloride source may be warranted.

Given these result, the pigmentation in the $CoCl_2$-HEA-AA, $CoCl_2$-PAA, and the CoBr2-HEA-AA films were found to originate from corresponding tetrahalometallate divalent anions (Fig. 3.6(b)). Tetrahalometallate compounds are typically prepared by adding excess of the halogen anion to a solution containing the metal halogen salt. In this case, no additional halogen anion is added to the system. For this reason we postulate that a ligand substitution reaction occurs, in which some cobalt chloride binds to the polymer releasing the chloride anion. This free chloride can then go bind with free cobalt chloride to form the tetrachlorocobaltate anion. This is not observed to occur in solutions comprised of acetic acid and cobalt chloride, the energetics of this system warrants additional study. To further evaluate the the formation of this complex, $CoCl_2$-HEA-AA films were exposed to a high humidity environment then UV/Vis spectra were collected as the sample was allowed to dry in room air (Fig. 3.7(d)). Of note as the film dries the peaks appear then increase in intensity as $CoCl_4^{2-}$ forms, however no other clear peaks are observed in the spectra, as such we can not draw meaningful conclusions about intermediary cobalt structures. Due to a shifting scattering background, the absorbances were shifted in intensity to present a more readable picture.

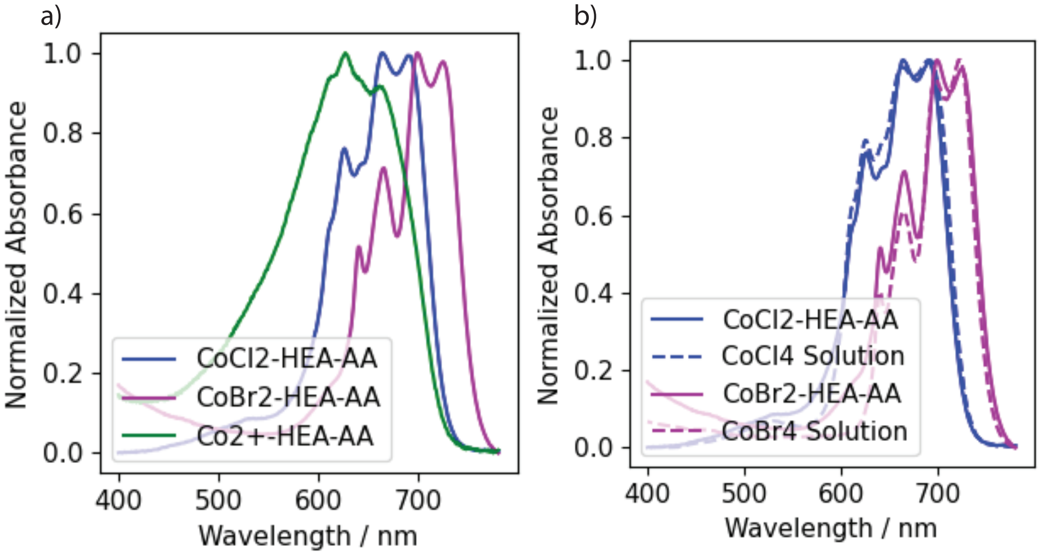

Figure 3.6: Spectroscopic evidence of tetrahalocobaltate formation in HEA-AA films. (a) UV/Vis spectroscopy of various dried ion-HEA-AA films (b) UV/Vis spectroscopy of dried $CoCl_2$-HEA-AA and $CoBr_2$-HEA-AA films compared to solution spectra of $CoCl_4^{2-}$ and $CoBr_4^{2-}$ (dashed lines, spectrum overlapping) showing formation of these complexes. This directly changes the number density of charge carriers due to aggregation effects.

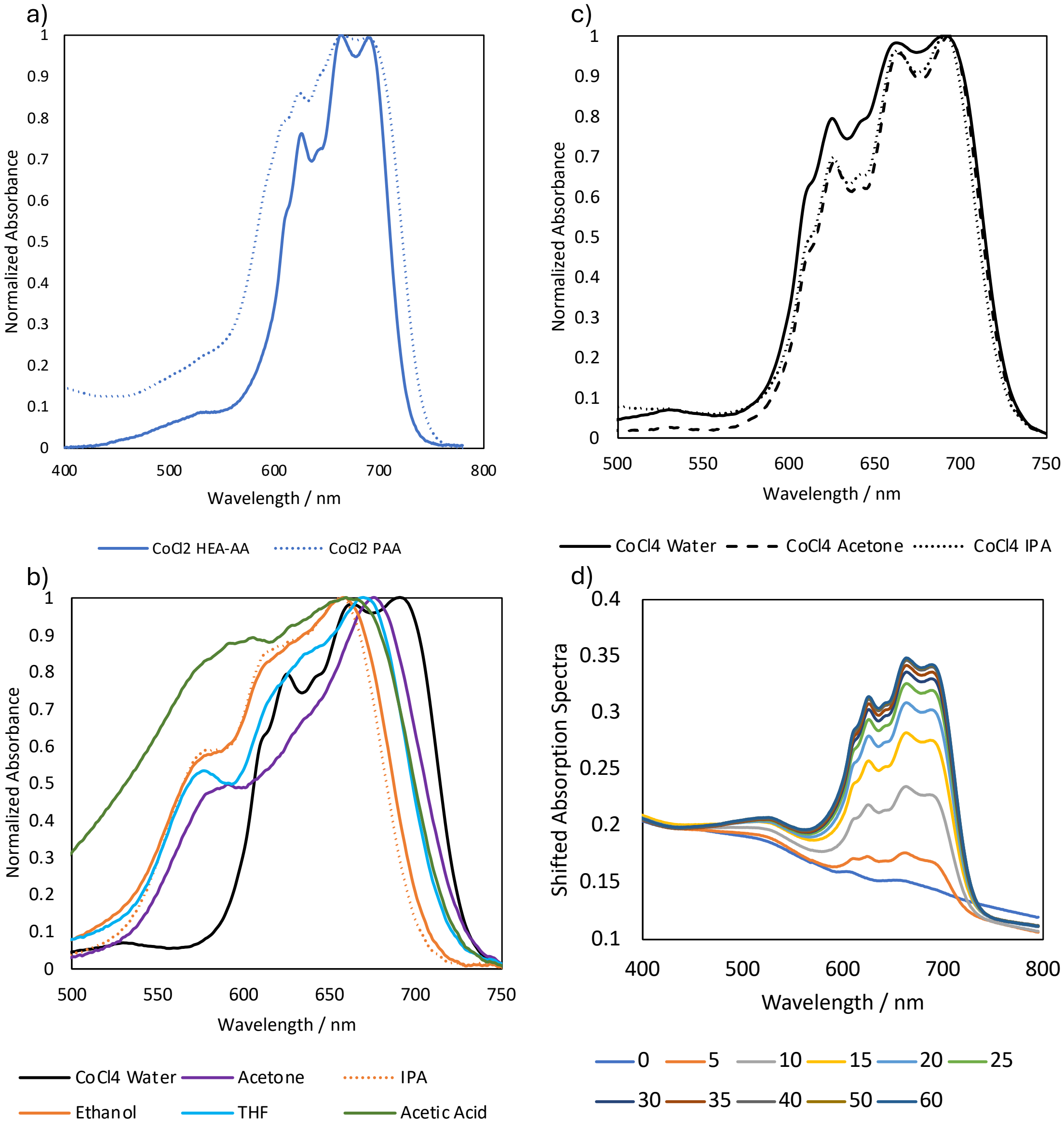

Figure 3.7: UV/Vis spectra of polymer samples and model complexes. (a) Spectra of dried $CoCl_2$ containing HEA-AA and Poly(acrylic acid) films. The similarities in the spectra imply the ionic species is the same/similar. (b) Spectra of $CoCl_2$ in various solvents showing the effects of the coordination site on the tetrahedral cobalt absorption peak. (c) Spectra of the tetrachlorocobaltate anion in various solvents. Note the match to the spectra of $CoCl_2$ polymer films. (d) Vertically shifted absorption spectra of $CoCl_2$-HEA-AA film exposed to a high humidity chamber then allowed to dry

under room air. Spectra were collected every 5-10 minutes. Note that the peak locations and peak shape does not shift as the film dries.

The formation of these tetrahalometellate complexes may play a role in modulating the number density of the metal cation charge carriers in the HEA-AA systems. While only preliminarily observed here for the cobalt ion, a similar mechanism for formation of tetrachlorocupurate has been proposed in a couple of thermoelectric polymer papers.[31,32] This mechanism may occur with a variety of salt systems, therefore this effect on the number density of charge carriers likely plays a role for a wide variety of salt-HEA-AA systems. Its observation in the PAA films further expands the scope of these results to other strongly coordinating polymers containing metal halide salts. Further studies into the implications of this material's formation are underway.

3.5 Ion Transport

Even though gravimetric, DSC, and FTIR are insightful to probe the dynamics of water absorption in the polymer, and its effect on the polymer matrix, solely they cannot describe water's effect on the electrical conduction and thermal response phenomena of HEA-AA. A very powerful tool to probe different conductivity dynamics in polymer electrolytes is dielectric spectroscopy, in which the samples' conductance and susceptance are measured as a function of the excitation frequency of the applied electric field. Fig. 3.8(a) shows a representative spectrum of the real conductance as a function of the excitation frequency. Three different regions can be observed: (i) at low frequencies a dispersive regime caused by the build-up of oppositely charged ions at the interface of the blocking electrode; (ii) a medium frequency region where the conductance is independent of the excitation frequency. This conductance is the DC conductance because in this region ions diffuse as if they are in the infinite medium; (iii) a high-frequency dispersive region where the real part of the conductivity starts to increase again. This phenomenon can be attributed to different relaxations: the α-relaxation, which is attributed to the segmental motion of polymer backbone and the sub-segmental β-relaxation, which occurs at a shorter time scale than the α-relaxation. The specific origin of the β-relaxation is still unclear, but it is commonly associated with the rotational motion of side groups and the cage-rattling effect.[33–35] Similar conclusions can be drawn by looking at the permittivity loss spectrum derived by the conductance: in region (i) an apparent relaxation peak appears due to the electrode polarization; region (ii) shows a slope of -1 indicating long-range transport of the ions; region (iii) includes multiple relaxation processes with one not fully formed at a higher frequency. In order to measure the influence of water content on the impedance spectrum, we recorded the dielectric loss as a function of RH (Fig. 3.8(b)). For increasing RH, the spectra move up and shift to the right, indicating that the increase in water content increases the absolute conductance and accelerates the conduction processes. Moreover, as frequently reported for temperature, the effect of RH on the high-frequency part of the spectra is limited if not absent. For low RH (below 29%) only the diffusive and dispersive regions are visible. Dehydration decreases the ion mobility, resulting in longer diffusion times for the ions, they therefore do not have time to travel to the electrode and form an ionic interface. Above RH 29%, the lower frequency electrode polarization region starts to appear.

To further quantify the effect of hydration on the DC conductivity and segmental relaxation, we fitted the (ii) and (iii) regions to the complex dielectric function with the following equation (Fig. 3.8(c)):

$$\epsilon(\omega) = \frac{G_{DC}}{i\omega\epsilon_0} + \frac{\Delta\epsilon_\alpha}{(1+(i\omega\tau_\alpha)^{a_\alpha})^{b_\alpha}} + \frac{\Delta\epsilon_\beta}{1+(i\omega\tau_\beta)^{a_\beta}} + \epsilon_\infty \tag{3}$$

where G_{DC} corresponds to the DC conductance, ϵ_∞ denotes the $\epsilon^{'}(\omega)$ at the high-frequency limit. $\Delta\epsilon_i$ and τ_i, describe the dielectric relaxations strengths and time constant of corresponding dielectric relaxation, where i = α, β. a_α , b_α and a_β are the shape parameters. a and b represent the symmetric and asymmetric broadening of the dielectric relaxation, respectively.[35] Since the second dielectric relaxation is not fully captured in the measured frequency range, only one shape parameter is used to avoid redundancy. The peak frequency v_{max} of the dielectric loss $\epsilon^{'}$ of the α-relaxation is usually used to represent the characteristic frequency of the segmental motion and can be obtained from the following relationship:[33,34]

$$\nu_{max} = \frac{1}{\tau_\alpha}\left(\sin\frac{a\pi}{2+2b}\right)^{1/a}\left(\sin\frac{ab\pi}{2+2b}\right)^{-1/a} . \qquad (4)$$

Fig. 3.8(d) shows the dependence of log(G_{DC}) and log(ν_{max}) on RH ranging from 5% to 50%. First, we observed that both G_{DC} and ν_{max} increase with hydration and start to plateau at high RH as expected. Secondly, a high correlation between log(G_{DC}) and log(ν_{max}) was observed with the Pearson correlation coefficient being 0.99. This suggests that the ion transport mechanism can be strongly coupled with the segmental motion, which has been observed in other ionomers with plasticizers.[36]

3.6 Relationship between Temperature Response and T_g

To further investigate the correlation between ion conductivity and polymer segmental motion, we studied the dependence of its dielectric response on temperature. In addition, the correlation between water content and calcium ion transport in the system has important implications for the temperature response of this material. Previous work on pectin has indicated that an increase in the water content degrades the temperature response of the polymer.[37] Similar results have been observed for the block copolymer that mimics pectin's structure.[3] In this latter work, however, a response degradation has also been measured for water content below a certain threshold. This is unexpected because a lower water content should increase the activation energy, and thus leads to a higher temperature response. The same behavior is expected in the related copolymer in this paper. As presented in Fig. 3.8(b), the increase in RH has the effect of shifting the conductance spectra up and to the right.

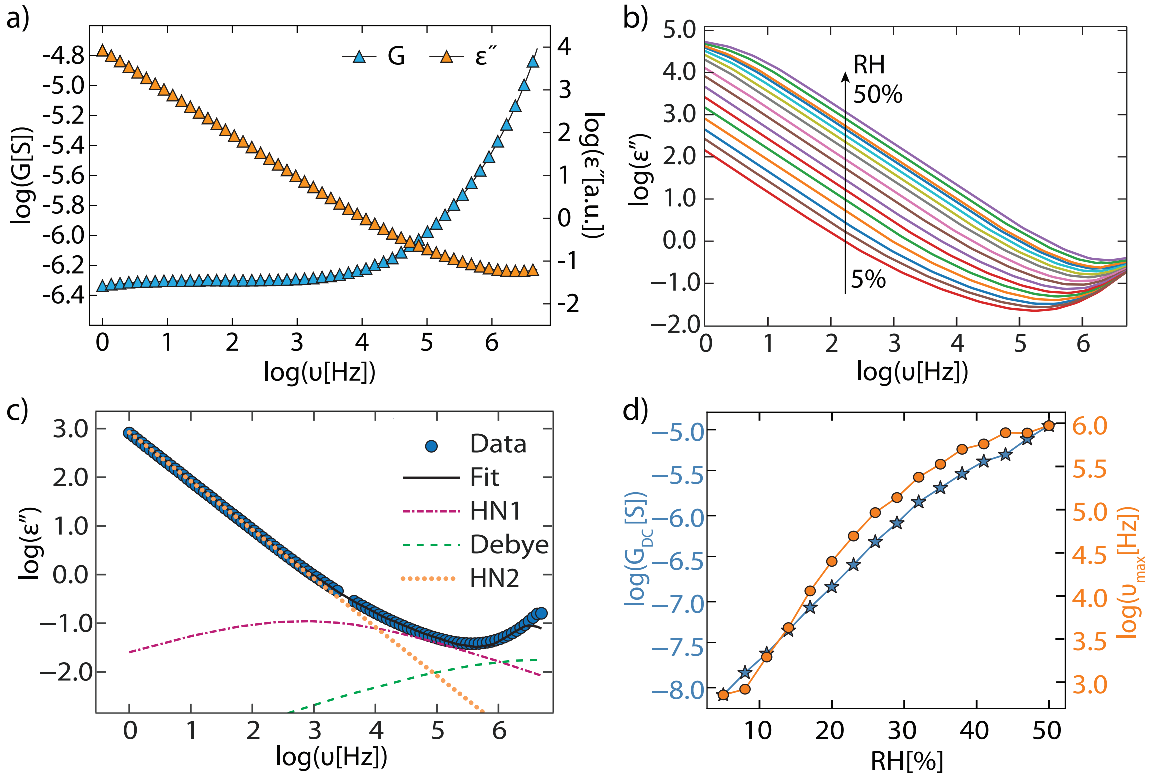

Figure 3.8: Water dependence of dielectric spectra. (a) Typical conductance and dielectric spectrum. Blue triangles represent the conductance, while the yellow triangles represent the dielectric loss for a sample at RH 35%. For clarity, markers are a subgroup of the data points. (b) Dielectric loss spectra as a function of RH. (c) Model fitting. The blue dots represent the dielectric loss spectrum of a sample at RH 14%. The red dotteddashed line and the green dashed line correspond to the α-relaxation and the β-relaxation, both modeled by the HN equation. The yellow dotted line represents DC conduction, while the black line corresponds to the overall fitting. (d) DC conductance and the characteristic segmental relaxation frequency as a function of different RH (between 5% and 50%).

A similar effect is expected when changing the temperature of the sample. Fig. 3.9(a) shows the result of an isochronical impedance spectra taken at constant RH (20%) for different temperatures (42 and 60 °C). Even though the analysis of the conduction mechanism as a function of temperature will be left to a sequent paper, it is important to note that, depending on the temperature, some spectra will show only the dispersive and diffusive regions, while others will also present the polarization of the electrodes, in the same frequency range. This leads to a dependence of the temperature response on the excitation frequency. Four regions can be observed: (i) one at a lower frequency where the spectrum at lower temperature does not show a fully developed electrode polarization while the one at higher temperature does; (ii) a low medium frequency region where both the spectra are in the diffusive regime; (iii) a high medium frequency region where the spectrum at a lower temperature is already in the dispersive regime while the higher temperature spectrum is still in the diffusive region, and (iv) a high-frequency region where both spectra present dispersive behavior. In region (i), the presence of the electrode polarization affects the effective conductivity, modifying the response. In region (ii) we can describe the temperature effect on the ion conduction since both the curves are in the diffusive regime. We will consider this region to calculate the bulk response R_{DC}. When transitioning to the region (iii) the response drops once more since one of the spectra shows increased conductivity as a result of the dispersive regime. Region (iv) follows a common trend of ion conductors near constant loss behavior with a weak dependence on temperature. The combination of these behaviors in different parts of the spectrum results in a dependence of the temperature response on the external frequency. The frequency at which the transition from regions (i) to (iv) can be observed, however, is a function of the water content. Fig. 3.9(b) shows the impact of different RH on the response spectra, illustrating how for increasing RH the characteristic transition frequencies shift to the right. This behavior can explain the decrease of response below a certain water content when measuring at a single frequency. Initially, the excitation frequency falls in the region (ii); as the water content decreases the transition frequency between region (ii) and (iii) shifts to the higher frequencies, and eventually, the excitation frequency falls in region (iii). This reasoning could also be applied to explain the decrease in response as the water content increase, resulting in an apparent lowering in the response. Nonetheless, Fig. 3.9(c) shows that the DC response spectra for different RH decrease with humidity. This is a result of a lowering in ion-hopping energy barriers with hydration.

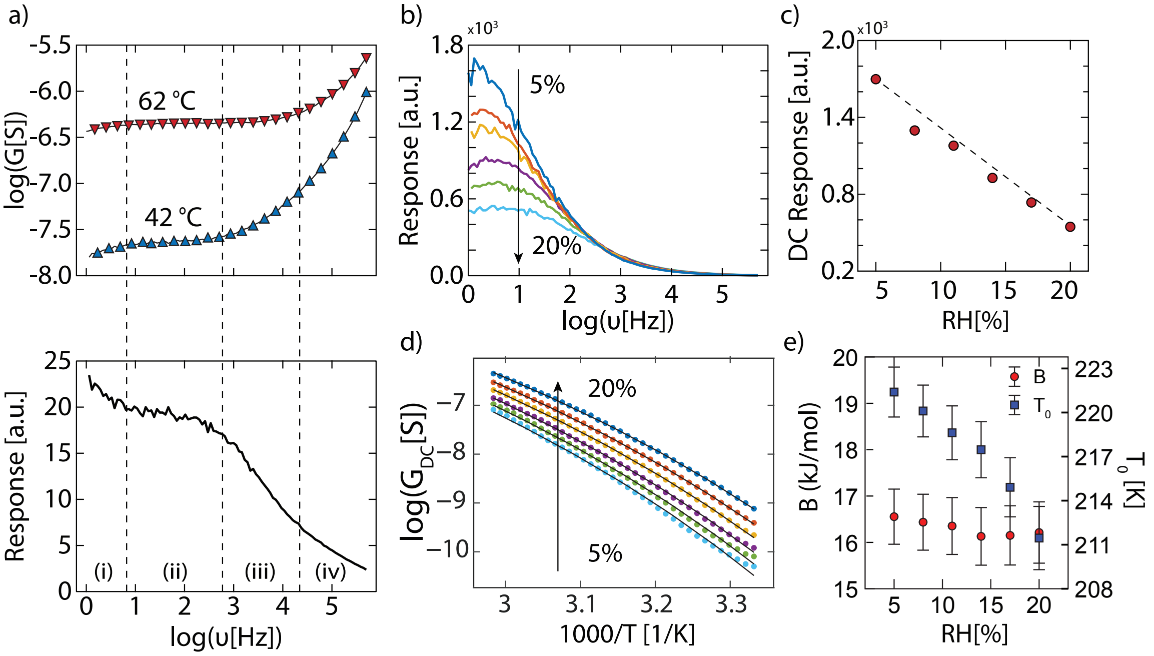

Figure 3.9: Effect of water content on HEA-AA temperature response. (a) Dielectric spectra as a function of temperature (top) measured at RH 20%. Blue triangles represent the conductance spectrum measured at 315.15 K, while the red triangles represent the conductance spectrum measured at 338.15 K. For clarity, markers are a subgroup of the data points. Corresponding temperature response spectra (bottom). The black line represents the conductance temperature response as a function of the frequency measured at 20% RH. The dashed lines indicate the four different regimes of the response. (b) Response spectra for different RH. Light blue, green, purple yellow, orange, and dark blue correspond respectively to 20%, 17%, 14%, 11%, 8%, and 5% RH. (c) DC temperature response was calculated from the response spectra. (d) Arrhenius plot of data (dots) and the VFT fits (black curves) for the different humidity values. Light blue, green, purple yellow, orange, and dark blue correspond respectively to 20%, 17%, 14%, 11%, 8%, and 5% RH. (e) VTF fitting parameter T_0 and B as a function of humidity. G_0 is set to be constant for varying RH.

To further analyze the effect of water on the temperature dependence of the conductivity, we extracted the Arrhenius plot for different humidity (5% to 20%). In this case, we do not observe a linear relationship in the Arrhenius plot, indicating that the ion transport is coupled with the segmental motion of the polymer (Fig. 3.9(d)). The conductance G in this scenario is often described by the Vogel–Fulcher–Tammann (VTF) model:

$$G = G_0 \exp(-\frac{B}{T - T_0}) . \quad (5)$$

Where B and T_0 are fitting parameters. In particular, B is the pseudo-activation energy and T_0 has been empirically found to be 50K lower than the glass transition temperature T_g in polymer electrolytes.[38] The pre-exponential factor G_0 is dependent on the number of charge carriers. In this study, it was kept constant across all RH levels as no significant changes in ion concentration were observed during hydration. During the fitting of the experimental data with the VTF equation, we observe B is relatively constant compared to k_BT for all RH, and changes in T_0 contributed to most of the difference in the temperature dependence at various RH (Fig. 3.9 (e)). In fact, all the VTF curves can be collapsed onto a master curve with shifted temperature (Fig. 3.10(a)). The shift factor T_0^* for each RH is calculated by keeping B and G_0 constant and only allowing T_0^* to vary during the VFT fitting. T_0^* deviates only slightly from T_0 . As a result, the DC conductivity of HEA-AA can be expressed as:

$$\sigma(T, RH) = \sigma(T - T_0^*) = \sigma_0 \exp(-\frac{B}{T - T_0^*}), \quad T_0^* = T_0^*(RH) . \quad (6)$$

This indicates that the drop in DC temperature response and the increase in DC conductivity with hydration can be contributed to decrease in T_0^*, which is related to the glass transition temperature. This further suggests that segmental motion is coupled with the calcium ion transport in HEA-AA. Furthermore, the impedance spectra with similar $T - T_0^*$ overlap across the measured frequency range, strongly suggesting that humidity and temperature affect ion transport and dielectric relaxation via the same mechanism (Fig. 3.10(b)). Similar temperature-humidity superposition over a large frequency range has only been reported in the polyelectrolyte complexes with dynamic modulus, where both temperature and water affect the polymer chain mobility through a hydrogen bonding mechanism.[39]

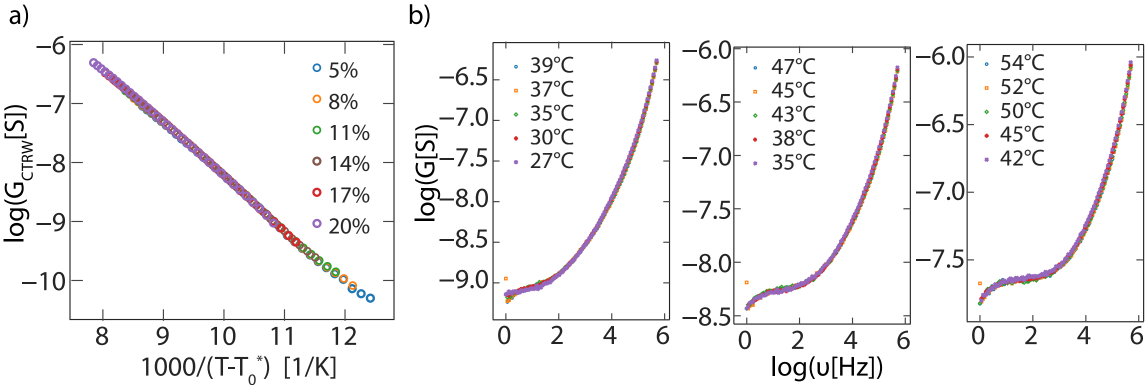

Figure 3.10: Equivalent effects of water and temperature. (a) Data in Fig. 3.9(d) plotted with temperature shifted by corresponding T_0^* (b) Impedance spectra were taken at similar $T - T_0^*$ values. The $T - T_0^*$ values of spectra plotted in three figures are: 92.45 ± 0.07 K,100.45 ± 0.07 K and 107.45 ± 0.07 K from left to right. Colors correspond to RHs (same as (a)): blue (5%), yellow (7%), green (11%), red (17%), and purple (20%).

3.7 Conclusions

In this work, we investigated the effect of water on the transport phenomena in a single ion conductor polymer composed of HEA-AA and calcium ions. We showed that at low RH the metal cations are the dominant carrier and main contributor to the thermal response. Using IR spectroscopy, we discovered that the water content does not modify the number density of the conducting ions. However, leveraging UV/Vis spectroscopy, we identified that the anions may play a role in modifying the number density of conducting ions. The humidity dependent behavior of conductivity predominantly stems from the variation in ion mobility. The relationship between DC conductivity and segmental relaxation frequency suggests a strong coupling between ion transport and polymer segmental motion. This observation was further supported by the fact that the dependence of DC temperature response on RH can be largely attributed to the change in glass transition temperature with RH. Remarkably, for the range of RH and temperature investigated in this paper, we have demonstrated that both water and temperature exert comparable influences on dielectric spectra. This similar impact suggests that both factors operate through similar mechanisms to affect ion transport. Further studies are underway to investigate the potential roles of the anion in ion transport and the humidity dependent behavior. Furthermore, additional research is needed to understand the implications of the formation of tetrahelometallate complexes in polyelectrolytes.

References

(1) Noorkami, M.; Robinson, J. B.; Meyer, Q.; Obeisun, O. A.; Fraga, E. S.; Reisch, T.; Shearing, P. R.; Brett, D. J. L. Effect of Temperature Uncertainty on Polymer Electrolyte Fuel Cell Performance. *Int. J. Hydrog. Energy* **2014**, *39* (3), 1439–1448.

(2) Zhang, J.; Tang, Y.; Song, C.; Xia, Z.; Li, H.; Wang, H.; Zhang, J. PEM Fuel Cell Relative Humidity (RH) and Its Effect on Performance at High Temperatures. *Electrochimica Acta* **2008**, *53* (16), 5315–5321.

(3) Kim, T. H.; Zhou, Z.; Choi, Y. S.; Costanza, V.; Wang, L.; Bahng, J. H.; Higdon, N. J.; Yun, Y.; Kang, H.; Kim, S.; Daraio, C. Flexible Biomimetic Block Copolymer Composite for Temperature and Long-Wave Infrared Sensing. *Sci. Adv.* **2023**, *9* (6), eade0423. https://doi.org/10.1126/sciadv.ade0423.

(4) Ge, G.; Lu, Y.; Qu, X.; Zhao, W.; Ren, Y.; Wang, W.; Wang, Q.; Huang, W.; Dong, X. Muscle-Inspired Self-Healing Hydrogels for Strain and Temperature Sensor. *ACS Nano* **2019**, *14* (1), 218–228.

(5) An, R.; Zhang, X.; Han, L.; Wang, X.; Zhang, Y.; Shi, L.; Ran, R. Healing, Flexible, High Thermal Sensitive Dual-Network Ionic Conductive Hydrogels for 3D Linear Temperature Sensor. *Mater. Sci. Eng. C* **2020**, *107*, 110310.

(6) Casalbore-Miceli, G.; Yang, M.; Li, Y.; Zanelli, A.; Martelli, A.; Chen, S.; She, Y.; Camaioni, N. A Polyelectrolyte as Humidity Sensing Material: Influence of the Preparation Parameters on Its Sensing Property. *Sens. Actuators B Chem.* **2006**, *114* (2), 584–590.

(7) Song, H. W.; Choi, W.; Jeon, T.; Oh, J. H. Recent Advances in Smart Organic Sensors for Environmental Monitoring Systems. *ACS Appl. Electron. Mater.* **2022**.

(8) Zhu, M.; Biswas, S.; Dinulescu, S. I.; Kastor, N.; Hawkes, E. W.; Visell, Y. Soft, Wearable Robotics and Haptics: Technologies, Trends, and Emerging Applications. *Proc. IEEE* **2022**, *110* (2), 246–272.

(9) Yang, J. C.; Mun, J.; Kwon, S. Y.; Park, S.; Bao, Z.; Park, S. Electronic Skin: Recent Progress and Future Prospects for Skin-Attachable Devices for Health Monitoring, Robotics, and Prosthetics. *Adv. Mater.* **2019**, *31* (48), 1904765.

(10) Yue, L.; Ma, J.; Zhang, J.; Zhao, J.; Dong, S.; Liu, Z.; Cui, G.; Chen, L. All Solid-State Polymer Electrolytes for High-Performance Lithium Ion Batteries. *Energy Storage Mater.* **2016**, *5*, 139–164.

(11) Arya, A.; Sharma, A. Polymer Electrolytes for Lithium Ion Batteries: A Critical Study. *Ionics* **2017**, *23* (3), 497–540.

(12) Mauritz, K. A.; Moore, R. B. State of Understanding of Nafion. *Chem. Rev.* **2004**, *104* (10), 4535–4586.

(13) Cramer, C.; De, S.; Schönhoff, M. Time-Humidity-Superposition Principle in Electrical Conductivity Spectra of Ion-Conducting Polymers. *Phys. Rev. Lett.* **2011**, *107* (2), 028301.

(14) An, H.; Habib, T.; Shah, S.; Gao, H.; Patel, A.; Echols, I.; Zhao, X.; Radovic, M.; Green, M. J.; Lutkenhaus, J. L. Water Sorption in MXene/Polyelectrolyte Multilayers for Ultrafast Humidity Sensing. *ACS Appl. Nano Mater.* **2019**, *2* (2), 948–955.

(15) De, S.; Cramer, C.; Schönhoff, M. Humidity Dependence of the Ionic Conductivity of Polyelectrolyte Complexes. *Macromolecules* **2011**, *44* (22), 8936–8943.

(16) Wang, L.; Kim, T. H.; Costanza, V.; Higdon, N. J.; Daraio, C. Ion Transport in Thermally Responsive Pectin Film. *Appl. Phys. Lett.* **2023**, *123* (2), 021903. https://doi.org/10.1063/5.0142020.

(17) Hodge, R.; Bastow, T.; Edward, G.; Simon, G.; Hill, A. Free Volume and the Mechanism of Plasticization in Water-Swollen Poly (Vinyl Alcohol). *Macromolecules* **1996**, *29* (25), 8137–8143.

(18) Son, C. Y.; Wang, Z.-G. Ion Transport in Small-Molecule and Polymer Electrolytes. *J. Chem. Phys.* **2020**, *153* (10).

(19) Commer, P.; Cherstvy, A.; Spohr, E.; Kornyshev, A. The Effect of Water Content on Proton Transport in Polymer Electrolyte Membranes. *Fuel Cells* **2002**, *2* (3–4), 127–136.

(20) Neese, F. The ORCA Program System. *WIREs Comput. Mol. Sci.* **2012**, *2* (1), 73–78. https://doi.org/10.1002/wcms.81.

(21) Neese, F. Software Update: The ORCA Program System, Version 4.0. *WIREs Comput. Mol. Sci.* **2018**, *8* (1), e1327. https://doi.org/10.1002/wcms.1327.

(22) Weigend, F.; Furche, F.; Ahlrichs, R. Gaussian Basis Sets of Quadruple Zeta Valence Quality for Atoms H–Kr. *J. Chem. Phys.* **2003**, *119* (24), 12753–12762. https://doi.org/10.1063/1.1627293.

(23) Neese, F. An Improvement of the Resolution of the Identity Approximation for the Formation of the Coulomb Matrix. *J. Comp. Chem.*, 2003, *24*, 1740–1747. https://doi.org/10.1002/jcc.10318.

(24) Neese, F.; Wennmohs, F.; Hansen, A.; Becker, U. Efficient, Approximate and Parallel Hartree-Fock and Hybrid DFT Calculations. A “chain-of-Spheres” Algorithm for the Hartree-Fock Exchange. *Chem. Phys.*, 2009, *356*, 98–109. https://doi.org/10.1016/j.chemphys.2008.10.036.

(25) Grimme, S.; Antony, J.; Ehrlich, S.; Krieg, H. A Consistent and Accurate Ab Initio Parametrization of Density Functional Dispersion Correction (DFT-D) for the 94 Elements H-Pu. *J. Chem. Phys.*, 2010, *132*, 154104–XXXX. https://doi.org/10.1063/1.3382344.

(26) Grimme, S.; Ehrlich, S.; Goerigk, L. Effect of the Damping Function in Dispersion Corrected Density Functional Theory. *J. Comput. Chem.* **2011**, *32* (7), 1456–1465. https://doi.org/10.1002/jcc.21759.

(27) Izsak, R.; Neese, F. An Overlap Fitted Chain of Spheres Exchange Method. *J. Chem. Phys.*, 2011, *135*, 144105. https://doi.org/10.1063/1.3646921.

(28) Izsak, R.; Hansen, A.; Neese, F. The Resolution of Identity and Chain of Spheres Approximations for the LPNO-CCSD Singles Fock Term. *Molec. Phys.*, 2012, *110*, 2413–2417. https://doi.org/10.1080/00268976.2012.687466.

(29) Izsak, R.; Neese, F.; Klopper, W. Robust Fitting Techniques in the Chain of Spheres Approximation to the Fock Exchange: The Role of the Complementary Space. *J. Chem. Phys.*, 2013, *139*. https://doi.org/10.1063/1.4819264.

(30) Neese, F. Approximate Second-Order SCF Convergence for Spin Unrestricted Wavefunctions. *Chem. Phys. Lett.*, 2000, *325*, 93–98. https://doi.org/10.1016/s0009-2614(00)00662-x.

(31) Chen, B.; Feng, J.; Chen, Q.; Xiao, S.; Yang, J.; Zhang, X.; Li, Z.; Wang, T. Specific Behavior of Transition Metal Chloride Complexes for Achieving Giant Ionic Thermoelectric Properties. *Npj Flex. Electron.* **2022**, *6* (1), 1–11. https://doi.org/10.1038/s41528-022-00213-4.

(32) Chen, B.; Zhang, X.; Yang, J.; Feng, J.; Wang, T. Giant Negative Thermopower Enabled by Bidirectionally Anchored Cations in Multifunctional Polymers. *ACS Appl. Mater. Interfaces* **2023**, *15* (20), 24483–24493. https://doi.org/10.1021/acsami.3c03143.

(33) Knight, C.; Voth, publisher=ACS P., Gregory A. ,. journal=Accounts of Chemical Research, volume=45, number=1, pages=101–109, year=2012; Tudryn, G. J.; O'Reilly, M. V.; Dou, S.; King, D. R.; Winey, K. I.; Runt, J.; Colby, R. H. Molecular Mobility and Cation Conduction in Polyether–Ester–Sulfonate Copolymer Ionomers. *Macromolecules* **2012**, *45* (9), 3962–3973.

(34) Popov, I.; Cheng, S.; Sokolov, A. P. Broadband Dielectric Spectroscopy and Its Application in Polymeric Materials. *Macromol. Eng. Precise Synth. Macrosc. Mater. Appl.* **2022**, 1–39.

(35) Kremer, F.; Schönhals, A. *Broadband Dielectric Spectroscopy*; Springer Science & Business Media, 2002.

(36) Zhang, S.; Dou, S.; Colby, R. H.; Runt, J. Glass Transition and Ionic Conduction in Plasticized and Doped Ionomers. *J. Non-Cryst. Solids* **2005**, *351* (33–36), 2825–2830.

(37) Costanza, V.; Bonanomi, L.; Moscato, G.; Wang, L.; Choi, Y. S.; Daraio, C. Effect of Glycerol on the Mechanical and Temperature-Sensing Properties of Pectin Films. *Appl. Phys. Lett.* **2019**, *115* (19), 193702. https://doi.org/10.1063/1.5121710.

(38) Diederichsen, K. M.; Buss, H. G.; McCloskey, B. D. The Compensation Effect in the Vogel–Tammann–Fulcher (VTF) Equation for Polymer-Based Electrolytes. *Macromolecules* **2017**, *50* (10), 3831–3840.

(39) Suarez-Martinez, P. C.; Batys, P.; Sammalkorpi, M.; Lutkenhaus, J. L. Time–Temperature and Time–Water Superposition Principles Applied to Poly (Allylamine)/Poly (Acrylic Acid) Complexes. *Macromolecules* **2019**, *52* (8), 3066–3074.

Chapter 4

ORGANIC SENSOR BASED CORE BODY TEMPERATURE MEASUREMENT

The work in this chapter has been adapted from:

Vincenzo Costanza, Dmitriy V. Zhukov, Johnathan Knecht, Nicole J. Higdon, Naresh Menon, and Chiara Daraio. Organic Temperature Sensitive Polyelectrolyte for Core Body Temperature Measurement. IEEE Sensors Journal (under revision)

4.0 Abstract

Core body temperature (CBT) is a vital phenotype that can provide information on an individual's health and metabolic activity. It is correlated to a variety of physical and mental conditions and should be monitored when an individual is under environmental or medical duress. Current sensing materials lack the desired temperature sensitivity to allow the fabrication of ultrathin and wearable CBT sensors with the required accuracy for medical applications. Here, the realization of an ultrathin CBT sensor based on dual heat flux (DHF) thermometry is reported, using a novel class of synthetic materials. By optimizing the chemical composition, the material's properties can be tuned to obtain the optimal temperature response. Furthermore, the measurement error in the device is evaluated based on a Finite Element analysis. Building on this knowledge, the temperature sensitive polymer is embedded into an ultrathin DHF sensor and its sensitivity and repeatability are characterized using an anthropomorphic phantom model. The results presented in this work open the way to a first-in-class wearable and accurate DHF sensor that will allow continuous CBT monitoring.

4.1 Introduction

In all mammals, core body temperature (CBT) is a highly conserved phenotype that is an accurate indicator of systemic metabolic activity and its regulation. Monitoring CBT in clinical settings has been shown to impact surgical outcomes[1–4] and is a leading indicator of immune system response from inflammation and infection.[5–9] Furthermore, in every day scenarios CBT has been linked to general wellbeing as it can be used to quantify calories burnt over time,[10,11] onset of ovulation cycles,[12] the circadian cycle and sleep quality,[13,14] mental health,[15] and degenerative diseases such as Alzheimer's and Parkinson's.[16,17] Continuously recording CBT can therefore be extremely beneficial for a wide spectrum of applications, spanning from hospital care to monitoring indoor and outdoor activity. However, the CBT cannot be easily measured to the required degree of accuracy. The gold standard for the measurement of CBT is the pulmonary artery catheter, which records the temperature of the blood flowing directly from the heart.[18] This method is highly invasive and is used only in specific surgeries. Other methods rely on the measurement of rectal temperature[19] or the ingestion of radio pills.[20] However, these methods are invasive and not suitable for continuous monitoring. At the same time, there are several methods to measure peripheral body temperature by placing thermometers or standoff IR scanners on the skin that are both continuous and non-invasive. However, peripheral body temperature is poorly correlated with core body temperature. In fact, thermoregulatory processes regulate the core body temperature, while the temperature at the surface and peripheries of the body are affected by various extraneous factors such as placement of the thermometer, ambient temperature, and perfusion that do not reliably correlate with the underlying metabolic function. As such, peripheral measurements tend to be inaccurate in predicting CBT. To overcome these limitations, some strategies that employ the measurement of heat flux have been used. Dual-heat flux (DHF) thermometry measures the flow of heat (flux) that flows out of the body along two different thermal paths, to decouple the system from the thermal resistance of the underlying tissue.[21–25] DHF sensors have demonstrated effective monitoring of CBT in patients both at rest and during exercise.[26] However DHF sensors are typically bulky and thick (up to 15 mm), the thinnest proposed device the authors have found measures 5.44 mm.[27] Furthermore, the limiting factor in current DHF sensors is the accuracy of the individual temperature sensing elements.[28] In this work, we employ a novel temperature responsive polymer that demonstrates record temperature sensitivity orders of magnitude higher than vanadium oxide and other cutting-edge temperature sensing materials,[29] to create ultra-thin and wearable DHF thermometers for CBT. We designed the sensors' geometry to optimize for tissue depth sensitivity, and evaluate its errors using Finite Element (FE) analysis. Furthermore, we characterized and improved the chemical composition of the temperature responsive polymer, to obtain higher temperature sensitivity. For data acquisition, we designed and fabricated a custom electronic board that achieved a readout accuracy of 4 mK. Finally, we fabricated an integrated prototype that was tested with an anthropomorphic phantom model demonstrating the ability to read CBT with an accuracy of ± 0.25 °C.

4.2 Results

4.2.1 DHF Calorimetry for Measuring CBT

In general, measurements of skin temperature do not correlate well with CBT since thermoregulatory processes keep peripheral areas at a lower temperature than the core. Nevertheless, under certain conditions, skin temperature can reflect with high precision the core temperature. For example, in the absence of heat flow, skin temperature equals the temperature of the inner tissues (deep core temperature): Zero-heat-flux (ZHF) thermometers are based on this principle. In ZHF thermometers a heat source is used to counterbalance the heat flowing out of the body to generate a zero-heat flow region on the skin. A pair of temperature sensors separated by a thermal insulator measures the heat flow and provides feedback to the heat source. Once isothermy is achieved, the bottom sensor measures the skin temperature which corresponds to the CBT. ZHF thermometers, however, require a constant power source for the heater and due to the inaccuracy of the temperature sensor they need a rather thick insulating layer. All these factors do not make ZHF thermometers suitable for wearable applications. To avoid the need of a heater to generate zero heat flux, dual heat flux (DHF) thermometers were developed.[21] In this device, a heat flux sensor consists of a pair of temperature sensors separated by an insulator. The DHF thermometer pairs two heat flux sensors, with different insulators' thicknesses, placed next to each other. By knowing the thermal resistance of the insulator dividing the temperature sensors, it is possible to rule out the thermal resistance of the tissues beneath the skin. As shown in Fig. 4.1(a), the CBT T_b is then calculated from the temperatures of the four sensors, T_1, T_2, T_3, T_4 as:[21]

$$T_B = T_1 + \frac{(T_1 - T_2)(T_1 - T_3)}{K(T_2 - T_4) - (T_1 - T_3)} \qquad (1)$$

where K is the ratio between the thermal resistance paths under the two heat flux sensors and must first be calibrated. K can be calculated using equation 1 and empirical measurements as:

$$K = \frac{(T_B - T_2)(T_1 - T_3)}{(T_B - T_2)(T_2 - T_4)}. \quad (2)$$

The thermal resistances of the two different paths determine the temperature difference between the bottom and the top surfaces. Therefore, the thickness of the insulating layers needs to allow the development of a thermal gradient that is measurable by the temperature sensors placed at the top and bottom of each heat flux sensor. To decrease the thickness of the heat flux sensors, extremely temperature sensitive materials, with high accuracy, must be used. It has been recently reported how a particular class of polyelectrolytes shows significantly high temperature sensitivity.[29–32] These synthetic polymers are characterized by carboxyl and hydroxyl groups placed along the backbone, which interact with metal cations (e.g., Ca^{2+}, Co^{2+}, Cu^{2+}) present in the polymer matrix. The temperature variation modifies the thermal energy of the system resulting in cations to proportionally hop from one coordination site to another, leading to a change in the conductivity. In this work, we synthesized 2-hydroxyethyl acrylate acrylic acid (HEA-AA)[29] with a combination of metal chloride salts to be used for the fabrication of the DHF sensor. The polymer was deposited on two thin polyimide (PI) layers. To generate two different thermal paths, the PI substrates had different thicknesses of 260 and 100 μm, respectively. On the surfaces of the PI layers, pre-patterned Cu/Au plated electrodes were used to electrically connect the HEA-AA to measure the change in conductivity. Two 10 μm thin HEA-AA layers were deposited on the electrodes and then insulated with 50 μm thick PET layers (Fig. 4.1(b) (top)) from external agents (e.g., room humidity). The resulting DHF sensor was less than 500 μm thick and highly flexible. This flexibility is a direct result of the ultrathin nature of these sensors and enables the resulting sensors to be conformally applied to the curvature of the body (Fig. 4.1(b) (bottom)).

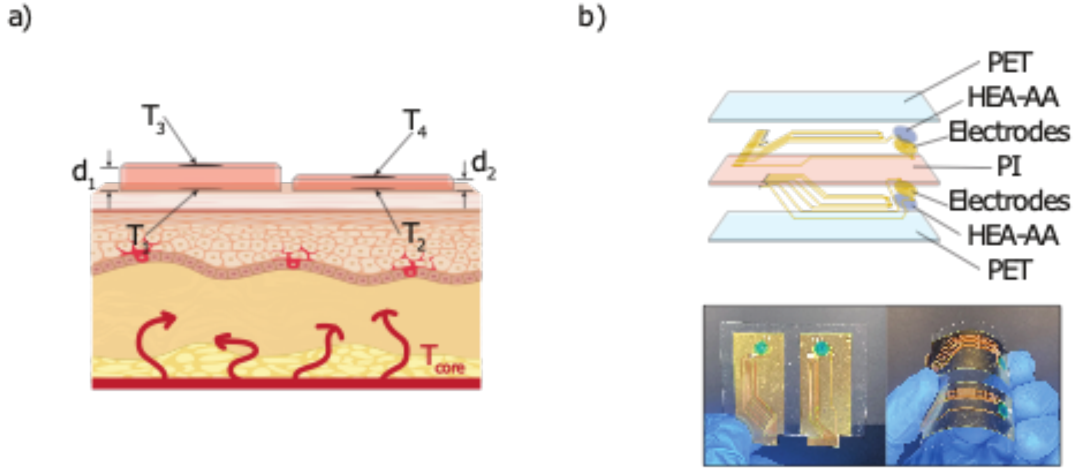

Figure 4.1: Dual Heat Flux sensor and HEA-AA integration. (a) Dual Heat Flux working principle. (b) Fabricated DHF sensor. Top: schematic of the sensor integrating HEA-AA in the architecture. Bottom: picture of the DHF sensor using Co^{2+} ions, flat (left) and bent (right).

4.2.2 Temperature Response Characterization

From a device perspective, the HEA-AA polymer can be approximated to act as a temperature dependent resistor since the polymer's conductivity varies as a function of temperature. However, the relationship between the temperature and resistance for this class of polymers is nonlinear and cannot be represented by a constant temperature coefficient of resistance.[29–32] The polymer's conductivity-temperature dependence needs to be generalized to a temperature dependence of the complex admittance Y (or impedance Z). In addition, to avoid charge accumulation in the devices, the change of the polymer response as a function of temperature needs to be characterized by an AC current. Previous work has characterized HEA-AA cross-linked with divalent calcium at specific frequencies, or in a narrow frequency range.[29] As a reference, Fig. 4.2(a) shows the absolute value of the admittance as a function of frequency (1 Hz to 100 kHz) measured at 35 ° and 45 °C and at a constant relative humidity (RH) of 10%. In the medium frequency region, a strong frequency dependence does not appear, while at low and high frequency the spectrum presents two strong dispersive regimes. This behavior is in line with the behavior of other ionic conductors, where polarization and dielectric relaxations arise in these frequency regions.[33,34] The phase of the admittance (i.e., the phase difference between the applied voltage and the resulting current) also shows a strong dependence on temperature as well as on the applied frequency (Fig. 4.2(b)). Therefore, we can define the material's temperature response $R^*(\omega)$ as the ratio between the admittance $Y^*(\omega, T)$ at highest temperature $T_{\max}$ divided by the admittance measured at the lowest temperature $T_{\min}$, for a specified temperature range:

$$R^*(\omega) = \frac{Y^*(\omega, T_{max})}{Y^*(\omega, T_{min})}. \quad (3)$$

As a result, the absolute value of the response $|R^*(j\omega)|$ corresponds to the ratio of the absolute value of the admittance $|Y_0(\omega, T)|$, while the phase of the response $R^*(j\omega)$ corresponds to the difference between the phase of admittance $\theta(\omega, T)$:

$$|R^*(\omega)| = \frac{|Y_0(\omega, T_{max})|}{|Y_0(\omega, T_{\min})|}$$

$$R^*(j\omega) = |\theta(\omega, T_{max}) - \theta(\omega, T_{min}). \quad (4)$$

To maximize the temperature sensitivity, we prepared different HEA-AA samples cross-linked with Ca^{2+}, Co^{2+}, Cu^{2+}, Mg^{2+}, and Zn^{2+}. Each of these ions has a different binding energy with the polymer backbone that results in a different temperature response. The temperature response is directly correlated to the activation/binding energy E_a of the metal ion with the acid and polar groups along the polymer backbone. This concept becomes clearer in the Arrhenius representation, when considering the ion bulk conductivity $\sigma_0(T)$ the temperature response is proportional to the activation energy for ion hopping:

$$E_a = \frac{\log(\sigma_0(T_{max})) - \log(\sigma_0(T_{min}))}{\frac{1}{T_{max}} - \frac{1}{T_{min}}} = \frac{\log\left(\frac{\sigma_0(T_{max})}{\sigma_0(T_{min})}\right)}{\frac{1}{T_{max}} - \frac{1}{T_{min}}} = \frac{\log R_0}{\frac{1}{T_{max}} - \frac{1}{T_{min}}} \quad (5)$$

where $R_0 = \sigma_0(T_{max})/\sigma(T_{min})$ is the conductivity DC response. Our previous work has shown how increasing the number of carboxyl and hydroxyl groups increases the polymer's temperature response.[29] This behavior is a direct consequence of the strength of the interaction between the polymer backbone and the metal ion; a higher number of functional groups, creating a coordination complex with higher binding/activation energy E_a. Stronger interaction between the polymer complex and the metal cation could also be achieved by choosing an ion whose affinity to the coordination complex is particularly high. Previous studies suggest that the geometry of the electronic orbitals combined with the spatial arrangement of the coordination complex will result in larger activation energies.[35–37] Therefore, we compared different polymer-metal chloride combinations (i.e., Ca^{2+}, Co^{2+}, Cu^{2+}, Mg^{2+}, and Zn^{2+}) to determine the one that has the highest temperature response. Fig. 4.2(c-d) shows the absolute value and phase response spectra for the different cations in the temperature range 35 ° to 45 °C. Co^{2+} shows the highest temperature response both in terms of absolute and phase response. As previously reported,[32] an optimal water content is needed to measure a high temperature response. Water can modify the ion's transport activation energy in multiple ways, for example by varying the coordination environment of the ions, as well as the polymer's segmental motion. Water molecules can also provide additional charge carriers (protons) with a lower activation energy, which can lower the temperature response. To minimize the effect of the water concentration within the polymer, we performed all characterization at constant humidity (RH 10 %). However, every ion has a different water affinity (Ca^{2+} is highly hygroscopic, while Co^{2+} and Cu^{2+} have lower water affinity). To evaluate the difference in water content between the various ions, we measured the conductance at constant temperature (35 °C) (Fig. 4.2(e)). Among the different ions, Co^{2+} has the lowest current, suggesting that the water content is within the optimal concentration to register an optimal temperature response. Based on this analysis, HEA-AA cross-linked with Co^{2+} ions was selected as the ideal material to fabricate a DHF calorimeter.

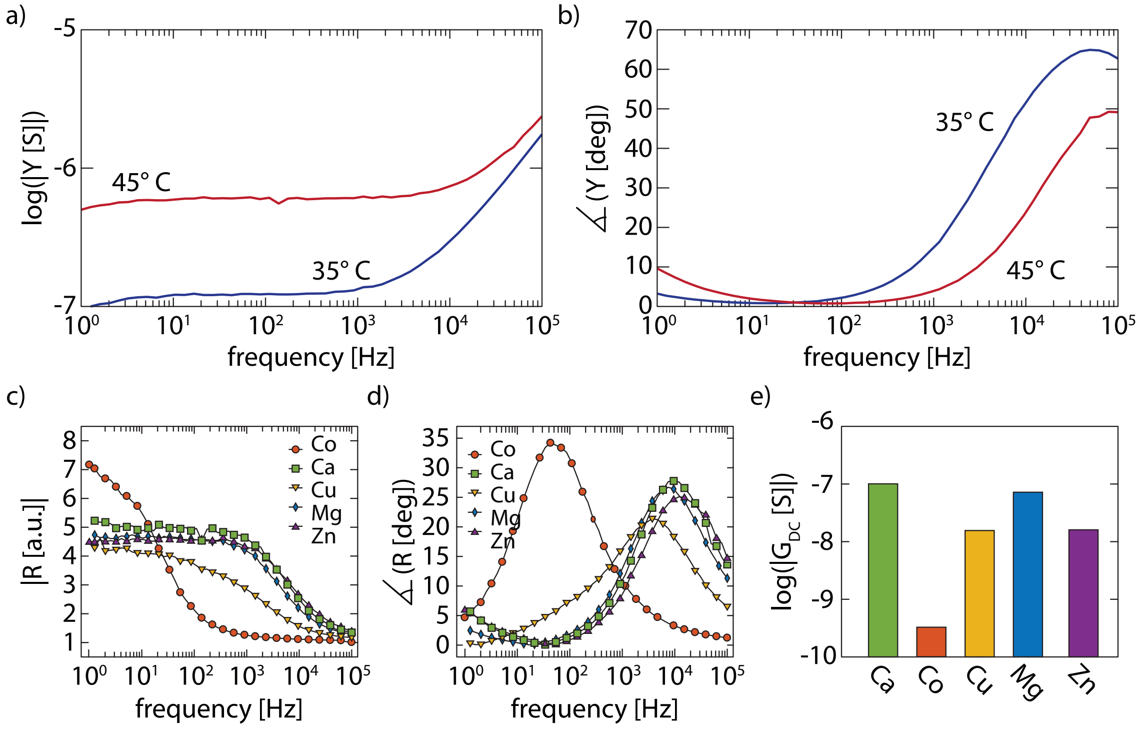

Figure 4.2: HEA-AA characterization. (a) Typical absolute value of the conductance spectra for a sample cross-linked with Ca^{2+} and measured at RH 10 %. Blue line absolute value measured at 35 °C, red line absolute value measured at 45 ° C. (b) Typical phase of the conductance spectra for a sample cross-linked with Ca^{2+} and measured at RH 10 %. Blue line phase measured at 35 °C, red line phase measured at 45 °C. (c) Absolute value of the response as a function of frequency for samples cross-linked with different ions measured at RH 10 %: orange dots Co^{2+}, green squares Ca^{2+}, yellow down triangles Cu^{2+}, blue diamonds Mg^{2+}, purple triangles Zn^{2+}. The markers represent a subset of the actual data set. (d) Phase of the response as a function of frequency for samples cross-linked with different ions measured at RH 10 %: orange dots Co^{2+}, green squares Ca^{2+}, yellow down triangles Cu^{2+}, blue diamonds Mg^{2+}, purple triangles Zn^{2+}. The markers represent a subset of the actual data set. (e) DC conductance of the samples cross-linked with different ions at 35 °C measured at RH 10%.

Fig. 4.3(a) shows the typical calibration curve for the selected material. The absolute value of the current increases from 300 pA to 2.2 nA, while the current phase difference decreases from 55 to 20 degrees over a 10 °C temperature change. The current's phase difference varies linearly with temperature, and the current's absolute value relationship to temperature is exponential. For optimal performance, we can mix and match the calibration methods of the four sensors, empirically determining the better one (phase vs. current) during characterization. A custom readout system was designed to accurately sample the current and phase response (Fig. 4.3(b-c)). A sine wave oscillator generates the harmonic voltage to be applied to the sensor through an analog multiplexer. The resulting current flowing through each individual sensor is then converted to a voltage and then amplified by means of an instrumentation amplifier. The applied voltage and the measured current were then converted to square waves. Because of the reactance of the polymer, the voltage and current have a phase difference. This phase difference is measured by a phase detector, which generates a pulse that corresponds to the time delay between the two signals. The pulse width is then quantified through a 2 MHz 16-bit counter. Given the frequency of the applied voltage $f_{excitation}$ and the frequency of the counter clock $f_{counter;}$ the phase difference $\Delta\Theta$ correlates to the counter counts n_{count} through the relation:

$$\Delta\Theta = \frac{n_{counter}}{f_{counter}} \cdot 360^\circ \cdot f_{excitation} \cdot \quad (6)$$

By measuring the phase response, not only the sensor's output is linearized with respect to temperature, but also considerably higher accuracy can be achieved without the need for a specific analog to digital converter (ADC) architecture. With the implemented circuit, a minimum phase shift of 0.006° can be measured, which corresponds to a resolution of circa 4 mK.

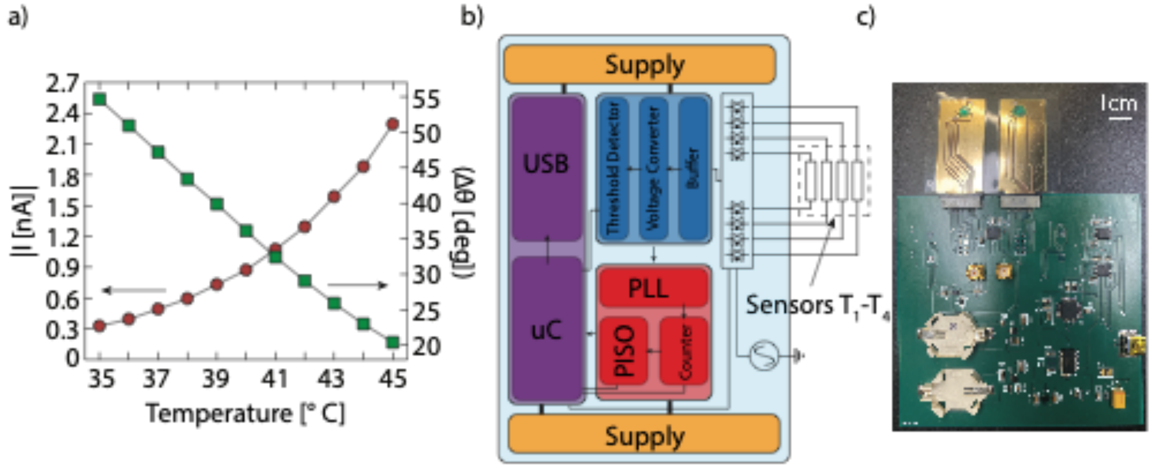

Figure 4.3: Sensors calibration and readout. (a) Sensor temperature calibration. Red circles current absolute value, green squares current phase. (b) Schematic of the readout system. (c) Picture of the readout system and the DHF sensor.

4.2.3 Error Analysis

The optimization of HEA-AA composition ensures that the temperature response of the polymer has the proper sensitivity to measure the small temperature differences across the DHF sensor. However, the precision of the temperature sensors is not the only factor that contributes to the DHF sensor's accuracy. More specifically, in the derivation of equation 1 some assumptions were made to reach a simple analytical solution. In particular, the heat flux was assumed to be totally transversal with no longitudinal component. We will show that this assumption is the major contribution to the theoretical error of the DHF architecture. Fig. 4.4(a) (top) shows the transversal and longitudinal thermal gradients that are established in the chosen geometry calculated from the FE simulation. The transversal thermal gradient develops from the bottom of the tissue layer and it is funneled towards the heat flux sensors. At this interface, two different thermal gradients appear because the heat flux sensors have different thickness. Because we chose to use very thin insulating layers for our sensors (260 and 100 μm, respectively), the temperature difference between the top and the bottom of the sensors is in the order of 50 mK. However, as it can be seen in Fig. 4.4(a) (bottom) there is a non-zero longitudinal temperature gradient that develops over the xy plane. The generation of a transversal thermal gradient has to be attributed to the non-uniform heat exchange along the surface boundaries on the xy plane. Previous works studied the system using radiation or convection boundary condition without taking into account how they affected the measurement error.[23,38] In order to analyze how the different heat exchange phenomena affect the measurement, we characterized the error e for the two different conditions and we correlated it with the temperature gradient ∇T between the temperature at the center of the top surface of one of the two heat flux, T_A, and the one at the corner on the same surface, T_B. By doing so, we can correlate the amount of transversal thermal gradient to the measurement error. First we analyzed the heat exchange at the boundaries through radiation only (Fig. 4.4(b)). The rate of heat exchange through radiation $-\boldsymbol{n} \cdot \boldsymbol{q}_0$ at a surface temperature T depends on the surface emissivity ϵ and the ambient temperature T_{amb} according to the Stefan-Boltzmann law:

$$-\boldsymbol{n} \cdot \boldsymbol{q}_0 = \epsilon\sigma(T_{amb}^4 - T^4) \quad (7)$$

where σ is the Stefan-Boltzmann constant. As T_{amb} increases, there will be a lower surface to ambient radiation which will create a smaller gradient on the xy plane. Fig. 4.4(c) indicates that the decrease in the thermal gradient proportionally leads to a smaller error. Similar to radiation, convective heat exchange q_0 is determined by ambient temperature T_{amb} and the heat transfer coefficient h:

$$q_0 = h(T_{amb} - T). \quad (8)$$

For convective heat exchange with the ambient, the heat transfer coefficient depends on several factors, among which include relative humidity and air flow speed. However, heat transfer coefficient in normal conditions ranges between 0.1 – 10 W/m^2 K. For this simulation, we only modified the heat transfer coefficient keeping the ambient temperature constant. Fig. 4.4(c) shows the error as a function of h: for values below 1 W/m^2K the error remains low, however it drastically increases above this threshold. This behavior correlates closely with the development of a larger thermal gradient as the heat transfer coefficient increases: for $h < 1$ W/m^2K the transversal gradient remains low, while above this value it starts to increase. It is therefore clear how the measurement error is caused by the thermal gradient on the xy plane, whose magnitude is set by the heat exchange characteristics at the boundaries. When combining both heat exchange physics, the complete measurement error can be further analyzed (Fig. 4.4(d)). When radiation is combined with convection, the effect of convection does not drastically impact on the error as long as the heat transfer coefficient is kept low. For higher h (e.g., above 1 W/m^2K), the convective heat exchange dominates leading to a larger error. The analysis of the theoretical error indicates that in order to reduce the measurement error in the experimental setting, both the radiation and convection need to be reduced to achieve accurate results. Radiation heat exchange is inevitable and can be only limited by lowering the emissivity of the substrates, which is constrained by the choice of the available materials used to fabricate flexible substrates. Convection can be drastically lowered by the use of materials to thermally insulate the sensor. This approach would lead to bulkier and less flexible sensors. However, as previously shown, it is sufficient to ensure that the heat transfer coefficient is below 1 W/m^{2}K in order to minimize the effect of convection. This is the case for most everyday conditions under normal clothing.[39] The use extensive thermal insulation on the device is not required and a clothing layer will be used to reduce to the minimum convective heat. Moreover, it has been shown that the error given by the transversal gradient can be minimized modifying equation 1 to:[23]

$$T_B = T_1 + \frac{(T_1 - T_2)(T_1 - T_3)}{K(T_2 - T_4) - (T_1 - T_2)}\,. \qquad (9)$$

Using the modified equation 9 and considering both radiative and convective heat exchange (fixed to 1 W/m^{2}K), it is possible to calculate the penetration depth as a function of the ambient temperature (Fig. 4.4(e)). The maximum penetration depth that this method can achieve is the maximum tissue thickness which allows the calculation of the CBT with an error below 0.25 °C. This error threshold was chosen to be well within the clinically acceptable limits of bias, as defined by previous studies.[40–44] The penetration depth varies from 6.4 mm at 20 °C to almost 10 mm at 30 °C. This analysis allows us to clarify the theoretical limitations of the DHF 1D model given the parameters of our device.

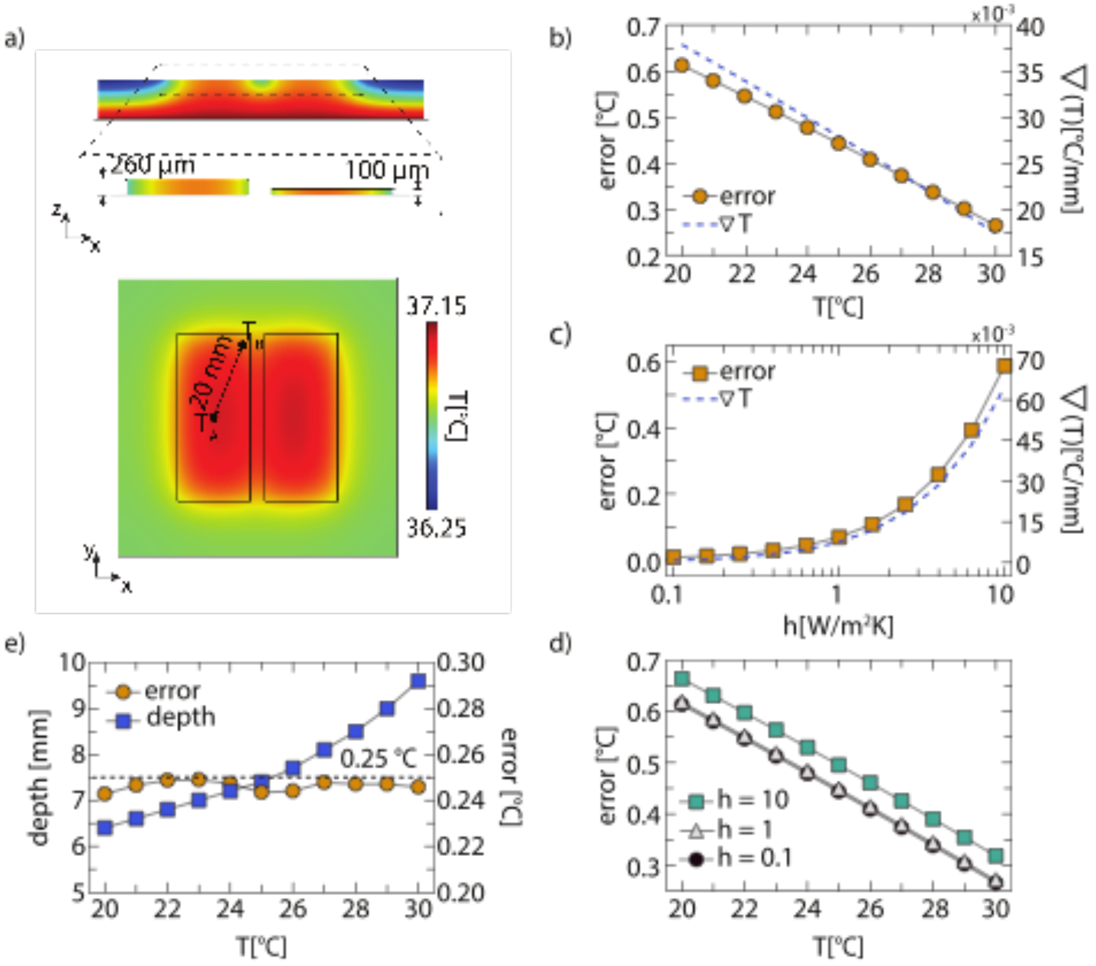

Figure 4.4: FEM Analysis on the DHF architecture. (a) Thermal gradient developed across the xz (Top) and xy (Bottom) planes. (b) Error (orange circles) and temperature gradient (blue dashed line) calculated as a function of external temperature for radiative heat transfer. (c) Error (orange squares) and temperature gradient (blue dashed line) calculated as a function of heat transfer coefficient for convective heat transfer. (d) Error calculated as a function of external temperature for both radiative and convective heat exchange at different heat transfer coefficients: teal squares h = 10 W/m^{2}K, gray triangles h = 1 W/m^{2}K, black circles h = 0.1 W/m^{2}K. (e) Penetration depth (blue squares) and corresponding error (orange circles) as a function of external temperature at constant heat transfer coefficient h = 1 W/m^{2}K.

4.2.4 CBT Measurement

Combining the results of the ion comparison in HEA-AA with the readout system and the information gathered by the theoretical error analysis, HEA-AA temperature sensors were successfully integrated in the designed DHF architecture. The individual temperature sensors were characterized between 35 °C and 45 °C to obtain the temperature calibration curve. The phase-temperature calibration data was then fit to a first-degree polynomial and the two fit parameters were used to convert the acquired phase to temperature values (Fig. 4.5(a)). The linear fit diverges for higher temperature, but it gives an optimal representation for $T < 43$ °C, with coefficient of determination R greater than 0.9989.

To simulate the CBT measurement, we built a custom-made setup, where both the accuracy and the time response of the sensor can be estimated (Fig. 4.5(b)). A water bath was used to achieve a constant temperature T_{set} of 37 °C, while a thin copper layer immersed in the bath was used to obtain a homogeneous temperature across the surface. To simulate the skin, we used a rubber mat with a thermal resistance similar to that of human tissue. To evaluate the sensor's performance for different skin thicknesses, rubber mats of 2, 4, 6, and 8 mm thicknesses were used. The DHF sensor was connected to the readout board which was then connected to a computer. At the same time, an IR camera measured the temperatures of the water bath and the copper layer to ensure that the correct temperature was established in the bath. A piece of regular clothing (few millimeters thick cotton shirt) was used to reduce the heat transfer coefficient with the ambient air. We first determined the ratio between the thermal resistance paths, K, using equation 2 with data obtained from the 2 mm thick rubber mat. Then, the T_{set} was computed from the individual temperatures using equation 9. Fig. 4.5(c) shows the estimated CBT using the DHF sensors for the different mat thicknesses. The green area in the plots indicates the ± 0.25 °C maximum allowed error. When the DHF sensor is not thermally insulated with clothing, the estimated T_{set} has an error greater than 0.25 °C for mats thicker than 2 mm, with a maximum error of 0.76 °C for the 8 mm thick mat. When the DHF thermometer is covered with clothing, the sensor's performance greatly improves. Error within the 0.25 °C bounds was measured for a mat thickness of 6 mm, while for an 8 mm thick mat the maximum error was 0.33 °C. These results are in line with the theoretical calculation presented in the previous section. The transversal heat flux is the main source responsible for the error in the DHF architecture. Reducing the heat transfer between the boundaries and the ambient air results in lower thermal gradient across the sensor which corresponds to a higher sensor accuracy. When covered with a piece of clothing, the heat transfer coefficient of the convective transfer between the sensor and the ambient is reduced, resulting in a smaller error. Lastly, we analyzed the transient behavior of the DHF thermometer. We increased the temperature of the thermal bath from 37 ° to 39 °C and estimated T_{set} using the 6 mm mat while the sensor was covered with a piece of clothing. Fig. 4.5(d) shows the time evolution of the reconstructed temperature when this step change was made. We calculated the response time as the time the system needed to recover to an error below 0.25 ° C. For the selected mat thickness, the reconstructed temperature fell within the accepted error roughly after 15 minutes.

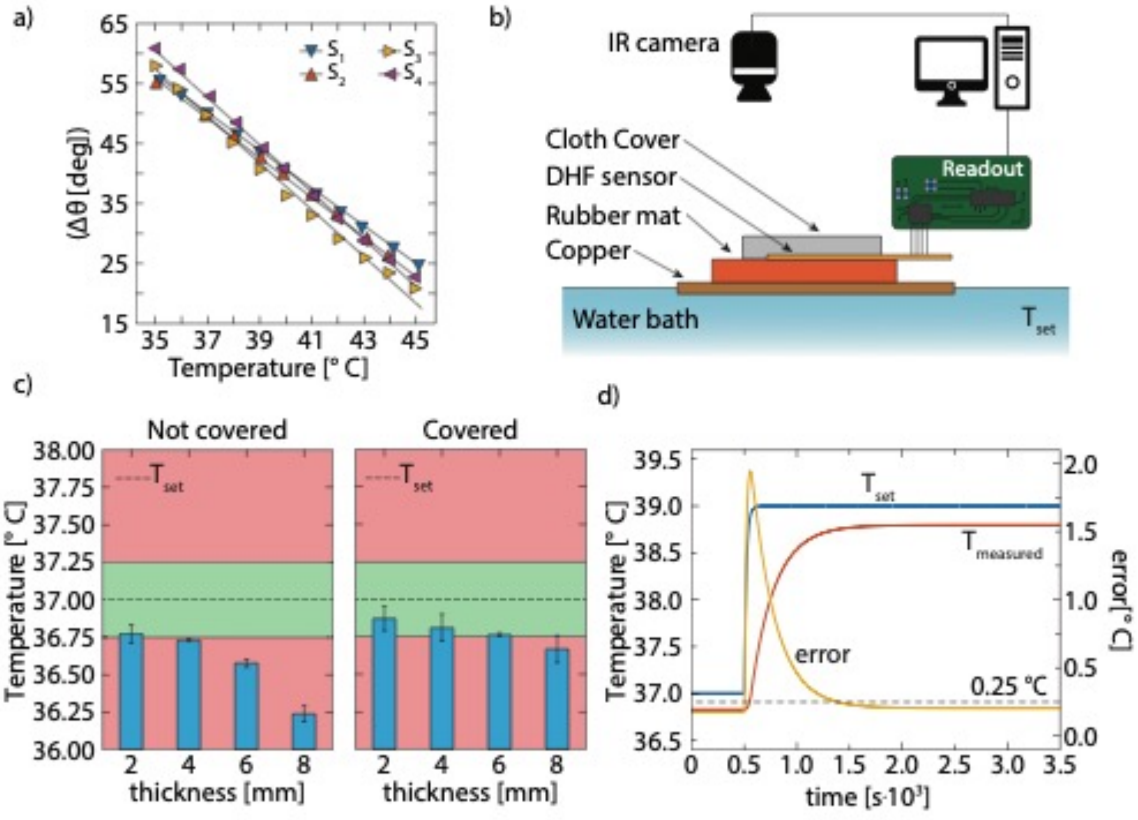

Figure 4.5: CBT measurement. (a) Phase calibration curves for the different temperature sensor in the range 35 ° and 45 °C. (b) Set up to measure the CBT. The core temperature is simulated by a water bath set to the desired value T_{set}. A thin copper layer is used to achieve homogeneous temperature over the analyzed surface. A rubber mat simulates the tissue layer between the core and the sensor. The DHF is placed on top of the rubber mat and then covered by a piece of clothing. (c) Calculated CBT for a set temperature of T_{set}= 37 °C, for different thickness of the rubber mat (2, 4, 6, and 8 mm, respectively). Measured CBT when the sensor is exposed to convective heat exchange (left) and when a piece of clothing is applied to insulate the sensor from the environment (right). (d) Step response for the DHF sensor calculated with the 6 mm rubber mat when T_{set} is increased from 37 ° to 39 °C. Blue line represents thermal bath temperature, orange line represents the DHF sensor output temperature, the yellow line represents the absolute error in the measurement.

Once we established the response time of our DHF setup, we investigated its CBT resolution on a human phantom model (Fig. 4.6). A thermocycler (Bio-Rad C1000) was used for precise temperature control and its temperature setting was considered ground truth CBT (Fig. 4.6(a)). We used a 5 mm thick 7% Agar gel to simulate human subcutaneous tissues as previously described,[45] which was sealed with Saran wrap to prevent water evaporation, with the entire assembly covered with a Petri dish to prevent fluctuations due to ambient convection (Fig. 4.6(b)). The DHF sensor was connected to the impedance analyzer (Zurich Instruments, MFIA 5 MHz) through our custom interface PCB, and both the phase and the absolute value of current calibrations were considered in selection of the optimal response to temperature for each of the polymer sensors. By using phase response calibrations for sensors T1 and T2, and current amplitude calibration curves for T3 and T4, we obtained the best fit between our CBT estimation and the ground truth in the region spanning hypothermic and hyperthermic temperatures (25 ° - 45 °C) (Fig. 4.6(c)).

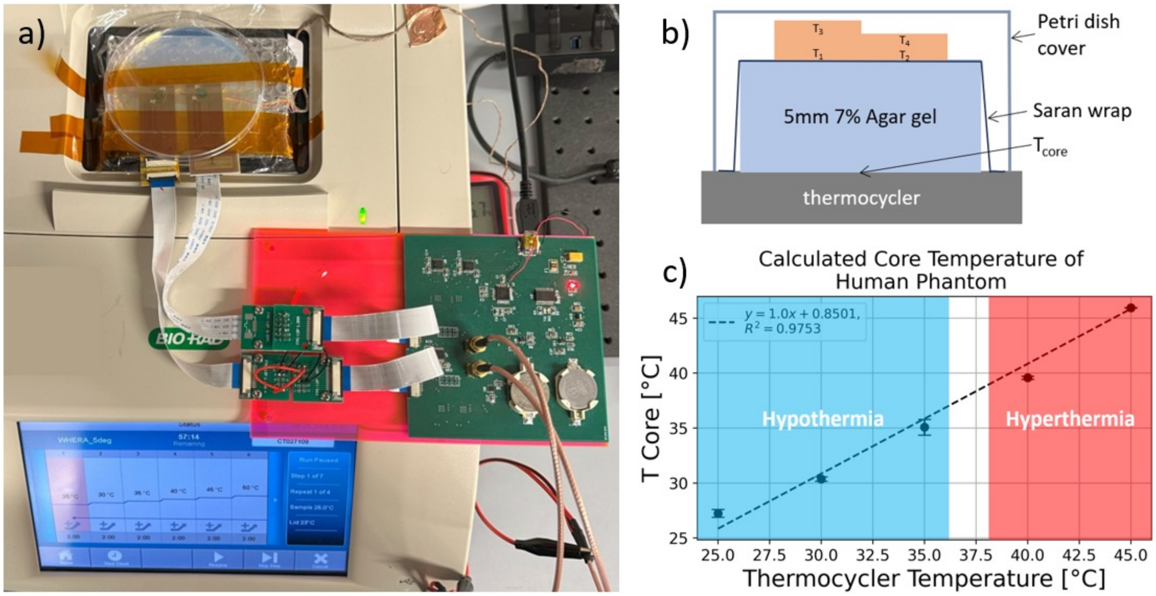

Figure 4.6: DHF sensor's CBT resolution. (a) Photo of human phantom experimental setup. The pixels are plugged into the breadboard PCB, which is interfaced with the impedance analyzer (not shown). (b) Schematic of the experimental setup for human phantom model. (c) Calculated CBT for various T_{set} = 25 °C, 30 °C, 35 °C, 40 °C, 45 °C, representing hypo and hyperthermia for the human body (identified in blue and red, respectively).

4.3 Conclusions

In this work, we showed the fabrication of a CBT sensor, integrating a thermally responsive polymer into the DHF thermometer architecture. We optimized the polymer's composition by choosing the best metal cation that showed the highest response. Co^{2+} was found to be the best cross-linking ion because it was linked to an optimal water content. We employed the complex temperature sensitivity to design a readout system, in which the temperature could be related to both the current response and the phase of the sensor's admittance, achieving a sensitivity of 3.5 ° / °C and a resolution of ± 4 °mC. By simulating the DHF architecture, we found a correlation between the theoretical error and the longitudinal thermal gradients that develop over the sensors. Furthermore, we analyzed the influence of different boundary conditions in the device performance and calculated the corresponding errors and penetration depth. We fabricated a DHF thermometer employing the optimal polymer's composition and used a custom-built readout system to measure CBT on a phantom setup. We showed that, as described by the FE simulations, the measurement error can be reduced by lowering the heat exchange at the boundaries. The fabricated sensor has an error below ± 0.25 °C for a thickness up to 6 mm and a time response of 15 minutes.

4.4 Experimental Section

4.4.1 Polymer Synthesis

Tert-butyl acrylate (1.28 g, 10 mmol) (Sigma Aldrich, 327182) and 2-hydroxyethyl acrylate (1.16 g, 10 mmol) (Sigma Aldrich, 292818) were dissolved in 1.13 mL and 1.46 mL of dimethylformamide (DMF), respectively, and purged with nitrogen. Next, we added 29 mg (0.1 mmol) of S,S-dibenzyl trithiocarbonate (Sigma Aldrich, 746304) to the reaction, while continuing nitrogen purging for 3 minutes. This is followed by the addition of azobisisobutyronitrile (AIBN) (0.8 mg, 5 μmol) (Sigma Aldrich, 441090) and stirring at 75 °C under protection of N2. The progress of polymerization was monitored using 1H NMR. The reaction was cooled down and vented to air at approximately 80% conversion rate. Residual tert-butyl acrylate and 2-hydroxyethyl acrylate were removed first by vacuum, followed by precipitation in 100 mL cold diethyl ether to yield a yellow oil as the macro-CTA (2.02 g, 80%). For deprotection, polymer (1 g) was dissolved in 3 mL dichloromethane (DCM), followed by the addition of 3 mL trifluoroacetic acid (TFA). The reaction was stirred at room temperature overnight. DCM and TFA were removed by vacuum, followed by precipitation in cold diethyl ether, to result in a highly sticky yellow oil as HEA-AA (100 %)[29]

4.4 2 FEM Analysis

The geometry was simulated using COMSOL Multiphysics. For simplicity, the skin was simulated as homogenous medium and the bioheat generation or blood perfusion were not taken into account. The substrate was implemented using the thin layer module to decrease computation time and achieve a better result. A general layer type was considered to take into account both the normal and tangential heat fluxes. Three different situations were considered for the boundary conditions: radiation heat exchange, convection heat exchange and mixed radiation and convection heat exchange. We first calculated the heat transfer in the system tissue/sensor. Then we used the output of this simulation to compute the heat exchange at the boundaries through radiation and convection. The error was calculated as the difference between the temperature set at the bottom boundary of the tissue and the temperature calculated with equation 1. The temperature gradient was estimated as the difference between the temperature at the center on the top surface of the thicker heat flux sensor and the temperature 20 mm away along the diagonal on the same surface (Fig. 4.4(a)). The maximum penetration depth was calculated as the thickness at which the error was below 0.25 °C. The thickness of the tissue was incremented by 100 μm.

4.4.3 Electrical Readout Circuitry

Details on the design and characterization of the readout circuit can be found in the supplementary information.

The phase difference between the input voltage and the resulting current flowing through the sample was measured by evaluating the corresponding time lag between the two signals. The harmonic signal used to excite the sample was generated by a Bubba oscillator in which every RC section provides a phase shift of 60° to trigger the oscillator. The component was chosen to achieve an oscillation at 80 Hz, but due to component mismatching the oscillator had an output frequency of 86 Hz. To avoid the use of a dual supply system, we biased the generated voltage at 2.5 V through a precision Zener diode. The output signal then had an amplitude control to allow flexibility on the excitation signal (Fig. 4.7(a)).The reference sine was then applied to one of the four temperature sensor through an analog multiplexer and then switched to the others. This approach allowed the use of only one oscillator and one phase detector/counter for all the sensors. The current flowing through the sample was then converted to a voltage through a resistor, which was then amplified to the desired amplitude through an instrumentation amplifier with a digitally controlled gain. The reference sine and the voltage-converted current were translated in to square waves through fast voltage comparators referenced to 2.5 V. The resulting square waves were then compared with a phase detector that generated a pulse proportional to the phase difference between the two inputs (Fig. 4.7(b)). This time lag was measured by gating a 2 MHz clock with the pulse generated by the phase detector, which was then fed to a 12 bit digital counter. The parallel output of the counter was then converted to a serial bit stream through a PISO register and sent to the μC for data processing. Synchronization and reset signals were generated by the μC to zero the count of the digital counter and to synchronize the data transfer at the end of each reading. We implemented this design on a 6 layers PCB manufactured by Eurocircuits. The functionality of the readout was characterized by an all-pass filter (Fig. 4.2(a)). This circuit is designed to have a zero and a pole at the same frequency, so that the resulting magnitude is constant with frequency while the phase varies from 180° to 0° according to the relation:

$$\Delta\Theta = \pi - 2\tan-1(2\pi f\, RC). \quad (10)$$

In this case, we wanted to generate a phase difference at a constant frequency (the one of the readout oscillator), therefore we varied the resistance value R by using a 10 bit, 100 kΩ digital potentiometer (Fig. 4.8(b)). We wanted to generate a phase difference at a constant frequency (the one of the readout oscillator), therefore we varied the resistance value R by using a 10 bit, 100 kΩ digital potentiometer (Fig. 4.8(b)).To evaluate the exact phase corresponding to a certain resistance value, we swept the potentiometer from 0 to 1024 while recording the phase difference with a lock-in amplifier at 86 Hz (Fig. 4.8(c)). Once a correspondence between the potentiometer value and the resulting phase difference was established, we connected the all-pass filter to the readout circuit and measured the phase difference (Fig. 4.8(d)). As expected, the measured phase saturates around 60° which corresponds to the maximum time lag that can be measured with a 16 bit counter and a 2 MHz clock.

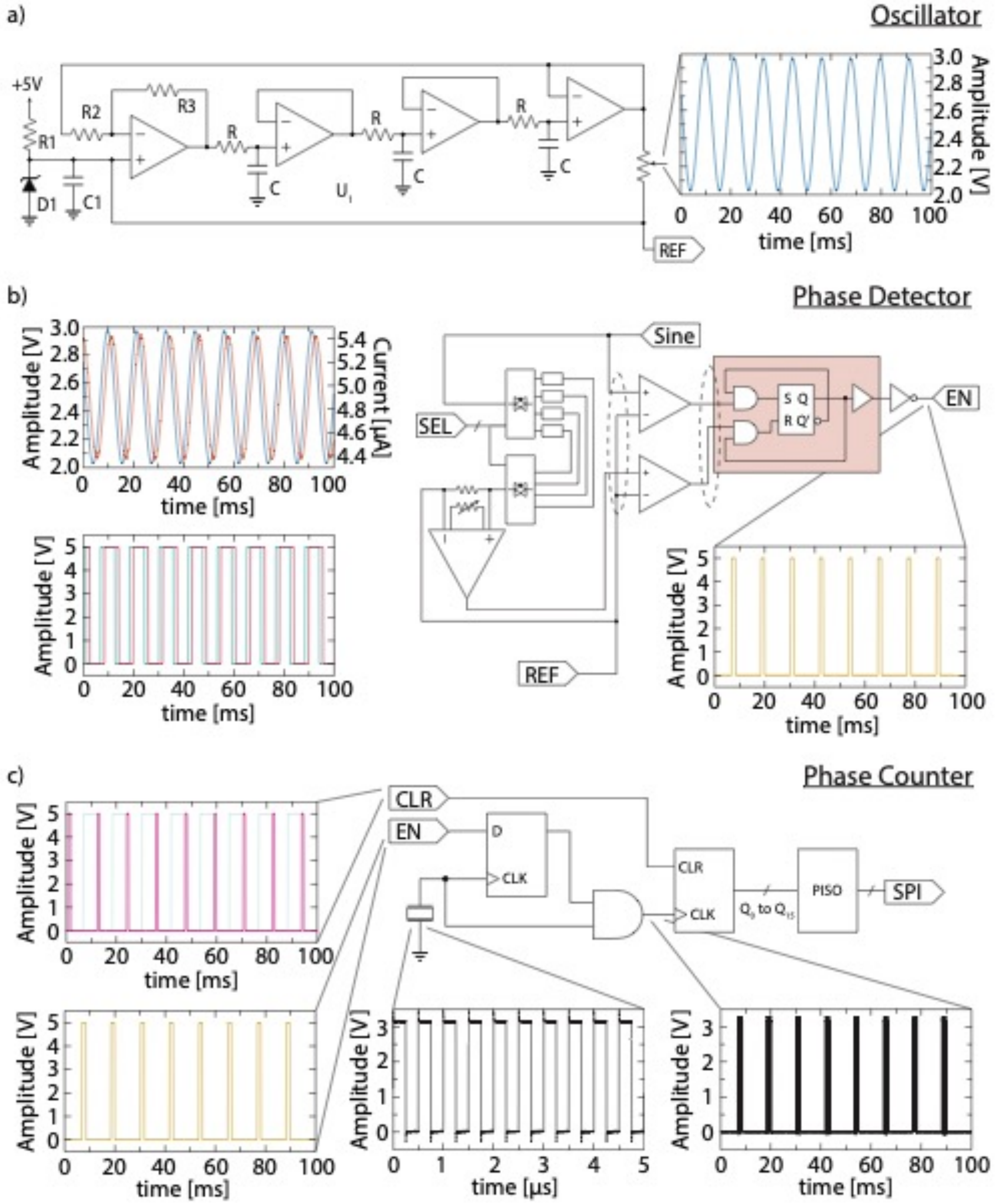

Figure. 4.7: Detailed implementation of the electrical readout. (a) Schematic of the harmonic Bubba oscillator. (b) Schematic of the phase detector. (c) Schematic of the phase counter.

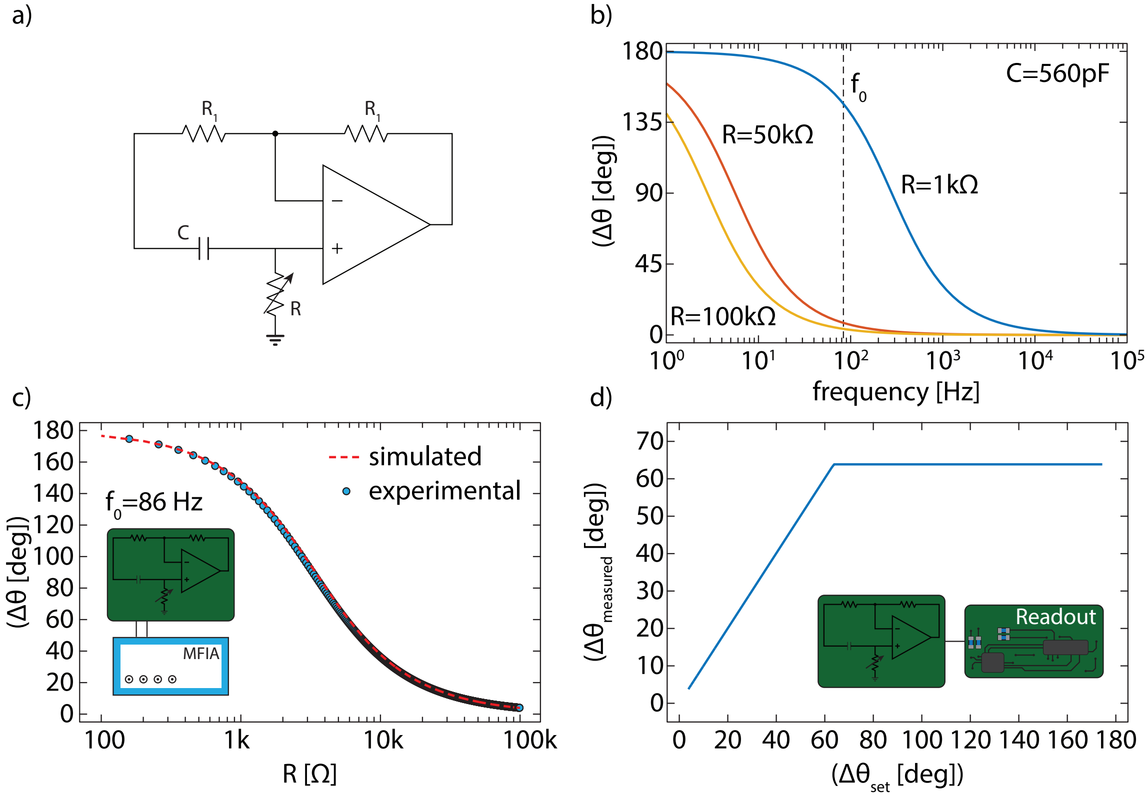

Figure. 4.8: Characterization of the readout circuit. (a) Schematic of the all-pass circuit used for the readout calibration. (b) Simulation of the phase difference as a function of frequency (1 Hz to 100 kHz) for different resistance values R: blue line R = 1 kΩ, orange line R = 50 kΩ, yellow line R = 100 kΩ. (c) Phase difference measured at constant frequency f0 = 86 Hz for the different resistance values R. Red dotted line simulated results, blue circles experimentally measured data. (d) Phase measured by the readout circuit for different phase values generated by the all-pass circuit.

4.4.4 Thermal Response and Calibration

Temperature cycles on the films were actuated by a Peltier- Element (model Qc-31-1.4-8.5m). The temperature was independently measured with a Pt100 platinum resistance thermometer placed on the polyimide substrate near the polymer. The Pt100 sensors were previously calibrated with a FLIR thermal camera (model A655sc). A PID controller was implemented to generate a sinusoidal temperature between 30 ° and 65 °C. The substrates and the reference Pt100 were connected to an interface board that could be connected with the impedance analyzer and the temperature control board. The current was measured with the impedance analyzer with an average sampling rate of 10 Hz. The temperature response as a function of frequency was isochronically measured; the frequency was kept constant within one temperature cycle and then changed to the next frequency at the next temperature cycle. Frequency was swept between 1 Hz and 100 kHz. To avoid the thermal hysteresis due to the sample mass we then considered only the raising part of the temperature cycle and sampled the current at different temperatures. The different temperature responses were calculated between 35 °C and 45 °C.

4.4.5 CBT Measurement at Various Depths

Polyimide substrates with double sided pre-patterned copper/immersion gold electrodes (35 μm and 3 μm, respectively) were purchased from PCBWay. On these substrates 5 μL of HEA-AA cross-linked with various ions was deposited and dried overnight under vacuum. The sensors were then insulated with a 50 μm PET layer to shield the polymer from humidity. Pt100 thermometers were placed on each of the four polymer sensors to obtain the calibration curves (Fig. 4.5(a)). Next, the assembled DHF thermometer was ready for CBT measurement. Rubber mats of different thicknesses were used to simulate human skin and subcutaneous tissue (Fig. 4.5(b)). To further reduce the effect of convective heat exchange with the environment, the DHF sensor was further covered with a piece of cloth. The experiment was performed at room temperature. The rubber mat along with the DHF sensor was placed on a thermal bath (Thermo Scientific Precision GP 05) to create a stable temperature, which simulates the core temperature, and is kept at 37 °C (Fig. 4.5(c)). Data from individual sensors were acquired through the previously described readout system at a sampling rate of 21.5 Hz. To measure the response time, we increased the bath temperature from 37 ° to 39 °C and analyzed the time evolution of the sensor's output when placed on the 6 mm mat (Fig. 4.5(d)).

To replicate the human skin 7% Agar gel was used, since it matches the thermal properties of human tissue well.[46] An Agar gel layer of 5 mm thickness was used. PCR thermocycler was used for accurate temperature control, and the temperature at the interface between Agar layer and thermocycler was verified using a thermistor. The agar gel was sealed using Saran wrap to prevent water evaporation. The pixels were pressed down to the Agar phantom layer using polyimide tape, which also ensured good thermal contact with the thermocycler. The entire assembly was covered with a Petri dish cover to prevent ambient perturbations. The CBT shown in Fig. 4.6(c) was calculated on the phantom data by using the K value from the calibration data. Error shown was taken from using the 95% confidence interval of the K value. Linear fit and R^2 was based on manually set slope of 1 (which assumes constant offset over entire T range). Error bars were based on K error propagation (95% confidence intervals), not multiple repeats (n=1 experiment).

References

(1) Paulikas, C. A. Prevention of Unplanned Perioperative Hypothermia. *Aorn J.* **2008**, *88* (3), 358–368.

(2) Torossian, A. Thermal Management during Anaesthesia and Thermoregulation Standards for the Prevention of Inadvertent Perioperative Hypothermia. *Best Pract. Res. Clin. Anaesthesiol.* **2008**, *22* (4), 659–668.

(3) Moola, S.; Lockwood, C. Effectiveness of Strategies for the Management and/or Prevention of Hypothermia within the Adult Perioperative Environment. *Int. J. Evid. Based Healthc.* **2011**, *9* (4), 337–345.

(4) Mehta, O. H.; Barclay, K. L. Perioperative Hypothermia in Patients Undergoing Major Colorectal Surgery. *ANZ J. Surg.* **2014**, *84* (7–8), 550–555.

(5) Aulick, L. H.; McManus, A. T.; Mason Jr, A. D.; Pruitt Jr, B. A. Effects of Infection on Oxygen Consumption and Core Temperature in Experimental Thermal Injury. *Ann. Surg.* **1986**, *204* (1), 48.

(6) Bagnall, N. M.; Vig, S.; Trivedi, P. Surgical-Site Infection. *Surg. Oxf.* **2009**, *27* (10), 426–430.

(7) Kluger, M. J. Body Temperature Changes during Inflammation: Their Mediation and Nutritional Significance. *Proc. Nutr. Soc.* **1989**, *48* (3), 337–345.

(8) Martelli, D.; Yao, S. T.; McKinley, M. J.; McAllen, R. M. Reflex Control of Inflammation by Sympathetic Nerves, Not the Vagus. *J. Physiol.* **2014**, *592* (7), 1677–1686.

(9) Tesch, T.; Bannert, E.; Kluess, J.; Frahm, J.; Hüther, L.; Kersten, S.; Breves, G.; Renner, L.; Kahlert, S.; Rothkötter, H.-J.; others. Relationships between Body Temperatures and Inflammation Indicators under Physiological and Pathophysiological Conditions in Pigs Exposed to Systemic Lipopolysaccharide and Dietary Deoxynivalenol. *J. Anim. Physiol. Anim. Nutr.* **2018**, *102* (1), 241–251.

(10) Walford, R.; Mock, D.; MacCallum, T.; Laseter, J. Physiologic Changes in Humans Subjected to Severe, Selective Calorie Restriction for Two Years in Biosphere 2:

Health, Aging, and Toxicological Perspectives. *Toxicol. Sci.* **1999**, *52* (2 Supplement), 61–65.

(11) Landsberg, L.; Young, J.; Leonard, W.; Linsenmeier, R.; Turek, F. Is Obesity Associated with Lower Body Temperatures? Core Temperature: A Forgotten Variable in Energy Balance. *Metabolism* **2009**, *58* (6), 871–876.

(12) Coyne, M. D.; Kesick, C. M.; Doherty, T. J.; Kolka, M. A.; Stephenson, L. A. Circadian Rhythm Changes in Core Temperature over the Menstrual Cycle: Method for Noninvasive Monitoring. *Am. J. Physiol.-Regul. Integr. Comp. Physiol.* **2000**, *279* (4), R1316–R1320.

(13) Middelkoop, H.; Lammers, G.; Van Hilten, B.; Ruwhof, C.; Pijl, H.; Kamphuisen, H. Circadian Distribution of Motor Activity and Immobility in Narcolepsy: Assessment with Continuous Motor Activity Monitoring. *Psychophysiology* **1995**, *32* (3), 286–291.

(14) Van Veen, M.; Sandra Kooij, J.; Marije Boonstra, A.; Gordijn, M.; Van Someren, E. Delayed Circadian Rhythm in Adults with Attention-Deficit/Hyperactivity Disorder and Chronic Sleep-Onset Insomnia. *Biol. Psychiatry* **2010**, *67* (11), 1091–1096.

(15) Bagheri Hosseinabadi, M.; Ebrahimi, M.; Khanjani, N.; Biganeh, J.; Mohammadi, S.; Abdolahfard, M. The Effects of Amplitude and Stability of Circadian Rhythm and Occupational Stress on Burnout Syndrome and Job Dissatisfaction among Irregular Shift Working Nurses. *J. Clin. Nurs.* **2019**, *28* (9–10), 1868–1878.

(16) Weldemichael, D.; Grossberg, G. Circadian Rhythm Disturbances in Patients with Alzheimer's Disease: A Review. *Int. J. Alzheimer's Dis.* **2010**, *2010*.

(17) Li, S.; Wang, Y.; Wang, F.; Hu, L.; Liu, C. A New Perspective for Parkinson's Disease: Circadian Rhythm. *Neurosci. Bull.* **2017**, *33*, 62–72.

(18) Hymczak, H.; Gołąb, A.; Mendrala, K.; Plicner, D.; Darocha, T.; Podsiadło, P.; Hudziak, D.; Gocoł, R.; Kosiński, S. Core Temperature Measurement—Principles of Correct Measurement, Problems, and Complications. *Int. J. Environ. Res. Public. Health* **2021**, *18* (20), 10606. https://doi.org/10.3390/ijerph182010606.

(19) Tsadok, I.; Scheinowitz, M.; Shpitzer, S. A.; Ketko, I.; Epstein, Y.; Yanovich, R. Assessing Rectal Temperature with a Novel Non-Invasive Sensor. *J. Therm. Biol.* **2021**, *95*, 102788.

(20) Moyen, N. E.; Bapat, R. C.; Tan, B.; Hunt, L. A.; Jay, O.; Mündel, T. Accuracy of Algorithm to Non-Invasively Predict Core Body Temperature Using the Kenzen Wearable Device. *Int. J. Environ. Res. Public. Health* **2021**, *18* (24), 13126.

(21) Kitamura, K.-I.; Zhu, X.; Chen, W.; Nemoto, T. Development of a New Method for the Noninvasive Measurement of Deep Body Temperature without a Heater. *Med. Eng. Phys.* **2010**, *32* (1), 1–6.

(22) Huang, M.; Tamura, T.; Chen, W.; Kanaya, S. Evaluation of Structural and Thermophysical Effects on the Measurement Accuracy of Deep Body Thermometers Based on Dual-Heat-Flux Method. *J. Therm. Biol.* **2015**, *47*, 26–31.

(23) Huang, M.; Tamura, T.; Tang, Z.; Chen, W.; Kanaya, S. A Wearable Thermometry for Core Body Temperature Measurement and Its Experimental Verification. *IEEE J. Biomed. Health Inform.* **2016**, *21* (3), 708–714.

(24) Feng, J.; Zhou, C.; He, C.; Li, Y.; Ye, X. Development of an Improved Wearable Device for Core Body Temperature Monitoring Based on the Dual Heat Flux Principle. *Physiol. Meas.* **2017**, *38* (4), 652.

(25) Fang, J.; Zhou, C.; Ye, X. Optimization of a Wearable Device for Core Body Temperature Monitoring Based on the Dual-Heat-Flux Model. In *IOP Conference Series: Materials Science and Engineering*; IOP Publishing, 2019; Vol. 677, p 032006.

(26) Tokizawa, K.; Shimuta, T.; Tsuchimoto, H. Validity of a Wearable Core Temperature Estimation System in Heat Using Patch-Type Sensors on the Chest. *J. Therm. Biol.* **2022**, *108*, 103294. https://doi.org/10.1016/j.jtherbio.2022.103294.

(27) Panunzio, N.; Marrocco, G. Flexible and Wireless Multi-Sensor Thermometer Based on Dual-Heat-Flux Model. In *2022 IEEE 12th International Conference on RFID Technology and Applications (RFID-TA)*; 2022; pp 29–32. https://doi.org/10.1109/RFID-TA54958.2022.9924064.

(28) Żmigrodzki, J.; Cygan, S.; Łusakowski, J.; Lamprecht, P. Analytical Analysis of Factors Affecting the Accuracy of a Dual-Heat Flux Core Body Temperature Sensor. *Sensors* **2024**, *24* (6), 1887. https://doi.org/10.3390/s24061887.

(29) Kim, T. H.; Zhou, Z.; Choi, Y. S.; Costanza, V.; Wang, L.; Bahng, J. H.; Higdon, N. J.; Yun, Y.; Kang, H.; Kim, S.; Daraio, C. Flexible Biomimetic Block Copolymer Composite for Temperature and Long-Wave Infrared Sensing. *Sci. Adv.* **2023**, *9* (6), eade0423. https://doi.org/10.1126/sciadv.ade0423.

(30) Di Giacomo, R.; Daraio, C.; Maresca, B. Plant Nanobionic Materials with a Giant Temperature Response Mediated by Pectin-Ca $^{2+}$. *Proc. Natl. Acad. Sci.* **2015**, *112* (15), 4541–4545. https://doi.org/10.1073/pnas.1421020112.

(31) Di Giacomo, R.; Bonanomi, L.; Costanza, V.; Maresca, B.; Daraio, C. Biomimetic Temperature-Sensing Layer for Artificial Skins. *Sci. Robot.* **2017**, *2* (3), eaai9251. https://doi.org/10.1126/scirobotics.aai9251.

(32) Costanza, V.; Bonanomi, L.; Moscato, G.; Wang, L.; Choi, Y. S.; Daraio, C. Effect of Glycerol on the Mechanical and Temperature-Sensing Properties of Pectin Films. *Appl. Phys. Lett.* **2019**, *115* (19), 193702. https://doi.org/10.1063/1.5121710.

(33) Huber, B.; Rossrucker, L.; Sundermeyer, J.; Roling, B. Ion Transport Properties of Ionic Liquid-Based Polyelectrolytes. *Solid State Ion.* **2013**, *247*, 15–21.

(34) Dyre, J. C.; Maass, P.; Roling, B.; Sidebottom, D. L. Fundamental Questions Relating to Ion Conduction in Disordered Solids. *Rep. Prog. Phys.* **2009**, *72* (4), 046501.

(35) Plazinski, W.; Drach, M. Binding of Bivalent Metal Cations by α-L-Guluronate: Insights from the DFT-MD Simulations. *New J. Chem.* **2015**, *39* (5), 3987–3994.

(36) Huynh, U. T.; Lerbret, A.; Neiers, F.; Chambin, O.; Assifaoui, A. Binding of Divalent Cations to Polygalacturonate: A Mechanism Driven by the Hydration Water. *J. Phys. Chem. B* **2016**, *120* (5), 1021–1032.

(37) Wang, L.; Kim, T. H.; Costanza, V.; Higdon, N. J.; Daraio, C. Ion Transport in Thermally Responsive Pectin Film. *Appl. Phys. Lett.* **2023**, *123* (2), 021903. https://doi.org/10.1063/5.0142020.

(38) Zhang, Y.; Chad Webb, R.; Luo, H.; Xue, Y.; Kurniawan, J.; Cho, N. H.; Krishnan, S.; Li, Y.; Huang, Y.; Rogers, J. A. Theoretical and Experimental Studies of Epidermal Heat Flux Sensors for Measurements of Core Body Temperature. *Adv. Healthc. Mater.* **2016**, *5* (1), 119–127.

(39) Mao, N.; Song, M.; Pan, D.; Deng, S. Computational Fluid Dynamics Analysis of Convective Heat Transfer Coefficients for a Sleeping Human Body. *Appl. Therm. Eng.* **2017**, *117*, 385–396.

(40) Fitzwater, J. A Comparison of Oral, Axillary, and Temporal Artery Temperature Measuring Devices in Adult Acute Care. *Medsurg Nurs.* **2019**, *28* (1).

(41) Iden, T.; Horn, E.-P.; Bein, B.; Böhm, R.; Beese, J.; Höcker, J. Intraoperative Temperature Monitoring with Zero Heat Flux Technology (3M SpotOn Sensor) in Comparison with Sublingual and Nasopharyngeal Temperature: An Observational Study. *Eur. J. Anaesthesiol. EJA* **2015**, *32* (6), 387–391.

(42) Rubia-Rubia, J.; Arias, A.; Sierra, A.; Aguirre-Jaime, A. Measurement of Body Temperature in Adult Patients: Comparative Study of Accuracy, Reliability and Validity of Different Devices. *Int. J. Nurs. Stud.* **2011**, *48* (7), 872–880.

(43) Edwards, B.; Waterhouse, J.; Reilly, T.; Atkinson, G. A Comparison of the Suitabilities of Rectal, Gut, and Insulated Axilla Temperatures for Measurement of the Circadian Rhythm of Core Temperature in Field Studies. *Chronobiol. Int.* **2002**, *19* (3), 579–597.

(44) Ibrahim, A. A.; Khan, M.; Nnaji, C.; Koh, A. S. Assessing Non-Intrusive Wearable Devices for Tracking Core Body Temperature in Hot Working Conditions. *Appl. Sci.* **2023**, *13* (11), 6803.

(45) Yoshida, A.; Kamon, R.; Naka, T.; Chigusa, N.; Kinoshita, S.; Kawabata, T. Evaluation of Conventional Invasive Measurements and Examination of Non-Invasive Measurement Technique on Human Body Core Temperature. In *IOP Conference Series: Materials Science and Engineering*; IOP Publishing, 2021; Vol. 1137, p 012038.

(46) Filippou, A.; Louca, I.; Damianou, C. Characterization of a Fat Tissue Mimicking Material for High Intensity Focused Ultrasound Applications. *J. Ultrasound* **2023**, *26* (2), 505–515. https://doi.org/10.1007/s40477-022-00746-4.

Chapter 5

HUMIDITY BUFFER MATERIALS TO EXTEND THE LIFETIME OF THIN-FILM TEMPERATURE SENSORS

The work in this chapter is derived from research conducted in collaboration with Valsem Industries. It was funded in part by Valsem Industries and the Center to Stream Healthcare In Place (C2Ship). In particular, I acknowledge the significant contributions by Frédéric Harny and intellectual contributions by Raphael Bingert, JF Daviet, and Chiara Daraio.

N.J.H. participated in the conception and design of this research, developed and characterized the humidity buffer material and contributed to the fabrication of these sensors. N.J.H. also carried out electrical characterization of these sensors, designed the experimental apparatuses and wrote the manuscript.

Note: Due to existing agreements, select technical details are intentionally omitted from the manuscript to protect proprietary information. This chapter utilizes a narrative approach for this reason.

5.0 Abstract

With the development of ionotronic devices, more systems require precise control of humidity within packaging beyond the use of a simple desiccant. Here we explore the challenges of developing thin-film temperature sensors based on $CaCl_2$-HEA-AA due to moisture uptake. We further develop a new class of materials, the humidity buffer material, based on humidity fixed point solutions and demonstrate several variants leveraging lithium chloride. We provide preliminary experimental results for $CaCl_2$-HEA-AA sensors packaged with this novel buffer material and discuss the implications of these results and their potential applications to commercialization of the HEA-AA polymer sensors.

5.1 Introduction

As we move beyond conventional materials such as traditional semiconductors and metals towards ionotronic devices and smart materials, we encounter a new technological challenge.[1–4] Many of these cutting-edge systems contain ion-coordinating polymers, metal salts, or hydrogels, which exhibit high degrees of hydrophilicity. The uptake of water will often affect the behavior of the devices constructed from these materials. Many of these devices require some concentration of water within the hydrophilic material to function necessitating a finer degree of humidity control than has been traditionally required.

For sensors or smart materials designed to respond to humidity, this sensitivity is an advantage. However, for devices intended respond to other stimuli, this presents a challenge. Conventional approaches of packaging dry, baking out, or incorporating a desiccator into the packaging can lead to non-functional devices as the material is fully stripped of water. In concept this could be resolved by packaging the sensors in a highly humidity-controlled environment at a fixed temperature. Provided the water vapor transmission rate (WVTR) is sufficiently low through the packaging for the planned lifetime of the device, this should result in stable consistent devices. In practice this approach is not compatible with industry requirements.[5]

First, many low-cost manufacturing environments lack precise humidity controls during fabrication. Incorporating these controls can greatly increase the cost of fabrication.[6–9] Second, many of the applications for which these devices show promise require flexible devices. Achieving the desired flexibility while maintaining a sufficiently low WVTR is challenging especially if the device is subjected to regular flexion.[10–13] Third, if the device is intended to respond to external stimuli, the packaging must be designed such that the stimuli is not significantly limited by the packaging material. For temperature sensors this is an added challenge as the thermal mass and thermal conductivity of the packaging material can significantly increase the response time of the temperature sensor. Finally, for many applications we are interested in the miniaturization of the sensors. As the sensor size is decreased, the surface area to volume ratio dramatically increases, thus the necessary WVTR is substantially lower for miniaturized sensors which further limits packaging options.

In laboratory studies of these devices, it is common to avoid humidity stability issues by precisely controlling the laboratory / device humidity, see Chapter 3. This is frequently achieved through active electronic control systems. The necessity for active humidity control is prohibitive for low cost devices. For select humidity values, an alternative passive approach has been utilized for over 100 years, saturated salt solutions also known as fixed point humidity solutions (FPS).[14–16] FPS are aqueous solutions containing excess salt beyond the saturation point. Due to salt-driven vapor pressure depression, at a given temperature the vapor pressure of water above the sample is fixed. If the solution is in a sealed container, the humidity in the container above the solution is held at a constant value. If water diffuses out of the container, water from the solution will evaporate and a constant humidity inside the container will be maintained. The evaporation of this water causes more of the salt to crystalize out of the solution. As long as liquid water remains in the container, the concentration of the salt solution remains fixed and the humidity above the solution in the container will remain fixed. If water vapor diffuses into the container, the additional water vapor will be adsorbed into the solution. This will lead some of the excess salt to dissolve. As long as the salt is not fully dissolved, the concentration of the salt solution will remain fixed and the humidity remains fixed. This allows the water-salt mixture to function effectively as a humidity buffer, allowing stable humidities even with a relatively large WVTR for the container/packaging. This approach has been leveraged extensively for laboratory studies and the preservation of museum artifacts.[16,17]

While the FPS approach has been leveraged for a variety of applications, it suffers from some limitations. First, the necessity of exposed aqueous salt solutions directly limits their applicability for any mobile application or any system that may be subjected to tilting. Second, concerns have been raised in the artifact preservation space about the potential of the resulting salt to corrode or damage specimens.[17] One can easily imagine this also presents a large limitation for ionotronic devices. From these limitations, it becomes extremely apparent that while the normal FPS approach works well for laboratory studies, it is not effective for packaged devices.

Alternative humidity / moisture buffer approaches have been explored, especially in the architectural space. Within this field, they have developed a variety of hydrophilic building materials that will adsorb moisture on high humidity days and release it on dry days.[18–20] These are relevant to mention here as they represent another example of a humidity buffer material. While important to discuss here, they typically show too large of a hysteresis of humidities for many ionotronic or smart material devices. The narrow humidity range of the FPS approaches created by leveraging the solid to aqueous phase transition of the salt presents a significant advantage when compared to other approaches.

The effort to make FPS approaches more useful outside of the lab has been pioneered in part by the high-end tobacco industry. Boveda® has several patents for a different approach to leverage FPS in humidors and similar applications.[21–24] Their technology leverages water-salt solutions mixed with a thickening agent to increase the solution's viscosity. This solution is then placed in a flexible waterproof pouch that exhibits a high WVTR. This allows the pouch to function as a small FPS and be placed in a variety of containers without the typical issues associated with FPS solutions. They offer pouches ranging in relative humidity (RH) from 32% - 84%.[25] Several competitors have developed similar FPS based pouch solutions. Of note, Integra Boost® is a competing buffer pouch technology leveraging glycerol/water mixtures instead of salt-based FPS for the range of 55%-84% relative humidity.[26] While these commercial products open doors for consumer humidity control, they exhibit limited utility for devices. First, they offer a highly limited range of available humidities. Many devices may require different humidity ranges. Second, they still represent bulk solution approach that will cause significant issues for devices subjected to vibrations, tilting, or bending. Under these cases the shifting water may introduce shifting internal mass effects on the device, in addition to probable device failure if the pouch fails. Furthermore, this architecture has fundamentally limited utility for miniaturized devices, microfabricated devices, and thin-film devices due to the limitations of using a bulk material approach. We find the FPS approach is a powerful tool leveraging fundamental physical chemistry that has demonstrated commercial applications, however the architecture of current FPS approaches inherently limits their utility for devices.

In this chapter, we will explore a novel class of FPS materials which leverage small droplets of a lithium chloride FPS embedded within a polymer matrix exhibiting a high WVTR. We believe that the structure of this humidity buffer material (HBM) resolves many of the issues in current FPS approaches. This material has been shown to function as an effective humidity control and can be fabricated through several processes depending on the demands of device fabrication. We will explore this material through the lens of attempts to fabricate thin-film HEA-AA temperature sensors.

$CaCl_2$-HEA-AA is an ionotronic copolymer which exhibits a record-breaking temperature response.[27] It has been proposed as a sensing material for applications ranging from IR imaging, core body temperature measurement, and temperature mapping. It has shown promise in laboratory studies; however, this material correspondingly exhibits an extremely high degree of sensitivity to environmental humidity.[27] Therefore, it requires high performance packaging which is difficult to achieve given the different demands of these sensing applications.

In collaboration with Valsem Industries, we have been attempting to develop roll-to-roll fabricated thin-film $CaCl_2$-HEA-AA temperature sensors. In this chapter we will explore the efforts to develop these sensors, the opportunity of buffer material to stabilize the sensors, and current challenges in their fabrication. Note – due to existing agreements, select technical elements will be excluded to ensure the protection of proprietary information.

5.2 Challenges with the $CaCl_2$-HEA-AA Material

The HEA-AA polymer represents a breakthrough in near room temperature sensing. It's sensing mechanism is reliant on ion-hopping from bound coordination sites. This leads to a near Arrhenius relationship between current and temperature. While this ion-hopping mechanism leads to a large temperature response (>800 from 25 ° - 65 °C), the corresponding conductivity of the material, especially at low temperatures, is extremely low. Due to challenges of this material, a concrete value for the resistivity has not been evaluated experimentally, however, we estimate it as above 1.14 x 108 Ohm * m at 1 Hz and ~ room temperature. This value was obtained from thin film sensors discussed in this chapter where we suspect errors in the electrode distance and the phase values imply that the films are not properly dried. These low conductivities present us with two options if we wish to reliably measure the temperature with low-cost electronics, first, the distance between electrodes can be minimized to reduce the length of the current path. Second, the area of the electrodes can be increased, increasing the cross-sectional area of the conducting polymer. This can lead to unusual architectures.

Second, while the polymer exhibits a high sensitivity to temperature, it exhibits a similarly impressive and exponential response to environmental humidity in the 5-20% humidity range which is optimal for temperature sensing. At 10% relative humidity, a ~1% change in relative humidity can drive a ~10% change in experimental current. This sensitivity is extraordinary and represents a significant challenge in developing stable sensors. Of note however, due to the hydrophilic nature of the polymer a 1% relative humidity change does not correspond to a 1% change in the water content of the polymer. Attempts to precisely characterize the hydrophilic nature of the polymer leveraging quartz microbalances have been inconclusive, further studies leveraging IR spectroscopy are in the planning stages to fully understand how relative humidity corresponds to the polymer's internal hydration level. Without having this understanding, we are limited to crude toy models to aid in the design of the packaged sensors and have to use approximate relative humidity changes as a guide for engineering decisions.

The final challenge also originates from the ionotropic nature of the HEA-AA sensors. With conventional thermistor sensors, a DC current readout is easily constructed. However, with HEA-AA sensors, an AC current must be used due to the blocking electrode effects.

5.3 Preliminary Work on Thin-Film HEA-AA Sensors

In order to evaluate the viability of HEA-AA thin-film sensors, a simplified test architecture was fabricated at Valsem Industries (Fig. 5.1). A strip of PET tape (50 um thick with silicone adhesive) with a 16mm circular hole punched out was applied to an Al sheet with a protective polymer film adhered to the backside. $CaCl_2$-HEA-AA was applied to the sensing region (the circular hole in the PET tape applied to the Al sheet) utilizing a Mayer rod to apply a smooth uniform thickness film. The film thickness largely determined by the spacer used. The film was then dried for various lengths of time at a set temperature in an oven. The top sheet was prepared using a second piece of the same protected Al sheet material. A circular punch out of tape was applied to the top sheet as a stencil for the glue application. This stencil prevented glue from being applied to the region of the Al top sheet that would be in contact with the active region of the sensor fabricated on the bottom sheet. An adhesive was applied to the Al top sheet utilizing a Mayer rod and allowed to dry to tackiness. The bottom sheet and top sheet were manually aligned then pressed together. The packaged sensor was then transferred to a hydraulic press and allowed to cure overnight. Electrical properties of the sensors were then characterized utilizing an impedance analyzer (Zurich Instruments MFIA 500 kHz). The sensors were held on a copper plate placed on a hot plate. A weight with a foam base was placed on the sensor to ensure even pressure across the sensing region. While this improves the electrical contacts, it leads to a large thermal mass during measurements which is especially apparent in temperature step experiments. The temperature was monitored through a thermistor coupled to a Circuit Playground Express and logged through the serial connection. Due to system noise, the temperature measurements were processed using a boxcar average.

Temperature step measurements of the thin-film sensor show a large temperature response (Fig. 5.2(a)). It has been observed previously within the lab that there is a correlation between the slopes of the current measurements and the phase with the hydration degree of the polymer. At high hydration levels the polymer tends to show a phase increase with a current increase. While at low hydration levels, the polymer tends to show a phase decrease with a current increase. This can be seen in the detailed high humidity phase data in Fig 5.3.a. From this we conclude that the phase response of the thin-film sensor is inline with the polymer in a high hydration state (Fig. 5.2(b)). We speculate this may originate from trapped water or solvent from the casting process. This explains the low temperature response of the thin film sensor compared to the laboratory measurements of $CaCl_2$-HEA-AA (Fig. 5.3(c)). While the response from the thin film sensor is disappointing relative to previous work with the $CaCl_2$-HEA-AA system, the response still outperforms other cutting edge temperature sensing materials.[28–30]

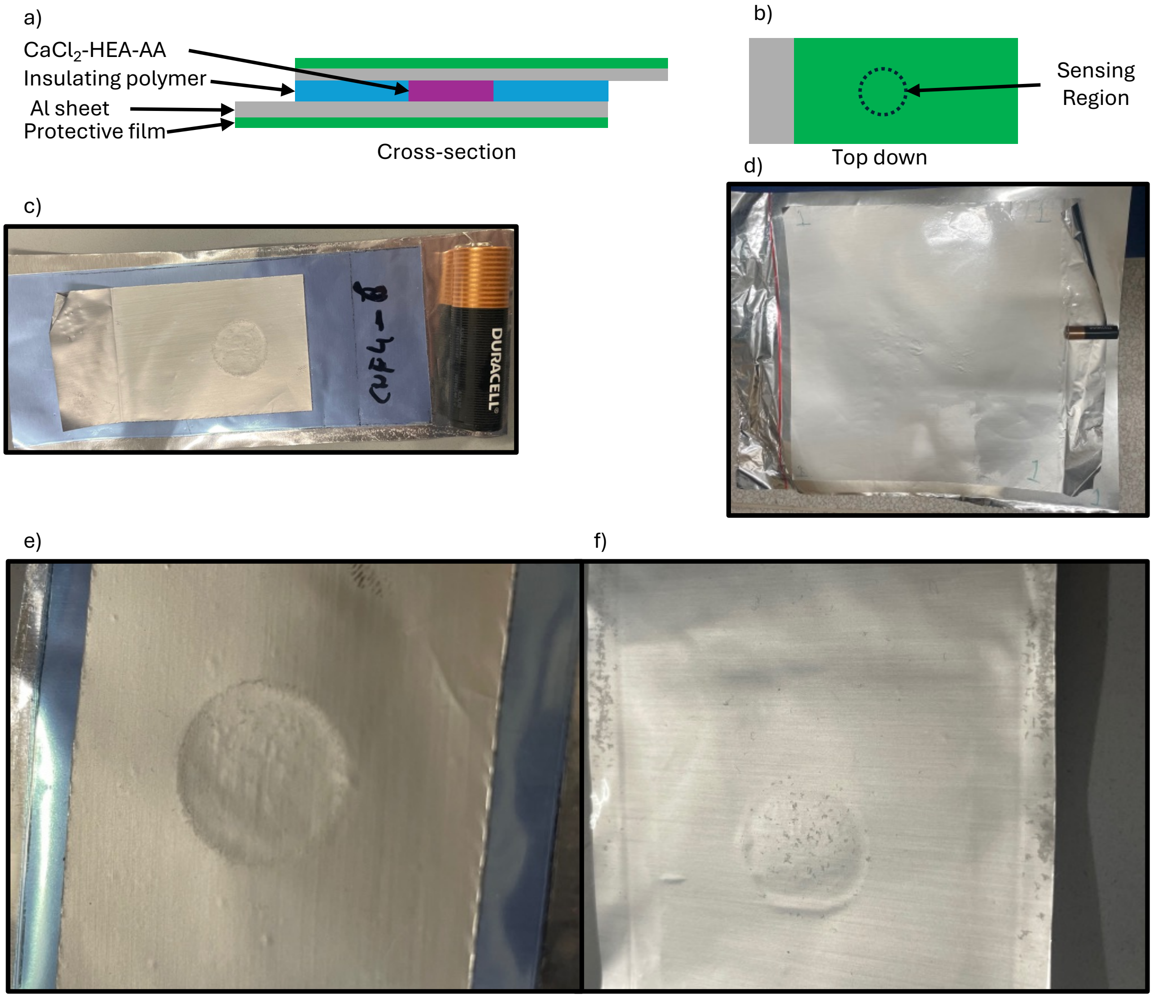

Figure 5.1: Simple HEA-AA thin-film sensors prepared at Valsem Industries. (a) Cross-section few of sensor architecture. (b) Top-down view of sensor architecture. (c) Initial prepared thin-film

sensors. (AA battery for scale) (d) Large sheet thin film sensors prepared to limit the potential role of between sheet water diffusion. Notice bubbling in the sheet away from the sensing region, this occurred after humidity exposure. (AA battery for scale) (e) Top of the thin-film sensor showing degradation of the Al sheet at the polymer sensing region. (f) Bottom of the thin-film sensor showing degradation of the Al sheet at the polymer sensing region and edges of the sheet not sealed from the environment.

In-order to design effective commercial sensors, the resistivity of the sensing material is a critical design parameter. Here we will estimate a floor temperature vs resistivity measurement for the system (Fig 5.2.d). This represents a floor value for the following reasons: 1) We believe that the polymer is in a hydrated state, this leads to a reduction resistivity of the material. 2) The calculation of the resistivity is dependent on the thickness of the HEA-AA film. In the calculations, we assume the HEA-AA film is fully filling the cylindrical cutout in the insulating polymer. However, due to the reduction in film thickness as the solvent evaporates, the HEA-AA film does not fully fill the cutout, thus the electrode spacing is less than what was used in the calculations. This can be seen visually in Fig. 5.1. Due to the viscoelastic flow of the polymer film the thickness difference cannot be measured with traditional thin-film processes. Because we are unable to accurately measure the final thickness of the film, we instead evaluate the minimum resistivity of the material, we suspect the effective resistivity of optimized commercial sensors may be more than an order of magnitude higher when higher quality devices are fabricated.

Preliminary experiments with these thin-film sensors showed significant sensor drift depending on the environmental humidity. In-order to eliminate lateral diffusion between sheets of the sensor, a large sheet sensor was developed (Fig 5.1.d) . The sealed region was expanded to an A4 sheet size (21 cm x 29.7 cm) while maintaining a 16mm sensing region in the center of the sheet. For these sensors the PET tape was replaced with a PET film adhered in accordance with Valsem Industries practices.

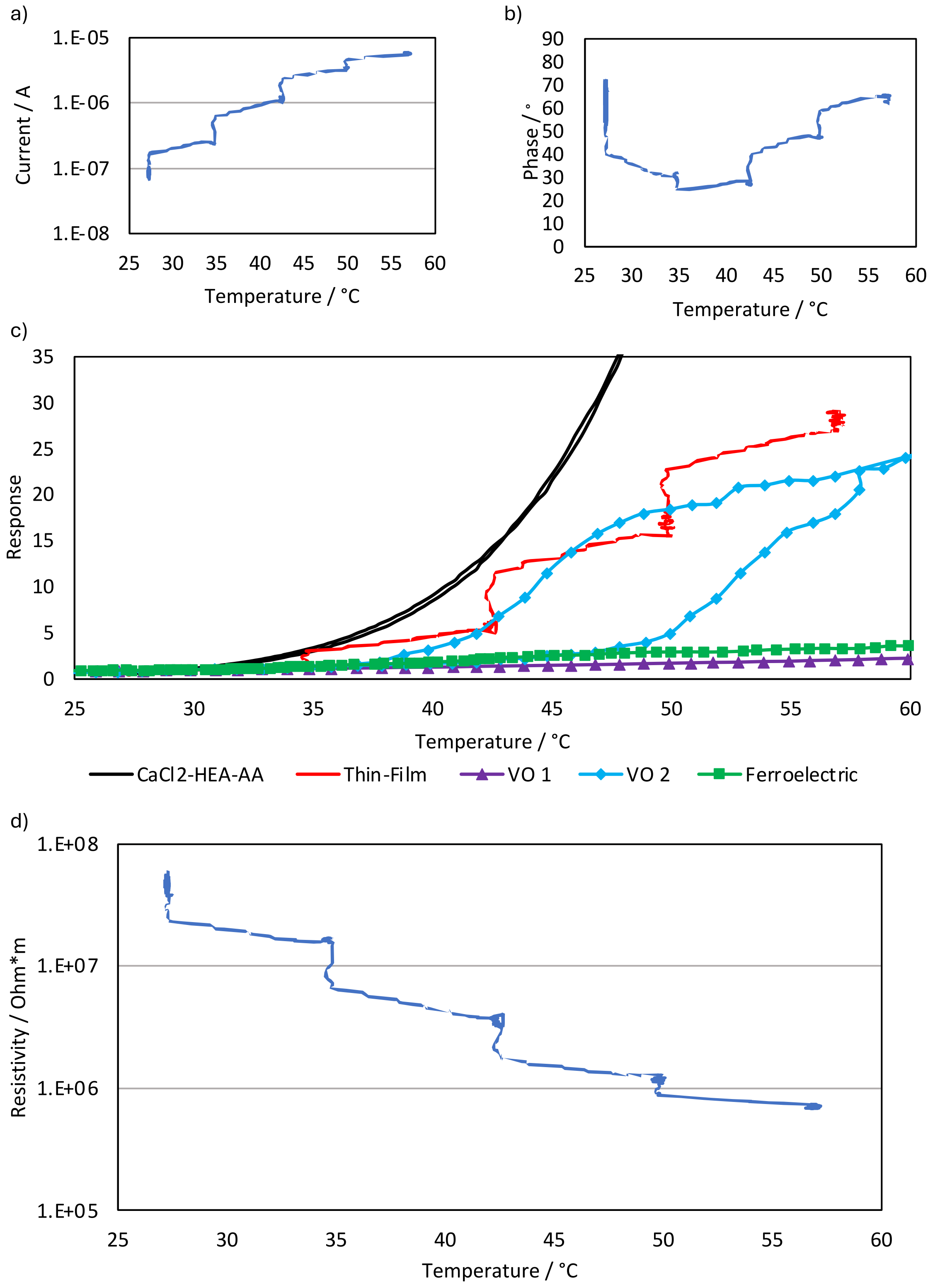
a)
1.E-05
1.E-06
1.E-07
1.E-08
Current / A
25 30 35 40 45 50 55 60
Temperature / °C
b)
90 80 70 60 50 40 30 20 10 0
Phase / °
25 30 35 40 45 50 55 60
Temperature / °C
c)
35 30 25 20 15 10 5 0
Response
25 30 35 40 45 50 55 60
Temperature / °C
CaCl2-HEA-AA
Thin-Film
VO 1
VO 2
Ferroelectric
d)
1.E+08
1.E+07
1.E+06
1.E+05
Resistivity / Ohm*m
25 30 35 40 45 50 55 60
Temperature / °C

Figure 5.2: Electrical characterization of thin-film sensor undergoing temperature steps measured at 1V and 15Hz. Lag effects are hypothesized to originate from the large thermal mass of the setup. (a) Temperature vs current. (b) Temperature vs phase. The shape of this graph implies the sample is at a fairly hydrated state. (c) Response of the thin film sensor vs the response of laboratory measurements of $CaCl_2$-HEA-AA at 20% RH and 14.16Hz. The response is significantly lower, again we attribute this behavior to a high hydration state of the polymer. While its performance is less than laboratory measurement of $CaCl_2$-HEA-AA, it is competitive with other cutting edge temperature sensing materials (VO 1,[29] VO 2,[28] Ferroelectric[30]). (d) Calculated resistivity vs temperature curve for the thin-film sensors. See main text for discussions of the flaws of these measurements.

In order to characterize the electrical properties during humidity exposures, electrical properties were monitored at 10Hz and 1V utilizing the Analog Devices CN0359 Eval Board. The sample was placed on an elevated platform in a plastic tub, the base of the tub was filled with water creating a pseudo high humidity chamber. After an appropriate interval the sample was removed from the chamber and the water was removed from the chamber. The chamber was then purged with dry N_2 and the sample replaced. After an appropriate time interval the N_2 purge was stopped and water was reintroduced to the chamber. This allowed us to reliably vary the chamber humidity between $< 10\%$ and $\geq 89\%$ RH. Humidity and temperature in the chamber was monitored through a SensorPush HT1 Smart Temperature Sensor and Humidity Sensor.

The results of the humidity trials demonstrated significant response of the sensor to the environmental humidity (Fig. 5.4). In high humidity, the measured conductivity is seen to increase. In low humidity the measured conductivity is seen to decrease. This indicates that the sensor is not well isolated from the environmental humidity. Further trials both at Caltech and Valsem Industries demonstrate the same trends.

5.4 Engineering Challenges Discovered from the Thin-Film Sensors

1) First and foremost, current packaging for the thin-film sensors has been found to not effectively protect the sensors from the environmental humidity. Improved packaging or passive humidity control is needed to produce stable, reliable sensors.

2) The sensors must be packaged / dried under a known controlled humidity for this architecture to work. This presents a significant fabrication challenge.

3) Select corrosion of the Al film is seen in the region in contact with the polymer (Fig. 5.1(e-f)). This corrosion presumably affects the electrical properties of the electrode and thus the sensor. This may also lead to an increase in the WVTR of the packaging if the material is compromised.

4) Due to the large area of the sensing region, it was observed that the electrical properties of the films change when the films are bent. This can lead to changes in the conductivity/phase of the signal from the sensor or the establishment of a shorting condition between the electrodes. We suspect this can be resolved in two manners. First, by reducing the size of the sensing region, the electrodes should be better held in contact with the polymer and the radii of curvature of the film relative to the size of the sensor region should increase. Second by maintaining the polymer in a drier state, the viscoelastic flow should be reduced which in turn should minimize changes in the effective shape of the sensor.

5) In attempting to fabricate thinner films by reducing the thickness of the insulating polymer, it was found that these sensors frequently shorted. This has preliminarily been attributed to clumping as the film dries leading to voids. Furthermore, as noted above, the polymer does not fully fill the spacer region which presents a fabrication challenge. We believe this can be resolved by adjusting the viscosity of the casting solutions and/or the casting solvent.

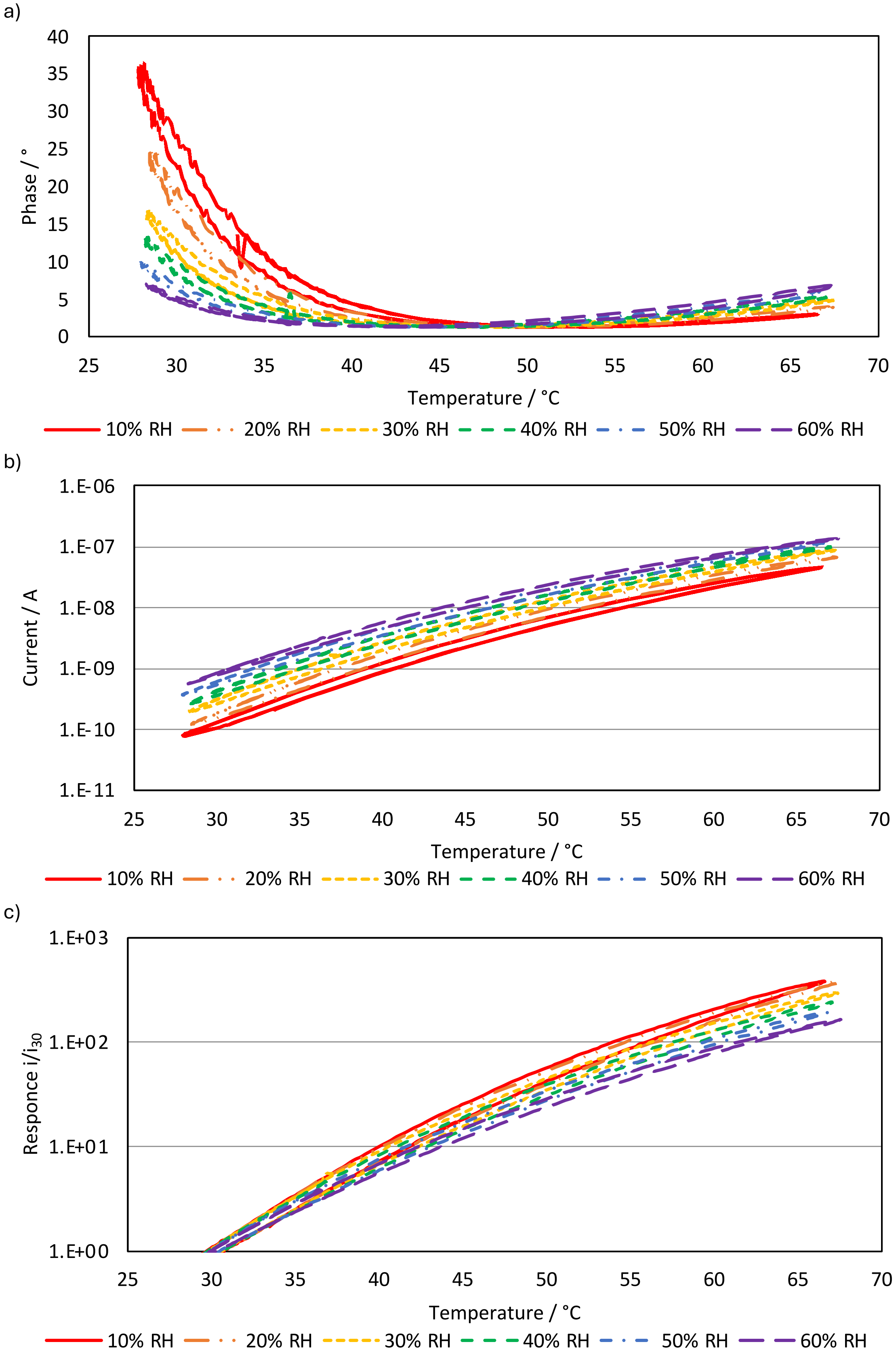
a)
Phase / °
40
35
30
25
20
15
10
5
0
25
30
35
40
45
50
55
60
65
70
Temperature / °C
10% RH
20% RH
30% RH
40% RH
50% RH
60% RH
b)
Current / A
1.E-06
1.E-07
1.E-08
1.E-09
1.E-10
1.E-11
25
30
35
40
45
50
55
60
65
70
Temperature / °C
10% RH
20% RH
30% RH
40% RH
50% RH
60% RH
c)
Responce i/i30
1.E+03
1.E+02
1.E+01
1.E+00
25
30
35
40
45
50
55
60
65
70
Temperature / °C
10% RH
20% RH
30% RH
40% RH
50% RH
60% RH

Figure 5.3: $CaCl_2$-HEA-AA electrical characterization from 10%-60% relative humidity. (a) Temperature vs phase at various humidities. At high humidities an increase in temperature leads to an increase in phase. (b) Temperature vs current at various humidities. (c) Current response relative to the current at 30 °C.

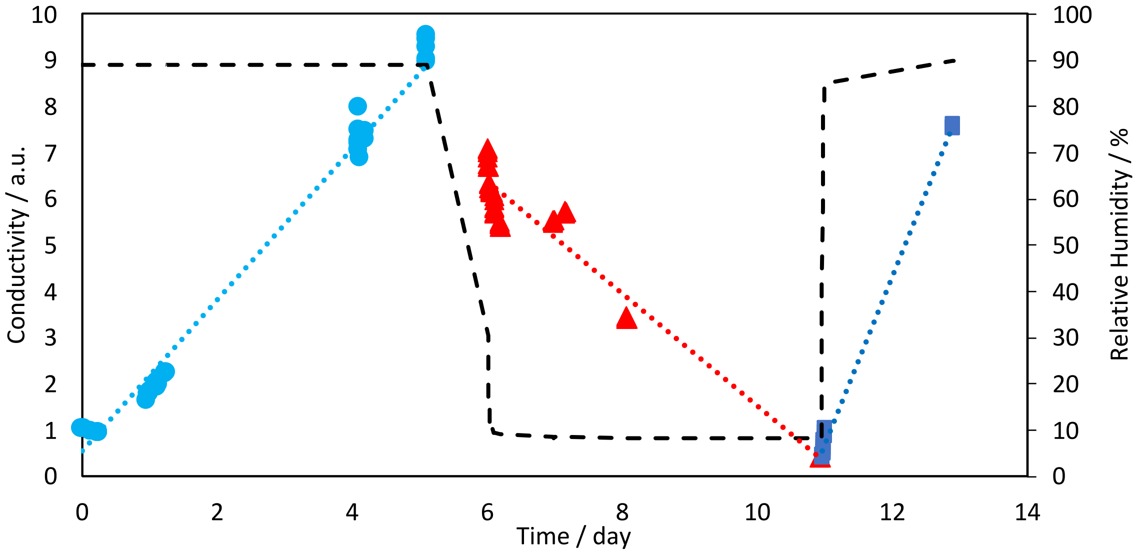

Figure 5.4: Humidity stability testing of large sheet thin-film sensor. Sample was initially exposed to a high humidity, at that time it is observed that the conductivity increased. The sample was then exposed to a low humidity and the conductivity decreased. When the sample was then exposed to a high humidity, the conductivity increases again. This demonstrated compellingly that the humidity sealing in these sensors is insufficient for reliable device performance.

5.5 Architectures of thin-film HEA-AA sensors

As discussed above, the thin-film sensors fabricated to date suffer from several significant challenges, beyond those discussed, this architecture is limited to a single pixel per sensing sheet. In this section we will discuss sheet architectures that limit these issues and may allow for easier commercialization of this technology. Furthermore, we discuss the design challenges and parameters that must be evaluated to produce viable sensors.

5.5.1 Electrode Architecture

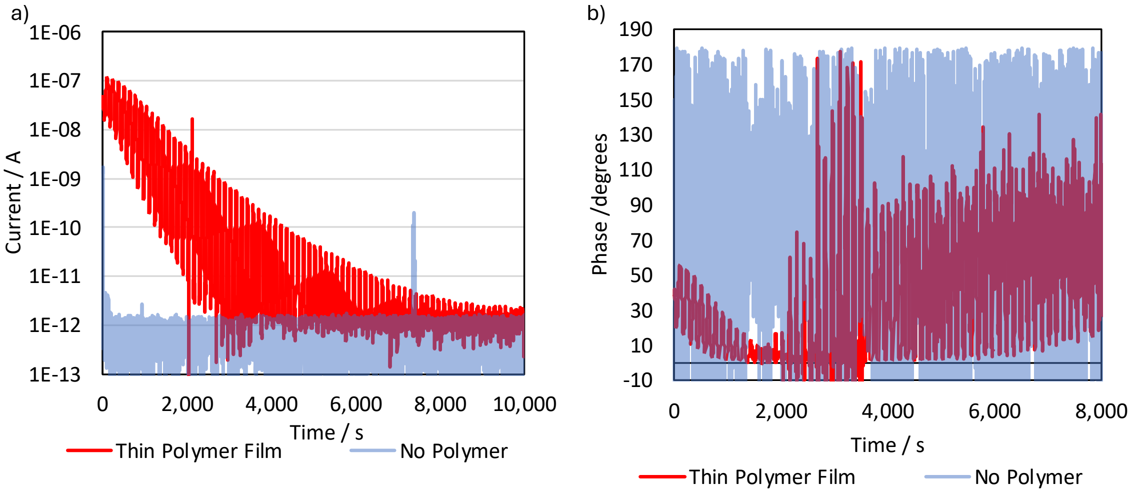

Figure 5.5: Temperature cycling experiment on thin samples of $CaCl_2$-HEA-AA measured on circular interdigitated electrodes compared to a sample without any polymer film. (a) Current data showing as the polymer dried, the conductivity merged with the floor noise. (b) Phase data showing as the current reaches the noise floor the measured phase stops providing meaningful data

One core challenge in designing these sensors, and the corresponding readout circuitry is their high resistivity. This can lead to low signal intensities relative to the noise inherent in any experimental setup. This has been directly measured utilizing a thin polymer sample cast onto a circular interdigitated electrode. The sample was then subjected to temperature cycling between ~65 °C and ~25 °C in 5% RH measured at 1V and 1Hz (Fig. 5.5). As the sample dries the low temperature measurements start to reach the noise floor (~1 pA) seen when no polymer is applied to the circular interdigitated electrodes. At a similar time, the measured phase starts fluctuating wildly as the impedance analyzer is unable to measure the signal.

This can be resolved in two ways. First the measurement frequency can be increased. However as discussed in Chapter 3, and shown in Fig. 5.6, increasing the frequency significantly decreases the current response thus decreasing the sensitivity to temperature. For $CaCl_2$-HEA-AA, the phase response is optimal at 100 Hz, for this and other reasons, phase readout is potentially more viable for commercial sensors.

The second way in which the low conductivity of the HEA-AA material can be resolved is by varying the architecture of the sensors. In a simple parallel plate sensor, there are two parameters which directly vary, the surface area of the electrodes A, and the distance between the electrodes D. The current is then governed by $I \propto A/d$. For the thin film sensors demonstrated earlier, this leads to large diameter sensors with a minimum insulating layer thickness with an A/d of approximately 4.

We can increase the conductivity of the sensors by increasing the area of the sensing region. This however has several trade offs. First, increasing the area of the sensing region reduces the ability of the sensor to measure small point sources resulting in as any temperature gradients across the sensor being averaged out in the signal. Second, as the sensors grow larger, they will be subjected to additional strain when the films are bent to the same radii of curvature. As the HEA-AA polymer in this form is more brittle than the block copolymer discussed in Chapter 2, high strains could damage the sensing material. This limits the utility of this approach for conformal mapping applications and may produce issues for sensors fabricated and stored on rolls. In addition, variability in materials properties tend to increase as the sensor active region increases unless tighter fabrication controls are used, limiting the practical size of commercially viable sensors with this architecture utilizing this material.

An alternative architecture change to increase the conductivity of the sensors is to decrease the distance, d, between the sensors. To date this approach has led to issues with the sensors undergoing shorting during handling or fabrication. We believe these issues can be resolved with improved manufacturing processes. As discussed in greater detail later in this chapter, this approach to increasing the conductivity of the sensors come at a direct cost regarding long-term humidity stability.

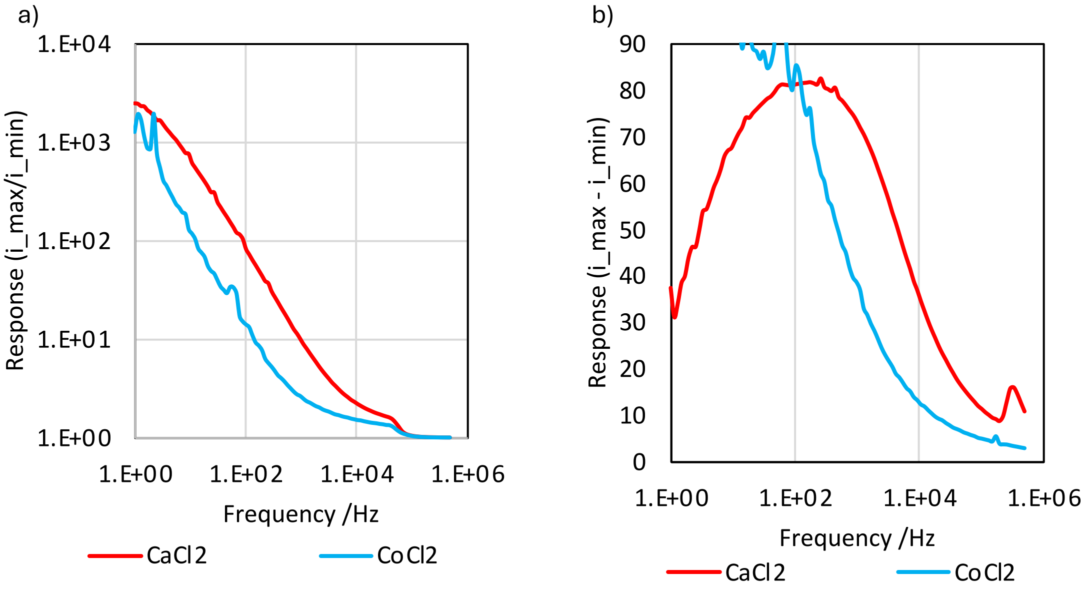

Figure 5.6: Response spectra from ion-HEA-AA subjected to temperature sweeps (~25 °C – ~65 °C) at 5% RH. (a) Current response showing as frequency is increased, the current response dramatically decreases. (b) Phase response showing that $CaCl_2$-HEA-AA shows a peak phase response at ~ 100 Hz while for $CoCl_2$-HEA-AA, the phase response decreases as the frequency increases.

5.5.2 Protecting Electrodes Through Capacitive Measurement

In addition to humidity sensitivity, electrode degradation was a significant issue observed for our experimental thin-film sensors. We believe this degradation is driven by chloride-ion saturated water in direct contact with the aluminum electrodes. Aluminum is frequently discussed as a material that self-limits corrosion due to the formation of aluminum oxide thin films. Unfortunately, in the presence of chloride ion solutions, the chloride ions can disrupt the aluminum oxide film and cause corrosion.[31] Due to the hydrophilic nature of $CaCl_2$-HEA-AA it preferentially exists in a hydrated state that readily corrodes aluminum. One approach to eliminate this corrosion mechanism is to operate the sensors in a capacitive mode instead of a conductive mode.

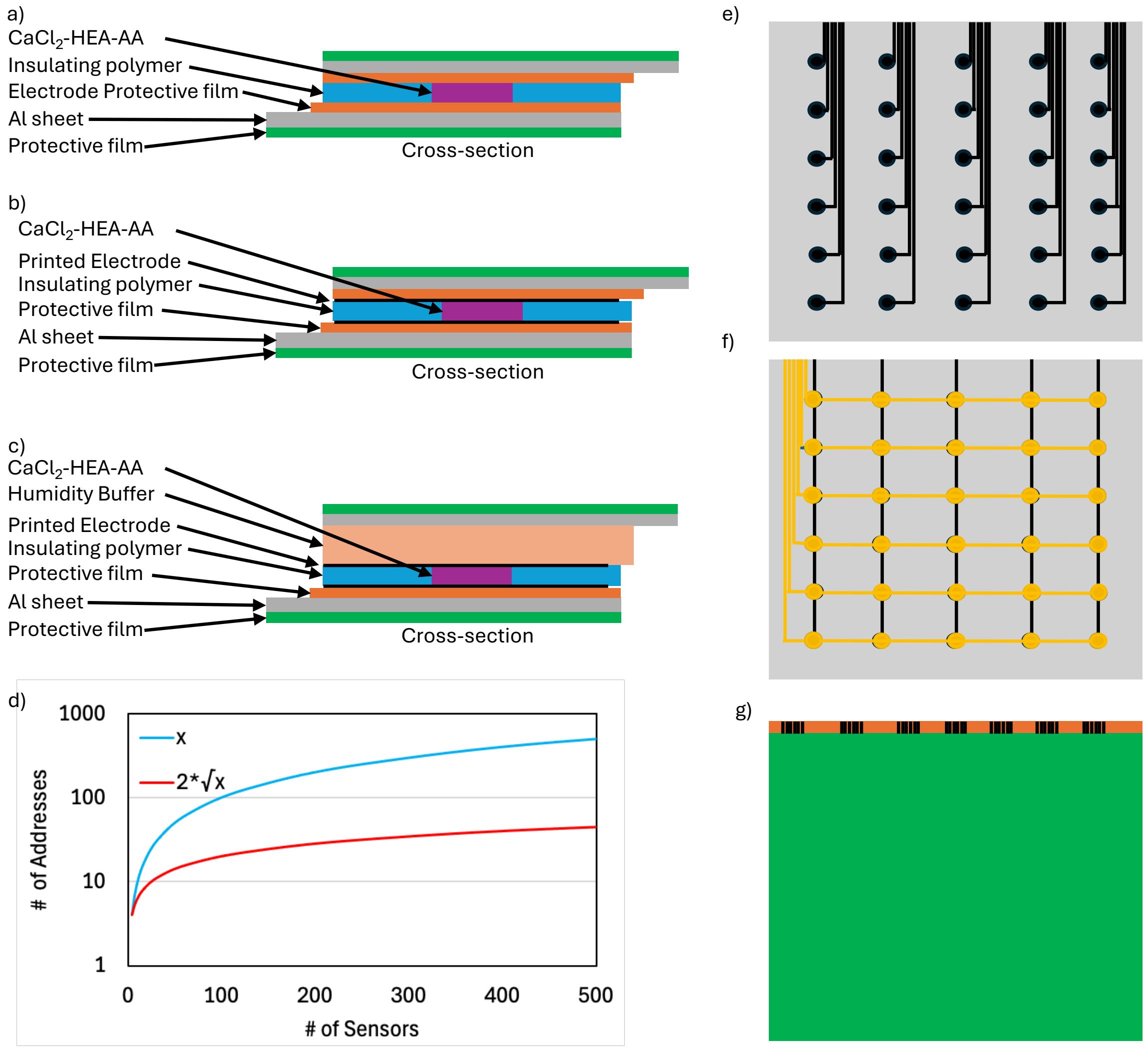

Figure 5.7: Sensor architectures for thin-film sensors. (a) Capacitive thin-film sensor protecting the electrode from corrosion. (b) Sensor leveraging printed electrodes to allow for multiple pixels per sheet. These could be produced as either conductive or capacitive sensors. (c) Proposed architecture for thin-film sensor leveraging the new humidity buffer material. (d) Comparison of number of readout addresses per sensor for individual pixel readout with common signal in (x) and row-and-column readout (2*√x). (e) Electrode layout for common signal-individual pixel readout. (f) Electrode layout for row-and-column readout. (g) Electrical connections at the edge of the fabricated sheet.

Capacitive sensing is an established approach in analytical chemistry for monitoring the conductivity of solutions.[32,33] This allows measurement of potentially electrode damaging samples without any exposure of the electrodes to the samples. However, for this approach, the measurement typically must occur at elevated frequencies due to it being reliant of capacitive coupling between the sample and the electrodes. For our applications, this presents a challenge as the temperature current response decreases with increasing frequency. This again is a case where phase readout of the sensor is potentially more useful than the current readout. For the $CaCl_2$-HEA-AA sensors, the optimal phase measurement frequency is ~ 100 Hz. We can imagine utilizing an extremely thin protective film (~10 μm) over any electrodes (Fig. 5.7(a)). Preliminary experiments performed at Valsem Industries demonstrated that this architecture can produce temperature responsive sensors. Further work needs to be done to optimize this approach and quantify the trade offs of using capacitive sensors vs conductive sensors.

5.5.3 Multiple Sensors Per Sheet – Electrode Printing

In order to have multiple sensors per sheet, we must move away from utilizing the humidity protective Al sheets as the electrodes. To facilitate roll-to-roll fabricated sensing sheets, we have to move to printed electrodes. By leveraging rotary printing and conductive inks (silver, carbon, etc.), we can pattern electrodes during standard roll-to-roll fabrication.

The selection of appropriate trace dimensions and ink material requires us to evaluate briefly the readout circuitry. As we vary the trace dimensions and the trace material, the impedance of the circuitry changes which can directly affect the current response of the sensors. The relevant parameter is the impedance of the sensing material vs the impedance of the readout electronics. The portion of the readout electronics that exhibits the highest impedance is the individual printed traces. Here we review various commercially available conductive Inks from LOCTITE® (table 5.1) assuming a 25 μm trace thickness. For this application we are assuming the trace length is ~ 1m, in line with the width of standard sheets. To evaluate these impedances vs the $CaCl_2$-HEA-AA sensing material, we can extract the minimum resistances from the previous thin-film experiments (Fig 5.8.a). As previously discussed, these represent the minimum resistances given the polymer was in a hydrated state during measurement. We can observe these sensors will exhibit a resistivity greater than 1 MΩ for any reasonable A/d ratio (Fig. 5.8(a)) at 30 °C. By constructing a simplified model of three resistors in series, we can observe how the measured response varies as we compare the resistance of the readout circuitry to the resistance of the sensing material. We can quickly observe that if the resistance of the readout circuitry is < 0.1 of the sensing element's high temperature resistance, the current response is not significantly degraded (Fig. 5.8(c)). At the temperature of 55 °C the minimum resistance ranges from ~755 kΩ to ~47kΩ for A/d ratios of 1-16 with a resistance of 19 kΩ at an A/d of 4. Therefore, the maximum trace resistance ranges from 37 kΩ to 2.4 kΩ. By evaluating from table 5.1, we can see that only one carbon ink is sufficiently conductive for this application, and it can only function for A/d ratios < 2. For this reason, we are limited to silver ink materials. There remain concerns about the relatively high costs of silver inks. However, given the low-density coverage, the cost of electrode printing remain relatively low even with expensive ink.

Table 5.1: Performance of LOCTITE® Conductive Inks at a Thickness of 25 µm[34]

Ink type	**Ink**	**Ω / sq**	**Ω 1m x 0.5mm**	**Ω 1m x 0.1 mm**	**€ / m^2**	**€ / 1m x 0.5mm**	**€ / 1m-0.1mm**	**€ / 10 mm pad**
Carbon	ECI 7007 E&C	10	2.0E+04	1.0E+05	€ 13	€ 0.01	€ 0.00	€ 0.00
Carbon	EDAG 6017SS	35	7.0E+04	3.5E+05	€ 91	€ 0.05	€ 0.01	€ 0.03
Carbon	EDAG 423SS	33	6.6E+04	3.3E+05	€ 108	€ 0.05	€ 0.01	€ 0.03
Silver	ECI 1010	0.0057	1.1E+01	5.7E+01	€ 119	€ 0.06	€ 0.01	€ 0.04
Silver	ECI 1006	0.021	4.2E+01	2.1E+02	€ 311	€ 0.16	€ 0.03	€ 0.10
Silver	ECI 1001	0.017	3.4E+01	1.7E+02	€ 363	€ 0.18	€ 0.04	€ 0.11
Silver	ECI 1016 E&C	0.006	1.2E+01	6.0E+01	€ 501	€ 0.25	€ 0.05	€ 0.16

The electrical conductivity data of the ink may not be the only factor that needs to be taken into consideration. We have speculated – however not tested, that silver inks may suffer from significant electrode corrosion by $CaCl_2$-HEA-AA during long term use. This degradation may mandate capacitive sensors as discussed above thus increasing the inherent impedance of the readout circuitry. Alternatively, carbon inks should not be susceptible to degradation by the $CaCl_2$-HEA-AA material thus eliminating the necessity of the protective film.

Regarding the electrical conductivity, these measurements of the $CaCl_2$-HEA-AA material's resistivity were conducted when the material was at a significantly hydrated state and with an unknown uncertainty in the film thickness. For this reason, the resistance of higher quality sensors likely will be significantly higher allowing for utilization of less conductive inks.

5.5.4 Row-and-Column Readout vs Common Signal

For multi-pixel sheets, it is necessary to consider how electrodes will be connected in the architecture. A relatively standard approach is row-and-column readout (Fig. 5.7(f)), in which rows of top electrodes are connected and columns of bottom electrodes are connected.[35–37] This has the direct benefit of allowing for individual pixels to be easily addressed by providing signal to a specific row and carrying out readout on a specific column. This becomes a highly scalable addressing approach as the number of sensors individually readable, x, only requires $2*\sqrt{x}$ addresses accounting for addressing of the input signal and the readout signal assuming square arrays. While promising, this approach suffers from a significant challenge for roll-to-roll fabrication. It requires the precise alignment of the top and bottom electrodes.

In order to address the alignment issue, a second approach was proposed. By providing the input signal to one of the Al sheets, the signal can be distributed to all pixels at once. As the sheet resistance of a 10 μm thick Al sheet is only 2.8×10-3 Ω / sq at 20 °C, the signal can be readily distributed across a large sensing sheet. This architecture eliminates this alignment challenge for these structures, note select other alignment issues remain in the fabrication of these multi-pixel sheets.

While simplifying fabrication, this common signal approach suffers from two significant issues, the coupling between the sheet and the circuit, and addressing each pixel. Depending on the dielectric effects of the insulating polymer vs the electrical properties of the sensing polymer, the additional coupling between the sheet and the traces may be significant. Additionally in this architecture, each pixel must have a an individual electrical address (Fig.

5.7(e)). For small sheets, this is manageable, however, as the number of sensors increases this becomes prohibitive and we recommend the row and column readout approach (Fig. 5.7(d))

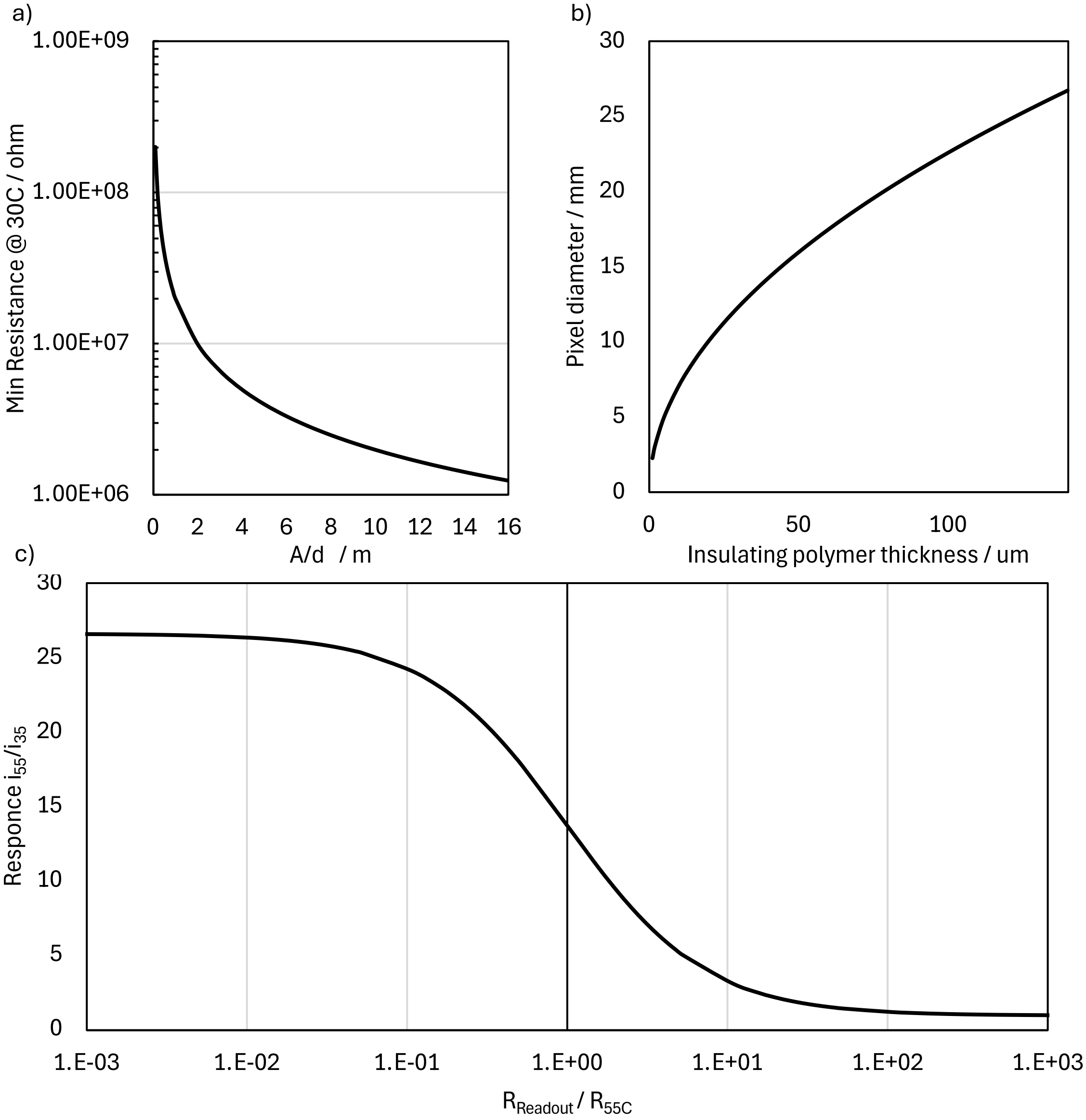

Figure 5.8: Electrical properties based on prior thin-film sensors. (a) Minimum sensor resistance at 30 °C vs the sensor's A/d ratio. (b) Pixel diameter vs insulating polymer thickness for a A/d ratio of 4. (c) Current response from 30 °C – 55 °C for differing relative resistance in the readout circuitry. When the ratio is exceeds 0.1, the measured response significantly decays.

5.5.5 Adding Flexibility to the Electrode Alignment

In the simplified drawings of the sensors, we typically assume the diameter of the sensing material is the same as the diameter of the electrodes. This however presents a significant alignment challenge in aligning the electrodes to the cutouts in the insulating polymer. A solution to this approach is to make the cutouts slightly larger (1-3mm) than the diameter of the electrodes. While this approach increases the amount of sensing material needed for the sheets, it reduces the necessary alignment of the electrodes to achievable degree and the alignment can be verified during QC testing of the sheets.

5.5.6 Electrical Readout from the Sheets

Electrical connection to roll-to-roll fabricated sensors presents an interesting challenge. For this application we propose that the sheets be aligned such that electrical connections can be directly made at the edge of the sheets to printed electrodes. These connections can be made with standard connectors used for printed electronics.

5.6 The Mathematical Challenges of Sealing this Architecture

The high degree of humidity sensitivity seen in the before detailed thin-film sensors significantly surprised the authors as the WVTR of the materials was extremely low. To help further understanding of these results, a mathematical evaluation of this architecture was undertaken. This presented a unique challenge as while the relative humidity vs the current is well characterized for the polymer, due to its hydroscopic nature of $CaCl_2$-HEA-AA, the relation between relative humidity and g_{water} / $g_{polymer}$ remains unknown. To simplify this evaluation we will assume the polymer is not present between the electrodes and evaluate the change in relative humidity of this void. We will further assume a cylindrical chamber with diffusion only occurring through the electrodes, thus assuming that the inter-sheet WVTR is insignificant. We will assume 90% RH at 38 °C external to the packaging in line with WVTR testing standards.

The WVTR, α, is commonly expressed in units of $g_{water} / m^2 \times day$. The relative humidity, RH, we can express as a function of the absolute humidity, AH, and the absolute humidity at 100% RH, c, as RH = AH/c. At 38 °C, c is 46 g/m^3. We can define the time, t, mass of water, m, radius of the cylinder, r, and height of the cylinder, d. We can then find that $\Delta m = \alpha \times t \times 2\pi r2$, thus $\Delta AH = (\alpha \times t \times 2\pi r2)/(d\times \pi r2) = (2\alpha t)/d$. From here we find that $\Delta RH = (2\alpha t)/(cd)$. Thus, the relative humidity change is coupled to the film thickness independent of the diameter of the pixel.

From the literature, we can find that the WVTR of protective aluminum films is ~0.01 $g/m^2 \times day$.[13] By applying the design values from the thin-film sensors, we can find that humidity in absence of polymer would very rapidly increase reaching 90% RH within 2.5 hrs (Fig. 5.9(a)). We can further probe the WVTR and find for a 10% RH change over 100 days, we would need a WVTR of ~1×10^{-6} (Fig. 5.9(b)). This result is not especially surprising as other polymer based microelectronics require extremely low WVTR. For organic light emitting diodes this value can be found at ~10^{-6} and for organic solar cells this value can range ~10^{-3} g/m2×day.[38] We can further evaluate that this limited stability is a function of the thin format of the sensor (Fig. 5.9(c-d)).

One aspect that is especially surprising given these results is the short time necessary to see these humidity swings in theory, while the thin-film sensor's took days to show a significant humidity swing. This is an inherent byproduct of the high hydrophilicity of these polymers and reflects the large water uptake prior to current change despite the extreme sensitivity of the polymer to humidity.

The key takeaway from this analysis is, if we are dealing with small sensors, either the system will require far smaller WVTRs than can be achieved through flexible aluminum packaging, or the humidity inside the packaging must be maintained in some manner. Which leads nicely to the discussion of the the need for the humidity buffer material.

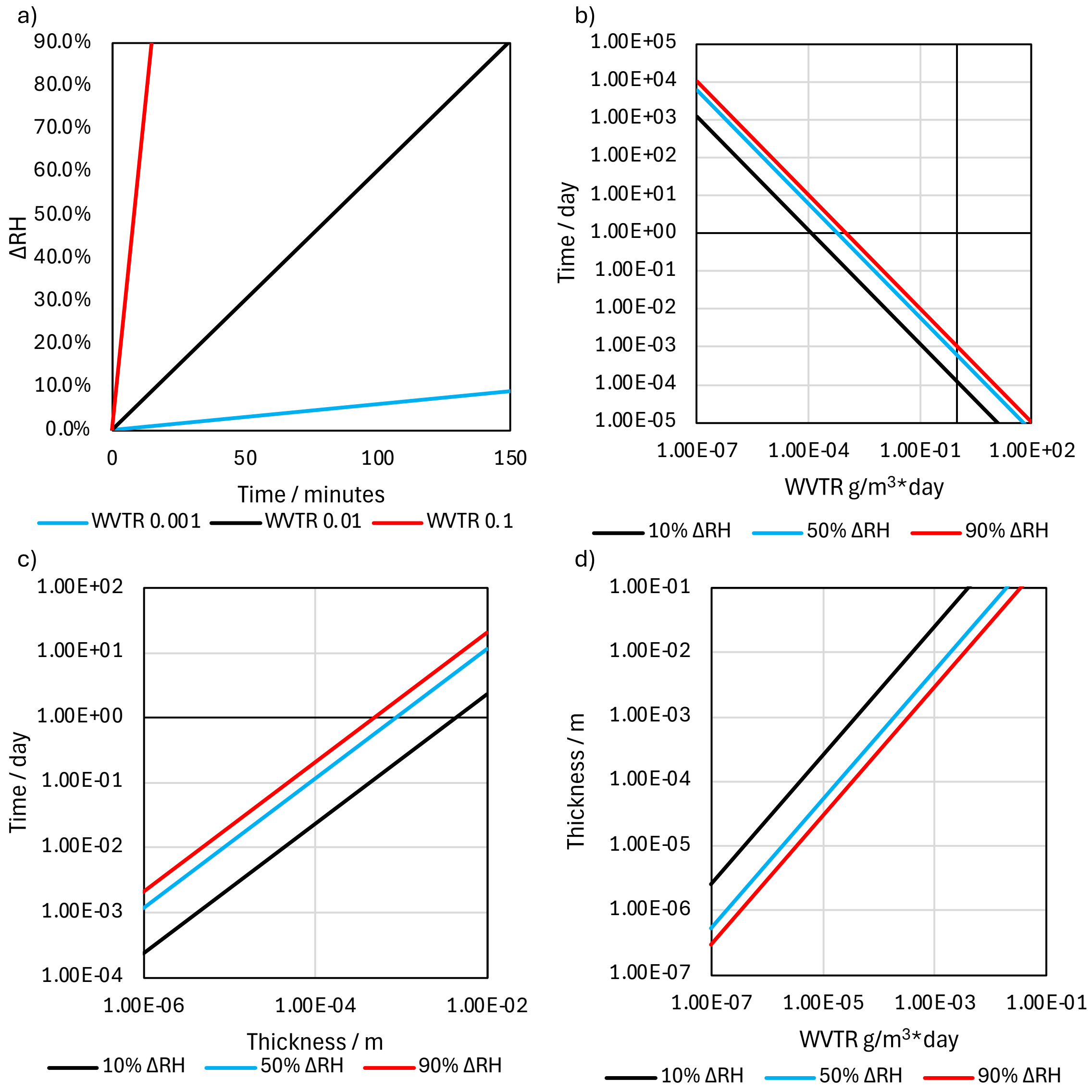

Figure 5.9: Theoretical model of humidity change in sealed cylinder. (a) Change in RH for a 50 µm height cylinder. (b) Time to change RH a set amount as WVTR varies for a sensor 50 µm thick. (c) Time to change RH a set amount for various thickness sensors given a WVTR of 0.01 g/m2 × day. (d) Minimum sensor thickness to maintain maximum RH change in 60 days as WVTR varies.

5.7 The Theoretical Humidity Buffer Material (HBM)

As demonstrated above a method to regulate the humidity inside the packaging is vital in order to create long term, reliable viable sensors. For this purpose, we here propose humidity buffer material. The proposed humidity buffer material is fabricated by depositing salt within polymer that does not allow the passage of liquid water, however, has a high WVTR. This allows each salt crystal to function as an individual fixed point solution jar. When exposed to humidities above the salt's humidity fixed point, water vapor diffuses through the polymer and is adsorbed by the salt. The salt then grows a 'bubble' of water surrounding it. As long as solid salt remains, the produced humidity remains fixed. If the buffer is exposed to humidities below the salt's humidity fixed point, water vapor diffuses through the polymer away from the salt as it evaporates. So long as liquid water remains, the produced humidity remains fixed.

Many potential salts are possible for use in these HMBs. To select an appropriate salt, we must consider several factors. 1) The humidity value produced vs the needed value for our sensors. HEA-AA sensors show improved sensitivity as the humidity is decreased (Fig. 5.3), however, as the humidity is decreased the resistivity increases limiting its utility. We consider the optimal range of humidities to be 5-10% RH with a usable range of 5-20% RH. Several salts will perform within this optimal range. 2) The toxicity of the salt. As target applications of HEA-AA sensors include medical devices and consumer electronics, reducing the quantities of potentially hazardous materials from our devices is preferable. This eliminates cesium fluoride, potassium hydroxide, and sodium hydroxide, which all have interesting RH ranges. 3) The temperature stability of the fixed point solution. It is well characterized that the RH range of saturated salt solutions varies with temperature. For cesium fluoride it varies from 5.5% RH at 5 °C to 2.6% at 80 °C.[16] For potassium hydroxide it varies from 14.3% RH at 5 °C to 1.6% at 75 °C.[16]

For these reasons, lithium chloride was selected as the salt for this application. Lithium chloride is minimally toxic, LD_{50} 757 mg / kg,[39] and exhibits a RH of 11.23% at 0 °C and 10.75% RH at 70 °C.[16] For commercial electronics, the relevant temperature range is 0 °C to 70 °C. In examining lithium chloride's phase diagram,[40] we can observe that lithium chloride exhibits a series of phase transitions within this temperature range. Lithium chloride initially transitions from LiCl to $LiCl + LiCl \cdot H_2O$. As more water is absorbed, the phase diagram separates at a 70% LiCl by mass, dependent on the critical temperature 20 °C. Below this temperature, it forms $LiCl•H_2O + LiCl•2H_2O$ until transitioning to solution + $LiCl•3H_2O$ at 54% LiCl by mass. Above this temperature, it goes straight to solution + $LiCl•H_2O$. Finally, the lithium chloride is fully dissolved dependent on the solution temperature. At 70 °C it occurs at 51% mass, at 20 °C it occurs at 45%, at 0 °C it occurs at 40%. If we define the buffering capacity as the range in which both liquid solution and solid salt is present, we can now calculate the buffering capacity for various temperatures. At 0 °C, we find the buffering capacity to be 0.65 g water / g LiCl. At just below 20 °C, we find the buffering capacity to be 0.37 g water / g LiCl. At 70 °C this gives us a buffering capacity of 0.54 g water / g LiCl. As it represents a minimum, we will utilize the buffering capacity of 0.37 g water / g LiCl.

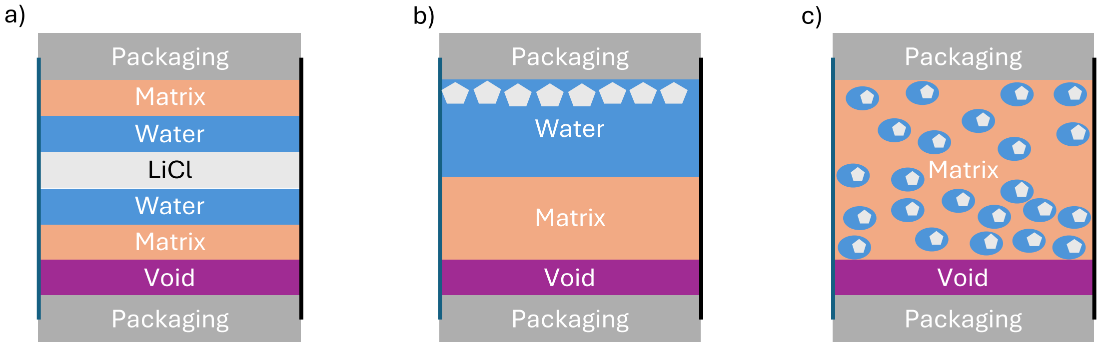

Figure 5.10: Simplified models for buffered thin-films. (a) Simplified 1D model of buffered thin-film. (b) Alternative buffered thin film assuming layer fabrication. This has direct relevance to some of the latex laboratory fabricated buffer materials, however, will have limited relevance to commercialized materials. (c) Realistic 2d model of buffered thin-films.

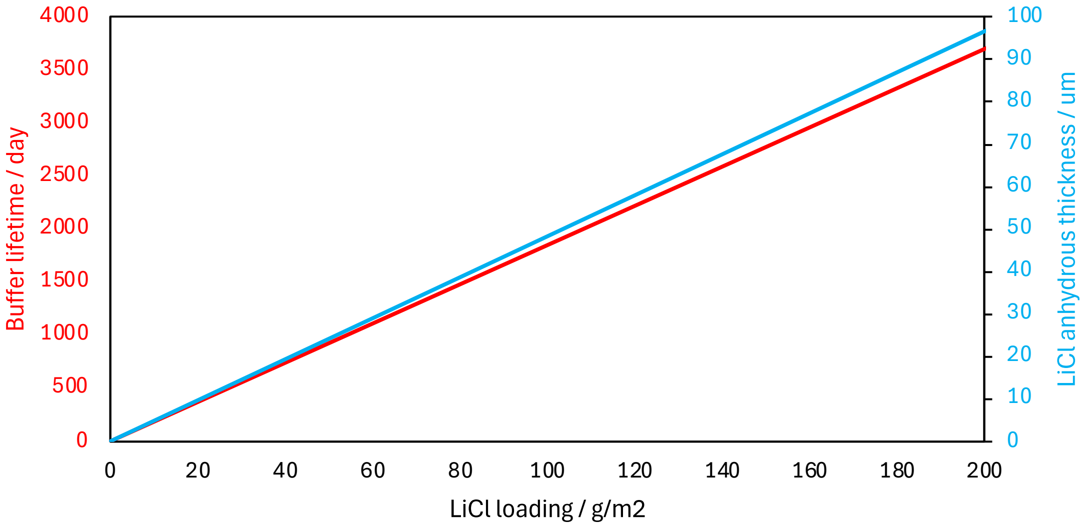

Figure 5.11: Theoretical sensor lifetimes and theoretical LiCl film thicknesses for a sensor with a packaging WVTR of 0.01 g/m^2*day assuming full window of the humidity buffer.

Given this, it is now possible to assess the lifetime of sensors for various amounts of buffers when assuming the before leveraged sensor motif (Fig 5.11.). By assuming the full range of buffering capacity, we can set the best-case situation of an almost fully dry buffer and sensing sheet exposed to a high humidity environment. We can quickly observe that long term stable sensors could be produced for reasonable buffer loadings.

Now that we have established that LiCl has sufficient buffering capacity to lead to long term stabilization of sensors subjected to high humidity and temperature. We can now evaluate a simplified 1D model of these sensors accounting for the diffusion across the packaging. This is especially important as for the devices to function, the salt / solution must be encased in a “leak proof” polymer matrix. The selection of an appropriate polymer matrix and the architecture of the buffer is vital to produce useful sensors and is partially governed by the diffusion behavior inside the packaging. For this investigation we will apply a simplified model (Fig 5.10.a). In order to build this model, we need to account for the WVTR of various films. From theory, we can find that $\mathrm{WVTR} = (\mathrm{P_0}\,(\mathrm{p_2} - \mathrm{p_1}))/\mathrm{x} * \mathrm{e}^{\frac{-\mathrm{E_A}}{\mathrm{RT}}}),$[41] where P_0 is the coefficient of permeation, p_1 and p_2 are the partial pressures of water vapor, x is the thickness of the film, and the Arrhenius expression takes its usual form. However, as we are dealing with both polymer and metallized films, and the activation energy is difficult to find for many materials. Thus, for this investigation, we shall ignore the temperature effects on the permittivity and so the equation becomes $\mathrm{WVTR} = \mathrm{P}\frac{p_2 - p_1}{x}$.[41] Next we leverage the ideal gas law to convert the equation, $p_2 - p_1 = \left(\frac{n_2}{V} - \frac{n_1}{V}\right)RT = \frac{\left(\frac{m_2}{V} - \frac{m_1}{V}\right)RT}{mw_{H_2O}} = \frac{(AH_2 - AH_1)RT}{mw_{H_2O}} = \frac{(RH_2 - RH_2)cRT}{mw_{H_2O}}$. To find c, we will apply the Arden Buck equation to find the saturation partial pressure of water vapor, p_s $= 0.00603e^{\left(18.678 - \frac{T-273.15}{234.5}\right)\left(\frac{T-273.15}{T-16.01}\right)}$ in units of atmospheres. Therefore, at 100% RH the AH can be found to be $AH_{Sat} = \frac{p_s mw_{H_2O}}{RT}$, and thus is equal to c. Thus we can find that, $p_2 - p_1 = (RH_2 - RH_1)p_s \times \frac{mw_{H_2O}}{RT} \times \frac{RT}{mw_{H_2O}} = (RH_2 - RH_1)p_s$. From these we can derive the permittivity of the previously modeled aluminum films, P/x, as 0.1698 g/m^2×day.

For initial calculations, let's assume the LiCl buffer film is half hydrated, thus is at 1.035 g water / g LiCl. We will artificially pick a LiCl loading of 20 g/m^2, thus giving us an anhydrous LiCl film thickness of ~9.7 μm. If we ignore solution effects, this leads to a total water layer thickness of ~21 μm. Let us set the void thickness to 50 μm and assume all sections are at an initial RH of 11% and assume that the LiCl solution has a vapor pressure corresponding to 11% RH. For initial calculations let us use a temperature of 38 °C and 90% RH external to the packaging. We will use the P/x of the matrix material as our core experimental variable. These initial models will be carried out in Excel® and a pseudo void will be used for the calculations between the packaging and the matrix at the top of the structure, its thickness is set to 5 μm (Fig. 5.10(a)). For these initial studies we will ignore buffer failure from hydration changes in the buffer material. From these calculations, we can observe that the P/x must be significantly higher than that of the packaging to produce the desired humidity within the packaging (Fig 5.12.). From initial measurements it is observed that P/x of the matrix must be > 10 for a P/x value of 0.1698 from the packaging material (Fig. 5.12(b)) to reduce the error in humidity to less than 1%.

Table 5.2: P/x for various polymer matrix materials

Polymer	Permeability (g/mm*m2*day) 25 °C, 1 atm	P/x 100 µm	P/x 50 µM
PDMS[12]	>10	>100	>200
PMMA[41]	5.25	52.5	105
Natural Rubber Latex[41]	3.76	37.6	75.2
Polycarbonate[41]	2.3	23	46
Neoprene G[41]	1.49	14.9	29.2
PVC[41]	0.451	4.51	9.02
PET[41]	0.213	2.13	4.26
Butyl Rubber[41]	0.181	1.8	3.62

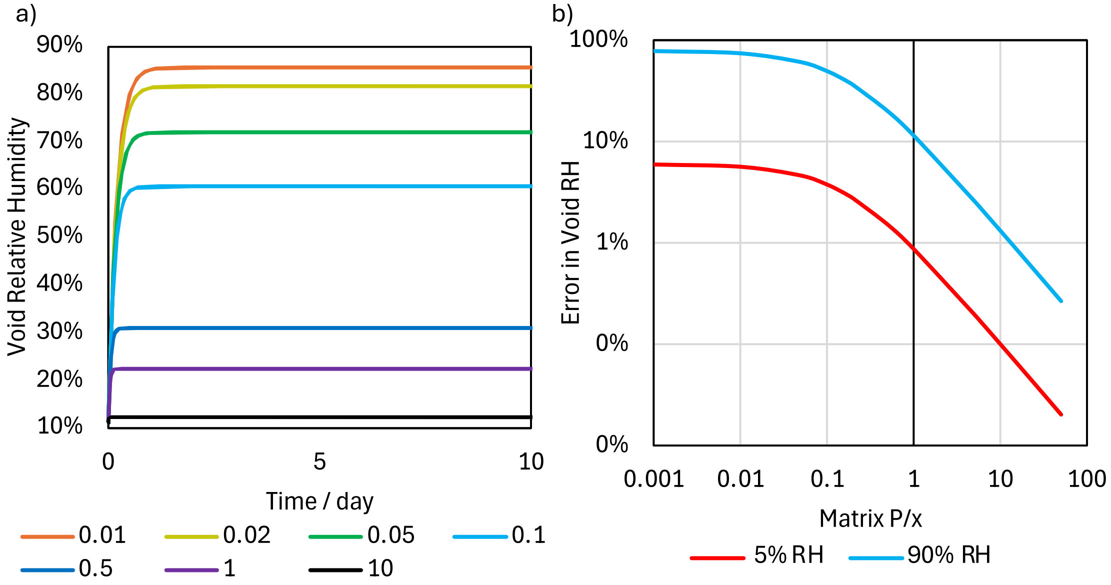

Figure 5.12: Approximate models for diffusion in 1D thin-film sensors. (a) Effect of varying the polymer matrix's value of P/x on the voids humidity vs time trace for 38 °C and an external RH of 90% (b) Difference between void RH and LiCl idealized RH at 38 °C for an external RH of 5% and 90%.

By examining table 5.2 we find that numerous polymers exhibit sufficient P/x values for these packaging problems. As discussed later, several polymers from this list have been attempted or considered. One interesting result of these calculations is the realization that with these buffering materials, conventional polymer humidity barriers may be viable. If we assume a humidity barrier P/x of 0.451 corresponding to 1 mm thick PVC, we can calculate that the matrix material must have a P/x > 36. Again, by referencing table 5.2, we can find several viable candidate materials.

In order to probe long-term device lifetime, a Python® script was written leveraging this simplified diffusion model. By leveraging the meteostat Python® library, we can subject our simulated devices to hourly historical weather data at locations around the globe. Locations were selected to provide a variety of typical climates. Preliminary calculations were carried out to evaluate time till buffer failure at various locations. A start time of 2010/01/01 12:00:00AM was selected. Preliminary results can be found in table 5.3. From these results we can observe that the lifetime of the sensors is highly dependent on the environment the sensor is subjected to. In temperate or dry environments, the sensor can exhibit a far longer lifetime.

Table 5.3: Simulated Sensor Lifetime in Days at Various Locations starting at 2010-01-01 vs LiCl Buffer Loading

Location	Country	5 g/m^2	10 g/m^2	15 g.m^2	20 g/m^2
1% RH 38 °C	-	3	6	11	19
99% RH 38 °C	-	3	7	13	25
Dubai International Airport	UAE	10	55	131	170
Mumbai	India	6	20	724	930
Honolulu International Airport	USA	7	31	962	1061
Tokyo International Airport	Japan	118	192	1046	1117
Campinas Airport	Brazil	7	33	922	1191
Auckland Airport	New Zealand	13	820	917	1228
Sydney Airport	Australia	8	26	1191	1264
Cape Town Airport	South Africa	9	63	1189	1275
Rome Fiumicino Airport	Italy	111	200	1053	1383
Los Angeles Airport	USA	15	1037	1110	1436
Cairo International Airport	Egypt	13	69	174	1441
Newark Airport	USA	94	157	1134	1445
San Francisco International Airport	USA	61	1047	1389	1716

Hamburg Airport	Germany	159	1031	1387	1755
Charles De Gaulle Airport	France	118	1040	1405	1758
Seattle-Tacoma Airport	USA	188	1052	1405	1773
Madrid / Barajas	Spain	111	187	1793	2160
Tucson International Airport	USA	21	128	160	2918
Denver International Airport	USA	142	184	2528	2965
China Lake NAWS	USA	55	154	180	4724

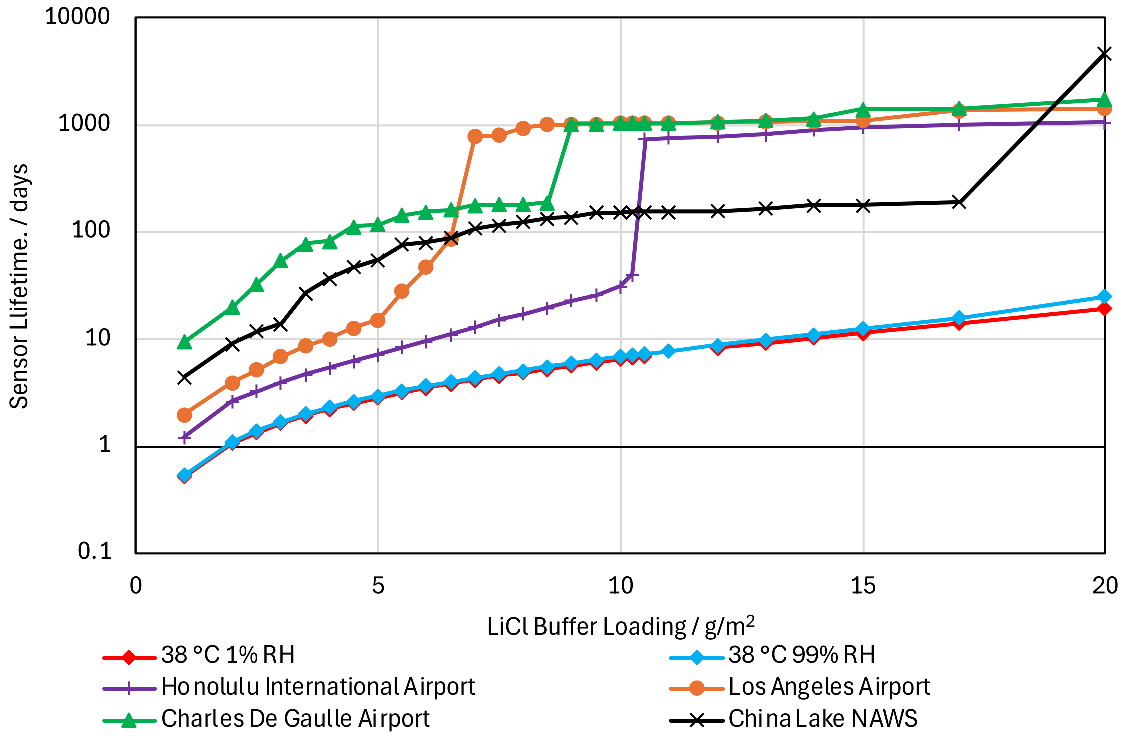

Figure 5.13: Simulated sensor lifetimes in various locations dependent on buffer loading. Note the step function effects in this data.

In Fig. 5.13. we can further examine this data. Of note, we find the sensors tend to undergo large jumps in lifetime as the buffer loading becomes sufficient to overcome periods of weather extremes within a given area. This presents an interesting opportunity for our sensors. If we can reliably measure the state of the buffer material, the useful lifetime of the commercialized sensors can be far higher than that of the worst-case scenario. In the case of buffered thin-film sensors such as the architecture in Fig. 5.7(c), then we here propose that the hydration state of the buffer can be determined by measuring the ac electrical properties (such as a capacitive evaluation of the dielectric constants)[42,43] between the two moisture barrier aluminum sheets. This measurement does not need to be continuous, measurements made weekly throughout the device's lifetime should provide sufficient the buffer state and its degradation. This has the potential to significantly extend the lifetime of these devices.

The diffusion models presented here represent preliminary analysis of these devices on a highly simplified 1D model. To date the work on these devices has been preliminary, further studies both with these and more advanced models are warranted for a better understanding of the potential devices and to facilitate scale-up and commercialization.

5.8 Experimental Results with HBMs

Lithium Chloride humidity buffer materials have been fabricated with a variety of matrix material. In this section we will review some of these composites and the results to date.

An initial test case was fabricated by placing LiCl onto a weight boat then applying a coating of an ethyl-2-cyanoacrylate adhesive (Loctite® Super Glue professional), The adhesive was cured in a high humidity jar. After the adhesive had cured, the sample was rinsed with DI water. This buffer material (Fig. 5.14(a)) was observed to maintain the RH of a sealed glass container at ~ 10%, it was found to restore this RH after being subjected to the addition of water to the jar (via micro pipet) or removal of moisture from the jar (dry nitrogen purge). Furthermore, unlike some later materials, no moisture was observed to buildup on the surface of the matrix. While these results are extremely promising for rigid packaging solutions such as those required for polymer based microbolometers, it was found through manual handling that the cyanoacrylate matrix material was overly brittle for flexible devices. Furthermore the heat generated during the curing of the matrix creates an added hazard during fabrication of large area devices.

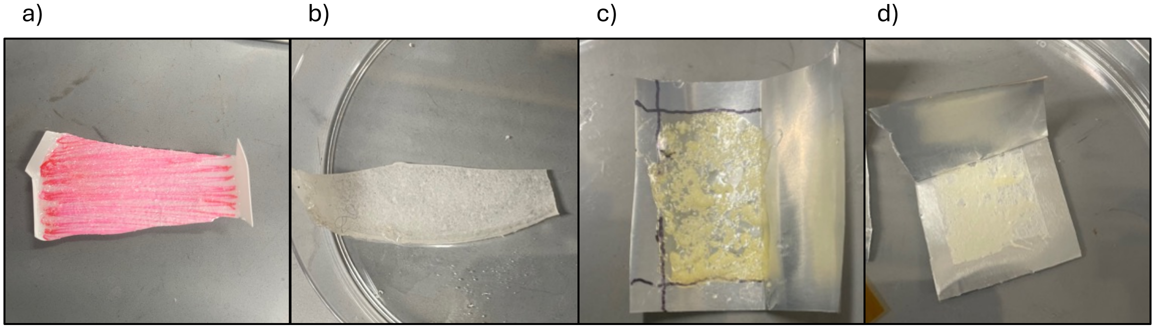

Figure 5.14: Various LiCl humidity buffer materials. (a) LiCl-cyanoacrylate on a weight boat. Note a red marker was applied to the weight boat prior to buffer creation to aid in visualization. (b) LiCl-silicone as a freestanding material. (c) LiCl-latex prepared via solid salt approach onto moisture barrier film. (d) LiCl-latex prepared via emulsion approach onto moisture barrier film.

In order to probe flexible matrix materials, platinum cured silicone type materials were selected next (Fig. 5.14(b)). Both Smooth-Ons EcoflexTM and DragonskinTM where leveraged and found to exhibit similar properties for this application. LiCl was placed in a petri dish then the silicone precursors were mixed per the manufacturer's guidelines and added to the petri dish. The silicone was then mixed with the LiCl and placed on a hot plate at 60 °C to cure. Elevated temperature curing was selected as otherwise the LiCl tends to settle out of the matrix during curing. After curing, the buffer was rinsed with DI water. Preliminary tests were carried out and showed that this material combination (silicone and LiCl) exhibits buffer behavior. It was observed that this material combination tends to maintain an elevated RH of ~ 18%. The origin of this elevation relative to LiCl solutions was not explored. Preliminary tests were carried out by placing a humidity and temperature logging sensor (SensorPush HT1 Smart Temperature Sensor and Humidity Sensor) within a bag prepared from Valsem Industries moisture barrier materials. The bag was then sealed within a humidity-controlled glovebox. The bag was then placed on an elevated platform within a plastic tub containing water. A simple humidity sensor showed the humidity within this chamber was ~ 89-90% RH. After 25 days, the humidity within the sealed bag containing just the logging sensor and no buffer material climbed from ~ 19.4% to ~ 20% at which point the test was terminated. An identical bag with logging sensor was prepared within the glovebox, LiCl-silicone humidity buffer material was also added before sealing the bag. After 1 day in the humidity-controlled glovebox, the bag was transferred to the high humidity chamber. An initial large swing in humidity was seen, we suspect due to the temperature differences between the glovebox room and the test chamber room. After settling, the humidity was measured at ~ 17.9-18.0% RH for the 54 day duration of the test. These results can be best seen in Fig. 5.15 and demonstrate that this buffer material can maintain a relatively constant humidity. Furthermore, with the silicone buffer materials no water droplets were observed on the material's surface, similar to observations of the cyanoacrylate materials. While extremely promising, the challenges in adhering silicone materials during roll-to-roll fabrication and the long curing times make these material combinations incompatible with the large scale production needed for commercialization of the HEA-AA thin-film sensors.

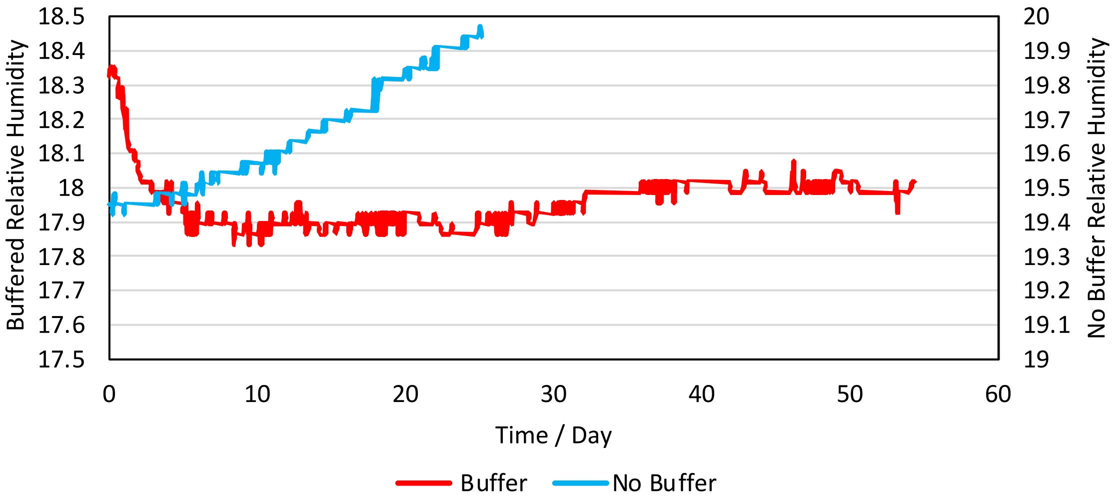

Figure 5.15: Humidity buffer test comprised of a sealed moisture barrier bag containing a humidity sensor with and without buffer material exposed to high relative humidity. Note the buffer material maintains the humidity within the bag.

To address the adhesion issue, natural rubber latex (Elmer's No Wrinkle Rubber Cement) was next explored as a buffer matrix material. This was prepared through two methods, a solid salt approach and a water/heptane emulsion approach. In the first approach, LiCl is scattered across a surface after which the latex in heptane was applied over the same surface. The latex is allowed to dry. The samples are then rinsed with DI water. This material (Fig. 5.14(c)) was observed to exhibit a buffered RH of 10-11%. To visualize the behavior of the buffer materials, a low LiCl loading buffer material was prepared through this method on a moisture barrier film and subjected to high and low humidities (Fig. 5.16(a-b)). From this we can observe that under high humidities the droplets grow until all salt is dissolved, however the liquid of the droplets remains encapsulated within the latex film. When subjected to drying, the droplets shrink and the LiCl crashes out. Again, remaining fully contained within the latex film. While interesting, it was observed that the produced film exhibited a highly variable LiCl concentration due to clumping. Furthermore, this material was found to exhibit water droplet growth on the surface of the matrix. The origin of this growth has not been identified, however, we suspect it may be indicative that the LiCl can migrate to the surface through some method.[44] It is known that ion transport through latex can occur, however its significance under these conditions is unknown. While these issues are under investigation, several studies have been undertaken with this material as it presents some opportunities for fabrication within the roll-to-roll approach.

To resolve the clumping issues and resolved other issues foreseeable in roll-to-roll fabrication, an alternative approach was attempted. By mixing latex in heptane with a saturated LiCl solution in water, and the addition of sodium dodecyl sulfate, a somewhat stable emulsion can be prepared. This is exciting for roll-to-roll fabrication as it allows the application of a single phase material. As the emulsion dries it forms droplets of water encapsulated in a thin latex film. Once the water dries it produces a largely porous latex material (Fig. 5.14(d)) with a thin layer of latex between the salt bubbles and the environment. We theorize this leads to a more optimal value of matrix P/x. Furthermore, as the latex film is dried with the buffer in a fully hydrated state, this leads to the latex material being under minimal strain as the buffer hydrates, this is notably the opposite of the solid salt approach. While the emulsion was found to be sufficiently stable for preliminary trials, it was observed that the emulsion typically separated within a week. Further work on this approach is needed.

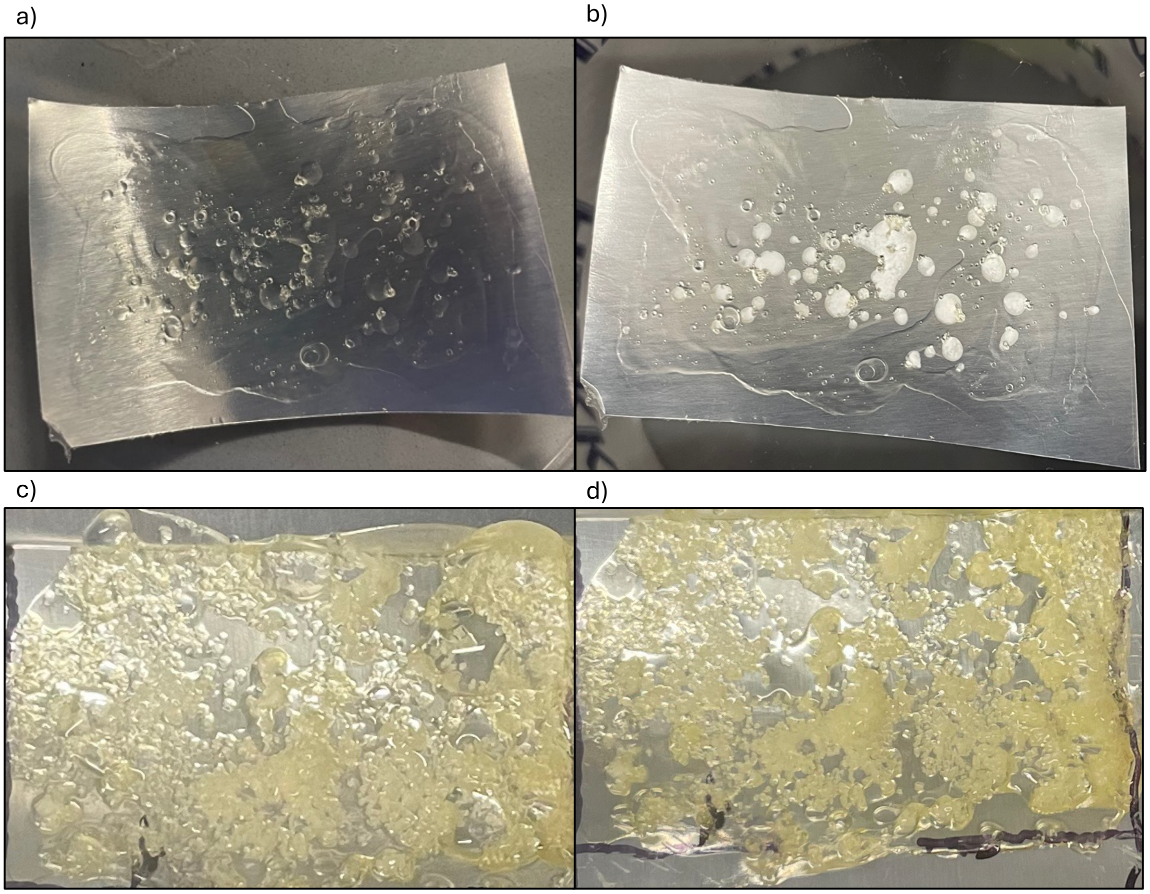

Figure 5.16: Hydration behavior of LiCl-Latex HBMs. (a) Extremely low loading HBM in a highly hydrated state. No solid salt is observed. (b) Extremely low loading HBM in a dried state. Note the small crystals of LiCl observed. (c) Typical loading HBM in a partially hydrated state. (d) Typical loading HBM in a partially dried state.

As other work within the group is exploring the potential applications of guayule latex, here we note that we do not believe there are any technical issues with substituting natural rubber latex for guayule latex for the humidity buffer application, however, it has not been tested. As guayule latex in water emulsion is currently within the group, attempts were made to incorporate the LiCl into the water emulsion. This is especially interesting as the removal of the organic solvents from the process significantly decreases the risk to workers. Additionally, the emulsions are extremely easy to apply to surfaces due to their tendency to crash out. However, to date we have not managed to stabilize the latex-water emulsion to the addition of lithium chloride. Further work in this direction is needed.

While promising, latex presents two major limitations, first for roll-to-roll fabrication latex is extremely challenging to handle as a freestanding film. Second, latex processing requires use of hydrocarbon solvents such as heptane which present significant risks to the workers. In examining table 5.2 and the solubilities of materials, PMMA was selected as a next step matrix material due to its high WVTR and solubility in less hazardous solvents such as acetone and ethyl acetate. Initial tests with PMMA showed it as too brittle for fabrication of flexible sensors. This issue was reduced by leveraging a plasticized PMMA film as the precursor. However, while somewhat flexible films could be fabricated it was observed that when LiCl was introduced, the bubble swelling causes cracking in the PMMA matrix leading to the solutions escaping the matrix. Further work into plasticizing PMMA for this application may be relevant, however other matrixes may be of more interest.

In the context of roll-to-roll fabrication, highly elastic materials such as PDMS and latex are difficult to process as freestanding films, as such it would be more optimal to cast the buffer material onto the device during fabrication. For highly brittle materials like PMMA similar challenges arise. As we consider where to explore further in developing the next set of humidity buffer matrixes, we turn our attentions to polycarbonate, PVC, and PET, as all exhibit acceptable WVTRs and allow freestanding roll-to-roll fabrication.

5.9 Potential Fabrication of Thin-Film Sensors Leveraging the HBM

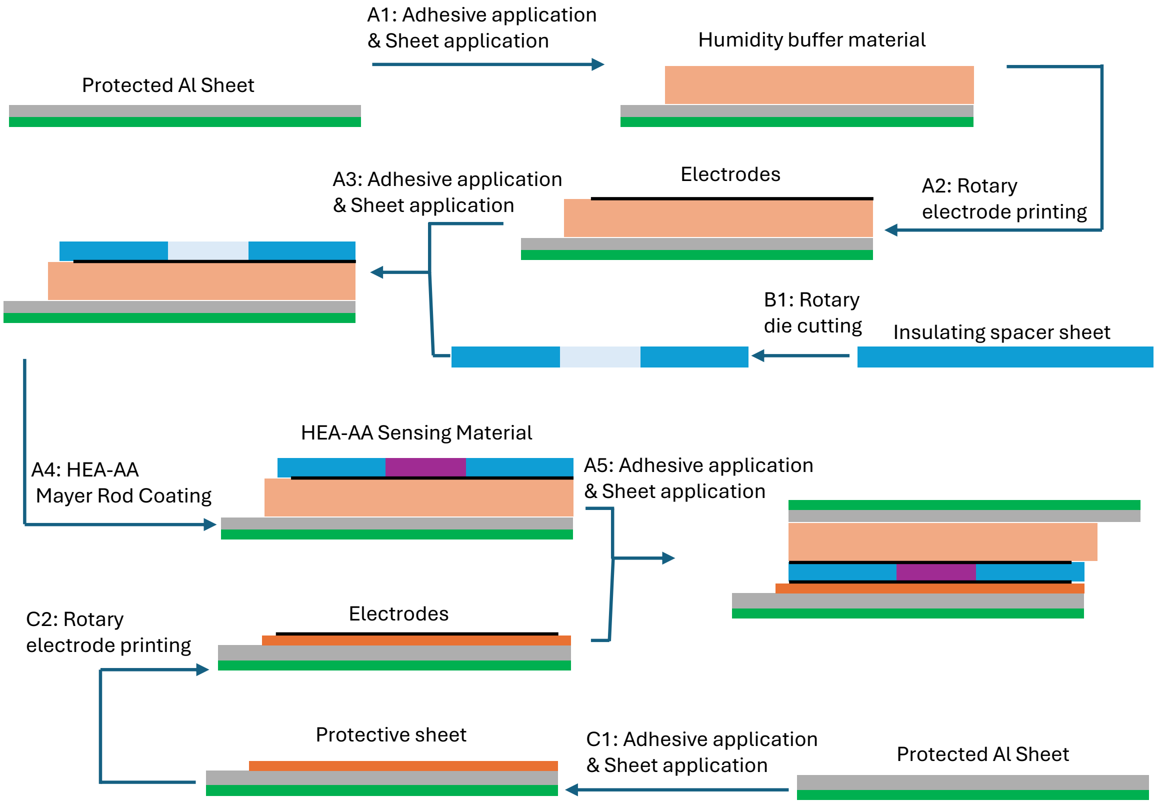

Figure 5.17: Potential fabrication approach for humidity buffered sensors.

A vital question when exploring a new material is how the introduction of this material effects the fabrication of the devices. We can visualize a process flow chart for the fabrication of these materials (Fig. 5.17). In this approach a top sheet (A1-A4) and a bottom sheet (C1-C2) are fabricated then adhered together in A5. For each step we utilize standard roll-to-roll fabrication processes. Here we examine the particular manufacturing challenges that we can foresee.

The first fabrication step, A1, presents a variety of challenges dependent on the humidity buffer matrix material. For materials such as silicone, latex, or PMMA, the buffer material will have to be applied as either a liquid or slurry onto the sheet then cured/dried on the sheet. This can be approached by leveraging standard drying oven approaches. If future work allows for flexible, non-brittle, non-elastic, freestanding HBMs, then fabrication becomes a simple challenge of sheet adhesion. This may be enabled by work towards polycarbonate and PVC HBMs. Of note, this remains the only step that is complicated by the addition of the HBMs.

The fabrication step A3 presents a large challenge, the alignment between the insulating layer sheet and the electrodes. As discussed before this issue can be reduced by increasing the size of the cutouts, however it remains a challenge in the fabrication of these devices.

Step A4 presents a small challenge as the concentration of the HEA-AA solution cast needs to be precisely tuned to the manufacturing process. This is ongoing work in our lab.

Step A5 presents the most significant alignment challenge, as small shifts in the relative electrode positions will significantly affect the electrical properties of the devices. This is perhaps the largest argument for the common signal approach to readout, however, due to the large scaling issues as the number of sensors is increased, we strongly recommend the row-and-column readout approach. Unfortunately, this requires the electrode alignment challenge to be solved in manufacturing not device architecture. Additionally, as presented, this step will lead to a thin coating of glue between the HEA-AA sensing material and the bottom electrode, which depending on the electrical measurement used may present a small challenge. From the information that we have it is reasonable to assume that if the sensor is operated in a pseudo capacitive manner, this thin coat may have only minimal effect on the device performance. Preliminary tests have demonstrated that the glue utilized in these steps does not intrude into the HEA-AA polymer when cast on top of it and does not shift the electrical performance.

We can now discuss one of the largest benefits of HBMs in this class of devices. Prior discussions on the fabrication of these devices presented a number of challenges, the largest challenge so far is controlling the hydration state of the HEA-AA polymer during device fabrication. Preliminary work focused on leveraging drying ovens at elevated temperatures to quickly drive the polymer into a low humidity state prior to sealing of the sheets. However, as room humidity during sheet fabrication is commonly not precisely controlled in roll-to-roll fabrication facilities, producing consistent sensors represents a massive challenge. However, with the utilization of the HBMs, as long as the HBM is within its functional hydration range, the hydration state of the HEA-AA polymer is known and well controlled. This allows for more reliable fabrication of consistent sensors. By examining the previously presented diffusion data and provided the hydration state of the HBM can be measured, this approach presents a simplified route to fabrication. The sheets can be fabricated on the typical production floor, the hydration state of the roll can then be measured, and the roll can then be stored in either a high humidity (~99% RH) or low humidity (0% RH) until the hydration of the HBM meets the required specification. This allows for a tuning of the material after fabrication making it more immune to variations in temperature and humidity on the production line.

5.10 Experimental Results of Packaged Sensors

To probe actual sensors leveraging the HBM, a simplified architecture was created. Due to fabrication issues, the planer circular interdigitated electrodes fabricated on polyimide boards (see Chapter 3) were substituted in the place of the thin-film sensors.

For these studies a small pouch of Valsem Industries humidity barrier film was prepared. In buffered sensors, ~ 150 mg of LiCl was placed on one side of the pouch, in the control devices the LiCl was excluded. To this side of the pouch, ~ 1 mL of natural rubber latex in heptane was cast and the LiCl was stirred in. The latex films were then allowed to dry. After the latex film solidified, they were rinsed with DI water before being dried in a N2 box.

The HEA-AA samples on the polyimide boards were prepared as outlined in Chapter 3. Wires where soldered to the electrical contacts of the boards. The boards were then stored in a N_2 box.

For glovebox prepared samples, the boards and pouches were then transferred into a humidity-controlled glovebox. They were held at < 10% RH at least overnight. The glovebox RH was then brought up to 10-11% and the boards were sealed into the pouches by a combination of hot-pressing and ironing. The samples were then held again overnight at 10-11% RH prior to being removed for testing.

For bench top prepared samples, the boards and pouches were removed from the N2 box. The boards were then sealed into the pouches by a combination of hot-pressing and ironing. Immediately after all boards were sealed, they were transferred to the testing apparatus.

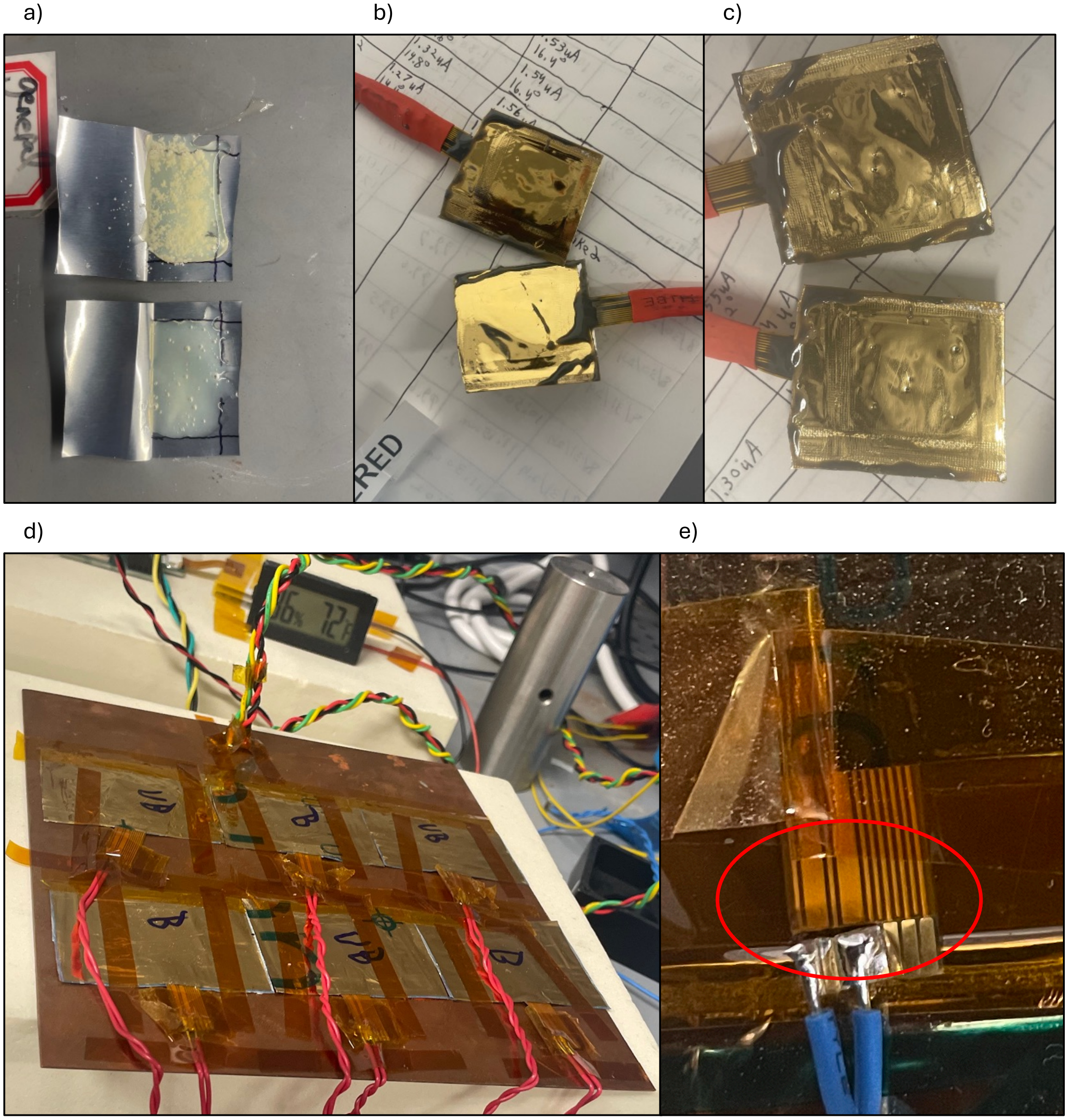

Figure 5.18: Experimental photos from buffer sensor tests. (a) Buffered and control pouch for 2 sensor test immediately after latex deposition. (b) Fabricated sensors for 2 sensor test, note the epoxide bead sealing the upper edge and the heat shrink tubing around the electrical connections. (c) 2 sensor test sensors after the test was terminated. Note the 6 holes in the sensor packaging. (d) Experimental setup for the 6 sensor tests. (e) Board damage at the contact from the first of the 6 sensor tests. Failure circled in red.

Measurements on all samples were carried out on an impedance analyzer (Zurich Instruments MFIA 500 kHz) with a 10 Hz, 100mV input signal. Connection to the sensors was manually switched and manually recorded.

As an early test two sensors were prepared in the glovebox as discussed before. Two modifications of that procedure were carried out. First, the connection between the wires and the board had a heat shrink tube applied to it. This was to reduce likelihood of the boards shorting from condensation, however it was removed from future tests as direct observation of the electrical contacts was desired (Fig 5.18.a). Second, a bead of epoxy (JB Weld® Original Steel Reinforced Epoxy) was applied around the edges of the packaging with especially thick coatings applied where the polyimide board exits the packaging (Fig 5.18.b). This epoxy was added as it was noticed previously that the heat seal method of the moisture barrier pouch does not form a good seal with polyimide.

For the tests, these sensors were suspended within a glass jar over a small quantity of liquid. This produces a high humidity environment we believed would drive the sensors into a quick failure. However, as can be seen from the electrical data (Fig. 5.19(a)) that for the initial period of this study the current of both sensors is decreasing at a fairly similar rate. The mechanism of this decrease is not yet understood but is observed in many of our packaged sensors. The question of why we do not observe the current increase as water is taken up into the control sensor, like is observed in the thin film sensors, is of central concern. While this packaging approach utilized a different packaging film, we do not expect the WVTR to be significantly different. However, if we revisit our models for the thin-film sensors, we can draw a strong hypothesis. We previously found that the change in RH of a cylindrical void varies inversely with the height of the void. If we extend this to the polymer films and stretch the model beyond reason to both the thin film sensors and the packaged polyimide sensors we can draw the following conclusion. In the thin film sensors, the polymer film's thickness is ~ 50 μm. For the polyimide sensors we can estimate the thickness from visual inspection to be ≥ 1mm. As such we should expect that if the WVTR is the same, the polyimide sensors should be at least 20-fold less responsive to external humidity. To artificially increase the WVTR, on day ~ 8 of the trial a hole was punctured in the center of the back of each sensor with a pin. This hole was pressed through the packaging layer into the latex layer. However, as the desired change was not observed by day ~ 9, five additional holes were punched with one in each corner and one additional hole in the center (Fig 5.18.c). The current was seen to rapidly increase in both sensors, with the increase less in the buffered sensor.

As we desired a higher WVTR through the packaging, however believed puncturing holes to be a suboptimal approach, we did not apply the epoxy bead to any further tests and hoped that the leakage through the packaging / polyimide interface would be sufficient to drive a noticeable difference between the buffered and the control sensors.

For the next trial, we prepared 3 control and 3 buffered sensors and packaged them on the bench top. The sensors were tapered to a copper plate. Two thermistors were also taped to the plate. The experiment was carried out with the samples exposed to the laboratory humidity and temperature (Fig 5.18.d).

It is vital here to note a significant issue that arose during this experiment. As we needed to view the electrical contacts during the experiments to rule out contact corrosion as a cause of the decreasing current, heat shrink tubing was not applied to the interface between boards and the wires. However, due to the flexible nature of the boards and the rigidity of the soldered joints, handling the boards placed an unusual stress on the boards at the narrow section where the pads connect to the traces. Over time this led to the traces snapping (Fig. 5.18(e)). In some cases, this could be mediated by holding the wire at such a position where the pads continued to make sufficient contact with the board's trace and to the maximum extent possible in these studies this was performed. However, many of the sensors were prematurely terminated from the study due to the failure of these electrical contacts.

In examining the electrical data (Fig 5.19.b), we can quickly observe that all buffered sensors follow a climb to a peak followed by a decrease over time. The sensor's initial currents exhibit a wide array of values and similarly the peak height are different between each sensor, however the peak shape and overall the general shape of the decay seems to be preserved. In particular, the slopes of the decay after the initial peak has decayed appear to be the same. We believe that this peak is indicative of the water uptake by the sensor during packaging. As the sensors were packaged individually while all of them rested on the bench top, different sensors up took different amounts of water.

Of note, we find that one of the control sensors S5 exhibits this same behavior, while S1 exhibits a steady increase in current and S3 exhibits wild fluctuations largely in line with changes to the laboratory's humidity. We hypothesize that these behaviors are indicative of different degrees of WVTR of the packaging. S5 has a low enough WVTR it behaves similarly to the buffered sensors as we saw in the two sensor experiment. S1 exhibits a higher WVTR which leads to a slow uptake of water and thus a slow increase in current. S3 suffers from a high WVTR and thus fluctuates wildly with laboratory humidity.

An additional trial was undertaken leveraging 3 control samples and 3 buffered samples packaged within the humidity-controlled glovebox. To eliminate the contact trace issue, several layers of polyimide tape where applied to the underside of the contact/trace to increase the stiffness of this region of the board, no issues with trace breakage were observed with these samples. In examining the electrical data from this trial, we can quickly observe that the no initial peak is observed. Furthermore, we can see that the three buffered sensors exhibit again very similar shapes and slopes. While for the control sensors UB2 exhibits a far slower decay, UB 6 exhibits a steady increase as water is up taken into the sensor, and UB 4 appears to behave similarly to the buffered sensors. In examining these slopes, we can apply a linear fit starting on day two. From this we find that B3 and UB4 exhibit a slope of -

1.10×10^{-9} and -1.22×10^{-9} respectively with $R^2 > 0.9$. B1 and B5 exhibit a slope of -2.31×10^{-10} and -2.60×10^{-10} respectively with $R^2 > 0.9$.

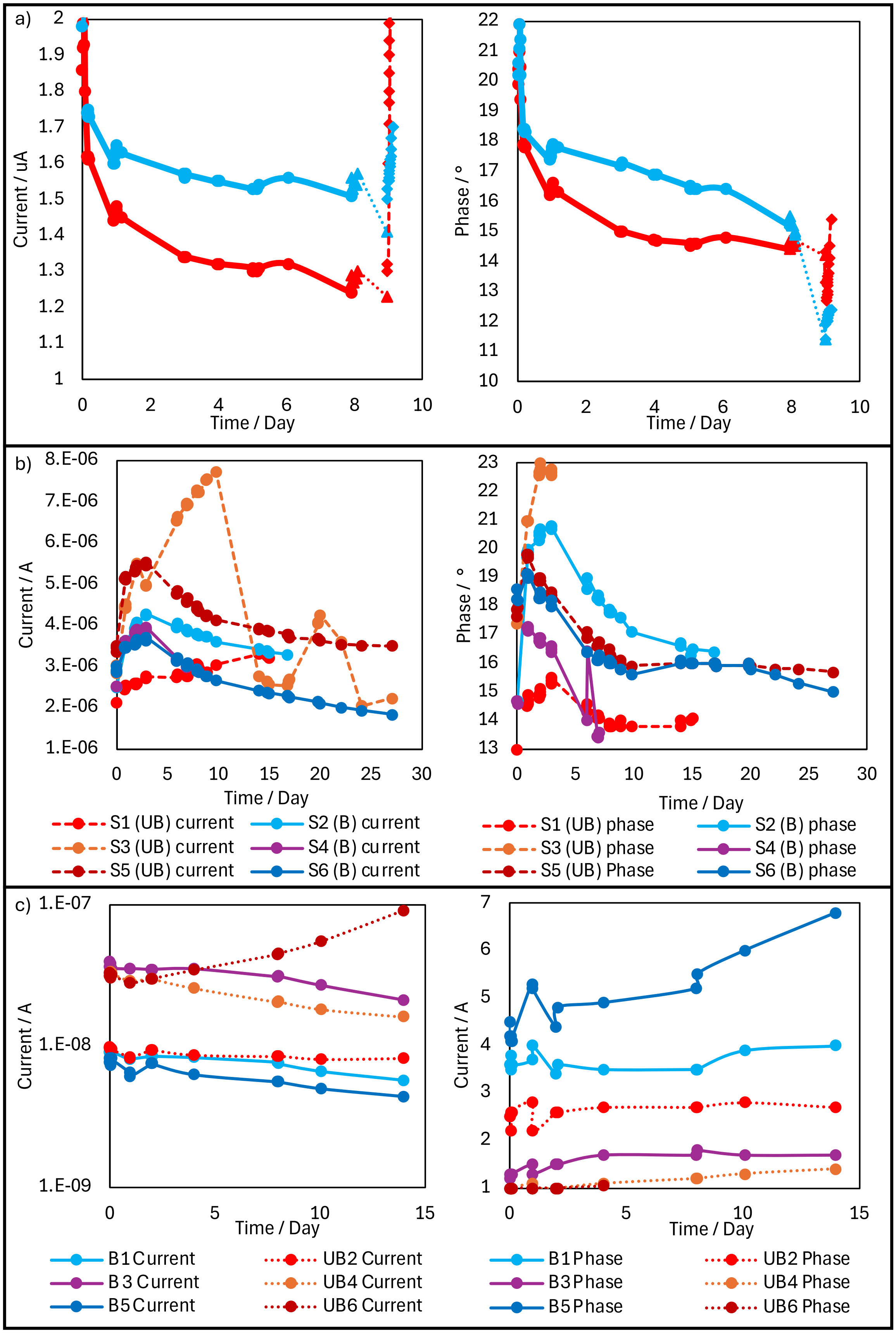
a)
Current / uA
2
1.9
1.8
1.7
1.6
1.5
1.4
1.3
1.2
1.1
1
0
2
4
6
8
10
Time / Day
Phase / °
22
21
20
19
18
17
16
15
14
13
12
11
10
0
2
4
6
8
10
Time / Day
b)
Current / A
8.E-06
7.E-06
6.E-06
5.E-06
4.E-06
3.E-06
2.E-06
1.E-06
0
5
10
15
20
25
30
Time / Day
Phase / °
23
22
21
20
19
18
17
16
15
14
13
0
5
10
15
20
25
30
Time / Day
S1 (UB) current
S2 (B) current
S3 (UB) current
S4 (B) current
S5 (UB) current
S6 (B) current
S1 (UB) phase
S2 (B) phase
S3 (UB) phase
S4 (B) phase
S5 (UB) Phase
S6 (B) phase
c)
Current / A
1.E-07
1.E-08
1.E-09
0
5
10
15
Time / Day
Current / A
7
6
5
4
3
2
1
0
5
10
15
Time / Day
B1 Current
B3 Current
B5 Current
UB2 Current
UB4 Current
UB6 Current
B1 Phase
B3 Phase
B5 Phase
UB2 Phase
UB4 Phase
UB6 Phase

Figure 5.19: Results of HBM sensor tests. (a) Results of two sensor test showing control (red) vs buffered sensor (blue). Notice both sensors follow the same trend until the packaging was punctured 6 times, at which time both sensors current measurement rapidly increases, however It increases less for the buffered sensor. (b) Results from 6 sensor test with the sensors packaged on the bench top. Control sensors are denoted with dashed lines and UB in the legend, while buffered sensors are denoted with solid lines and B in the legend. Note, due to issues leading to breakage of the polyimide boards, many sensors are terminated prematurely. Notice hydration behaviors of the control sensors S1 (UB) and S3 (UB) (c) Results from 6 sensor test with the sensors packaged in the glove box. Control sensors are denoted with dashed lines and UB in the legend, while buffered sensors are denoted with solid lines and B in the legend. Notice the failures of sensors UB2 and UB6.

From these studies, we find that to date the buffered sensors appear to exhibit similar decay functions, we attribute variations in them to variations in their manufacturing and believe with higher precision each sensor should behave more consistently. We especially note that none of the buffered sensors appeared to exhibit large fluctuations as the laboratory humidity varied day to day. If this decay function is inherent to the sensors, as long as it is consistent, it can be removed through data processing. The origin of it remains unknown, however, we may speculate that it originates from a slow corrosion of either the electrode's copper or the packaging's aluminum leading to a change in the electrical contacts and/or a decrease in the water content inside the packaging.

As to the buffer's effectiveness, we cannot at this time conclusively prove its effectiveness. From the control samples we can observe that the WVTR of this packaging approach varies widely sample to sample. That we have seen the effects of the laboratory humidity clearly in 3/6 control samples and its possible effect in 1/6 additional control samples while it has not been seen in any of the buffered samples, implies the buffer is functional, however, further tests precisely controlling the WVTR are needed to prove this.

5.11 Summary and Conclusions

In this chapter we demonstrated that thin-film polymer sensors fabricated with the HEA-AA sensing element suffer severely from changes in the environmental humidity. We discussed details concerning the manufacture of these sensors in commercial roll-to-roll fabrication. We developed toy models and experimentally demonstrated a new approach to controlling the humidity within packaging and through theory calculations showed its potential for HEA-AA based thin-film sensors. We carried out experimental studies leveraging these buffered sensors, which while promising remain incomplete.

This chapter represents a significant step towards taking the HEA-AA sensing polymer from bench top to bedside, however significant further work is needed. A full understanding of the HBMs and the slow decay seen in the packaged sensors is needed. As discussed before, this decay need not be fully arrested, however it must be well understood enough to model the behavior consistently. With these present results, we can propose one application in which this should be a minimal problem, heat mapping insoles for detection of diabetic foot ulceration. As the patient should remove their shoes every night and only relative heat across the heat map are required, renulling of each sensing element to a single conventional thermistor can be performed overnight after the temperature has normalized across the map. This represents a significant application for this technology that should be viable within the near-term.

References

(1) Li, Y.; Bai, N.; Chang, Y.; Liu, Z.; Liu, J.; Li, X.; Yang, W.; Niu, H.; Wang, W.; Wang, L.; Zhu, W.; Chen, D.; Pan, T.; Guo, C. F.; Shen, G. Flexible Iontronic Sensing. *Chem. Soc. Rev.* **2025**. https://doi.org/10.1039/D4CS00870G.

(2) Yiming, B.; Guo, X.; Ali, N.; Zhang, N.; Zhang, X.; Han, Z.; Lu, Y.; Wu, Z.; Fan, X.; Jia, Z.; Qu, S. Ambiently and Mechanically Stable Ionogels for Soft Ionotronics. *Adv. Funct. Mater.* **2021**, *31* (33), 2102773. https://doi.org/10.1002/adfm.202102773.

(3) Yang, S.; Liu, Q.; Ren, J.; Ling, S. Influence of Hydrated Protons on Temperature and Humidity Responsiveness of Silk Fibroin Hydrogel Ionotronics. *Giant* **2021**, *5*, 100044. https://doi.org/10.1016/j.giant.2020.100044.

(4) Choi, S.-G.; Kang, S.-H.; Lee, J.-Y.; Park, J.-H.; Kang, S.-K. Recent Advances in Wearable Iontronic Sensors for Healthcare Applications. *Front. Bioeng. Biotechnol.* **2023**, *11*. https://doi.org/10.3389/fbioe.2023.1335188.

(5) Kim, J.-E.; Kim, S.-S.; Zuo, C.; Gao, M.; Vak, D.; Kim, D.-Y. Humidity-Tolerant Roll-to-Roll Fabrication of Perovskite Solar Cells via Polymer-Additive-Assisted Hot Slot Die Deposition. *Adv. Funct. Mater.* **2019**, *29* (26), 1809194. https://doi.org/10.1002/adfm.201809194.

(6) Greener, J. Roll-to-Roll Manufacturing. In *Roll-to-Roll Manufacturing*; John Wiley & Sons, Ltd, 2018; pp 1–17. https://doi.org/10.1002/9781119163824.ch1.

(7) Soueid, A.; Teague, E. C.; Murday, J. Temperature and Humidity Control. In *Buildings for Advanced Technology*; Soueid, A., Teague, E. C., Murday, J., Eds.; Springer International Publishing: Cham, 2015; pp 21–34. https://doi.org/10.1007/978-3-319-24892-9_3.

(8) Bell, S.; Benyon, R.; Böse, N.; Heinonen, M. A Roadmap for Humidity and Moisture Measurement. *Int. J. Thermophys.* **2008**, *29* (5), 1537–1543. https://doi.org/10.1007/s10765-008-0419-8.

(9) Xu, X. Design of Temperature and Humidity Control System for Semiconductor Manufacturing Workshop. In *Third International Conference on New Materials, Machinery, and Vehicle Engineering (NMMVE 2024)*; SPIE, 2024; Vol. 13420, pp 397–403. https://doi.org/10.1117/12.3055249.

(10) Erlat, A. G.; Yan, M.; R. Duggal, A. Substrates and Thin-Film Barrier Technology for Flexible Electronics. In *Flexible Electronics: Materials and Applications*; Wong, W. S., Salleo, A., Eds.; Springer US: Boston, MA, 2009; pp 413–449. https://doi.org/10.1007/978-0-387-74363-9_13.

(11) Vacca, P. 8 - Flexible Barriers and Packaging. In *Organic Flexible Electronics*; Cosseddu, P., Caironi, M., Eds.; Woodhead Publishing Series in Electronic and Optical Materials; Woodhead Publishing, 2021; pp 225–248. https://doi.org/10.1016/B978-0-12-818890-3.00008-4.

(12) Dhere, N. G. Flexible Packaging for PV Modules. In *Reliability of Photovoltaic Cells, Modules, Components, and Systems*; SPIE, 2008; Vol. 7048, pp 206–215. https://doi.org/10.1117/12.795718.

(13) Bayus, J. Environmental Life Cycle Comparison of Aluminum-Based High Barrier Flexible Packaging Laminates. *Theses* **2015**.

(14) WILSON, R. E.; FUWA, TYLER. Humidity Equilibria of Various Common Substances. *J. Ind. Eng. Chem.* **1922**, *14* (10), 913–917. https://doi.org/10.1021/ie50154a017.

(15) Carr, D. S.; Harris, B. L. Solutions for Maintaining Constant Relative Humidity. *Ind. Eng. Chem.* **1949**, *41* (9), 2014–2015. https://doi.org/10.1021/ie50477a042.

(16) Greenspan, L. Humidity Fixed Points of Binary Saturated Aqueous Solutions. *J. Res. Natl. Bur. Stand. Sect. Phys. Chem.* **1977**, *81A* (1), 89–96. https://doi.org/10.6028/jres.081A.011.

(17) Eggert, G. Saturated Salt Solutions in Showcases: Humidity Control and Pollutant Absorption. *Herit. Sci.* **2022**, *10* (1), 54. https://doi.org/10.1186/s40494-022-00689-3.

(18) Abadie, M. O.; Mendonça, K. C. Moisture Performance of Building Materials: From Material Characterization to Building Simulation Using the Moisture Buffer Value Concept. *Build. Environ.* **2009**, *44* (2), 388–401. https://doi.org/10.1016/j.buildenv.2008.03.015.

(19) Cerolini, S.; D'Orazio, M.; Di Perna, C.; Stazi, A. Moisture Buffering Capacity of Highly Absorbing Materials. *Energy Build.* **2009**, *41* (2), 164–168. https://doi.org/10.1016/j.enbuild.2008.08.006.

(20) Cascione, V.; Maskell, D.; Shea, A.; Walker, P. A Review of Moisture Buffering Capacity: From Laboratory Testing to Full-Scale Measurement. *Constr. Build. Mater.* **2019**, *200*, 333–343. https://doi.org/10.1016/j.conbuildmat.2018.12.094.

(21) Egberg, D. C.; Esse, R. L. Humidity Control System for Wood Products. US8748723B1, June 10, 2014. https://patents.google.com/patent/US8748723B1/en?q=(Boveda)&oq=Boveda (accessed 2025-05-17).

(22) Biernath, R. W.; Schmitz, J. L.; Esse, R. L.; Knutsen, S. A.; Rice, B. Systems, Methods and Devices for Controlling Humidity in a Closed Environment with Automatic and Predictive Identification, Purchase and Replacement of Optimal Humidity Controller. US10909607B2, February 2, 2021. https://patents.google.com/patent/US10909607B2/en?q=(Boveda)&oq=Boveda (accessed 2025-05-17).

(23) O'Shea, T.; Esse, R. L.; DeVries, J. W.; Rice, B. Humidity Control Slurries, Apparatuses, and Methods of Making Same. US20230285894A1, September 14, 2023. https://patents.google.com/patent/US20230285894A1/en?q=(Boveda)&oq=Boveda&page=1 (accessed 2025-05-17).

(24) Egberg, D. C.; Esse, R. L. Devices and Methods for Controlling Headspace Humidity and Oxygen Levels. US10201612B2, February 12, 2019. https://patents.google.com/patent/US10201612B2/en?q=(Boveda)&oq=Boveda (accessed 2025-05-17).

(25) *Two Way Humidity Control Packs - Boveda® Official Site*. Boveda® New Official-Site. https://bovedainc.com/ (accessed 2025-05-17).

(26) Products, I. *How Integra Boost® Works*. Integra Products. https://integra-products.com/pages/how-integra-works (accessed 2025-05-17).

(27) Kim, T. H.; Zhou, Z.; Choi, Y. S.; Costanza, V.; Wang, L.; Bahng, J. H.; Higdon, N. J.; Yun, Y.; Kang, H.; Kim, S.; Daraio, C. Flexible Biomimetic Block Copolymer Composite for Temperature and Long-Wave Infrared Sensing. *Sci. Adv.* **2023**, *9* (6), eade0423. https://doi.org/10.1126/sciadv.ade0423.

(28) Wang, B.; Lai, J.; Li, H.; Hu, H.; Chen, S. Nanostructured Vanadium Oxide Thin Film with High TCR at Room Temperature for Microbolometer. *Infrared Phys. Technol.* **2013**, *57*, 8–13. https://doi.org/10.1016/j.infrared.2012.10.006.

(29) Dai, J.; Wang, X.; He, S.; Huang, Y.; Yi, X. Low Temperature Fabrication of VOx Thin Films for Uncooled IR Detectors by Direct Current Reactive Magnetron Sputtering Method. *Infrared Phys. Technol.* **2008**, *51* (4), 287–291. https://doi.org/10.1016/j.infrared.2007.12.002.

(30) Park, J.; Kim, M.; Lee, Y.; Lee, H. S.; Ko, H. Fingertip Skin–Inspired Microstructured Ferroelectric Skins Discriminate Static/Dynamic Pressure and Temperature Stimuli. *Sci. Adv.* **2015**, *1* (9), e1500661. https://doi.org/10.1126/sciadv.1500661.

(31) Natishan, P. M.; O'Grady, W. E. Chloride Ion Interactions with Oxide-Covered Aluminum Leading to Pitting Corrosion: A Review. *J. Electrochem. Soc.* **2014**, *161* (9), C421. https://doi.org/10.1149/2.1011409jes.

(32) Kubáň, P.; Hauser, P. C. A Review of the Recent Achievements in Capacitively Coupled Contactless Conductivity Detection. *Anal. Chim. Acta* **2008**, *607* (1), 15–29. https://doi.org/10.1016/j.aca.2007.11.045.

(33) Gregory J. Tudryn, Michael V. O'Reilly, Shichen Dou, Daniel R. King, Karen I. Winey, James Runt, and Ralph H. Colby *Macromolecules* **2012** *45* (9), 3962-3973 DOI: 10.1021/ma202273j.

(34) *Conductive*. Conductive. https://print-your-electronics-with-loctite.com/Conductive (accessed 2025-05-17).

(35) Saxena, R. S.; Bhan, R. K.; Aggrawal, A. Reducing Readout Complexity of Large Resistive Sensor Arrays. *IEEE Sens. J.* **2008**, *8* (11), 1862–1863. https://doi.org/10.1109/JSEN.2008.2005165.

(36) Yarahmadi, R.; Safarpour, A.; Lotfi, R. An Improved-Accuracy Approach for Readout of Large-Array Resistive Sensors. *IEEE Sens. J.* **2016**, *16* (1), 210–215. https://doi.org/10.1109/JSEN.2015.2477494.

(37) Hidalgo-López, J. A.; Romero-Sánchez, J.; Fernández-Ramos, R. New Approaches for Increasing Accuracy in Readout of Resistive Sensor Arrays. *IEEE Sens. J.* **2017**, *17* (7), 2154–2164. https://doi.org/10.1109/JSEN.2017.2662803.

(38) Cros, S.; de Bettignies, R.; Berson, S.; Bailly, S.; Maisse, P.; Lemaitre, N.; Guillerez, S. Definition of Encapsulation Barrier Requirements: A Method Applied to Organic Solar Cells. *Sol. Energy Mater. Sol. Cells* **2011**, *95*, S65–S69. https://doi.org/10.1016/j.solmat.2011.01.035.

(39) Lagerkvist, B. J.; Lindell, B. *The Nordic Expert Group for Criteria Documentation of Health Risks from Chemicals : 131. Lithium and Lithium Compounds*; Arbetslivsinstitutet, 2002.

(40) Kamali, A. R.; Fray, D. J.; Schwandt, C. Thermokinetic Characteristics of Lithium Chloride. *J. Therm. Anal. Calorim.* **2010**, *104* (2), 619–626. https://doi.org/10.1007/s10973-010-1045-9.

(41) Paul E. Keller; Richard Kouzes. *Water Vapor Permeation in Plastics*; PNNL-26070; Pacific Northwest National Laboratory, 2017. https://www.pnnl.gov/main/publications/external/technical_reports/PNNL-26070.pdf (accessed 2025-05-17).

(42) Tsamis, E. D.; Avaritsiotis, J. N. Design of Planar Capacitive Type Sensor for "Water Content" Monitoring in a Production Line. *Sens. Actuators Phys.* **2005**, *118* (2), 202–211. https://doi.org/10.1016/j.sna.2004.07.008.

(43) Dahim, M.; Al-Mattarneh, H.; Ismail, R. Simple Capacitor Dielectric Sensors for Determination of Water Content in Transformer Oil. *Int. J. Eng. Technol.* **2018**, *7* (3.32), 157–160. https://doi.org/10.14419/ijet.v7i3.32.24667.

(44) Zhou, Y. R.; Effendy, S.; Zhu, J.; Petr, M. T.; Cwalina, C. D.; Bazant, M. Z.; Yildiz, B.; Li, J.; Short, M. P. Coupled Effect of Water Absorption and Ion Transport in Hydrated Latex Anti-Corrosion Coatings. *J. Coat. Technol. Res.* **2023**, *20* (1), 187–200. https://doi.org/10.1007/s11998-022-00676-0.

Chapter 6

OBSERVATIONS AND OUTLOOK

6.0 Chapter Preamble

This chapter provides a window into unusual observations made during this thesis work, factors not explored in other chapters that we believe may influence HEA-AA performance, and proposes some future directions for the work. It is aimed squarely at providing useful information to the next generation of researchers working on HEA-AA or other ionotronic temperature sensors.

6.1 Crystallization in ion-HEA-AA

One of the most enduring mysteries in the saga of HEA-AA is the formation of crystalline regions within the polymer. Early spectroscopic studies into HEA-AA comprised examining the polymer with a wide array of different di- and trivalent metal chlorides. It was observed that drop casting dilute $CuCl_2$-HEA-AA onto a glass slide on most days produces an opaque film due to the formation of what appeared to be crystalline regions (Fig. 6.1(a)). As there was interest in this crystal formation, a day was selected when crystallization was observed in the pectin lab. After confirming crystallization within the pectin lab, the preparation materials were moved < 100 ft through an open doorway to the microscopy station in the adjacent room. When multiple samples were cast, at the microscopy station, both under the microscope and on the bench top, crystallization was not observed. When the preparation materials were moved back into the pectin lab and another sample was prepared, crystallization occurred. From this we speculate that minute differences in the temperature and humidity during casting can cause large changes morphology of the produced film. Further experiments have found that when $CuCl_2$-HEA-AA is cast from a more concentrated (higher viscosity) solution, immediate crystallization has not been observed.

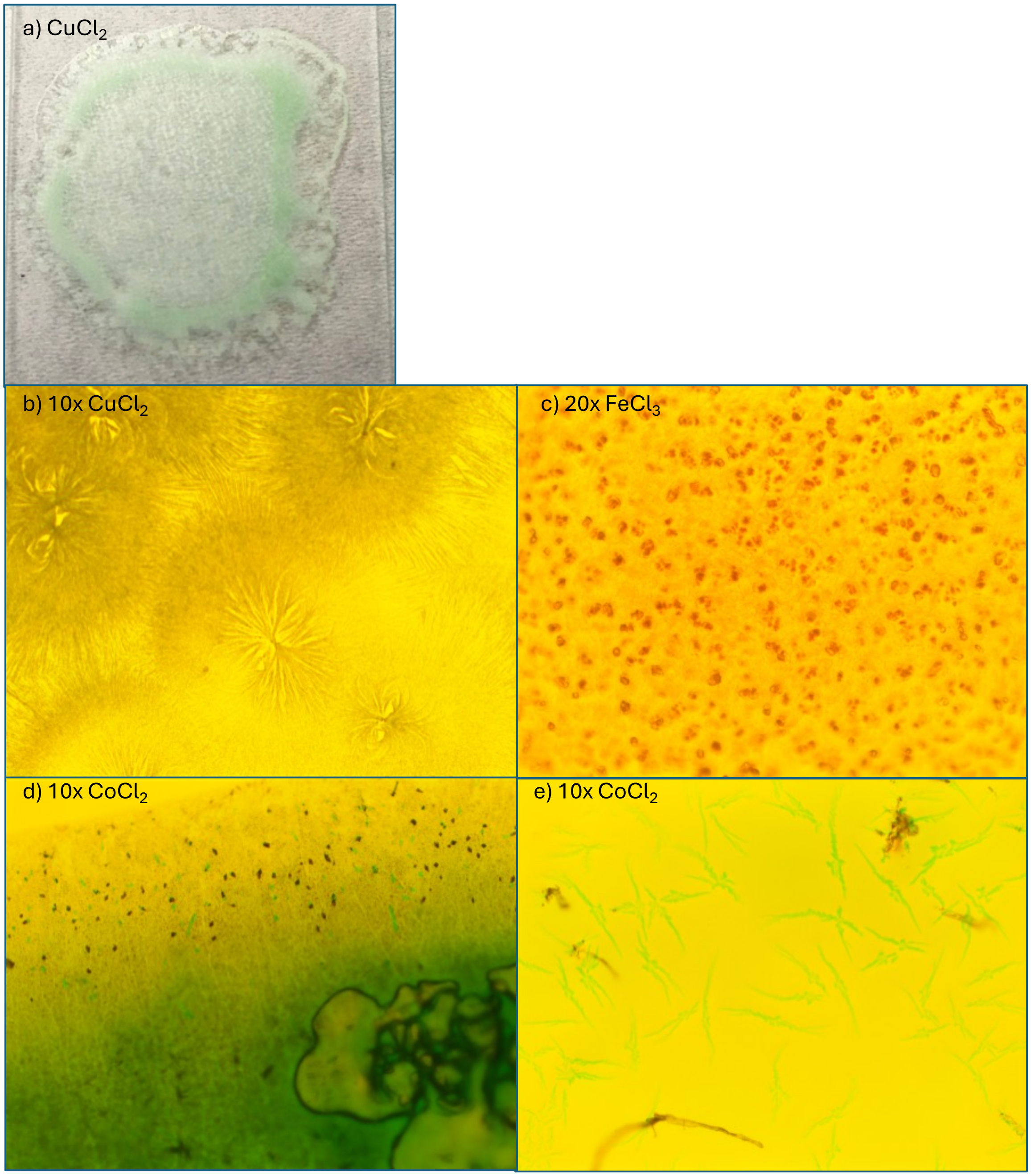

Figure 6.1: Images of various crystalline regions within HEA-AA films. (a) $CuCl_2$-HEA-AA film exhibiting opacity driven by crystal formation. (b) Microscopy of $CuCl_2$-HEA-AA (10x). (c) Microscopy of $FeCl_3$-HEA-AA (20x). (d) Microscopy of $CoCl_2$-HEA-AA under standard concentration(10x). (e) Microscopy of $CoCl_2$-HEA-AA under ½ standard concentration (10x).

Puzzled by this phenomenon, microscopy was carried out on a variety of older spectroscopy samples each prepared by drop casting dilute solutions onto glass slides. While not observed for every sample, nor every sample that nominally was prepared and stored in the similar manners, many samples exhibited microscopic regions that appeared to show crystallization. The $CuCl_2$-HEA-AA samples showed this distinct star pattern (Fig. 6.1(b)). The $FeCl_3$-HEA-AA samples showed blocky crystals (Fig. 6.1(c)). While the $CoCl_2$-HEA-AA samples showed these long thin structures (Fig 6.1(d)). When we examined some samples at ½ typical $CoCl_2$ ion loading, the crystals observed were seen to be somewhat longer (Fig. 6.1(e)). When we examined one $CoCl_2$-HEA-AA sample at 1/40th typical ion loading, occasional points of distinct coloration appearing to be potentially small regions of crystallization were still observed.

A reasonable question arises when examining these microscopy images, are the regions really crystallization or originating from some other polymer film morphology? To address this concern, film x-ray diffraction (XRD, Rigaku SmartLab) was performed on a $CoCl_2$-HEA-AA, $CuCl_2$-HEA-AA, and $FeCl_2$-HEA-AA films exhibiting crystalline regions under microscopy. Additionally, a $CaCl_2$-HEA-AA film was included. The $CaCl_2$-HEA-AA and $FeCl_3$-HEA-AA films were found to exhibit no distinct peaks, while the $CoCl_2$-HEA-AA and $CuCl_2$-HEA-AA films were found to exhibit distinct diffraction spectra that did not match other spectra within the powder x-ray diffraction database (Fig. 6.2). This demonstrates clear crystal formation within these films. An extraction of 3D crystal parameters from this one-dimensional data is beyond the scope of this thesis.[1–3]

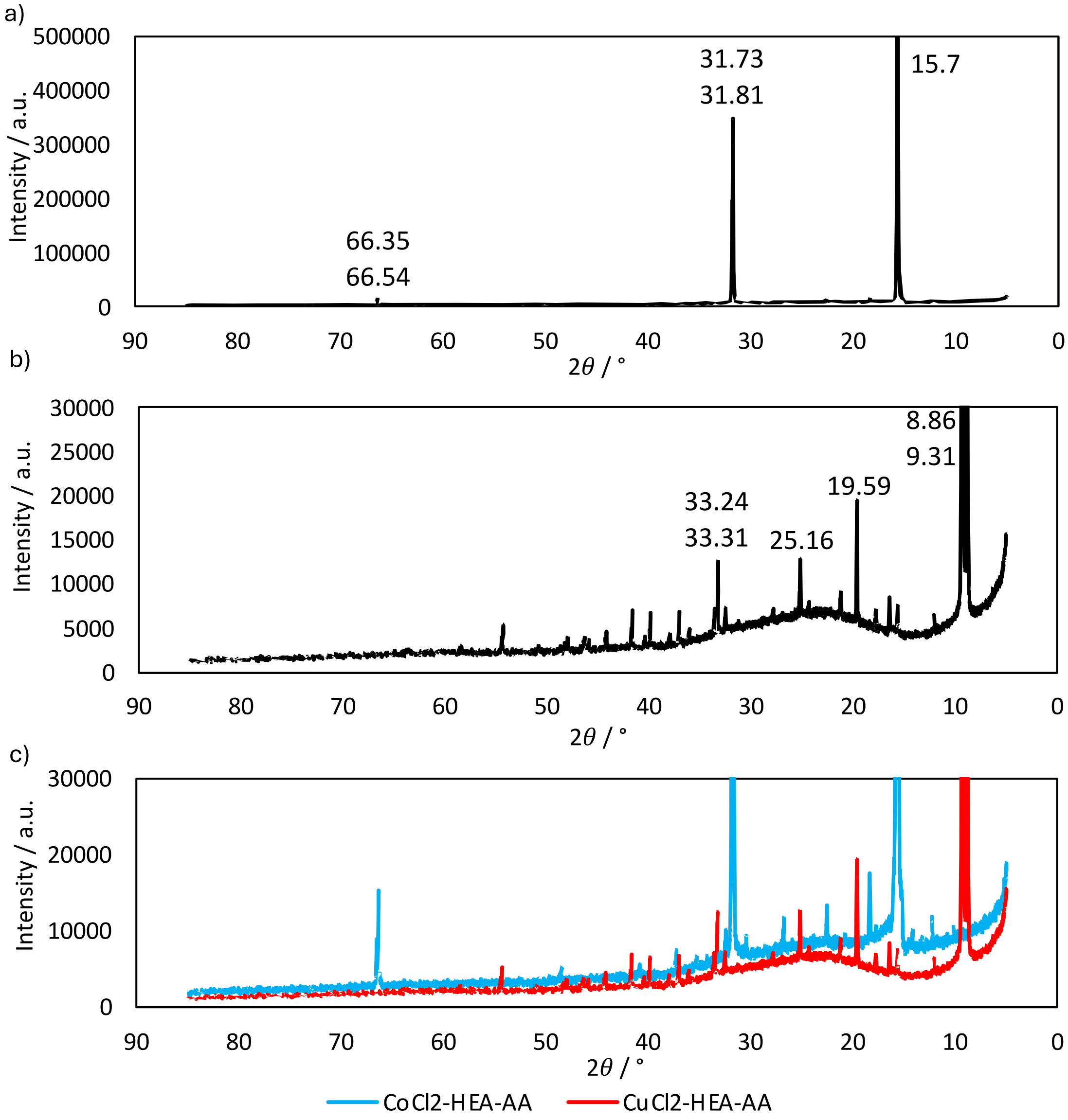

Figure 6.2: XRD of HEA-AA films exhibiting crystal formation. (a) $CoCl_2$-HEA-AA. (b) $CuCl_2$-HEA-AA. (c) Comparison of the ions.

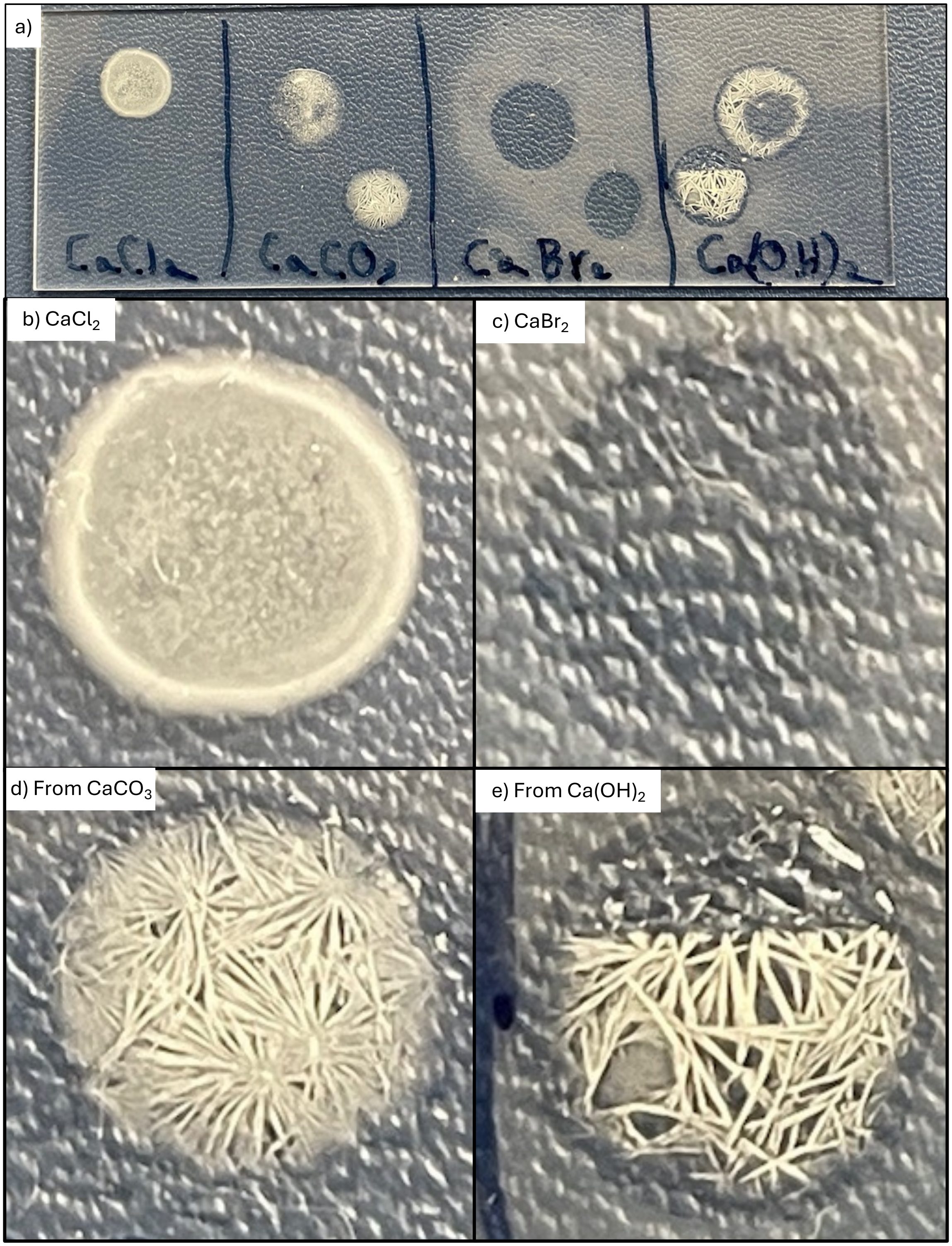

Figure 6.3: Crystal formation in old calcium films. (a) Variety of films exhibiting crystal formation. (b) $CaCl_2$-HEA-AA film exhibiting small crystal formation. (c) $CaBr_2$-HEA-AA film exhibiting no visible crystallization. (d) Ca^{2+}-HEA-AA anion free film prepared from $CaCO_3$

exhibiting large crystal growth. (e) Ca^{2+}-HEA-AA anion free film prepared from $Ca(HO)_2$ exhibiting large crystal growth.

As shown in Chapter 3, the blue coloration within our $CoCl_2$-HEA-AA films is consistent with tetrachlorocobaltate, as the crystalline regions in these films show this distinct blue coloration (Fig 6.1(d-e), due to instrumentation issues a yellow filter is shifting the coloration in the images). From this one may wonder if these crystalline regions consist of the tetrachlorometallate salts. While it appears the $CoCl_2$-HEA-AA crystalline regions likely contain tetracchlorocobaltate, we can see from the following data that the presence of the chloride is not necessary to produce crystalline regions. For a spectroscopic study, $CaCl_2$-HEA-AA, $CaBr_2$-HEA-AA, and two Ca^{2+}-HEA-AA films, one prepared by the reaction of $CaCO_3$ with HEA-AA, the other prepared by the reaction of $Ca(OH)_2$, were drop cast from concentrated (high viscosity) ethanol solution onto the same glass slide. No crystalized regions were observed at this time. The film became a demo sample that was pulled out for laboratory tours. As such it was rarely interacted with but was subjected to heating at 60 °C under room air, bench top storage, and storage under dry nitrogen. After a few months of non-observation, crystalline regions were observed to have grown (Fig. 6.3(a)). The $CaCl_2$-HEA-AA film was observed to grow small crystalline regions (Fig. 6.3(b)). The $CaBr_2$-HEA-AA film was observed to produce no crystalline regions (Fig. 6.3(c)). While the two anion free Ca^{2+}-HEA-AA films were observed to produce large crystalline regions (Fig. 6.3(d-e)). While considered, a method of extracting these crystalline regions for x-ray studies was not found. However, this demonstrates that the anion need not be present for these crystalline regions to form in the polymer.

For now, the mechanism of the crystal formation, the factors that lead to its formation, and the structure of the crystalline regions remain mysteries. Further studies leveraging the microcrystal electron diffraction may shed a light on these structures.[4–6] Studies leveraging the humidity-controlled glovebox may provide new insights into the factors that drive crystal formation. If the macroscopic crystals observed in Fig. 6.3(d-e) can be consistently produced, studies into the effect of these crystal regions on both the bulk and localized electrical properties may provide exciting insights into both these regions of the polymer and the mechanisms of charge transport.

6.2 Factors That May Affect the Polymer's Performance

In this section, we will explore factors that may significantly affect the polymer's performance that we find are understudied and warrant further investigations and/or controls during materials processing. This discussion is not meant to be all inclusive.

6.2.1 Purity During Synthesis.

During our typical synthesis of the polymer, a precipitation in diethyl ether is carried out to remove monomers and other impurities. The necessity of this purification step is often debated as to if it affects device performance and industry partners would greatly prefer this purification step being removed. Additionally, once the polymer is dissolved in ethanol, the solution can take a slightly cloudy appearance, this is often removed through a syringe filtration. The identity of this solid has not been determined, nor has its effect on device performance and stability been evaluated. Systematic studies examining the effects of these purification steps on device performance are warranted.

6.2.2 HEA/AA Ratio.

If the synthesis is carried out properly every time, the ratio of 2-hydroxyethyl acrylate (HEA) to acrylic acid (AA) should remain fixed, however, the verification of this via NMR is rarely carried out. Furthermore, although there is limited experimental results regarding the HEA/AA ratio in the BTS polymer (Fig. 2.2(d)), these measurements were carried out without humidity controls.[7] We expect variations in these ratios to lead to variations in the hydrophilicity, the hydrogen bonding interactions, and the binding of metal ions. Detailed studies in the effect of varying the HEA/AA ratio are warranted in addition to occasional QC measurements after polymer synthesis. Without these studies we cannot reliably know how vital this synthetic parameter is.

6.2.3 Chain Length and Dispersity

Similarly, the chain length and dispersity of the produced polymer is rarely characterized. However, changes in the chain length should have direct effects on the glass transition temperature of the polymer and the chain segmental motion.[8,9] As shown in Chapter 3, the chain segmental motion plays a critical role in the charge transport. As such this critical parameter warrants a careful study into its effects and verification of the degree of variation synthesis to synthesis. Preliminary NMR studies carried out during reaction scale-up showed variations from chain lengths of 57 to 75 monomers.

6.2.4 Viscosity During Casting

As discussed in section 6.1, the morphology of the produced polymer film is highly dependent on the viscosity of the casting solution. During the drop casting procedure, the viscosity coupled with the surface tension governs the thickness of the resulting film. Furthermore, low viscosity solutions lead to a strong coffee ring effect with notable thickness variations (Fig. 6.1(a)).[10,11]

In preparing samples for measurement on the polyimide circular interdigitated electrodes, if the sample is too thin, the measured currents will be below the noise floor once the sample is dried (Fig. 5.5). One approach to resolve this with low viscosity polymer solutions is repeated casting until the desired thickness is reached. This approach can work, however frequently leads to trapped pockets of air and/or solvent within the resulting polymer. These pockets can swell into bubbles upon heating of the sensors causing disruptions to measurements of the electrical properties.

If the polymer is instead cast from a high viscosity solution (between honey and molasses), a single casting of the polymer can produce a sufficiently thick sample. As long as air bubbles are not introduced from pipette tip motions and the sample is not initially dried too hot, bubble formation does not occur during temperature cycling electrical measurements.

6.2.4 Ion Concentration

For the vast majority of studies discussed in this thesis, the concentration of the ions within the polymer remained fixed. This is somewhat critical as at high ion concentrations, the ion-ion interactions can start to affect the charge transport.[12] We would expect that changes in the ion concentration may lead to changes in the response and the sensitivity of the polymer to humidity. This is especially relevant as the metal carbonate prepared films cannot be prepared to the standard concentration for these studies due to incomplete reaction between the polymer and the salt. A systematic study examining the effects of ion concentration on the electrical properties of the polymer is critical. A preliminary study (Fig. 6.4) shows that the effect of ion concentration appears to be significant, however, as this data set is plagued by instrumentation issues, further studies are needed.

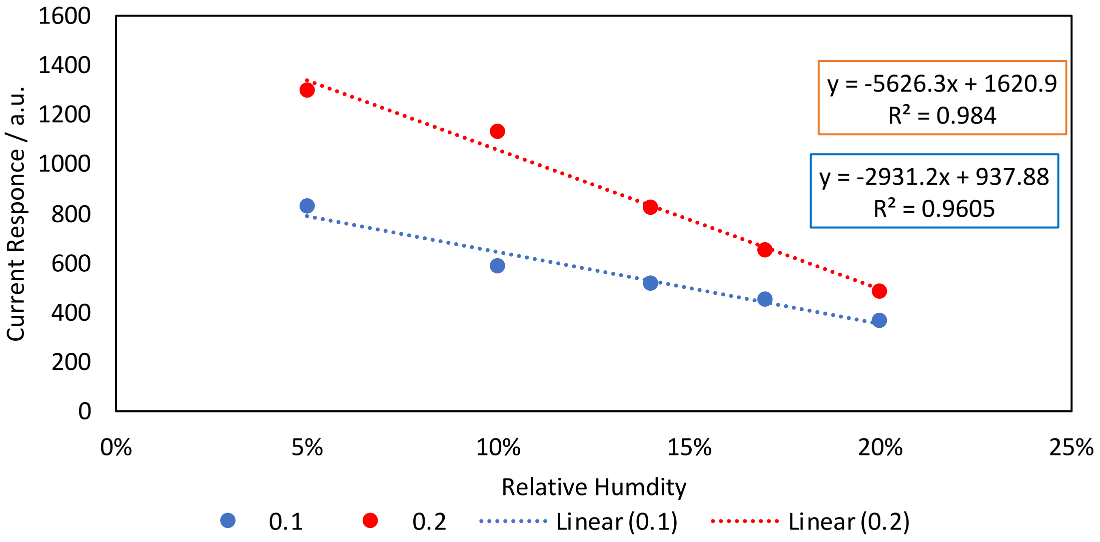

Figure 6.4: Current responses at various humidities for $CaCl_2$-HEA-AA at two ion concentrations.

6.2.5 Temperature and Humidity During Casting

As examined in section 6.1, we suspect that the temperature and humidity may play a significant role in the morphology of the polymer film after casting. We suspect this is driven by solvent evaporation rates and water driven formation of interpolymer complex hydrogen bonding networks (IPC) within the polymer. To date, the temperature and humidity during casting has largely remained uncontrolled. By leveraging the humidity-controlled glovebox, we can systematically look at how relative humidity and temperature during casting effect the performance of the films.

6.2.6 Solvent Water Content

Similar to the previous point, the casting solvent, ethanol, is hydroscopic and will uptake water from the air. In the current studies, the casting solvent is largely assumed to not contain meaningful quantities of water. However, it was found during cobalt chloride spectroscopy studies that some of the ethanol solvent containers where grossly contaminated with water. If this is not accounted for we would expect this to affect the film morphology both through changes to the solvent evaporation rates and changes to the formation of hydrogen bonding networks.

6.2.7 Drying Temperature and Conditions

Understanding the effects of drying conditions on the polymer performance is critical to producing useful polymer films. It has been observed that transferring the polymer to elevated temperatures such as during hot plate drying, or placing the samples within a vacuum chamber too soon after the polymer is cast can lead to bubble formation. However, once this window has past, successful devices have been prepared by drying the samples in all of the following methods: 1) Drying the samples on a hot plate on the bench top (50-70 °C). 2) Drying the samples in a vacuum chamber. 3) Drying the samples under dry nitrogen purge. 4) Drying the samples on the electrical measurement apparatus either at elevated temperature or cycling temperature. Most typically samples are dried initially on the hot plate before being stored under nitrogen purge. Note, due to the hydroscopic nature of the samples it is critical that samples on polyimide boards are stored dry either at elevated temperatures or under nitrogen purge as otherwise the Au/Cu electrodes will show corrosion of the copper.

6.3 Future Directions

In this section we will outline several future research directions for this material.

6.3.1 Variations in the HEA-AA Monomers

As discussed in Chapter 3, questions remain about details of the mechanism driving the high temperature response. Additionally, we suspect that other polymers may lead to an even higher temperature response. To improve our understanding of HEA-AA and develop this next generation of ion conductive temperature sensing polymers, we propose a systematic variation to the monomers comprising HEA-AA to explore three core questions. First, how changes to the ion binding strength of the acrylic acid affects the electrical properties and the temperature response. Second, how changes to degree and strength of the IPC affect the electrical properties and temperature response. Finally, how changes that affect the chain mobility and/or glass transition temperature drive the electrical properties and temperature response.

6.3.2 Simultaneous Electrical and Spectroscopic Measurement

Our current understanding of current vs humidity behavior in ion-HEA-AA systems does not provide us with quantifiable values for how the water content of the polymer affects electrical properties. Nor does it tell us how water content correlates with the relative humidity. This value would be extremely useful for both device development/modeling (Chapter 5), and for enabling molecular mechanics simulations. We believe a powerful approach to resolve this question is simultaneous electrical and NIR/IR measurements under controlled humidities. The development of an instrument enabling these should be a high priority.

6.3.3 Mechanical Properties of HEA-AA

While some studies have been conducted on the mechanical properties of HEA-AA composite materials, to date, no studies on pure HEA-AA or ion-HEA-AA's mechanical properties have been quantitative. It is apparent that the mechanical properties should vary depending on the ions present, the ion concentration, and the polymer's water content. As such each of these factors should be studied within the framework of the material's mechanical properties. These measurements will likely be comprised of a combination of rheology and film on elastomer tensile testing. While this work may provide interesting data sets for fundamental science, its primary value is for the development of devices. Knowledge about the mechanical properties of the polymer in various humidity states is critical for the design and manufacturing of commercial devices.

6.3.4 Temperature Extremes Sensor Performance and Stability

When discussing the development of commercializable sensors, two core questions are repeatedly asked, first, what is the measurement range of the sensor, and second, what is the stability range of the sensor for shipping and storage. In our case, the current limits of the measurement range that has been evaluated 10 °C – 65 °C is limited by the current instrumentation. However, further studies are needed to expand this range to the materials limits.

Similarly, the storage stability limitations have not been fully explored. Typical sensor drying can occur at 70 °C without noticeable sample degradation. However, a preliminary high temperature trial comprised of 140 °C for 48 hrs led to discoloration of the polyimide board and the current response (25-65 °C) shifted from > 1000 before treatment to < 10. Further trials are needed to establish the high temperature stability of the polymer. The low temperature limits of the sensor's stability similarly needs to be explored.

6.3.5 Sensor Development

As discussed in Chapter 5, further work into sensor development, packaging, and the humidity buffer material is critical to transition these materials from the lab bench to the factory.

6.4 Conclusions on Outlook

HEA-AA sensors represent a potential breakthrough for both IR imaging and healthcare. But before they are ready to impact people's lives, many open questions must be answered. To reach these goals, the research directions must simultaneously solve fundamental science questions relate to the mechanism/behavior of the polymer and ions, at the same time make strides towards solving the issues that prevent commercialization and explore the application space of the material.

References

(1) Hušák, M.; Jegorov, A.; Czernek, J.; Rohlíček, J.; Žižková, S.; Vraspír, P.; Kolesa, P.; Fitch, A.; Brus, J. Successful Strategy for High Degree of Freedom Crystal Structure Determination from Powder X-Ray Diffraction Data: A Case Study for Selexipag Form I with 38 DOF. *Cryst. Growth Des.* **2019**, *19* (8), 4625–4631. https://doi.org/10.1021/acs.cgd.9b00517.

(2) E. Hughes, C.; Manjunatha Reddy, G. N.; Masiero, S.; P. Brown, S.; Andrew Williams, P.; M. Harris, K. D. Determination of a Complex Crystal Structure in the Absence of Single Crystals: Analysis of Powder X-Ray Diffraction Data, Guided by Solid-State NMR and Periodic DFT Calculations, Reveals a New 2′-Deoxyguanosine Structural Motif. *Chem. Sci.* **2017**, *8* (5), 3971–3979. https://doi.org/10.1039/C7SC00587C.

(3) Lai, Q.; Xu, F.; Yao, L.; Gao, Z.; Liu, S.; Wang, H.; Lu, S.; He, D.; Wang, L.; Zhang, L.; Wang, C.; Ke, G. End-to-End Crystal Structure Prediction from Powder X-Ray Diffraction. *Adv. Sci.* **2025**, *12* (8), 2410722. https://doi.org/10.1002/advs.202410722.

(4) Jones, C. G.; Martynowycz, M. W.; Hattne, J.; Fulton, T. J.; Stoltz, B. M.; Rodriguez, J. A.; Nelson, H. M.; Gonen, T. The CryoEM Method MicroED as a Powerful Tool for Small Molecule Structure Determination. *ACS Cent. Sci.* **2018**, *4* (11), 1587–1592. https://doi.org/10.1021/acscentsci.8b00760.

(5) Nannenga, B. L.; Gonen, T. MicroED: A Versatile cryoEM Method for Structure Determination. *Emerg. Top. Life Sci.* **2018**, *2* (1), 1–8.

https://doi.org/10.1042/ETLS20170082.

(6) Mu, X.; Gillman, C.; Nguyen, C.; Gonen, T. An Overview of Microcrystal Electron Diffraction (MicroED). *Annu. Rev. Biochem.* **2021**, *90* (Volume 90, 2021), 431–450. https://doi.org/10.1146/annurev-biochem-081720-020121.

(7) Kim, T. H.; Zhou, Z.; Choi, Y. S.; Costanza, V.; Wang, L.; Bahng, J. H.; Higdon, N. J.; Yun, Y.; Kang, H.; Kim, S.; Daraio, C. Flexible Biomimetic Block Copolymer Composite for Temperature and Long-Wave Infrared Sensing. *Sci. Adv.* **2023**, *9* (6), eade0423. https://doi.org/10.1126/sciadv.ade0423.

(8) Wang, Y.; Fan, F.; Agapov, A. L.; Saito, T.; Yang, J.; Yu, X.; Hong, K.; Mays, J.; Sokolov, A. P. Examination of the Fundamental Relation between Ionic Transport and Segmental Relaxation in Polymer Electrolytes. *Polymer* **2014**, *55* (16), 4067–4076. https://doi.org/10.1016/j.polymer.2014.06.085.

(9) O'Driscoll, K.; Sanayei, R. A. Chain-Length Dependence of the Glass Transition Temperature. *Macromolecules* **1991**, *24* (15), 4479–4480. https://doi.org/10.1021/ma00015a038.

(10) Yang, M.; Chen, D.; Hu, J.; Zheng, X.; Lin, Z.-J.; Zhu, H. The Application of Coffee-Ring Effect in Analytical Chemistry. *TrAC Trends Anal. Chem.* **2022**, *157*, 116752. https://doi.org/10.1016/j.trac.2022.116752.

(11) Kaliyaraj Selva Kumar, A.; Zhang, Y.; Li, D.; Compton, R. G. A Mini-Review: How Reliable Is the Drop Casting Technique? *Electrochem. Commun.* **2020**, *121*, 106867. https://doi.org/10.1016/j.elecom.2020.106867.

(12) Dobrynin, A. V.; Colby, R. H.; Rubinstein, M. Scaling Theory of Polyelectrolyte Solutions. *Macromolecules* **1995**, *28* (6), 1859–1871. https://doi.org/10.1021/ma00110a021.

Chapter 7

CONCLUSIONS

7.1 Thesis Summary

We have explored in this thesis the development of a novel temperature sensing material comprised of an ion conductive polymer. We have examined it from both a fundamental science lens (Chapters 2-3) and an applications lens (Chapters 2,4-5). In Chapter 1, we explore the potential impacts of these materials to IR imaging and healthcare.

In Chapter 2, we introduce this polymer, poly(acrylic acid-co-2-hydroxyethyl acetate) (HEA-AA), and explore its performance and functionality within a block co-polymer. We demonstrate the large temperature sensitivity of the material and many of its electrical properties. In this section we briefly explore this material's application to temperature mapping and IR sensing. To further dive into the unique characteristics of this polymer, we explore the formation of interpolymer complex by HEA-AA and the ability of water to strip ions from the polymer.

In Chapter 3, we dove into the mechanism behind HEA-AA's record-breaking temperature response. Through ion substitution studies we demonstrate that the metal cation is necessary and sufficient to produce the large temperature response in the HEA-AA complex. From FTIR studies, we demonstrate that increases in the water content from humidity is not sufficient to free metal ions from carboxylic binding sites. From UV/Vis studies of $CoCl_2$-HEA-AA and $CoBr_2$-HEA-AA, we demonstrate that some portion of the cobalt cation ends up bound as tetrahalocobaltate despite no additional chloride being added. We discuss a potential mechanism and observe that this is also seen in $CoCl_2$-poly(acrylic acid) films. We explore that this is a mechanism that affects the number density of cobalt cations that can engage in charge transport and extrapolate that it may occur with many other salts and other systems utilizing polymers that tightly bind metal chlorides. We then demonstrate the water uptake decreases the glass transition temperature of the polymer. By applying the Vogel-

Tamman-Fulcher (VTF) model to variable-temperature variable-humidity impedance spectroscopy, we showed that water uptake primarily shifts the T_0 term, thus changes in the water content primarily affect the glass transition temperature. We additionally note the ability to superimpose the spectra implies the humidity and temperature affect the current response through the same mechanism. From this we can extrapolate the key role of chain segmental motion and speculate from the literature the potential influences of a hydrogen bonding mechanism.

In Chapter 4, we pivot to discussing the application of HEA-AA to dual heat flux (DHF) core body temperature measurement (CBT). We characterize the temperature response of a variety of metal chlorides–HEA-AA films. We demonstrate an ultra-thin DHF CBT device more than 10-fold thinner than the thinnest device we have found in the literature. We evaluate the sensor's error through finite element analysis. We evaluate the time response of our DHF sensor then demonstrate its accuracy leveraging an agar tissue phantom.

Chapter 5 explores the challenges presented by roll-to-roll fabrication of thin-film HEA-AA temperature sensors and the development of humidity buffer materials (HBM) to stabilize these sensors. We demonstrate fabrication of sandwich thin-film sensors and characterize their electrical performance. We discuss the engineering challenges presented by this class of sensor and demonstrate experimentally that they are not sufficiently sealed from environmental humidity. From this, we construct a crude toy model and demonstrate for thin sensors a substantially lower water vapor transmission rate would be required. We then discuss the architecture of the HBM and analyze its potential lifetime through a simple WVTR model. We expand to a more complete diffusion model and demonstrate that the WVTR of the humidity buffer's matrix must be substantially higher than the WVTR of the packaging. We further simulate the lifetime of the sensors for a variety of locations and demonstrate that the sensors lifetime in temperate climates far exceeds the worst-case scenario. From there we demonstrate HBMs with a variety of matrix materials and demonstrate its ability to maintain the humidity within a sealed bag. We then explore challenges in fabricating the thin-film sensors with HBMs in a roll-to-roll manner. Finally, we discuss experimental results for several trials of packaged sensors with HBMs. We discuss the limitations of this data set and substantial unknowns presented by it.

In Chapter 6, we first discuss the unusual data surrounding crystallization within the ion-HEA-AA films. We then go on to discuss factors to consider controlling for in future studies. Finally, we discuss several future directions for this research that are vital to understand the fundamental science of the HEA-AA material and vital to develop commercialize sensors.

7.2 Conclusion

In this thesis, we have made substantial steps towards understanding the mechanism behind HEA-AA temperature response. However, beyond solving fundamental science challenges, we have made substantial progress towards the commercialization of this material enabling direct impacts to peoples lives. It is this merging of hard fundamental science challenges and high societal impact within the study of a complex material that has made both working on this project and writing this thesis so fascinating.

Appendex A

SI FOR CHAPTER 2

A.1 Figures

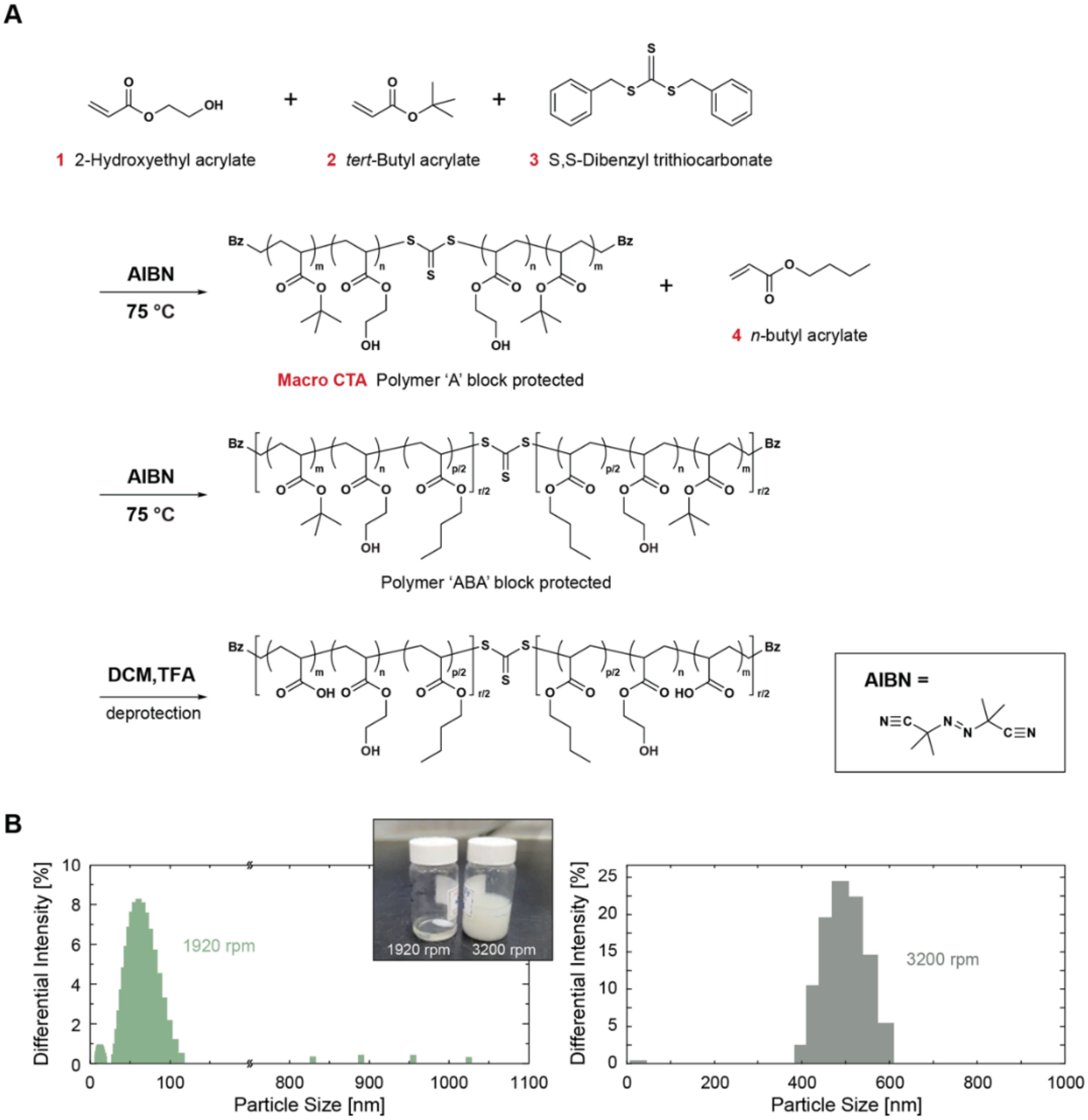

Figure A.1: Synthesis procedure of the ABA type block copolymers. (a) ABA type block copolymers are prepared via a reversible addition-fragmentation chain transfer (RAFT) polymerization method. (b) Increasing the rotation speed during sample vortex, the polymer solution became opaque. This change in opacity relative to the mixer speed is a typical behavior found in emulsion systems through Ostwald Ripening, indicating that the synthesized polymer exists in colloidal states in ethanol. The particle size in the transparent (left, 1920 rpm) and opaque solution (right, 3200 rpm) is 97 ± 29 nm and 491 ± 151 nm, respectively.

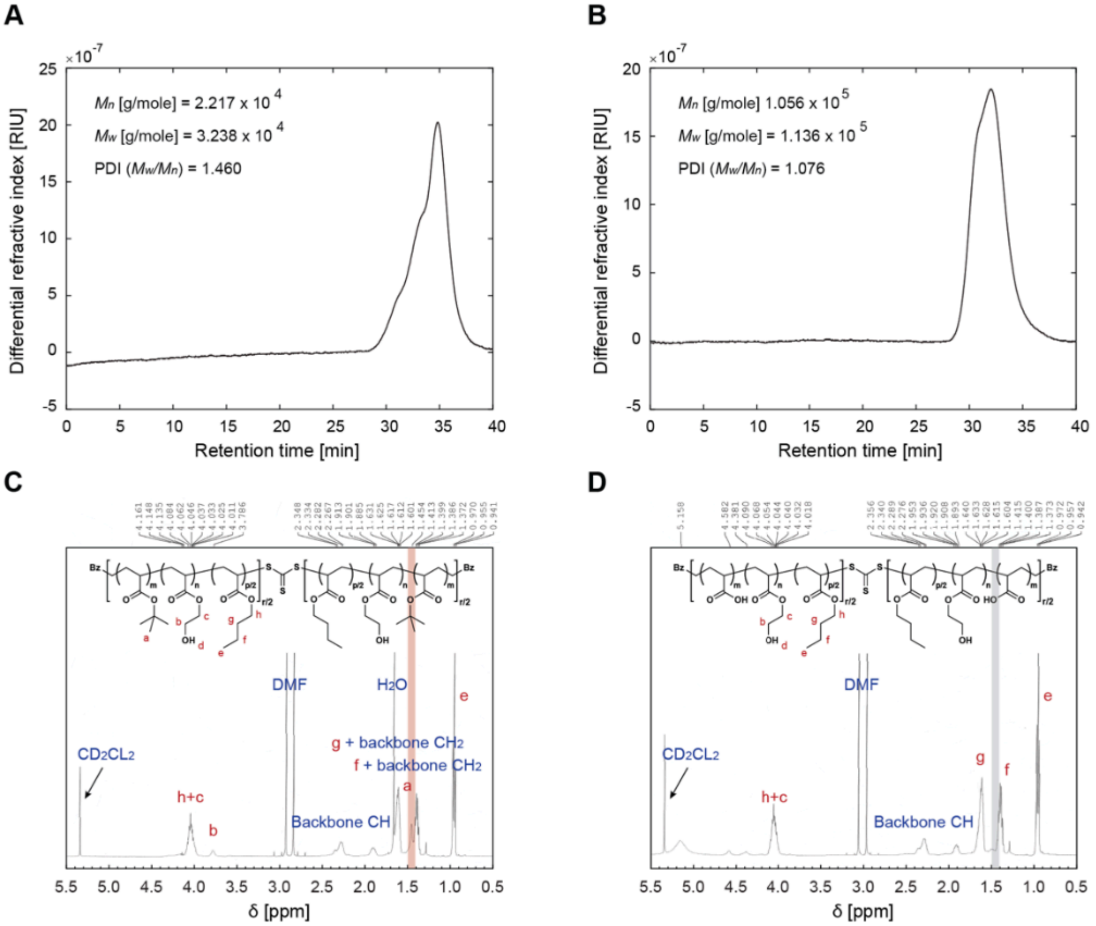

Figure A.2: Polymer characterization using GPC and NMR. (a) GPC traces of *bis*[p(*t*-BA-*r*-HEA)$_{10}$] trithiocarbonate (macro-CTA) and (b) p[(*t*-BA5-*r*-HEA$_5$)-*b*-(*n*-BA)$_{100}$-*b*-(*t*-BA$_5$-*r*-HEA$_5$)]$_r$ (deprotected copolymer). The weight average molecular weight (M$_w$) and number average molecular weight (M$_n$) of the final deprotected block copolymer are high and comparable to that of pectin, but with a very narrow molecular weight distribution (dispersity = M$_w$/M$_n$). Because of this narrow dispersity, the molecular weight distribution effect can be neglected while comprehending the thermal sensing properties and the mechanical performance of the block copolymer. (c) ^{1}H NMR spectrum of p[(*t*-BA$_5$-*r*-HEA$_5$)-*b*-(*n*-BA)$_{100}$-*b*-(*t*-BA$_5$-$_r$-HEA$_5$)]$_r$ dissolved in CD$_2$Cl$_2$, prior to deprotection of *tert*-

butyl group. (d) 1H NMR spectrum of p[(AA_5-*r*-HEA_5)-*b*-(*n*-BA)$_{100}$-*b*-(AA_5-*r*-HEA_5)]$_r$ dissolved in CD_2Cl_2, after deprotection of *tert*-butyl group. The disappearance of the peak at 1.45 ppm indicates complete removal of *tert*-butyl group, resulting in free acid.

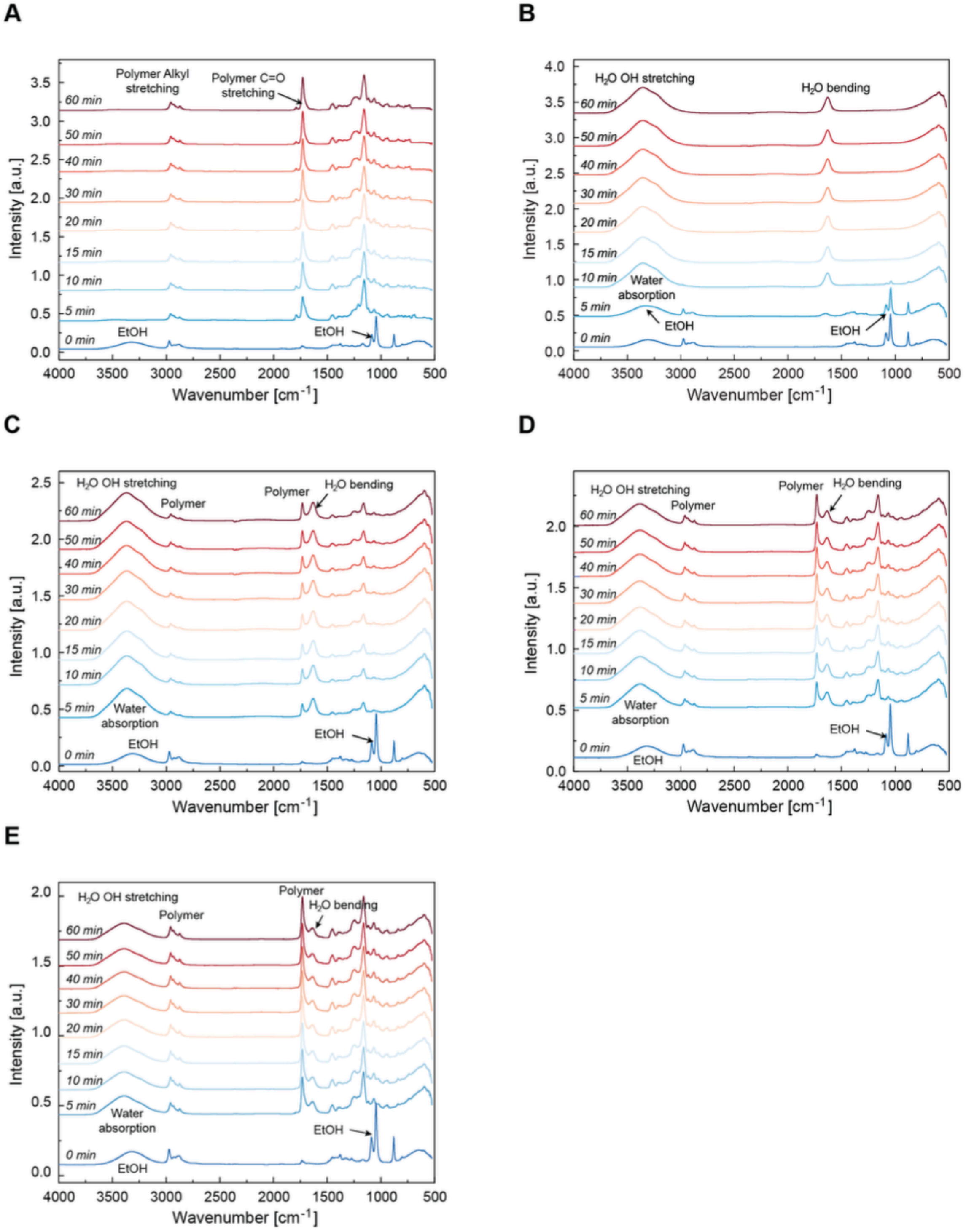

Figure A.3: ATR-FTIR spectra of the block copolymer and CaCl2 dissolved in ethanol, and the block copolymer-metal ion complex. Prior to observing the in-situ film formation behavior of the block copolymer-metal ion complex, the ATR-FTIR spectra of each component is measured for control and plotted with respect to drying time: (a) the block copolymer and (b) $CaCl_2$. In both cases, ethanol evaporates with less than 10 minutes. After this solvent removal, water molecules are absorbed on the metal ions, whereas no water absorption is observed in the block copolymer. ATR-FTIR spectra of the composite mixture of block copolymer with (c) 50%, (d) 25%, and (e) 10% concentration of $CaCl_2$ (table A.7) plotted with respect to drying time. In the beginning, characteristic peaks of the solvent, ethanol, appear dominantly on the spectrum; O-H stretching (3314 cm^{-1}), CH stretching (2972 cm^{-1} - 2878 cm^{-1}), and C-O stretching (1087 cm^{-1} and 1045 cm^{-1}), respectively. However, after 5 minutes, the peaks near the O-H stretching region broaden due to water absorption (3678 cm^{-1} - 3011 cm^{-1}) and peaks initially assigned to the CH stretching and C-O stretching disappear. Ethanol evaporation and water absorption occur very fast due to the relative hydrophobicity of polymer. Meanwhile new peaks also emerge; H_2O bending (1636 cm^{-1}); CH_3 stretching of *n*-BA (2958 cm^{-1}), CH stretching of AA (2934 cm^{-1}), CH_2 stretching of HEA (2873 cm^{-1}); C=O stretching of *n*-BA (1730 cm^{-1}), AA (1723 cm^{-1}), HEA (1719 cm^{-1}); C-O stretching of *n*-BA and HEA (1065 cm^{-1} and 1160 cm^{-1}). The arising new peaks correspond to the ABA block copolymer. The unique H_2O bending peak at 1636 cm^{-1} from the ATR-FTIR spectra after 1 hour elucidates that the intensities around 3678 cm^{-1} - 3011 cm^{-1} are due to water molecules absorbed on $CaCl_2$, confirming complete removal of ethanol.

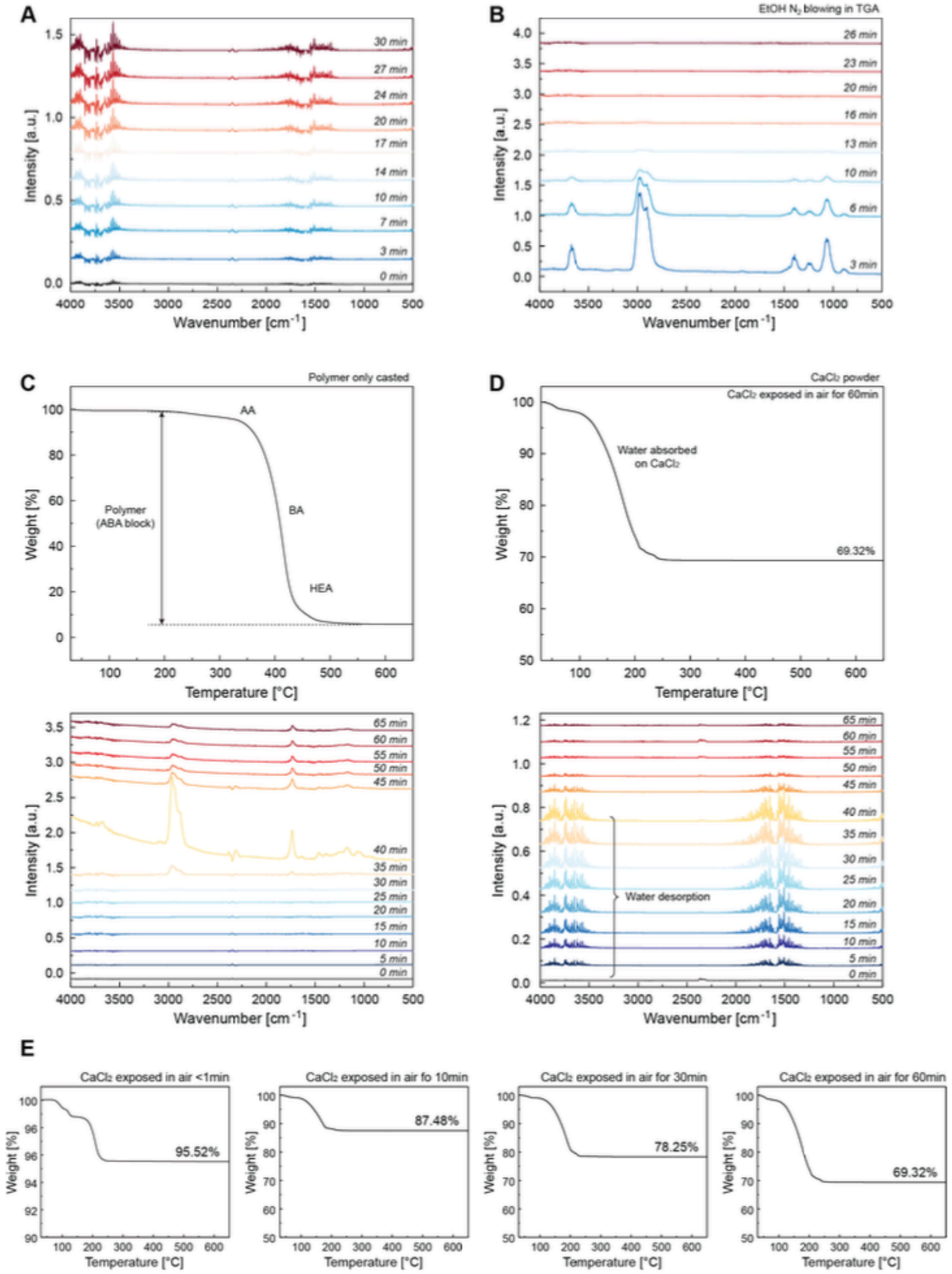

Figure A.4: TGA-FTIR spectra of water, ethanol, the block copolymer casted film, and $CaCl_2$ powder. TGA-FTIR spectra of (a) water and (b) ethanol plotted over time to distinguish the gas-phase materials diffused from TGA. The gas-phase FTIR spectra of water shows discrete peaks in the temperature range of 30 °C - 250 °C. Ethanol exhibits a strong alkyl stretching (3056 cm^{-1} - 2746 cm^{-1}) and OH vibration (3747 cm^{-1} - 3574 cm^{-1}) when purged with N_2 at RT. (c) TGA profile and the corresponding FTIR spectra of the non-crosslinked polymer solution previously dried for 12 hours. A first plateau appears in the temperature range of 30 °C - 210 °C, followed by a dip in the weight loss at 210 °C - 500 °C, indicating polymer degradation. A second plateau appears between 500 °C - 650 °C (residue: 5.798%). No sign of water is detected even after an additional 12 hours of drying time. (d) TGA profile and the corresponding FTIR spectra of $CaCl_2$. The first, stepwise weight loss is observed below 210 °C, revealing the presence of water molecules absorbed on the metal ions. This is further confirmed from the gas phase FTIR spectra. Later, a slow weight loss is detected between 210 °C - 650 °C. (e) TGA profiles of $CaCl_2$ powder exposed in air for different time period. The water absorbed on the metal ions increases with increasing time of exposure to the atmosphere.

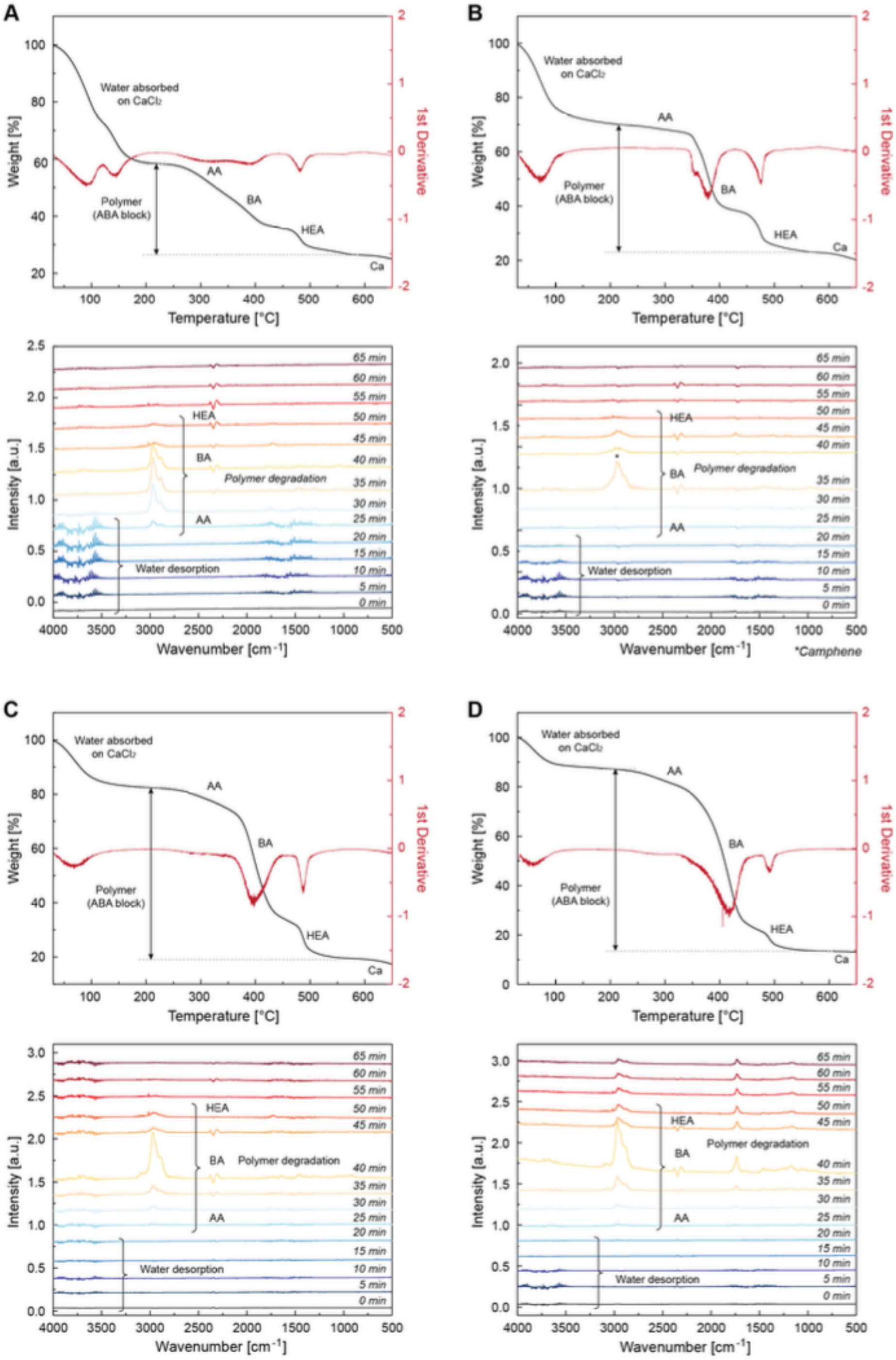

Figure A.5: TGA-FTIR spectra of the block copolymer-metal ion complex. TGA profiles and corresponding gas-phase FTIR spectra of the composite film formed using the ionically crosslinked block copolymer solution with varying amount of $CaCl_2$ concentration: (a) 100%, (b) 50%, (c) 25%, and (d) 10% (table A.7). The films are dried for 12 hours before measurement. The first weight loss appears between RT and 210 °C and represents the evaporation of the water molecules bound to $CaCl_2$, as shown in the characteristic peaks of the gas-phase FTIR spectra measured in the first 20 minutes. The following weight loss observed in the temperature range between 210 °C - 550 °C corresponds to the degradation of the block copolymer (AA, *n*-BA, HEA, and IPC), which is confirmed from the gas-phase FTIR spectra observed between 25 to 55 minutes. Finally, the slow weight loss detected in the range of 550 °C - 650 °C is caused by $CaCl_2$, confirmed by the gas-phase FTIR spectra between 55 to 65 minutes. The corresponding temperature of these events are identified by the 1st derivative of the TGA profile (red line). As the amount of $CaCl_2$ is increased, the following amount of water adsorbed in the polymer matrix increased, showing a linear relationship of $R^2 = 0.987$.

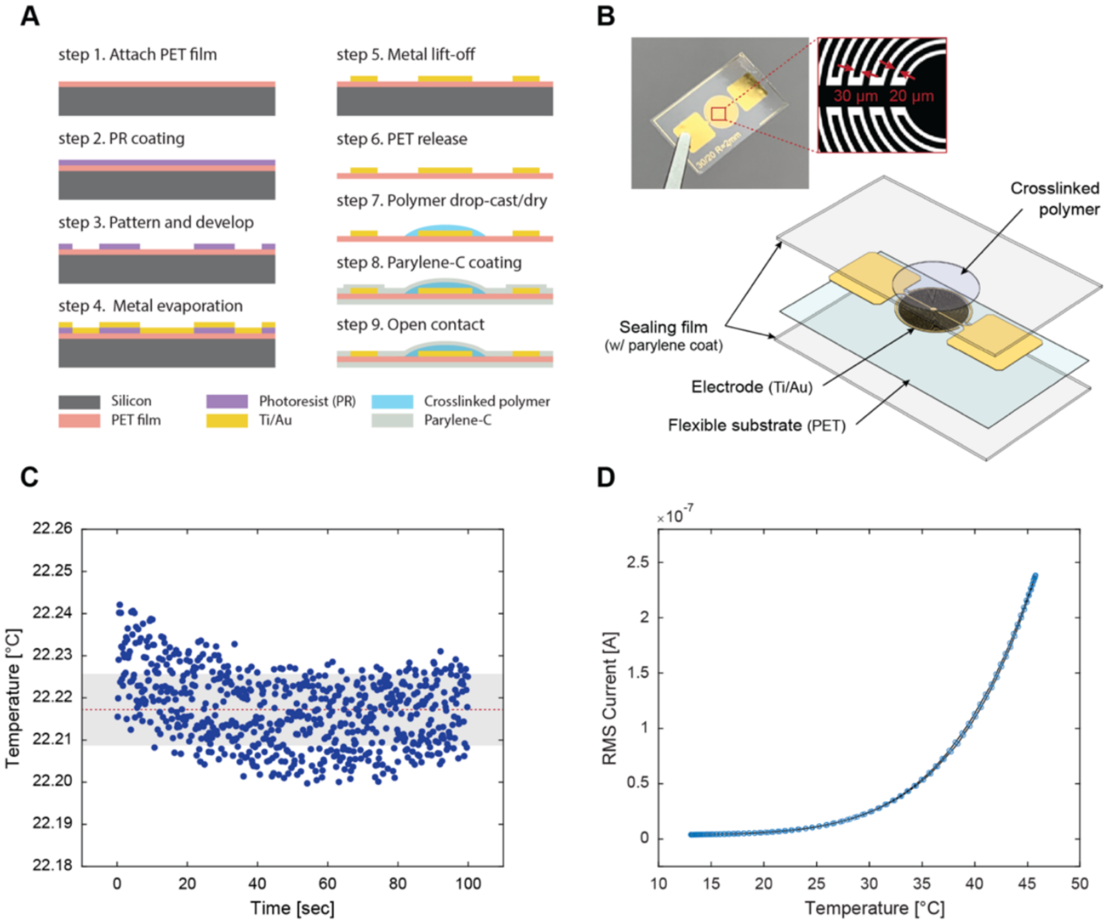

Figure A.6: Schematic and fabrication process of the block copolymer temperature sensor and

the measured noise level and hysteresis curve. (a) Device fabrication procedure. (b) Schematic (bottom) and optical image (top) of the fabricated sensor. (c) Temperature variation measured in air. The sensor's sensitivity is derived by calculating the standard deviation of the temperature fluctuation measured while placing the sensor on a constant temperature reservoir for 100 seconds. AC voltage of 300 mV used at 200 Hz for readout. (d) The sensor displays negligible hysteresis in the current readout.

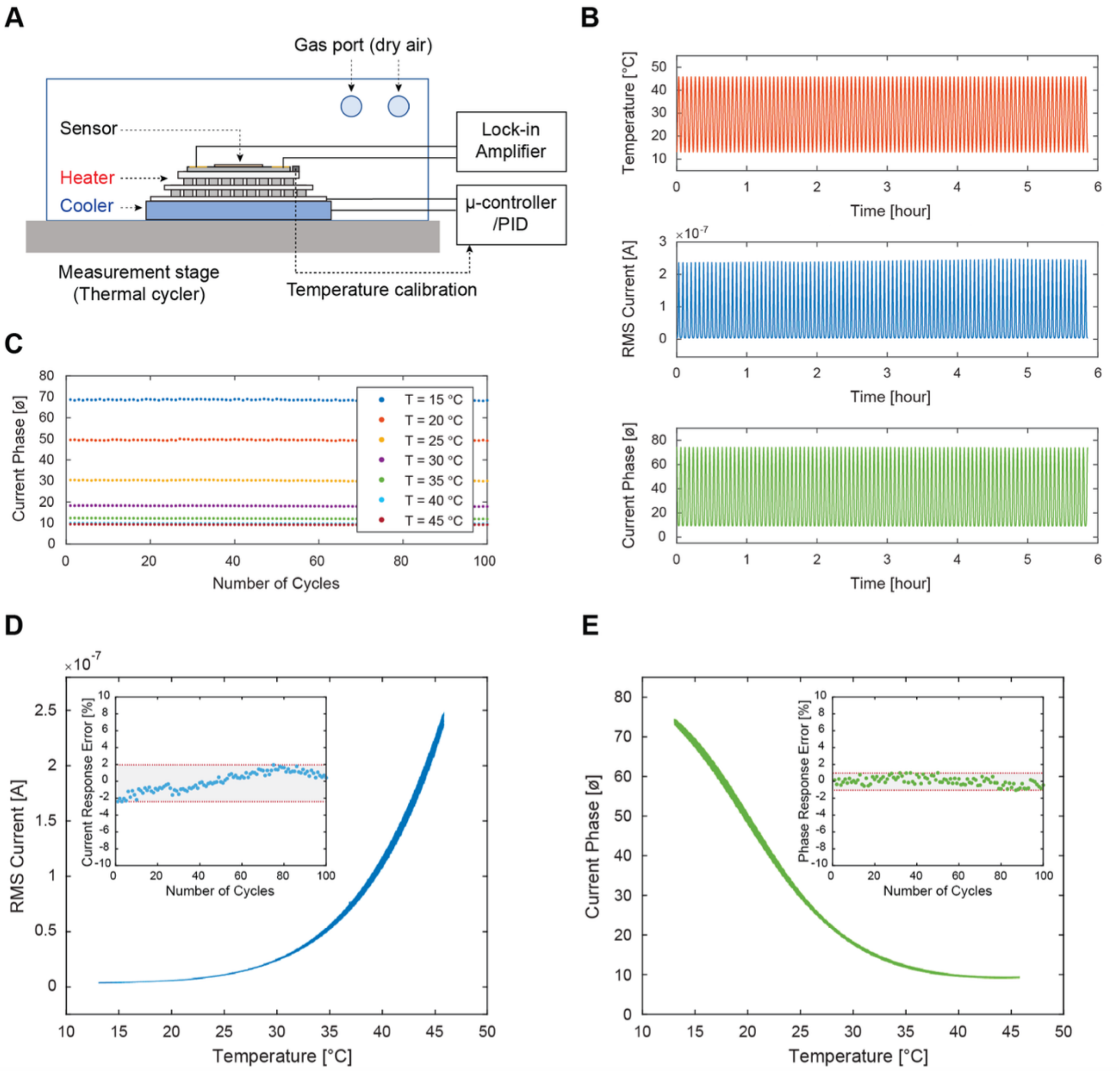

Figure A.7: Cyclic stability characterization of the block copolymer temperature sensor. (a) Schematic of the measurement set up. (b) Profile of the temperature cycles applied over time and the recorded RMS current and phase. (c) Current phase plotted by temperature during the 100-cycle measurement. Overlaid (d) RMS current (e) and phase recorded during 100 cycles of continuous measurement. Inset: The current response error and phase error between each cycle.

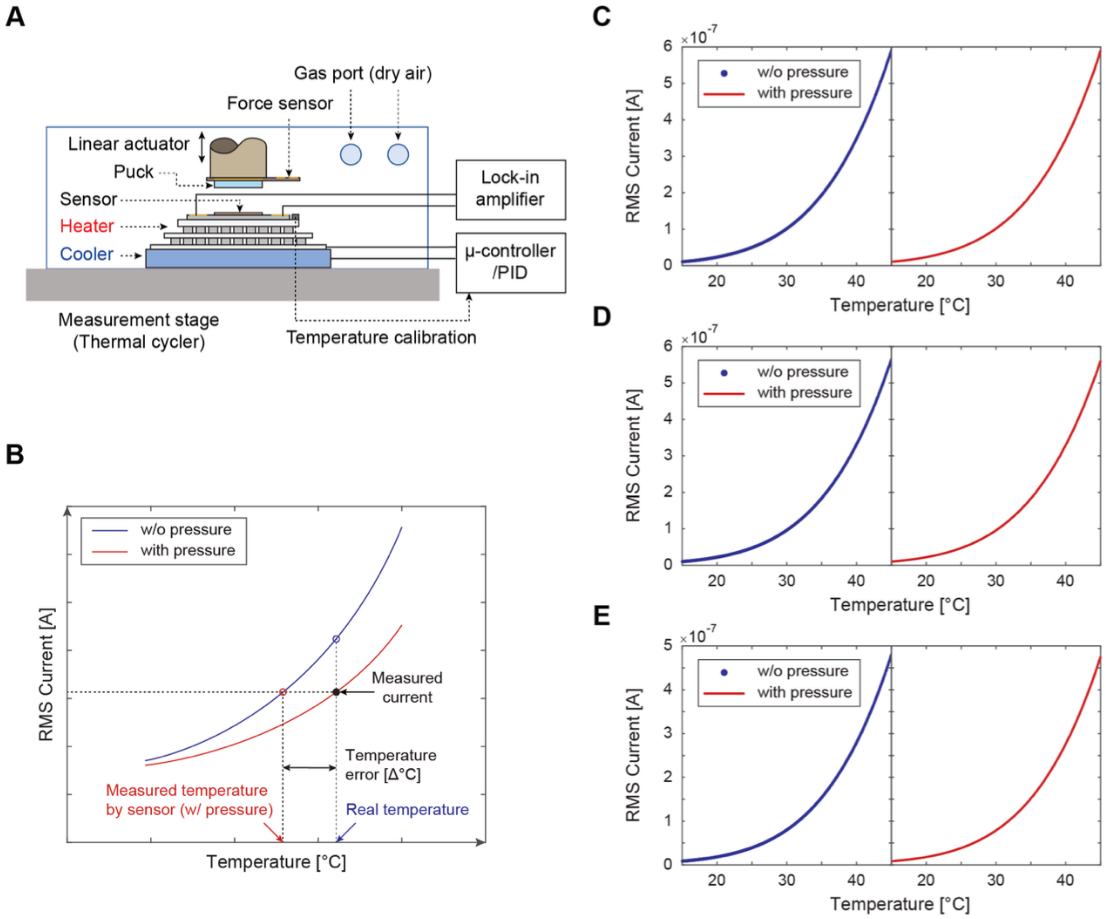

Figure A.8: Effect of normal strain on the block copolymer temperature sensor. (a) Schematic of the measurement set up. An external pressure is applied through a linear actuator vertically placed on top of the sensor. (b) Diagram illustrating method for calculating temperature error induced by the applied external pressure. The blue line represents the ideal RMS current measured when no pressure is applied, while the red line represents the RMS current measured when external pressure is applied. Current as a function of temperature measured with and without (c) 2.5 kPa, (d) 25 kPa, and (e) 250 kPa of normal pressure applied to the sensory material.

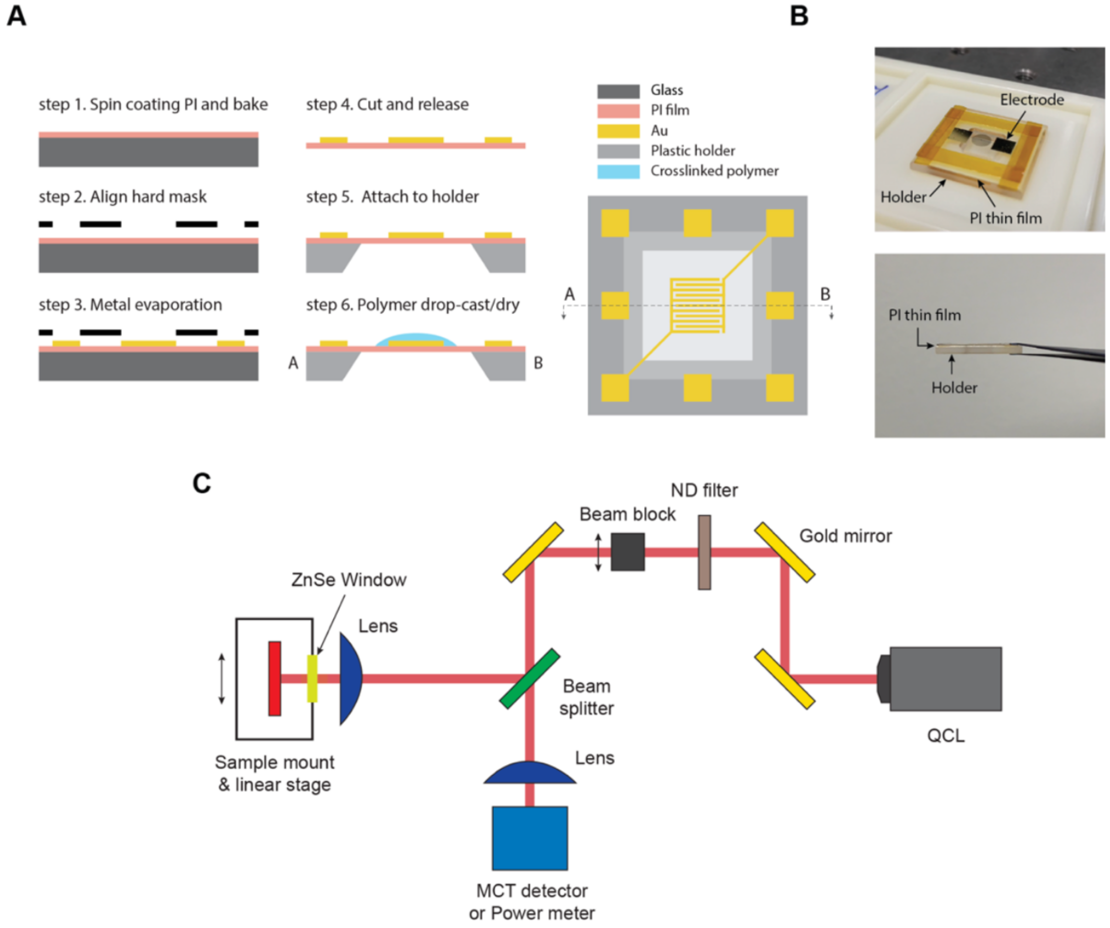

Figure A.9: Schematic and fabrication process of the block copolymer IR detector and the optical setup for IR measurement. (a) Device fabrication procedure. (b) Optical image of the fabricated sensor. (c) The power and wavelength of the IR beam is independently controlled by the QCL. The sensor is placed in a hermetically sealed chamber. All measurements are performed at room temperature.

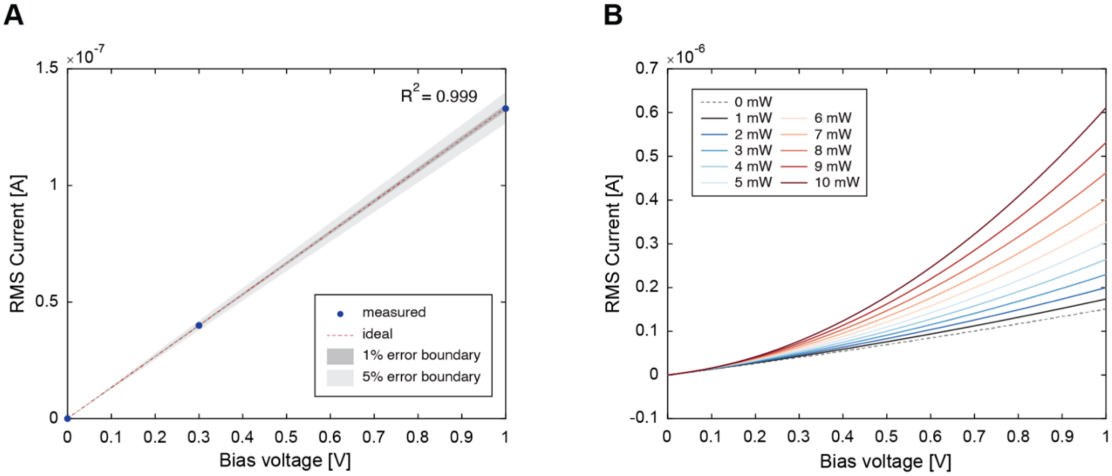

Figure A.10: Voltage-current curves of the IR sensor. (a) Current as a function of AC voltage bias (200 Hz) measured under dark state, and (b) under different IR irradiation power at a wavelength of 8.5 µm. A linear relationship between the bias voltage and current, when no power is applied, indicates negligible joule heating effect during readout.

A.2 Tables

Table A.1: HLB calculation of the polymer's 'A' block.

Hydrophilic and hydrophobic groups in the 'A' block		Group number (a)	Number of group number (b)	(a) x (b)
Hydrophilic	ester (free)	2.4	0.934	2.24
	-COOH	2.1	1	2.1
	OH (free)	1.9	0.934	1.77
	-O-	1.3	0.934	1.21
Hydrophobic	CH-	-0.475	1.934	-0.91
	-CH2-	-0.475	3.802	-1.80
HLB value of the 'A' block (Davies' method)		$HLB = 7 + \sum_{n=1}^{m} H_i - n \times 0.475$		13.03

m: number of hydrophilic groups in the molecule

n: number of lipophilic groups in the molecule

Hi: value of the ith hydrophilic group

Table A.2: ^{1}H NMR measurement of the synthesized polymer.

Functional Groups	δ [ppm]	Protected Intensity	Deprotected Intensity
h+c (*n*-BA, HEA, Methylene (CH_2) -OC(=O)-C)	4.01 - 4.09	0.71	0.68
b (HEA, Methylene (CH_2) -O)	3.78 → 4.38	0.1	0.08
Backbone (Methine (CH))	2.26 - 2.34	0.35	0.35
Backbone (Methylene (CH_2))	1.88 - 1.91	0.18	0.18
g+Backbone (*n*-BA, Methylene (CH_2))	1.60 - 1.63	0.94	1.06
a (*t*-BA, Methyl (-CH_3))	1.45	0.37	(trace)
f+Backbone (*n*-BA, Methylene (CH_2))	1.38 - 1.41	0.70	0.73
e (*n*-BA, Methyl (CH_3))	0.94 - 0.97	1	1

The monomer ratio of the as-synthesized copolymer (protected form) was determined by the peak ratio between HEA ethylene (**b**, 3.78 ppm) and *t*-BA methyl (**a**, 1.45 ppm) as well as *n*-BA methyl (**e**, 0.94 - 0.97 ppm) and *t*-BA methyl (**a**, 1.45 ppm): HEA/*t*-BA = (**b**/2)/(**a**/9) = 0.97, *n*-BA/*t*-BA = (**e**/3)/(**a**/9) = 8.1 (Fig. A.2(c-d)). The conversion of *t*-BA to AA was confirmed by the disappearance of *t*-BA methyl (**a**, 1.45 ppm) peak after the reaction with TFA in the deprotection step. (Deprotection rate = 100%)

Table A.3: Estimation of repeating unit numbers based on the NMR spectrum.

Monomer	Feed mole [μmol] (molar ratio)	Measured NMR ratio	Molecular weight [g/mol]	Adjusted mass of monomers with NMR ratio [g/mol]	Calculated mass of copolymer [g/mol]	Monomer numbers in the copolymer chain
HEA	10 (1)	0.97	116	112.64	9,292.4	80
***t*-BA**	10 (1)	1	128.17	128.17	10,981.5	86
***n*-BA**	100 (10)	8.1	128.17	995.88	85,326.1	694
Sub sum	***120 (12)***	***10.07***	***372.34***	***1,236.69***	***105,600***	***860***

Molecular weight GPC (*Mn*) [g/mol]	Mass of repeating unit [g/unit]	Repeating unit numbers in the block copolymer chain
105,600	1,236.69	85.4

Table A.4: ATR-FTIR peak assignment

0 min	3314 $[cm^{-1}]$	2972 $[cm^{-1}]$	2927 $[cm^{-1}]$	2878 $[cm^{-1}]$	Polymer Film + $CaCl_2$										1087 $[cm^{-1}]$	1045 $[cm^{-1}]$
Assign	OH Stretching EtOH	CH Stretching EtOH													C-O stretching EtOH	
5 min	3610 - 3200 ①	2958 ②	2934 ②	2872 ②	1729 ③	1723 ③	1719 ③	1634 ④	1454 ⑤	1397 ⑥	1378 ⑥	1246 ⑦	1160 ⑦	1065 ⑧		
10 min	3610 - 3200	2959	2933	2872	1730	1723	1719	1636	1450	1397	1378	1243	1160	1065		
15 min	3610 - 3200	2958	2934	2873	1730	1723	1719	1634	1450	1397	1378	1245	1160	1065		
20 min	3610 - 3200	2958	2934	2873	1730	1723	1719	1636	1450	1397	1378	1243	1160	1065		
30 min	3610 - 3200	2958	2934	2873	1730	1723	1719	1636	1450	1397	1378	1243	1160	1065		
40 min	3610 - 3200	2958	2934	2873	1730	1723	1719	1636	1450	1397	1378	1245	1160	1065		
50 min	3610 - 3200	2958	2934	2873	1730	1723	1719	1636	1450	1397	1378	1243	1160	1065		
60 min	3610 - 3200	2958	2934	2874	1730	1723	1719	1636	1454	1397	1378	1242	1160	1065		
Assign	Free OH (3630 - 3670 cm^{-1}) Dimer OH (OH-OH) Intramolecular OH (OH-O=C) (3540 - 3550 cm^{-1}) Intermolecular OH (3400 - 3450 cm^{-1}) OH Stretching HEA+AA+H_2O on Ca Aggregate OH (3240 - 3280 cm^{-1})	CH_3 Stretching *n*-BA	CH Stretching AA	CH_2 Stretching HEA	C=O Stretching (Interpolymer Complex, IPC) *n*-BA 1730 cm^{-1} AA 1723 cm^{-1} HEA 1719 cm^{-1}			H_2O Bending	CH in-plane bending *n*-BA	C-O-H Deformation AA		C-O Stretching *n*-BA	C-O Stretching HEA AA (IPC)	C-O Stretching HEA		

Table A.5: Composition of the tested mixtures during the ATR-FTIR and TGA-FTIR spectra measurement. (in-situ monitoring of film formation)

Materials	**Percentage of $CaCl_2$ mixed**			
	100 %	**50 %**	**25 %**	**10 %**
ABA block copolymer (140 mg/10 mL)	100 μL	100 μL	100 μL	100 μL
Ca (1 M in EtOH)	52 μL	26 μL	13 μL	6.5 μL

Table A.6: Percentage of IPC formed in the composite film.

Material	Molecular weight [g/mol]	Input solution volume [μL]	Mass in input solution [g]	Number of molecules	Number of repeating unit	Total number of AA and Ca^{2+} ions input
Polymer	105600	99.90	1.40 x 10^{-2}	7.95 x10^{16}	85.7	***6.81 x 10^{19}***
$CaCl_2$ (100 %)	110.98	172.80	5.75 x 10^{-3}	3.11 x 10^{19}	1	***3.11 x 10^{19}***

Number of bound Ca^{2+}	***3.11 x 10^{19}*** x 11.62 %	0.36 x 10^{19}
Number of bound AA	(Number of bound Ca^{2+}) x 2	0.72 x 10^{19}
Number of AA that can form IPC	***6.81 x 10^{19}*** – (Number of bound AA)	6.09 x 10^{19}
Maximum number of AA involved in IPC formation	(Number of AA that can form IPC) x 0.97 * AA to HEA ratio in polymer = 0.97	5.91 x 10^{19}

Free AA (Ca^{2+} bound)	0.72 x 10^{19} / ***6.81 x 10^{19}*** x 100	**10.61 %**
AA forming IPC	5.91 x 10^{19} / ***6.81 x 10^{19}*** x 100	**86.13 %**

Number of AA functional groups and Ca^{2+} ions in the polymer-$CaCl_2$ solution mixture (top). Estimating the number of AA involved in Ca^{2+} binding and IPC formation based on AA-Ca^{2+} titration analysis (middle). Percentage of AA forming IPCs in the composite film (bottom). The total number of bound Ca^{2+} is first calculated based on the total number of input metal ions and the percentage of the unwashed portion measured during titration analysis. By subtracting the total number of Ca^{2+} bound AA to the total number of AA present in the BTS polymer, the amount of AA that can form IPCs can be obtained. Since the AA to HEA ratio in the polymer is 0.97, the maximum number of AA that can engage in the IPC formation becomes 5.91 x 10^{19}. Finally, the percentage of AA that forms IPC can be calculated by dividing this value with the total number of AA existing in the block copolymer.

Table A.7: Composition of the three different types of polymers synthesized for response comparison.

	Type 1	Type 2	Type 3
AA:HEA ratio	5:5	4:7	10:0
Amount of AA + HEA content	10	11	10
Amount of AA content	5	4	10
Amount of IPC content	5	4	0

Polymer structure	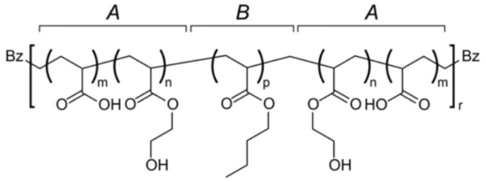

Appendex B

SI FOR CHAPTER 3

B.1 Materials and Methods

B.1.1 HEA-AA Synthesis

Polymer films were prepared following the procedure reported in the previous paper, employing reversible addition-fragmentation chain transfer (RAFT) polymerization as shown in Fig. B.1.[1] Unlike as reported in Kim et al.[1], we did not synthesize a block copolymer but we only used the 2-Hydroxyethyl acrylate and the tert-Butyl acrylate units for this work. Nitrogen purged tert-butyl acrylate (1.28 g, 10 mM) and 2-hydroxyethyl acrylate (1.16 g, 10 mM) is dissolved in 2 mL DMF, followed by S,S-Dibenzyl trithiocarbonate 3 (29 mg, 0.1 mM). The mixture is further purged under nitrogen for 3 minutes, added with AIBN (0.8 mg, 5 μM), and then stirred at 75 °C under protection of N_2, and the progress in polymerization was monitored using ^{1}H-NMR. The reaction was cooled down and vented to air at approximately 80% conversion rate. Residual tert-butyl acrylate and 2-hydroxyethyl acrylate was removed first by drying. For deprotection, the polymer (1 g) was dissolved in 3 mL dichloromethane (DCM), followed by addition of 3 mL trifluoroacetic acid (TFA). The reaction was stirred at room temperature overnight. DCM and TFA were removed by drying, to result in a highly sticky yellow oil, HEA-AA (100%). We then mixed the deprotected HEA-AA with a calcium chloride solution (300 mM) in ethanol 1:2 in volume to obtain the final solution.

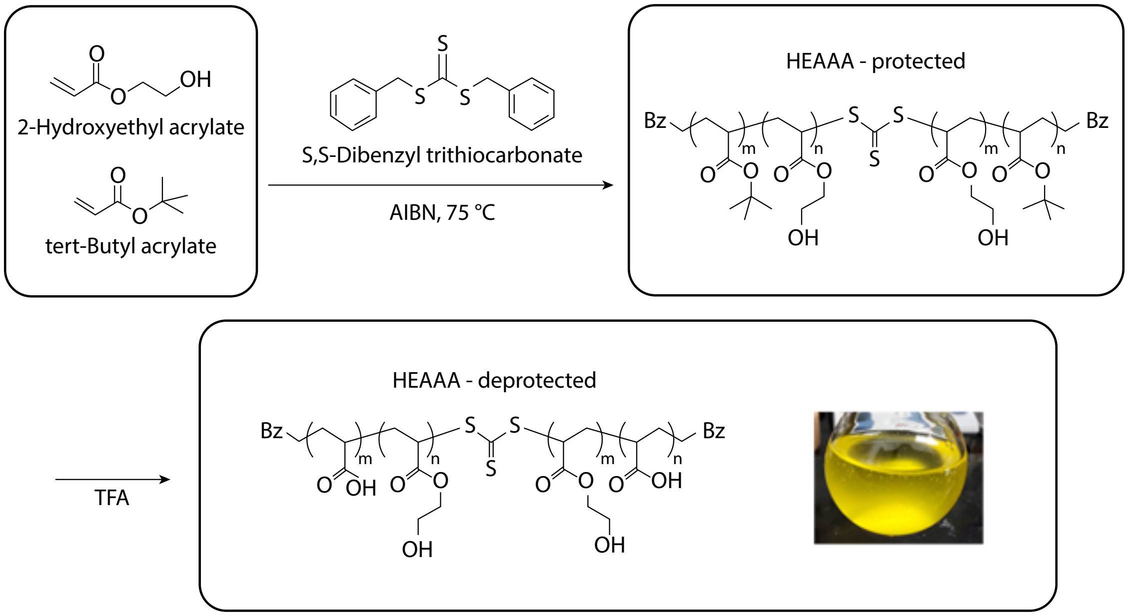

Figure B.1: HEA-AA Synthesis.

B.1.2 Density Functional Theory (DFT) Calculation

In-order to evaluate the potential mechanisms of ion conduction and the origin of the temperature response behavior, binding energy was evaluated in density functional theory (DFT) studies. Due to the complexity of ion binding in the polymer system, crude model complexes were constructed that we believe will approximate the possible binding energies of individual ligating atoms. We do not believe that these models capture the actual binding energies of the ions to our polymer, however they provide approximate numbers to evaluate the relative strengths of the interaction energies. DFT studies were conducted through ORCA (version 4.2.0) with the B3LYP functional. A def2-TZVP basis set with a def2/J auxiliary basis set was applied. The structures were optimized and frequency calculations were carried out. Only the calcium acetic and calcium acetate structures exhibited imaginary frequencies (consistent with their methyl rotor structures). From these structures, single point energy calculations were carried out utilizing ORCA's atom-pairwise dispersion correction and/or ORCA's conductor-like polarizable continuum model for a water solvent. The introduction of dispersion was found to only slight effect the calculated binding energy. While the inclusion of solvent dramatically effects the binding energies, due to the typically dry state of the polymer, the significance of these results in the experimental system are questionable. Due to the crudeness of these models and their relatively small contributions (based on prior calculations by the authors on related complexes), we selected to not apply a diffuse basis set, nor account for basis set superposition exchange.

Table B.1: Binding energies calculated using DFT

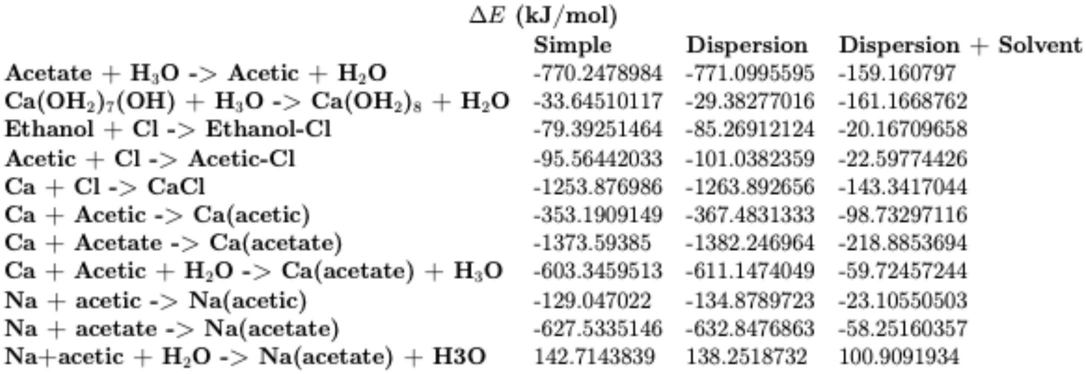

	ΔE (kJ/mol)		
	Simple	**Dispersion**	**Dispersion + Solvent**
Acetate + H_3O -> Acetic + H_2O	-770.2478984	-771.0995595	-159.160797
$Ca(OH_2)_7(OH)$ + H_3O -> $Ca(OH_2)_8$ + H_2O	-33.64510117	-29.38277016	-161.1668762
Ethanol + Cl -> Ethanol-Cl	-79.39251464	-85.26912124	-20.16709658
Acetic + Cl -> Acetic-Cl	-95.56442033	-101.0382359	-22.59774426
Ca + Cl -> CaCl	-1253.876986	-1263.892656	-143.3417044
Ca + Acetic -> Ca(acetic)	-353.1909149	-367.4831333	-98.73297116
Ca + Acetate -> Ca(acetate)	-1373.59385	-1382.246964	-218.8853694
Ca + Acetic + H_2O -> Ca(acetate) + H_3O	-603.3459513	-611.1474049	-59.72457244
Na + acetic -> Na(acetic)	-129.047022	-134.8789723	-23.10550503
Na + acetate -> Na(acetate)	-627.5335146	-632.8476863	-58.25160357
Na+acetic + H_2O -> Na(acetate) + H3O	142.7143839	138.2518732	100.9091934

B.1.3 *Differential Scanning Calorimetry (DSC)*

Thermal measurements were conducted using Differential Scanning Calorimetry 250 from TA instruments. Nitrogen gas purging was set at 50 ml/min flow rate. 40 μL HEA-AA was deposited in a Tzero aluminum pan. After dehydration in a nitrogen box at room temperature over 24 hours, its weight was measured to be 3.3 mg. The temperature scanning was performed at 10 °C/min, cycling from -40 °C to 100 °C. During the measurement, the remaining water in the sample evaporates at high temperature. After the DSC scans, the weight of the sample decreased to 3.1 mg.

B.1.4 Gravimetric Measurement

Gravimetric measurements of the samples were performed via a precision quartz microbalance (openQCM Q-1, 5MHz). 500 nL of HEA-AA with a concentration of 0.3 g/mL was deposited on the active area of the quartz (12 mm diameter) and dehydrated in a vacuum chamber for half an hour. The so prepared samples were kept overnight in a glove box flushed with nitrogen to eliminate excess ethanol and water from the polymer matrix. The resonance of the so prepared sample was then measured in the humidity box at different RH.

B.1.5 FTIR

$CaCl_2$-HEA-AA was drop cast onto a piece of silicon wafer and dried at 70 °C on a hotplate for several days. The sample was then stored in a desiccator. Transmission Fourier transform infrared spectroscopy (FTIR) was acquired on a Nicolet 6700 FTIR purged with nitrogen. A blank spectrum was taken on silicon wafer at several intervals over a 25 minute period to observe the removal of gases introduced during the sample placement. The spectrum taken at 25 minutes was used as the reference for calculating absorption of the sample. FTIR of the dried sample was then taken at several intervals over a 20 minute period. The spectrum taken at 20 minutes was used at the dried sample spectrum. The sample was then placed on an elevated platform in a sealed container with a small quantity of water or detereum oxide, for 15 minutes. The sample was removed from the humidity chamber and FTIR was then taken at several intervals over a 180 minute period.

The FTIR data was fit utilizing a custom python script for the data from 1519.66-1897.64 cm^{-1}. It was fit with 8 gaussian peaks and a linear background. Peak locations and widths were identically constrained for all fits, constraints were set by visual inspection of the data. Peaks at ~1563 cm^{-1} and ~1597 cm^{-1} were assigned to the calcium bound carboxylic acid. The peak at ~1620-1630 cm^{-1} was assigned to water. The areas of the peaks were evaluated and plotted (Fig. B.2).

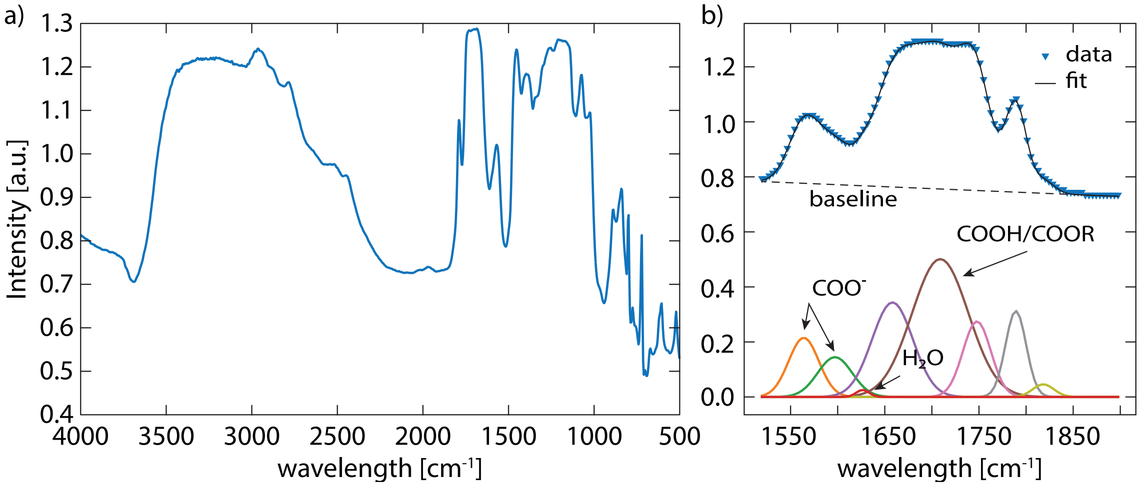

Figure B.2: FTIR Analysis of Drying Behavior (a) Transmission FTIR spectrum of HEA-AA after 30 min under N_2. (b) Peak identification and fitting of the FTIR region between 1500 and 1900 cm^{-1}.

B.1.6 UV/Vis

CoC_2-HEA-AA and $CoBr_2$-HEA-AA solutions in ethanol were prepared at a 0.2 M ion concentration and 0.2 g/mL polymer concentration. Films were prepared by depositing 200 µL onto a glass slide

$CoCO_3$ was prepared by reacting $CoCl_2$ with Na_2CO_3 in water. The precipitate was washed with ethanol and dried under vacuum. To prepare a Co^{2+}-HEA-AA solution, excess $CoCO_3$ was added to a 0.2 g/mL solution of HEA-AA in ethanol and left stirring overnight. Films were then prepared by depositing 200 µL of the supernatant onto a glass slide.

The films were dried in a desiccator and then spectra of the films were taken on a Carry 500 UV/Vis/NIR spectrophotometer.

A $CoCl_4^{2-}$ solution was prepared by dissolving $CoCl_2$ in water then adding hydrocholric acid, the sample was diluted with water and hydrocholric acid until a suitable absorbance was achieved. A $CoBr_4^{2-}$ was prepared by dissolving $CoBr_2$ in a saturated aqueous solution of LiBr. Spectra of these solutions were collected on a HP8453 spectrophotometer.

B.1.7 Humidity Control

A custom humidity-controlled box was built to control humidity between 0% and 60%. A mix between air flow passing through desiccants beads was mixed with air flow coming from a water tank. By adjusting the air speed and the mix between the two flows the correct humidity can be achieved in the chamber. The humidity was then measured by a humidity sensor (Sensoria SHT16) placed in close proximity to the sample and used to keep the humidity constant in the chamber. A breakout board was placed into the humidity box in order to connect sample to the impedance analyzer. The computer was connected to the humidity controller, the temperature controller and the impedance analyzer in order to set the set points and collect the humidity, temperature and impedance data (Fig. B.3(a)). The humidity value was stable over time, as shown in Fig. B.3(b)) and the controller achieved a good accuracy (less ± 0.3 %) for all the RH values used in this study. (Fig. B.3(c)).

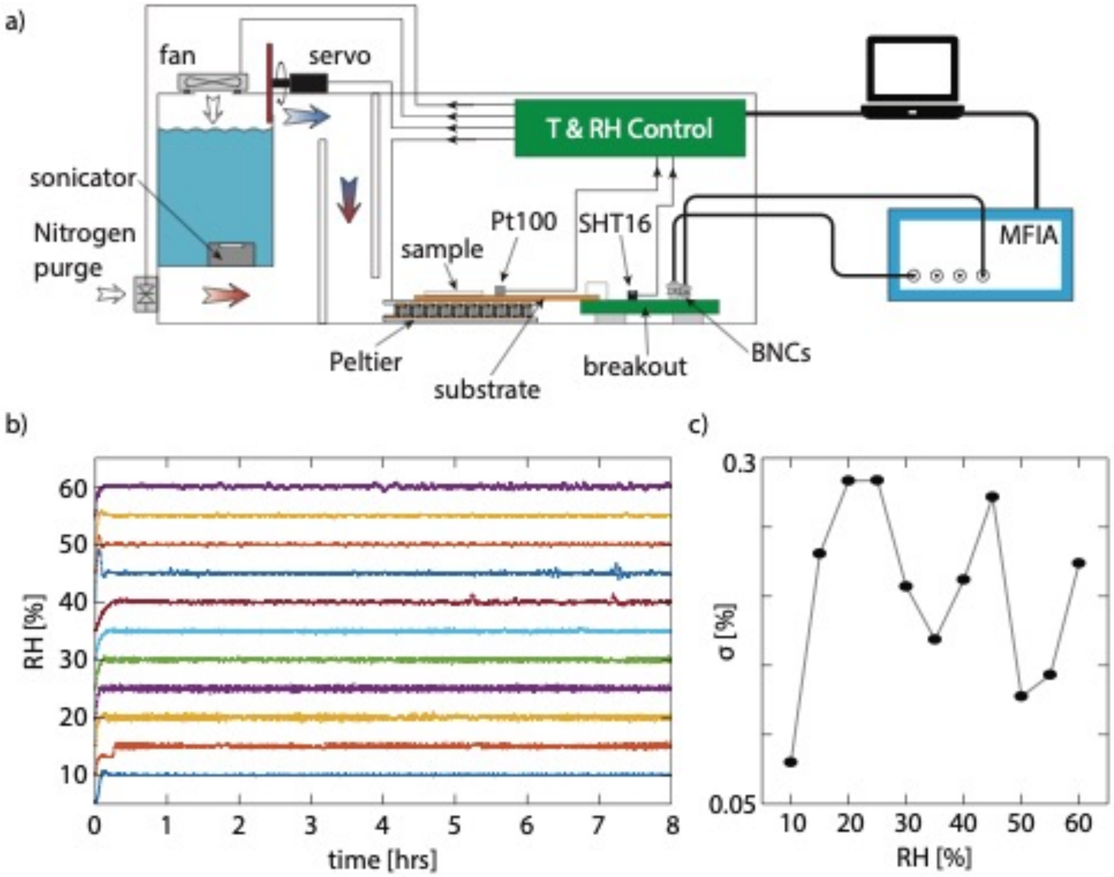

Figure B.3: Humidity Control Instrumentation. (a) Schematic of the custom made environmental controlled chamber to performed the humidity/temperature controlled experiments. (b) Recorded RH over time (8 hours) for various set points. (c) Measured standard deviation over the experiment time for various RH levels.

B.1.8 Impedance Spectrum

5 µL of ion-HEA-AA (1g/mL) were then deposited on polyimide substrates, prepatterned with gold electrodes and dried under vacuum for half an hour. The so prepared samples were kept overnight in a glove box flushed with nitrogen to eliminate ethanol/water excess from the polymer matrix. The impedance spectra were acquired by an impedance analyzer (Zurich Instrument, MFIA 5 MHz). The samples were kept at room temperature (40 °C) for the whole duration of the experiment. This temperature was chosen in order to obtain an appropriate water content for the humidity range tested. In addition, to ensure that the water content reached the equilibrium we kept the samples at the specific humidity for 8 hours at

1Hz before starting the frequency sweep. After this time, we acquired the impedance spectra between 1 Hz and 5 MHz with different current ranges (i.e., 1 µA, 10 µA and 100 µA), to ensure the highest accuracy. The data sets were then merged. The humidity was increased from 5% to 50%. It should be noted that the data shown in this work, are presented in form of conductance rather than its dimensionless counterpart conductivity, given the planar geometry at which the measurements were performed. This might sound uncommon practice, however, when looking at the same sample, the ion conductivity will scale in the same way, therefore when calculating the slopes of group of points over frequency or measure temperature response, it will be independent from the geometry of the sample. We measured the impedance of the empty cell (comprising of the substrate, connectors and cables) and subtracted these values from the one of the full sample to eliminate parasitic effects arising from spurious capacitance (Fig. B.4)

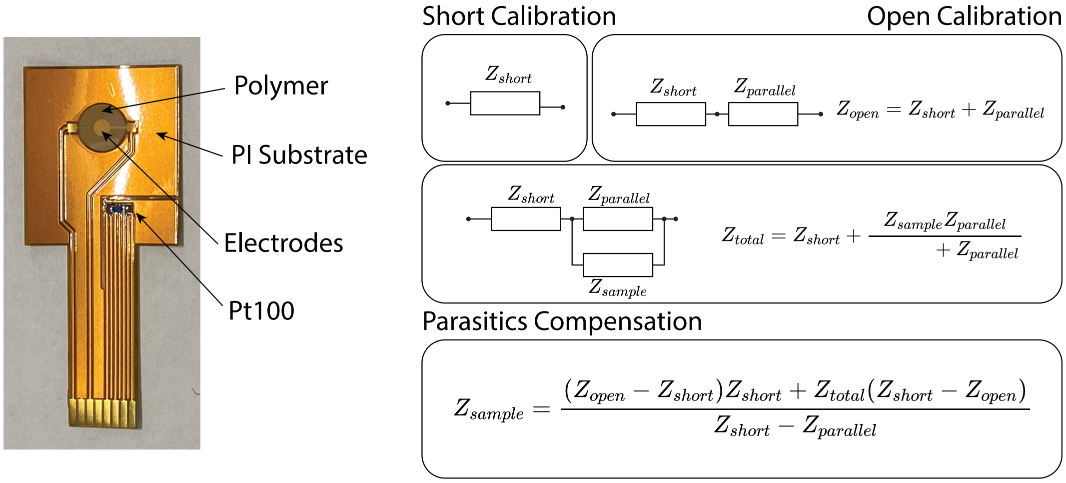

Figure B.4: Parasitics compensation. (a) Image of the substrates used for the impedance spectroscopy measurements. (b) Parasitics compensation procedure.

B.1.9 Response Calculation

Temperature cycles on the films were actuated by a Peltier-Element (model Qc-31-1.4-8.5m). The temperature was independently measured with a Pt100 platinum resistance thermometer placed on the polyimide substrate near the polymer. The Pt100 sensors were previously calibrated with a FLIR thermal camera (A655SC). A PID controller was implemented to generate a sinusoidal temperature between 27 ° and 62 °C. The substrates and the reference Pt100 were electrically connected through an interface board that could be connected with the impedance analyzer and the temperature control board. The current was measured with the impedance analyzer with an average sampling rate of 10 S/s. The temperature response as a function of frequency was isochronically measured: the frequency was kept constant within one temperature cycles and then changed to the next frequency at the next temperature cycle. The frequency was swept from 1 Hz to 500 kHz. To avoid the thermal hysteresis due to the sample mass we then considered only the increasing part of the temperature response and sampled the current at different temperatures. The real part of the temperature response after each thermal cycle were calculated as the ratio between the conductance measured at 62 °C and 27 °C. The humidity was kept constant for 10 hours and then switched to the next value. Relative humidity was swept from 5% to 20% in increase of 3%.

B.1.10 Data Fitting

All the impedance data were corrected for the parasitic effect before the fitting routine using methods described above. Both the real and imaginary parts of the conductance data were used for the nonlinear regression. We chose the mean squared logarithmic error (MSLE) as the loss function because the fitted conductance spans several orders of magnitude over the measured frequency range and MSLE is a better measure to minimize the percentage error of our fitting. Basin hopping minimization method was used to find the global minimum of the loss function.

For the VTF fitting, we assume that G_0 is the same for measurements at all RH. Due to experimental constraints, the conductivity data were collected for a relatively small temperature range. Fitting B, T_0 and G_0 simultaneously, for each RH results in multiple local fitting minimums. Since G_0 is the conductance at the infinite temperature and is proportional to the concentration of all the possible current carriers in the system, it should not change with RH. Therefore, during the fitting we set G_0 as the shared parameter for all RH.

B.1.11 Time-Humidity-Superposition

To check whether impedance spectrum at various RH superimpose and follow the Summerfield scaling, we plotted them in the scaled axes G/G_{DC} and v/G_{DC}. As shown in Fig. B.5, significant deviations could be observed in the dispersion regime. Time-Humidity-Superposition principle does not apply in our system because the ion hopping process and the high-frequency relaxation respond to humidity change differently.

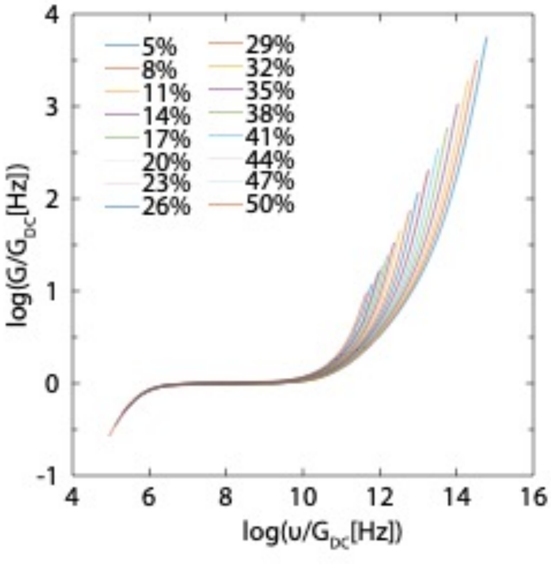

Figure B.5: Superimposed spectra at different RH.

Reference

(1) Kim, T. H.; Zhou, Z.; Choi, Y. S.; Costanza, V.; Wang, L.; Bahng, J. H.; Higdon, N. J.; Yun, Y.; Kang, H.; Kim, S.; Daraio, C. Flexible Biomimetic Block Copolymer Composite for Temperature and Long-Wave Infrared Sensing. *Sci. Adv.* **2023**, *9* (6), eade0423. https://doi.org/10.1126/sciadv.ade0423.